

SPINAL CORD DEFORMATION DURING AXIAL IMPACT INJURY  
OF THE CERVICAL SPINE

by

AMY SAARI

B.Sc. (Eng), University of Guelph, 2003

A THESIS SUBMITTED IN PARTIAL FULFILLMENT OF THE REQUIREMENTS  
FOR THE DEGREE OF

MASTER OF APPLIED SCIENCE

in

THE FACULTY OF GRADUATE STUDIES  
(Mechanical Engineering)

THE UNIVERSITY OF BRITISH COLUMBIA

January 2007

© Amy Saari, 2006

## Abstract

Head-first impact can occur during home and occupational falls, automotive rollovers, various sports, and other activities. These incidents often result in both spinal column and spinal cord trauma. To better understand the resulting bony and neurological injuries, and to develop devices to prevent them, several investigators have studied the response of the cervical spinal column under axial impact. In general these studies have not related the spinal column injuries sustained to the accompanying spinal cord injury. As such, the relationship between these two aspects of trauma is not well understood. Furthermore, most of the models used to study dynamic axial impact do not account for musculature present *in vivo* which may influence the response of the model to the impact.

The objectives of this work were to develop an appropriate cervical spine model that incorporates the effect of musculature so as to assess its effect on the kinematic response of the cervical spine to the impact, and to quantify spinal cord deformation during injury sustained during dynamic head to ground impact. Insight into the relationship between spinal column and spinal cord injuries could improve animal models used to study spinal cord injury at a cellular level by providing data on depth and area of compression and velocity of compression. Previously there has been little data on these parameters which are needed to recreate clinically relevant injuries in these animal models.

The impact model developed for this work was a cadaveric human cervical spine model that used a follower preload to simulate vertebral loading due to musculature. A novel method of visualizing the deformation of the spinal cord paired high speed cineradiography with a radiodense biofidelic surrogate spinal cord placed within the cadaveric human cervical spine. This system provided a continuous sagittal profile of the spinal cord deformation resulting from the impact induced injuries.

The influence of the simulated musculature was assessed via the response of the spine to impact. During impact none of the specimens were observed to respond with a snap-through and/or complex buckling response as has been previously reported in axial impact studies. The corresponding spinal cord deformations were used to correlate injury mode to severity of cord damage. The degree and velocity of the compression of the spinal cord were used to determine the expected neurological injury from *in vivo* animal tests assessing these in terms of probability of recovery. Thus the relationship between bony injury and neurological injury could be made in an *in vitro* model.

# Table of Contents

ABSTRACT.....	ii
TABLE OF CONTENTS.....	iii
LIST OF TABLES .....	ix
LIST OF FIGURES .....	x
ACKNOWLEDGEMENTS.....	xiv
CO-AUTHORSHIP STATEMENT.....	xv
CHAPTER 1: INTRODUCTION .....	1
1.1    MOTIVATION.....	1
1.2    CERVICAL SPINE ANATOMY .....	3
1.2.1    Cervical Vertebrae.....	3
1.2.2    Ligaments of the Cervical Spine .....	6
1.2.3    Muscles of the Cervical Spine.....	7
1.2.4    The Spinal Cord.....	7
1.3    CLINICAL PATHOLOGY.....	8
1.3.1    Hyperflexion.....	8
1.3.2    Hyperextension.....	9
1.3.3    Compression.....	10
1.3.4    Dislocation of Occipito-Atlanto-Axial Complex.....	10
1.4    CERVICAL SPINE INJURY.....	11
1.4.1    Spinal Column Injury .....	11
1.4.2    Spinal Cord Injury .....	13
1.5    OBJECTIVES .....	14
1.6    ROAD MAP.....	14
1.7    REFERENCES .....	17
CHAPTER 2: DROP TOWER DEVELOPMENT .....	19
2.1    INTRODUCTION .....	19
2.2    BACKGROUND.....	19
2.2.1    Horizontal Impactor .....	19
2.2.2    Vertical Impactor.....	21
2.2.3    Inverted Drop .....	22
2.3    REQUIREMENTS .....	24
2.3.1    Drop Height.....	24
2.3.2    Specimen Visibility .....	25

2.3.3	Structure .....	25
2.3.4	Portability .....	25
2.3.5	Carriage .....	25
2.3.6	Platen.....	26
2.3.7	Release .....	26
2.3.8	Stoppers.....	26
2.3.9	Triggering.....	26
2.4	MATERIALS.....	26
2.4.1	Structure .....	26
2.4.2	Guides.....	27
2.4.3	Carriage .....	27
2.4.4	Impact platen.....	28
2.4.5	Release .....	28
2.4.6	Trigger.....	28
2.4.7	Drop Height.....	29
2.5	CONCLUSION.....	29
2.6	REFERENCES .....	30
<b>CHAPTER 3: MOTION CAPTURE SYSTEM .....</b>		<b>31</b>
3.1	INTRODUCTION .....	31
3.2	BACKGROUND.....	31
3.3	REQUIREMENTS .....	33
3.3.1	Cameras.....	33
3.3.2	Marker Tracking.....	33
3.3.3	Three-dimensional Reconstruction.....	34
3.4	MATERIALS AND METHODS .....	34
3.4.1	Cameras.....	35
3.4.2	Marker Tracking Software .....	35
3.4.3	Three dimensional Reconstruction.....	36
3.4.4	Repeatability Assessment.....	38
3.5	RESULTS .....	38
3.5.1	Spatial Resolution.....	38
3.5.2	Accuracy.....	38
3.5.3	Repeatability of Marker Tracking .....	39
3.6	DISCUSSION .....	40
3.7	CONCLUSIONS.....	41
3.8	REFERENCES .....	42
<b>CHAPTER 4: KINETIC DATA ACQUISITION .....</b>		<b>43</b>



4.1	INTRODUCTION .....	43
4.2	BACKGROUND.....	43
4.3	METHODS AND MATERIALS .....	45
4.3.1	Transducers .....	45
4.3.2	Data Collection.....	46
4.3.3	Data Synchronization .....	46
4.3.4	Filtering .....	46
4.3.5	Calibration .....	47
4.4	RESULTS .....	47
4.4.1	Calibration/Validation .....	47
4.5	DISCUSSION .....	49
4.6	CONCLUSION.....	49
4.7	REFERENCES .....	50
<b>CHAPTER 5: PHYSIOLOGIC FOLLOWER PRELOAD.....</b>		<b>51</b>
5.1	INTRODUCTION .....	51
5.2	BACKGROUND.....	51
5.3	MATERIALS AND METHODS .....	55
5.3.1	Guides.....	55
5.3.2	Load Application.....	57
5.4	RESULTS .....	58
5.4.1	Lower Cervical Spine.....	58
5.4.2	Upper Cervical Spine .....	58
5.5	DISCUSSION .....	58
5.6	CONCLUSION.....	60
5.7	REFERENCES .....	61
<b>CHAPTER 6: HIGH SPEED CINERADIOGRAPHY .....</b>		<b>62</b>
6.1	INTRODUCTION .....	62
6.2	BACKGROUND.....	62
6.2.1	X-ray Generation.....	62
6.2.2	Radiographic image capture .....	63
6.2.3	Cineradiography in Biomechanics.....	64
6.3	REQUIREMENTS .....	64
6.4	METHODS & MATERIALS .....	65
6.4.1	Generator.....	65
6.4.2	X-ray Tube .....	65
6.4.3	Image Intensifier.....	65
6.4.4	X-ray Machine Settings.....	66

6.4.5	Synchronization.....	66
6.5	RESULTS .....	66
6.5.1	X-ray Machine Settings.....	66
6.5.2	Resulting Image.....	67
6.6	DISCUSSION .....	67
6.7	CONCLUSION.....	69
6.8	REFERENCES .....	70
<b>CHAPTER 7: RESPONSE OF THE CERVICAL SPINE TO HEAD-FIRST HIGH SPEED AXIAL IMPACT IN THE PRESENCE OF FOLLOWER PRELOAD .....</b>		<b>71</b>
7.1	INTRODUCTION .....	71
7.2	BACKGROUND.....	72
7.2.1	Buckling .....	72
7.2.2	Influence of preload.....	73
7.2.3	Goals.....	74
7.3	METHODS .....	74
7.3.1	Specimen Preparation.....	74
7.3.2	Preload Application.....	76
7.3.3	Impact Simulation .....	77
7.3.4	Load and Motion Analysis .....	77
7.3.5	Injury Analysis .....	78
7.4	RESULTS .....	78
7.4.1	Qualitative Description of Individual Impacts .....	78
7.4.2	Kinematic Response to Impact.....	80
7.4.3	Kinetic Data.....	85
7.4.4	Buckling .....	89
7.5	DISCUSSION .....	90
7.5.1	Limitations .....	91
7.6	CONCLUSION.....	92
7.7	REFERENCES .....	93
<b>CHAPTER 8: SPINAL CORD DEFORMATION DURING AXIAL IMPACT INDUCED INJURIES IN THE CERVICAL SPINE .....</b>		<b>95</b>
8.1	INTRODUCTION .....	95
8.2	BACKGROUND.....	96
8.2.1	Goals.....	102
8.3	MATERIALS AND METHODS .....	102
8.3.1	Specimens Preparation .....	102
8.3.2	Surrogate Spinal Cord .....	103

8.3.3	High Speed X-ray .....	104
8.3.4	Drop Tower and Procedure .....	104
8.3.5	Analysis .....	105
8.4	RESULTS .....	106
8.4.1	Spinal Cord Deformation .....	106
8.4.2	Spinal Cord Compression Time Course .....	109
8.4.3	Spinal Kinetics and Cord Injury .....	114
8.5	DISCUSSION .....	116
8.5.1	Limitations .....	118
8.6	CONCLUSION .....	119
8.7	REFERENCES .....	120
<b>CHAPTER 9: CONCLUSION .....</b>		<b>121</b>
9.1	SUMMARY .....	121
9.2	SPINAL COLUMN RESPONSE AND CORD INJURY .....	121
9.2.1	Spinal Column Response in the Presence of Physiologic Preload .....	121
9.2.2	Spinal Cord Deformation during Injury .....	122
9.3	APPARATUS PERFORMANCE EVALUATION .....	122
9.3.1	Drop Tower .....	122
9.3.2	Cervical Spine Motion .....	123
9.3.3	Kinetic Data Acquisition .....	123
9.3.4	Physiologic Follower Preload .....	124
9.3.5	High Speed Cineradiography and Surrogate Cord .....	124
9.3.6	Surrogate Head .....	125
9.4	FUTURE DIRECTIONS .....	126
<b>APPENDIX A: MATLAB CODE .....</b>		<b>127</b>
A.1	CALIBRATION OF SPACE .....	127
A.2	THREE-DIMENSIONAL RECONSTRUCTION .....	128
<b>APPENDIX B: RELATIVE MARKER MOTION .....</b>		<b>130</b>
B.1	H1091 MARKER MOTION .....	131
B.2	H1096 MARKER MOTION .....	132
B.3	H1116 MARKER MOTION .....	135
B.4	H1177 MARKER MOTION .....	137
B.5	H1183 MARKER MOTION .....	139
B.6	H1184 MARKER MOTION .....	141
<b>APPENDIX C: LOAD CELL TRACES .....</b>		<b>143</b>
C.1	H1091 LOAD CELL TRACES .....	144

C.2	H1096 LOAD CELL TRACES .....	145
C.3	H1116 LOAD CELL TRACES .....	146
C.4	H1177 LOAD CELL TRACES .....	147
C.5	H1183 LOAD CELL TRACES .....	148
C.6	H1184 LOAD CELL TRACES .....	149
<b>APPENDIX D: SURROGATE HEAD DESIGN .....</b>		<b>150</b>

## List of Tables

TABLE 3-1: ASSESSMENT OF ACCURACY OF THE DLT ALGORITHM.....	39
TABLE 4-1: AVERAGE PEAK FORCES AND MOMENTS FROM NIGHTINGALE AND COLLEAGUES (GIVEN IN OUR COORDINATE SYSTEM AS SEEN IN FIGURE 4-1) <sup>15</sup> .....	43
TABLE 4-2: LOAD SPECIFICATIONS FOR THE MULTI-AXIS LOAD CELL.....	45
TABLE 7-1: SUMMARY OF MAXIMUM PRINCIPLE FORCES, TIME OF EACH, LAG TIME, AND TIME TO PRIMARY INJURY EVENT.....	89
TABLE 8-1: SUMMERY OF THE BONY INJURIES MODES AND THE ASSOCIATED SPINAL CORD DEFORMATION AS SEEN AT THE MAXIMUM COMPRESSION .....	107
TABLE 8-2: DEFORMATION CHARACTERISTICS .....	109
TABLE 8-3: VELOCITY OF THE CORD COMPRESSION AND VISCOUS RESPONSE OF THE CORD TO IMACT.....	114
TABLE 8-4: SUMMARY OF AXIAL IMPACT CHARACTERISTICS AND CORD DEFORMATION CHARACTERISTICS	115

## List of Figures

FIGURE 1-1: CAUSES OF SPINAL CORD INJURY IN CANADA (MODIFIED FROM THE CANADIAN PARAPLEGIC ASSOCIATION AND THE RICK HANSEN SPINAL CORD REGISTRY <sup>1,2</sup> ) .....	1
FIGURE 1-2: SCHEMATIC OF AN AUTOMOTIVE ROLLOVER ILLUSTRATING THE AXIAL HEAD TO GROUND IMPACT EXPERIENCED BY THE OCCUPANT THAT MAY RESULT IN CERVICAL SPINE INJURY <sup>3</sup> .....	2
FIGURE 1-3: LATERAL RADIOGRAPH OF A NORMAL CERVICAL SPINE (FROM <a href="http://www.mdchoice.com/xray/xr.asp">HTTP://WWW.MDCHOICE.COM/XRAY/XR.ASP</a> ) .....	3
FIGURE 1-4: ANATOMY OF A TYPICAL CERVICAL VERTEBRA (MODIFIED FROM GRAY'S ANATOMY <sup>5</sup> ) .....	4
FIGURE 1-5: JOINTS BETWEEN TWO ADJACENT VERTEBRAE <sup>6</sup> .....	4
FIGURE 1-6: AXIS OR THE SECOND CERVICAL VERTEBRA <sup>5</sup> .....	5
FIGURE 1-7: ATLAS OR FIRST CERVICAL VERTEBRA <sup>5</sup> .....	5
FIGURE 1-8: JOINTS OF THE ATLANTO-AXIAL AND ATLANTO-OCCIPITAL COMPLEXES <sup>6</sup> .....	6
FIGURE 1-9: LIGAMENTS OF A CERVICAL SPINE UNIT .....	7
FIGURE 1-10: CROSS SECTION OF THE SPINAL CORD SHOWING THE MENINGES <sup>6</sup> .....	8
FIGURE 1-11: PROGRESSION OF HYPERFLEXION INJURY TO THE CERVICAL SPINE RESULTING IN BILATERAL FACET DISLOCATION AND TEARS TO THE INTERSPINOUS LIGAMENT <sup>9</sup> .....	9
FIGURE 1-12: INJURIES TO THE ANTERIOR ASPECTS OF THE VERTEBRA FROM HYPERFLEXION LOADING. WEDGE FRACTURE ON THE LEFT AND A TEAR DROP FRACTURE ON THE RIGHT. <sup>9</sup> .....	9
FIGURE 1-13: PROGRESSION OF HYPEREXTENSION INJURIES RESULTING IN DISRUPTION TO THE INTERVERTEBRAL DISC, A TEAR DROP FRACTURE, AND FRACTURE OF THE SPINOUS PROCESS. <sup>9</sup> .....	10
FIGURE 1-14: ATLANTO-AXIAL DISLOCATION SHOWING THE COMPLETE FRACTURE OF THE DENS AND THE COMPRESSION OF THE SPINAL CORD. <sup>10</sup> .....	11
FIGURE 1-15: SOME OF THE ANTROPOMETRIC TEST DEVICES (ATDs) DEVELOPED. THE DEVICES RANGE FROM CHILDREN TO THE 95 <sup>TH</sup> PERCENTILE MALE DUMMY AND INCLUDES FEMALE MODELS. <sup>20</sup> .....	12
FIGURE 2-1: SCHEMATIC OF THE HORIZONTAL IMPACTOR USED BY NUSHOLTZ AND COLLEAGUES. <sup>35</sup> .....	20
FIGURE 2-2: SCHEMATIC OF DIFFERENT SPECIMENS PREPARED FOR IMPACT IN A VERTICAL IMPACTOR. <sup>39</sup> .....	21
FIGURE 2-3: TWO METHODS OF HEAD RESTRAINT USED BY YOGANANDAN, PINTAR, AND COLLEAGUES: A) DIRECT CONNECTION TO THE PISTON <sup>18</sup> B) SPRING AND MASS SYSTEM <sup>40</sup> .....	22
FIGURE 2-4: VERTICAL DROP OF FULL BODY CADAVERS FOR HEAD TO GOROUND IMPACT SIMULATION. <sup>35</sup> .....	23
FIGURE 2-5: SCHEMATIC OF THE DROP TOWER AND INSTRUMENTATION USED BY NIGHTINGALE AND COLLEAGUES IN THEIR HEAD TO GROUND SIMULATIONS. <sup>45</sup> .....	24
FIGURE 2-6: DROP TOWER STRUCTURE SHOWING ONLY THE FOUR GUIDE SHAFTS, TOP AND BOTTOM FRAMES, AND BASIC CARRIAGE .....	27
FIGURE 2-7: CARRIAGE WITH SIX-AXIS LOAD CELL AND BEARINGS.....	28
FIGURE 2-8: IMPACT PLATEN COVERED IN UHMWPE TAPE WITH UNI-AXIAL LOAD CELL .....	29
FIGURE 3-1: CALIBRATION CAGE CONSTRUCTED FOR THIS THREE DIMENSIONAL RECONSTRUCTION SYSTEM	36

FIGURE 3-2: REPEATABILITY ASSESSMENT OF MARKER TRACKING SOFTWARE: THREE REPETITIONS OF TRACKING ONE MARKER. ....	40
FIGURE 4-1: LOCATION AND ORIENTATION OF THE LOAD CELLS AND THEIR AXES IN THE SET UP.....	45
FIGURE 4-2: SAE DATA FILTER REQUIREMENTS FOR NECK IMPACTS <sup>54</sup> .....	47
FIGURE 4-3: VALIDATION OF THE Y DIRECTION AND X AND Z ROTATIONAL COMPONENTS OF THE CALIBRATION MATRIX OF THE 6 AXIS LOAD CELL. ....	48
FIGURE 4-4: VALIDATION OF THE CALIBRATION VALUE OF THE UNI-AXIAL LOAD CELL .....	48
FIGURE 5-1: ILLUSTRATION OF THE LOADING PATH OF A VERTICAL LOAD (A) AND A FOLLOWER LOAD (B) (ADAPTED FROM PATWARDHAN ET AL, 2000) <sup>7</sup> .....	52
FIGURE 5-2: PATWARDHAN AND COLLEAGUES' APPARATUS FOR FOLLOWER LOAD APPLICATION IN THE CERVICAL SPINE <sup>7</sup> . ....	53
FIGURE 5-3: THE COMPLEX FOLLOWER LOAD APPLICATION DEVELOPED BY PANJABI AND COLLEAGUES TO SIMULATE CERVICAL MUSCULATURE <sup>61</sup> .....	54
FIGURE 5-4: PLACEMENT OF SCREW EYES IN LATERAL MASSES OF THE C3 THROUGH C7 VERTEBRAE.....	56
FIGURE 5-5: POSITIONS OF THE CENTRES OF ROTATIONS FOR EACH CERVICAL VERTEBRAL PAIR FROM IN VIVO FLEXION/EXTENSION MEASUREMENTS <sup>63</sup> .....	56
FIGURE 5-6: LOAD APPLICATION BY COMPRESSION SPRING AT THE SURROGATE HEAD IN THE DEVELOPED FOLLOWER PRELOAD SYSTEM (SPECIMEN IS INVERTED).....	57
FIGURE 6-1: SCHEMATIC OF AN X-RAY IMAGE INTENSIFIER SHOWING THE MAJOR COMPONENTS REFERRED TO ABOVE. A) PHOSPHORESCENT SCREEN B) PHOTOCATHODE C) FIRST VACUUM D) MICROCHANNEL PLATE E) AMPLIFIED ELECTRON STREAM F) PHOSPHOR SCREEN.....	63
FIGURE 6-2: PLACEMENT OF X-RAY TUBE AND IMAGE INTENSIFIER RELATIVE TO THE SPECIMEN .....	67
FIGURE 6-3: TYPICAL X-RAY IMAGE FROM THE HIGH SPEED IMAGE SYSTEM. SPECIMEN IS AN INVERTED CERVICAL SPINE THAT HAS BEEN PREPARED FOR TESTING .....	67
FIGURE 7-1: TWO BUCKLING MODES SEEN DURING AXIAL IMPACT OF THE CERVICAL SPINE. A IS THE FIRST ORDER MODE, B IS THE SECOND ORDER OR SERPENTINE MODE .....	72
FIGURE 7-2: SPECIMEN DURING PREPARATION SHOWING THE LOCATION OF THE PRELOAD GUIDES, AFTER THE REMOVAL OF THE TRANSVERSE PROCESSES, AND MARKERS FOR MOTION TRACKING.....	75
FIGURE 7-3: SURROGATE HEAD SHOWING IT COMPONENTS AND THE COMPRESSION SPRINGS FOR FOLLOWER PRELOAD APPLICATION .....	76
FIGURE 7-4: LOCATION AND ORIENTATION OF AXES OF THE LOAD CELLS AND THREE-DIMENSIONAL MARKER COORDINATES.....	78
FIGURE 7-5: MARKER MOTION ALONG THE X-AXIS FOR THE 25 MARKERS OF SPECIMEN H1091. MARKERS 1 THROUGH 3 WERE ON C2, 4 TO 8 ON C3, 9 TO 11 ON C4, 12 TO 15 ON C5, 16 TO 19 ON C6 AND 20 TO 23 ON C7. MARKERS 24 AND 25 WERE ON THE MOUNTING CUP.....	81
FIGURE 7-6: MARKER MOTION ALONG THE Y-AXIS FOR THE 25 MARKERS OF SPECIMEN H1091. ....	81
FIGURE 7-7: MARKER MOTION ALONG THE Z-AXIS FOR THE 25 MARKERS OF SPECIMEN H1091.....	82

FIGURE 7-8: Z-AXIS TRACE OF SPECIMEN H1091 SHOWING ONE MARKER ON EACH VERTEBRA.....	82
FIGURE 7-9: Z-AXIS TRACE OF SPECIMEN H1096 SHOWING ONE MARKER ON EACH VERTEBRA.....	83
FIGURE 7-10: Z-AXIS TRACE OF SPECIMEN H1116 SHOWING ONE MARKER ON EACH VERTEBRA.....	83
FIGURE 7-11: Z-AXIS TRACE OF SPECIMEN H1177 SHOWING ONE MARKER ON EACH VERTEBRA.....	84
FIGURE 7-12: Z-AXIS TRACE OF SPECIMEN H1183 SHOWING ONE MARKER ON EACH VERTEBRA.....	84
FIGURE 7-13: Z-AXIS TRACE OF SPECIMEN H1184 SHOWING ONE MARKER ON EACH VERTEBRA.....	85
FIGURE 7-14: FORCE /MOMENT TRACES FROM THE LOAD CELL AT T1 OF SPECIMEN H1096. ....	86
FIGURE 7-15: THE AXIAL REACTION FORCES AT T1 FOR EACH OF THE SPECIMENS .....	87
FIGURE 7-16: HEAD IMPACT AND NECK AXIAL LOAD TRACES SHOWING THE KEY ANALYSIS POINTS: IMPACT, ONSET OF NECK LOADING, INJURY, AND LAG USING SPECIMEN H1096 .....	88
FIGURE 8-1: EXPERIMENTAL SET UP OF THE WATER PRESSURE BASED OCCLUSION TRANSDUCER <sup>31</sup> .....	97
FIGURE 8-2: TRANSDUCER DEVELOPED BY RAYNAK AND COLLEAGUES TO MEASURE OCCLUSION VIA CHANGES IN THE CORE FLUID'S ELECTRICAL RESISTANCE <sup>38</sup> .....	98
FIGURE 8-3: TRANSDUCER PLACEMENT USED BY PANJABI AND COLLEAGUES <sup>32</sup> .....	99
FIGURE 8-4: SETUP USED BY WILCOX AND COLLEAGUES TO CAPTURE THE TRANSVERSE PROFILE OF CANAL OCCLUSION DURING SIMULATED BURST FRACTURE INJURY. <sup>76</sup> .....	100
FIGURE 8-5: TYPICAL PRESSURE TRACE RECORDINGS FROM THE INSTRUMENTED SURROGATE SPINAL CORD DEVELOPED BY PINTAR AND COLLEAGUES <sup>33</sup> .....	101
FIGURE 8-6: BILSTON AND COLLEAGUES' SPINE AND SKULL MODEL WITH THE SURROGATE SPINAL CORD <sup>29</sup> .....	102
FIGURE 8-7: SPECIMEN PREPARED FOR TESTING WITH FOLLOWER LOAD, SURROGATE HEAD, AND MARKERS IN PLACE .....	103
FIGURE 8-8: EXAMPLE OF TWO FRAMES FROM THE SAME SPECIMEN (THE FIRST FRAME ON THE LEFT AND ONE FROM MAXIMUM DEFORMATION ON THE RIGHT) DURING ANALYSIS OF CORD DEFORMATION SHOWING TRANSVERSE MEASUREMENTS OF THE DEFORMATION AND THE LONGITUDINAL MEASUREMENTS .....	106
FIGURE 8-9: TIME COURSE PLOT OF SPINAL CORD DEFORMATION OF SPECIMEN H1091 .....	110
FIGURE 8-10: TIME COURSE PLOT OF SPINAL CORD DEFORMATION OF SPECIMEN H1177 .....	110
FIGURE 8-11: TIME COURSE PLOT OF SPINAL CORD DEFORMATION OF SPECIMEN H1184 .....	111
FIGURE 8-12: TIME COURSE PLOT OF SPINAL CORD DEFORMATION OF SPECIMEN H1096 .....	112
FIGURE 8-13: TIME COURSE PLOT OF SPINAL CORD DEFORMATION OF SPECIMEN H1183 .....	112
FIGURE 8-14: TIME COURSE PLOT OF SPINAL CORD DEFORMATION OF SPECIMEN H1116 .....	113
FIGURE 8-15: MAXIMUM CORD COMPRESSION VERSES MAXIMUM AXIAL RESPONSE AT THE NECK DURING IMPACT TO ILLUSTRATE THEIR RELATIONSHIP VIA INJURY MODE.....	114
FIGURE B-1: LOCATION AND ORIENTATION OF COORDINATE SYSTEM USED IN THE THREE-DIMENSIONAL RECONSTRUCTION RELATIVE TO THE SPECIMEN AND LOAD CELL AXES.....	130
FIGURE B-2: LOCATION OF MARKERS ON SPECIMEN H1091 .....	131
FIGURE B-3: MARKER MOTION ALONG THE X-AXIS OF H1091 .....	131
FIGURE B-4: MARKER MOTION ALONG THE Y-AXIS OF H1091 .....	132



FIGURE B-5: MARKER MOTION ALONG THE Z-AXIS OF H1091 .....	132
FIGURE B-6: LOCATION OF MARKERS ON SPECIMEN H1096.....	133
FIGURE B-7: MARKER MOTION ALONG THE X-AXIS OF H1096 .....	133
FIGURE B-8: MARKER MOTION ALONG THE Y-AXIS OF H1096 .....	134
FIGURE B-9: MARKER MOTION ALONG THE Z-AXIS OF H1096 .....	134
FIGURE B-10: LOCATION OF MARKERS ON SPECIMEN H1116.....	135
FIGURE B-11: MARKER MOTION ALONG THE X-AXIS OF H1116 .....	135
FIGURE B-12: MARKER MOTION ALONG THE Y-AXIS OF H1116 .....	136
FIGURE B-13: MARKER MOTION ALONG THE Z-AXIS OF H1116 .....	136
FIGURE B-14: LOCATION OF MARKERS ON SPECIMEN H1177 .....	137
FIGURE B-15: MARKER MOTION ALONG THE X-AXIS OF H1177 .....	137
FIGURE B-16: MARKER MOTION ALONG THE Y-AXIS OF H1177 .....	138
FIGURE B-17: MARKER MOTION ALONG THE Z-AXIS OF H1177 .....	138
FIGURE B-18: LOCATION OF MARKERS ON SPECIMEN H1183 .....	139
FIGURE B-19: MARKER MOTION ALONG THE X-AXIS OF H1183 .....	139
FIGURE B-20: MARKER MOTION ALONG THE Y-AXIS OF H1183 .....	140
FIGURE B-21: MARKER MOTION ALONG THE Z-AXIS OF H1183 .....	140
FIGURE B-22: LOCATION OF MARKERS ON SPECIMEN H1184.....	141
FIGURE B-23: MARKER MOTION ALONG THE X-AXIS OF H1184 .....	141
FIGURE B-24: MARKER MOTION ALONG THE Y-AXIS OF H1184 .....	142
FIGURE B-25: MARKER MOTION ALONG THE Z-AXIS OF H1184 .....	142
FIGURE C-1: LOCATION AND ORIENTATION OF AXES OF LOAD CELLS RELATIVE TO THE SPECIMEN.....	143

## Acknowledgements

I would like to first thank my supervisor Dr. Peter Crompton for his mentorship and for allowing me to push this project forward to fulfill my desire to see it through to the end. His encouragement, patience, and help have made my graduate experience a rewarding one.

Many thanks to my fellow students, the research engineers, faculty, and other members of the Injury Biomechanics Laboratory and the Division of Engineering Research for all of their support, ideas, advice, and technical assistance. Special thanks to Dr. Eyal Itshayek for his guidance and help with the specimens, Tim Nelson for the extra set of hands during testing even in the wee hours, Phil Morley for bringing the drop tower to life, and for their support in the form of caffeine, chocolate and chit-chat: Carolynne Albert, Chad Larson, Claire Jones, and Josh Levitz.

Research grants from the Natural Sciences and Engineering Research Council of Canada (NSERC) are gratefully acknowledged.

I would like to acknowledge and thank the donors of the specimens used in my work. Without their generosity, this work would not have been possible.

A very special thank you to my family and friends who have been with me for all, or even only part, of my journey. Your support and encouragement has been greatly appreciated. Mom and Dad, thank you for having so much confidence in me and being there to listen and to offer advice. Brian, even in just the last bit of this journey you have been a source of so much strength, motivation, and help, thank you for everything, big and small, that made my life easier. Dan, thank you for your serenity, unwavering belief in me, and for keeping me grounded. And lastly to both of my Nanas, thank you for showing so much patience with me and for understanding why I could not come for dinner as often as I should have in the last three years.

## **Co-Authorship Statement**

The experimental designs and studies reported in this thesis were conducted primarily by the author. Input and feedback were provided by Dr. Peter Cripton in his role as supervisor. Construction of the drop tower apparatus was assisted by Mr. Phillip Morley, a research assistant in the Injury Biomechanics Laboratory. Mr. Morley was also a member of the undergraduate team at the University of British Columbia who developed the surrogate head for use in this work. Assistance during testing was supplied by Mr. Tim Nelson. Diagnosis of the injuries sustained was completed by Dr. Eyal Itshayek. It is the intension of the author to publish versions of Chapters 7 and 8. Mr. Nelson and Drs. Itshayek and Cripton will be listed as coauthors on these publications.

## Chapter 1: Introduction

### 1.1 Motivation

Spinal cord injury is one of the most catastrophic and debilitating medical conditions. The results of injury to the spinal cord vary depending on the severity of injury and the level of incidence. These effects range from partial to total paralysis and even death. Every year spinal cord injury affects 35 people per million population in Canada. The majority of spinal cord injuries occur in automotive accidents followed by falls, Figure 1-1.<sup>1, 2</sup> Males under the age of 30 are most commonly injured. Spinal cord injury costs approximately \$750 million annually in Canada.<sup>2</sup>

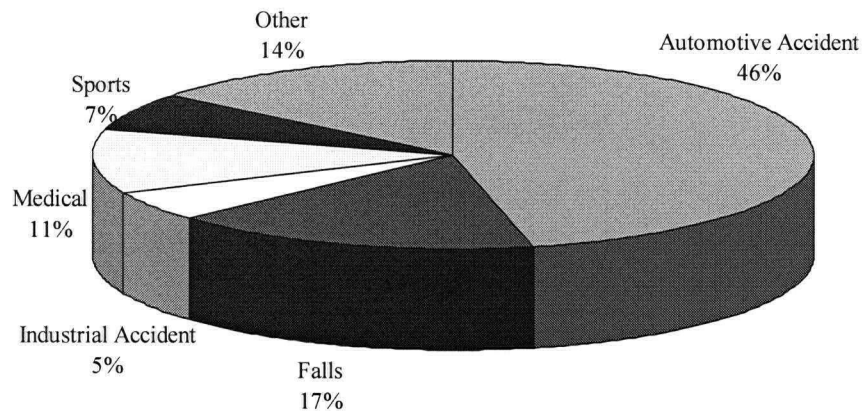
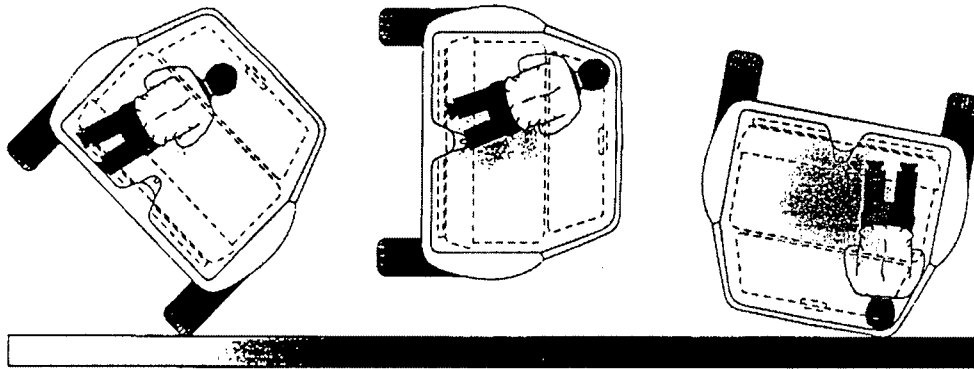


Figure 1-1: Causes of Spinal Cord Injury in Canada (data from the Canadian Paraplegic Association and the Rick Hansen Spinal Cord Registry<sup>1, 2</sup>)

Cervical spinal cord injury is associated with more instances of tetraplegia and a higher mortality rate than injury to other levels. It accounts for approximately 50% of cases.<sup>1</sup> Injury to the cervical spine is a frequent result of axial head first impact where the head is suddenly arrested and the neck is loaded by the in-coming torso, Figure 1-2. This loading scenario is common in automotive rollovers or sporting injuries such as diving into shallow water.



Reprinted with permission from SAE paper 980362 © 1998 SAE International

Figure 1-2: Schematic of an automotive rollover illustrating the axial head to ground impact experienced by the occupant that may result in cervical spine injury<sup>3</sup>

Cervical spine injury has traditionally been divided into two areas of research: bony injury and cord injury. Spinal column or bony injury has been studied as a mechanical system whose response to loading conditions can be readily quantified. In these studies little regard has been given to the neurological consequences due to spinal cord deformation. Spinal cord injury is typically studied at the cellular level in animal models.<sup>4</sup> The relationship between the two fields is not well understood. There has been limited work done to provide information on the influence of bony injury on cord injury in biomechanical terms.

This work was motivated by the need to further understanding of the relationship between column and cord injury. The parameters of cord injury such as velocity of bony impact, area impacted, and the pattern of deformation of the cord are largely unknown for clinically relevant injuries. This information can be used to improve the concordance of animal models to real world human injury, develop and assess the effectiveness of new preventative devices, and to provide insight into the post injury conditions seen in the clinical setting. Furthermore, there is a need to determine if a more biofidelic *in vitro* model of the human cervical spine for impact testing can be developed by incorporating the effect of musculature present *in vivo*. The influence of musculature has not been assessed in an *in vitro* axial impact model.

## 1.2 Cervical Spine Anatomy

Seven vertebrae make up the bony column of the cervical spine, Figure 1-3. Housed within this column is the spinal cord which extends almost the length of the spine via the spinal canal. The cervical spine is the most mobile section of the human spine. The bony structures are loosely held together by the ligaments. The head and neck are further stabilized by small, deep muscles which lie against the vertebrae. In a neutral relaxed posture the cervical spine curves concave posterior (lordosis).



Figure 1-3: Lateral radiograph of a normal cervical spine

### 1.2.1 Cervical Vertebrae

There are seven cervical vertebrae. The lower five are all of similar morphology and are the typical cervical vertebrae. They are all composed of a cylindrical anterior vertebral body which constitutes the majority of the mass and a posterior arch, Figure 1-4.

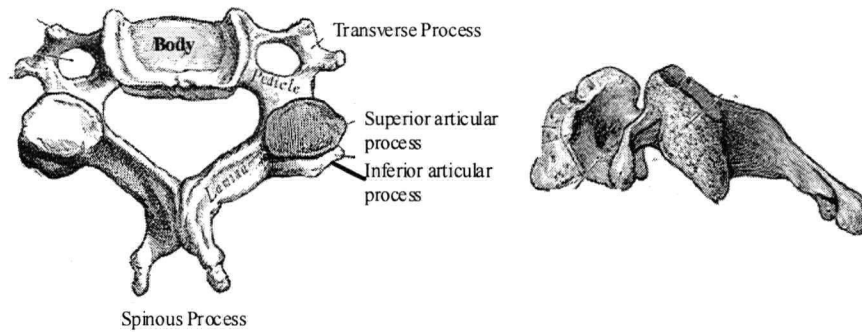
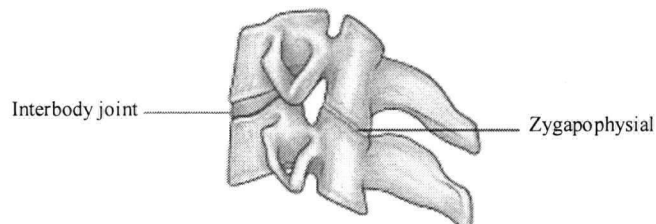


Figure 1-4: Anatomy of a typical cervical vertebra (modified from Gray's Anatomy<sup>5</sup>)

There are three main joints between each typical vertebrae: an interbody joint and two zygapophysial joints, Figure 1-5. Between each vertebral body there is an intervertebral disc which is the main component of the interbody joint. These connected vertebral bodies form a central articulated column. Two smaller columns paralleling this are formed by the lateral masses. The anterior and inferior articular processes of the adjacent vertebrae are encased by a loose capsule to form the zygapophysial joint. The facet surfaces of these joints are angled upward and backward allowing for a good deal of flexion and extension with some rotation and lateral flexion.



Reprinted with permission from Elsevier © 2004

Figure 1-5: Joints between two adjacent vertebrae<sup>6</sup>

The upper two vertebrae are unique. The second cervical vertebra (C2) is referred to as the axis, Figure 1-6. The inferior portion of the body and lateral masses resembles that of a typical vertebra. The joints connecting the axis to the third vertebra are those discussed above. The superior portion of the axis is unique. Most notable is the pivot like extension called the dens. In addition the superior articular facets are more anteriorly located and are more horizontal.

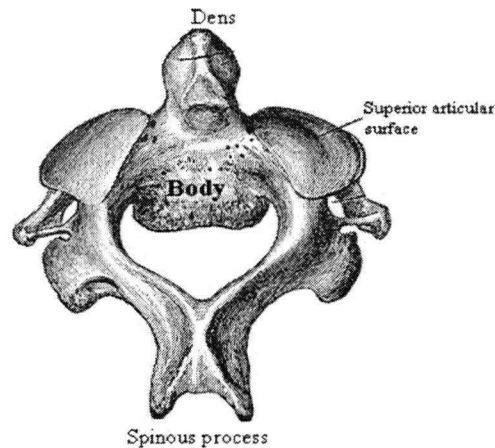


Figure 1-6: Axis or the second cervical vertebra<sup>5</sup>

The first cervical vertebra (C1) is referred to as the atlas, Figure 1-7. It is a ring like structure that does not resemble the other cervical vertebrae. The atlas does not have a body but has enlarged lateral masses which have superior and inferior articulating surfaces for articulation with the occiput of the skull and the axis respectively.

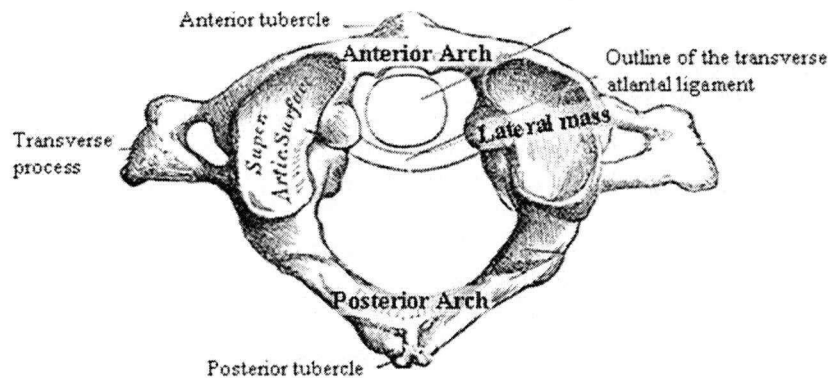
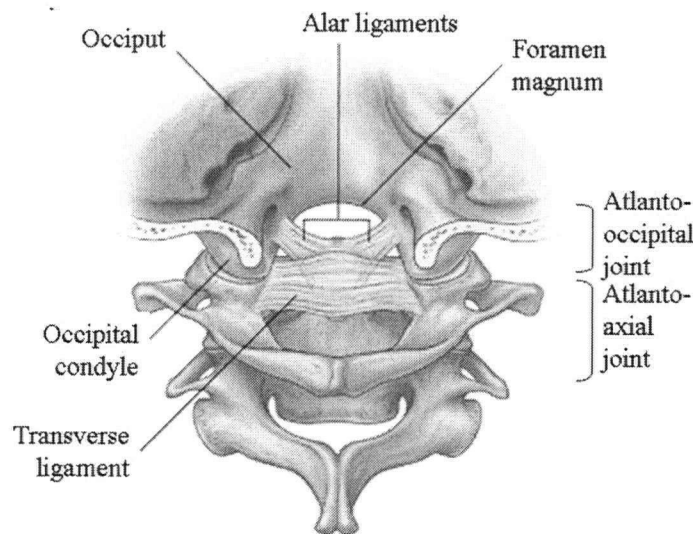


Figure 1-7: Atlas or first cervical vertebra<sup>5</sup>

The joints between the atlas and axis are collectively referred to as the atlanto-axial joint (AA joint), Figure 1-8. This is actually made up of 3 separate joints. A vertical pivot joint between the dens of the axis and the anterior arch of the atlas is held in place by several ligaments including the transverse ligament. These limit the rotation of the atlas on the axis. Flanking this pivot joint are two facet joints which are similar to the zygapophysial joints of the lower vertebra. They are planar joints and allow rotational motion of the AA joint about the dens. The majority of the axial rotation of the cervical spine occurs at the atlanto-axial joint about the dens.



There are two joints between the atlas and the occiput of the skull comprising the atlanto-occipital joint (AO joint). The two occipital condyles of the skull are cradled in the shallow cups of the superior articular facets of atlas. As the lateral edges of the articular facets are higher than the median edges movement is restricted to the sagittal plane. The lateral joints are encapsulated by the atlanto-occipital ligaments. A thin, baggy fibrous capsule encases the AA and AO joints without restricting movement.

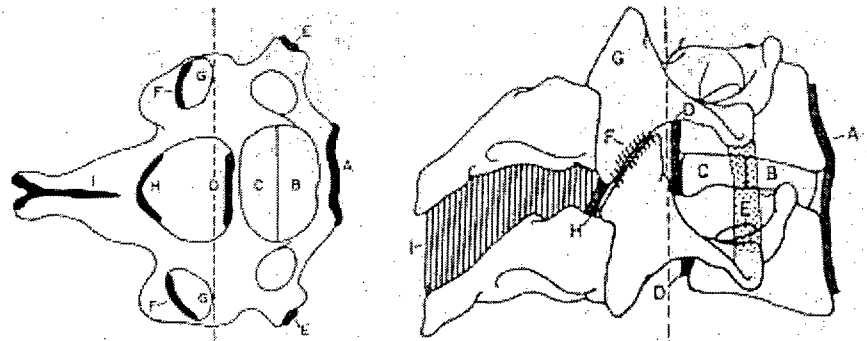


Reprinted with permission from Elsevier © 2004

Figure 1-8: Joints of the atlanto-axial and atlanto-occipital complexes<sup>6</sup>

### 1.2.2 Ligaments of the Cervical Spine

There are several important ligaments in the cervical spine. Those of the upper cervical spine have been discussed above. The upper cervical spine ligaments are unique to the AA and AO joints. There are several that are common throughout the entire cervical spine. Two longitudinal ligaments run along the anterior and posterior of the vertebral bodies, Figure 1-9A. The posterior longitudinal ligament is inside of the canal and is not visible from the exterior. Both the anterior and posterior longitudinal ligaments contain fibers of different lengths which extend as short as adjacent vertebrae and as far as four vertebrae. Laterally, articular capsules loosely encase the zyapophyseal joints. Small intertransverse ligaments connect adjacent transverse processes. In the posterior, the lamina are connected by the ligamentum flava, Figure 1-9B and the interspinous and supraspinous ligament connect the adjacent spinous processes, Figure 1-9C.



Reprinted with permission from Elsevier © 1975

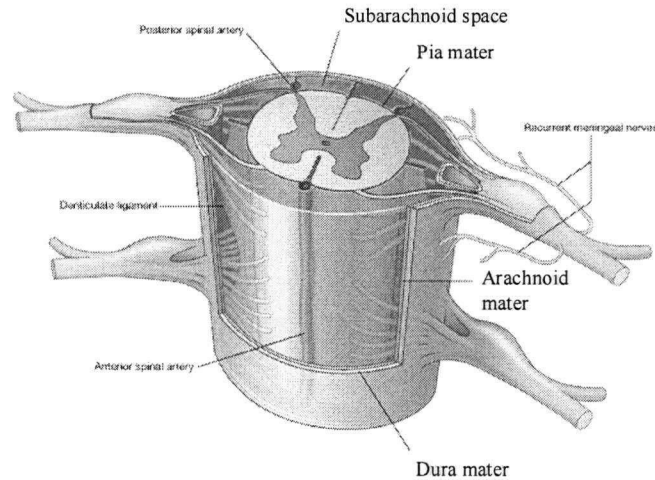
Figure 1-9: Ligaments of a cervical spinal unit A) Anterior longitudinal ligament (ALL). B) Anterior half of disc. C) Posterior half of disc. D) Posterior longitudinal ligament (PLL). E) Intertransverse ligament. F) Facet joint capsule. G) Facet joints. H) Ligamentum Flavum. I) Interspinous and supraspinous ligaments.<sup>7</sup>

### 1.2.3 Muscles of the Cervical Spine

There are deep and superficial muscles of the cervical spine. The superficial muscles provide most of the gross motion whereas the deep muscles stabilize the spinal column and assist in smaller portions of motion. The deep muscles are of various lengths and span different sections of the spinal column. The majority of these muscles lie laterally and posteriorly to the spinal column. The sum of all the muscle forces acting on the spine induces a natural lordotic curvature in the column. The resultant force vector is thought to be a tangent to the curve passing through the centres of rotation of the vertebrae.<sup>8</sup>

### 1.2.4 The Spinal Cord

The vertebral foramen of the vertebrae align and create the spinal canal which encases the spinal cord. The spinal cord transmits the signals from the brain to the rest of the body and vice versa to provide movement and feedback. The cervical spinal cord has an oval cross section which is larger at the upper cervical spine than at the lower. The cord is made up of long neurons with axons that run along its length. These nerves are bundled together and surrounded by meninges, Figure 1-10: pia mater, arachnoid mater, and dura mater. The outermost layer, the dura mater, is the toughest of the three meninges. Between the arachnoid mater and the pia mater is a fluid filled space called the subarachnoid space. Cerebrospinal fluid fills this space. Neurons leave the spinal cord via spinal nerves. These nerves are encased in dura and pass through the intervertebral foramen.



Reprinted with permission from Elsevier © 2004

Figure 1-10: Cross section of the spinal cord showing the meninges<sup>6</sup>

### 1.3 Clinical Pathology

During axial impact there are three common sagittal plane loading directions that the cervical spine may experience either on their own or in combination: flexion, extension, anterior/posterior translation and compression. Hyperflexion or hyperextension injury mechanisms occur generally when flexion or extension beyond the physiologic ROM is applied. Most commonly, flexion or extension is coupled with a compressive load during these events resulting in a combination of injuries.<sup>9</sup> Bony injury can be used to identify the direction of loading. Knowledge of the loading direction and spinal column response can help identify the potential injury mechanisms acting on the spinal cord.

#### 1.3.1 Hyperflexion

Crush type injuries to the anterior aspects and distraction to the posterior of the column are characteristic of this load direction. Bilateral facet dislocation is also a possibility, Figure 1-11. This is characterized by an anterior displacement of the dislocated vertebra. Anterior fracture patterns include wedge fractures and teardrop fractures, Figure 1-12. In the posterior, disruption of the interspinous ligaments and some tears of the ligamentum flava can be found.<sup>9</sup>

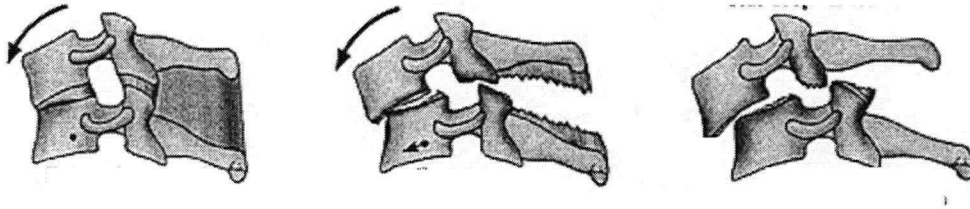


Figure 1-11: Progression of hyperflexion injury to the cervical spine resulting in bilateral facet dislocation and tears to the interspinous ligament<sup>10</sup>

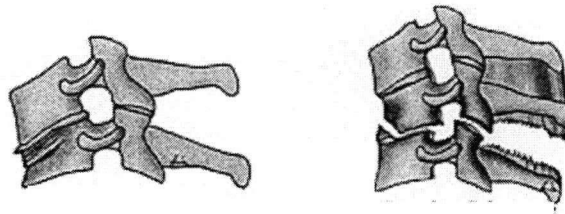


Figure 1-12: Injuries to the anterior aspects of the vertebra from hyperflexion loading. Wedge fracture on the left and a tear drop fracture on the right.<sup>10</sup>

At the hyperflexed levels the spinal cord is elongated. The posterior of the cord, which is mostly white matter, is subjected to more elongation than the anterior aspects. There is some chance of encroachment of the vertebral body into the canal space during tear drop fractures resulting in localized anterior contusion of the spinal cord<sup>9</sup>. Also, during bilateral facet dislocation the cord must assume an S-shape to pass through the canal. The cord experiences additional transverse compressive forces at over a larger surface area as a result.

### 1.3.2 Hyperextension

In opposition to hyperflexion, hyperextension results in anterior distraction and posterior compression injuries. Hyperextension dislocation of the vertebral bodies is accompanied by disruption of the anterior longitudinal ligament and intervertebral disc, Figure 1-13. An avulsion fracture involving the lower anterior lip of the vertebral body is often present. Posterior fractures include laminar and spinous process fractures in the lower cervical vertebrae and axis. The posterior arch of the atlas may also be fractured. Fracture of the pedicles of the axis ("Hangman's fracture") may also occur.<sup>9, 11</sup>

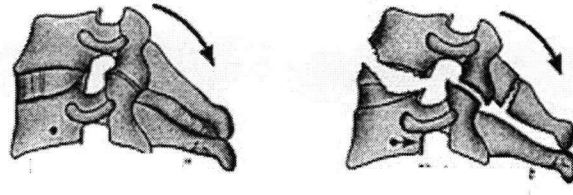


Figure 1-13: Progression of hyperextension injuries resulting in disruption to the intervertebral disc, an avulsion fracture, and fracture of the spinous process.<sup>10</sup>

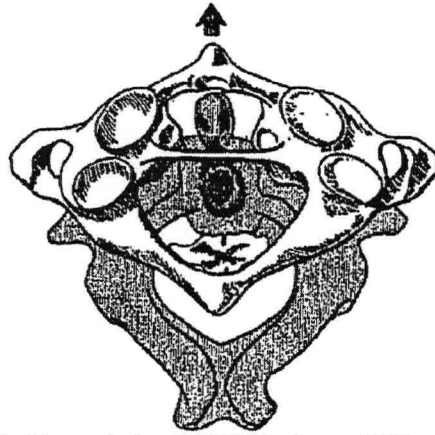
Spinal cord injury during this motion is often a result of a “pinch”. The cord is compressed between the inferior posterior edge of the vertebrae and posterior arch of the adjacent inferior vertebra. Additionally the ligamentum flava may encroach on the canal space and further compress the spinal cord.<sup>9, 11</sup>

### 1.3.3 Compression

Pure axial loading usually results in a symmetrical (both sagittally and laterally) fracture pattern in the vertebral body. The most common vertebral body injuries are burst fractures. During these fractures the vertebral body explodes and bony fragments may be retro-pulsed into the spinal column contusing the spinal cord.<sup>9, 11</sup> Burst fractures at the atlas are referred to as Jefferson fractures. They have a symmetrical, four-part fracture pattern involving both the anterior and posterior arches of the atlas. There is often no neurological damage with a Jefferson Fracture.<sup>11</sup>

### 1.3.4 Dislocation of Occipito-Atlanto-Axial Complex

Atlanto-occipital dislocation is not usually associated with bony injury but rather with ligament disruption.<sup>11</sup> It is often associated with neurological trauma and at this high level of the spinal cord results in death. During dislocation, the spinal cord is forced into an S-shape and is subjected to longitudinal elongation due to the shearing action of the vertebrae and transverse compression as the cord is compressed between the anterior and posterior aspects of adjacent vertebrae. Atlanto-axial dislocation often occurs in conjunction with atlanto-occipital dislocation. Evidence of this mechanism of injury can be seen as a disruption of the alar and transverse ligaments (in combination these are also known as the cruciform ligament) or a fracture to the base of the dens, Figure 1-14.<sup>11</sup>



Reprinted with permission © 1990 Lippincott, Williams & Wilkins

Figure 1-14: Atlanto-axial dislocation showing the complete fracture of the dens and the compression of the spinal cord.<sup>11</sup>

## 1.4 Cervical Spine Injury

### 1.4.1 Spinal Column Injury

Axially induced spinal column injury at the cervical level has been studied using a variety of models including *in vivo* animal, *in vitro*, anthropomorphic test devices and mathematical models. Each of these is an approximation of the real life injury event.

Simulated spinal injuries with associated neurological injuries have been induced using a hyperextension model with porcine subjects *in vivo*.<sup>12</sup> The models allowed for a physiologic impact response as they included the musculature, skin, and other structures that surround the cervical spine and may influence its response to impact. However animal models are not anatomically identical to human. The size and structure of the cervical column can differ significantly especially in quadrupedal mammals. Also the ethical implications of using animals in such tests in current day research have restricted the use of this type of model.

*In vitro* cervical spine models are widely used to study the biomechanics of axial impact injury.<sup>13-19</sup> Human cadaveric specimen models offer physiologic osteology and bone material properties but do not generally include the musculature present *in vivo*. These models allow for measurement of the individual vertebral kinematics and the general kinetic response of the column. However by not incorporating musculature in the model, the model neglects its effects on the impact response. These effects include pre-

compression of the spine prior to impact and the influence of the preload on the buckling response commonly seen at impact.

Anthropomorphic test devices, Figure 1-15, have been developed based on *in vivo* and *in vitro* human tolerances to injury.<sup>20</sup> Crash test dummies such as the Hybrid III are commonly used in automotive test environments to assess safety devices such as airbags. The neck and head of these devices can provide a foundation for testing preventative devices such as helmets. These models allow for repetitive testing without having to use valuable biologic tissues. However most (notably the Hybrid III) are not modeled on the anatomy of human cervical column and do not provide a realistic kinematic response to impact. These devices are designed to predict the likelihood of injury. They do not simulate fracture, rupture, or dislocation of anatomical elements. They do not allow further understanding of the column's response to the injury event.

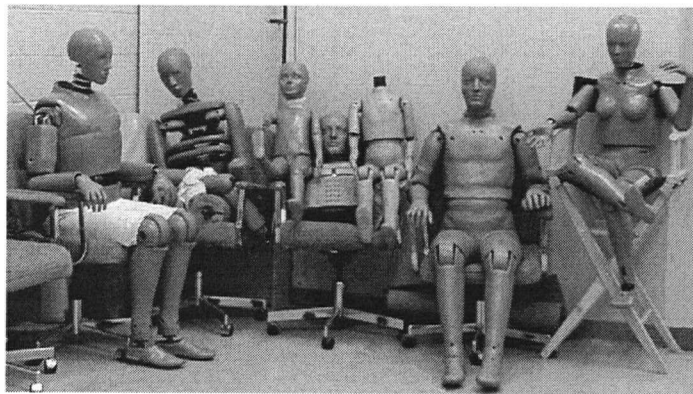


Figure 1-15: Some of the antropometric test devices (ATDs) developed. The devices range from children to the 95<sup>th</sup> percentile male dummy and includes female models.<sup>21</sup>

Mathematical models of the cervical column have been developed as a tool to assess injury.<sup>22-26</sup> These finite element and multi-dynamic models have been developed for specific injuries and range from simple two-dimensional models to detailed three-dimensional models that can include musculature or the spinal cord. These models allow for the determination of site specific loads and strains as well as a more general response. Although mathematical models used for impact assessment purposes can be adapted to include musculature, there is little experimental data to validate the model for use in axial impact simulations.

An *in vitro* human cervical spine model was selected for use in this work. This model offered the best compromise of anatomy, material, mechanical, and biomechanical

properties in comparison to the other available models. The cadaveric model offers anatomically correct bony and ligamentous anatomy. The mechanical material properties of the ligamentous spine and its components including bones, ligaments and discs have been shown to not be grossly influenced by freezing and thawing the specimen.<sup>27</sup>

To the best of our knowledge, no previous axial impact studies using *in vitro* models have accounted for and modeled the effects of musculature on the impact response. Musculature of the spine *in vivo* is thought to contribute to the stabilization of the structure. This same stability is not seen *in vitro*.<sup>28</sup> In past impact studies using *in vitro* models, high speed and complex buckling have been reported.<sup>14,15</sup> This could be an effect of the instability of the *in vitro* spine. Incorporating musculature may mitigate the buckling response and result in more realistic injury patterns. Simulated musculature has been recently applied to a whiplash model and has been shown potential to increase the biofidelity of impact injury models.<sup>29</sup> These methods could be used to develop better models to test new preventative devices and assess the conditions in sporting and automotive environments that can be to improve safety.

#### 1.4.2 Spinal Cord Injury

During impact injury, the bony anatomy may encroach into the spinal canal impinging or contusing the spinal cord resulting in neurological damage. The neurological effects of cervical spine injury have been studied extensively in animal models.

Spinal cord injury has mostly been studied at the cellular level. Animal models have been developed to replicate injury conditions using machines to deliver the injury.<sup>4</sup> Effects of loading conditions, injury time lines, and treatment methods have all been studied using these models. The injury conditions such as speed of the impactor, degree of compression of the spinal cord or area of contusion of the spinal cord used in these models are often not based on experimentally established parameters.<sup>4</sup>

The relationship between bony and cord injury during an injurious event is currently not well understood. Clinical evidence of injury to both the cord and osteoligamentous anatomy can be used to draw relationships between the two but does not give an indication of the transient conditions during the event such as velocity of the bony anatomy, degree of compression, or area of compression. These values in any injury scenario are largely unknown. Work in the area of canal occlusion has provided some



indication of these parameters.<sup>30-35</sup> However, the majority of methods used in most of these studies have largely neglected the issue of biofidelity of the bone-cord interface. The most relevant work done to address this issue has reported pressures experienced by the cord at discrete points and not the desired information on degree of compression and the characteristics of the deformation as a continuous profile of the cord.<sup>34</sup>

## 1.5 Objectives

The two primary goals of this work are as follows:

1. **Assess the effect of including simulated musculature in an in vitro cervical spine axial, head first impact model.** Simulating musculature will mimic the stabilizing behaviour of *in vivo* musculature thereby increasing the stability of the specimen. It is hypothesized that this will eliminate the snap through and complex buckling patterns reported in previous models. This new model can be used to provide a standard for assessment of new preventative and safety devices. The kinematic and kinetic data collected can be used to develop and validate new anthropometric test devices and mathematical models which incorporate musculature.
2. **Quantify spinal cord deformation during cervical spine impact injuries.** While it is known that post-traumatic measures of canal occlusion do not reflect the degree of occlusion occurring during the injury event, the degree of dynamic spinal cord compression is not known. Furthermore a sagittal profile of the spinal cord during injury would provide enlightenment on the deformations experienced. A catalogue of the relationship between bony and spinal cord injury could be developed from this information and be used to improve the correlation between animal models and real world injury.

## 1.6 Road Map

The main body of this manuscript is divided into two sections. The first section addresses the development and construction of methodologies and apparatus used in the pursuit of the goals of this project. There are five chapters in this section each written as a short technical paper focused on the development and validation of each apparatus or methodology.

- ♦ Chapter 2 describes the construction of the drop tower apparatus used for injury simulation. The previously used approaches and the reasoning behind our choice are discussed here.
- ♦ Chapter 3 presents the motion capture methodologies used for kinematic analysis. The various motion capture systems available were reviewed. A dual high speed digital camera based system was selected. The algorithm used for three-dimensional reconstruction is also described and optimized.
- ♦ Chapter 4 discusses the selection and placement of the kinetic instrumentation. Previous studies on the cervical spine in axial impact were used to determine the load cell ranges required. The data acquisition and synchronization systems are also discussed here.
- ♦ Chapter 5 reviews the different methods used to simulate musculature in the *in vitro* cervical spine and describes the method used in this work. The follower preload models previously developed for *in vitro* biomechanical studies are reviewed and assessed for usability in our model.
- ♦ Chapter 6 describes the development of a novel method of visualizing the spinal cord within the spinal canal. The components of the system consisting of a high speed digital cineradiograph paired with a radiodense biofidelic surrogate spinal cord are specified here.

The second section consists of two chapters, each focused on one of the two main goals of this project. These chapters are treated as separate studies and are written in traditional manuscript format.

- ♦ Chapter 7 focuses on the effect of simulated musculature on the cervical spine response to axial impact. The hypothesis about the elimination of the buckling response of the preloaded spine to impact is tested in this study. The kinematic and kinetic results collected are used to determine the effects of follower preload.
- ♦ Chapter 8 focuses on the deformation of the spinal cord during cervical spine injury. Canal occlusion measurement techniques and other spinal cord deformation measurement techniques are reviewed. Rudimentary relationships between bony and cord injury are drawn based on the results from the limited number of specimens tested in this preliminary study.

This introductory chapter (Chapter 1) discusses the relevant of this work; reviews the anatomy of the human cervical spine and the pathology of cervical spine injury at both the bony and cord levels; and states the research goals, to be addressed in this work. The final chapter (Chapter 9) summarizes the entire work and gives the final conclusions, limitations, recommendations, and proposes future work ideas.

## 1.7 References

1. Spinal Cord Injury in Canada, Canadian Paraplegic Association. 2000.
2. Spinal Cord Injury Facts and Statistics, Rick Hansen Spinal Cord Injury Registry. 2005.
3. Piziali, R., et al., Injury causation in rollover accidents and the biofidelity of Hybrid III data in rollover tests, in SAE International Congress and Exposition, SAE: Detroit, Michigan. 1998: p. 105-118.
4. Kwon, B.K., T.R. Oxland, and W. Tetzlaff. Animal models used in spinal cord regeneration research. *Spine*, 2002: 27(14): p. 1504-10.
5. Gray, H. and C.D. Clemente. *Anatomy of the human body*. 30th American ed, Lea & Febiger, Philadelphia. 1985: xvii, 1676 p.
6. Drake, R.L., W. Vogl, and A.W.M. Mitchell, eds. *Gray's Anatomy for Students*. 2004, Churchill Livingstone: New York.
7. Panjabi, M.M., A.A. White, and R.M. Johnson. Cervical spine mechanics as a function of transection of components. *J Biomech*, 1975(8): p. 327-336.
8. Patwardhan, A.G., et al. Load-carrying capacity of the human cervical spine in compression is increased under a follower load. *Spine*, 2000: 25(12): p. 1548-54.
9. Harris, J.H. and S.E. Mirvis. *The radiology of acute cervical spine trauma*. 3rd ed, Williams & Wilkins, Baltimore. 1996: xiv, 512 p.
10. Argenson, C., et al., A scheme for the classification of lower cervical spine injuries: Nice, France. 2000.
11. White, A.A. and M.M. Panjabi. *Clinical biomechanics of the spine*. 2nd ed, J.B. Lippincott Company, New York. 1990.
12. Svensson, M.Y., et al. [Nerve cell damages in whiplash injuries. Animal experimental studies]. *Orthopade*, 1998: 27(12): p. 820-6.
13. Alem, N.M., G.S. Nusholtz, and J.W. Melvin. Head and Neck Response to Axial Impacts. in 28th Stapp Car Crash Conference, Chicago, Illinois, USA, Society of Automotive Engineers, Inc., Warrendale, Pennsylvania, USA. 1984
14. McElhaney, J.H., et al. Cervical spine compression responses, Warrendale, PA, 27th Stapp car crash conference. 1983
15. Nightingale, R.W., et al. Experimental impact injury to the cervical spine: relating motion of the head and the mechanism of injury. *Journal of Bone and Joint Surgery. American Volume*, 1996: 78-A(3): p. 412-421.
16. Nightingale, R.W., et al. Dynamic response of the head and cervical spine to axial impact loading. *Journal of Biomechanics*, 1996: 29(3): p. 307-318.
17. Yoganandan, N., et al. Strength and kinematic response of dynamic cervical spine injuries. *Spine*, 1991: 16(10 Suppl): p. S511-7.
18. Yoganandan, N., et al. Experimental spinal injuries with vertical impact. *Spine*, 1986: 11(9): p. 855-860.
19. Yoganandan, N., et al. Injury biomechanics of the human cervical column. *Spine*, 1990: 15(10): p. 1031-1039.
20. Mertz, H.J., *Anthropomorphic Test Devices*, in *Accidental Injury Biomechanics and Prevention*, A.M. Nahum and J.W. Melvin, Editors. 2001, Springer Verlag. p. 72-88.
21. Denton ATD, [www.radenton.com](http://www.radenton.com): Rochester Hills, MI. 2006.

22. Bilston, L.E. Finite Element Analysis of Some Cervical Spinal Cord Injury Modes. in Proceedings of the 1998 IRCOBI conference, Goteborg, Sweden. 1998
23. Deng, Y.-C. and W. Goldsmith. Response of a human head/neck/upper-torso replica to dynamic loading -- II. analytic/numerical model. Journal of Biomechanics, 1987: 20(5): p. 487-497.
24. Greaves, C.Y., Spinal Cord Injury Mechanisms: A Finite Element Study, in Department of Mechanical Engineering, University of British Columbia: Vancouver, Canada. 2004.
25. Williams, J.L. and T.B. Belytschko. A three-dimensional model of the human cervical spine for impact simulation. Journal of Biomechanical Engineering, 1983: 105(4): p. 321-331.
26. Yoganandan, N., et al. Finite element applications in human cervical spine modelling. Spine, 1996: 21(15): p. 1824-1834.
27. Panjabi, M.M., et al. Biomechanical time-tolerance of fresh cadaveric human spine specimens. Journal of Orthopaedic Research, 1985: 3: p. 292-300.
28. Panjabi, M.M., et al. Critical load of the human cervical spine: an *in vitro* experimental study. Clinical Biomechanics, 1998: 13(1): p. 11-17.
29. Ivancic, P., et al. Biofidelic whole cervical spine model with muscle force replication for whiplash simulation. European Spine Journal, 2005: 14(4): p. 346-355.
30. Bilston, L.E. and L.E. Thibault. Biomechanics of cervical spinal cord injury in flexion and extension: a physical model to estimate spinal cord deformations. International Journal of Crashworthiness, 1997: 2(2): p. 207-218.
31. Carter, J.W., et al. Canal geometry changes associated with axial compressive cervical spine fracture. Spine, 2000: 25(1): p. 46-54.
32. Chang, D.G., et al. Geometric changes in the cervical spinal canal during impact. Spine, 1994: 19(8): p. 973-980.
33. Panjabi, M.M., et al. Dynamic canal encroachment during thoracolumbar burst fractures. J Spinal Disord, 1995: 8(1): p. 39-48.
34. Pintar, F., et al. Cervical Spine Bony Injury and the Potential for Cord Injury. in Proceedings of the 5th CDC Symposium for Injury Prevention. 1995
35. Wilcox, R., A Biomechanical Study of Thoracolumbar Burst Fractures, in School of Mechanical Engineering, The University of Leeds. 2002.

## **Chapter 2: Drop Tower Development**

### **2.1 Introduction**

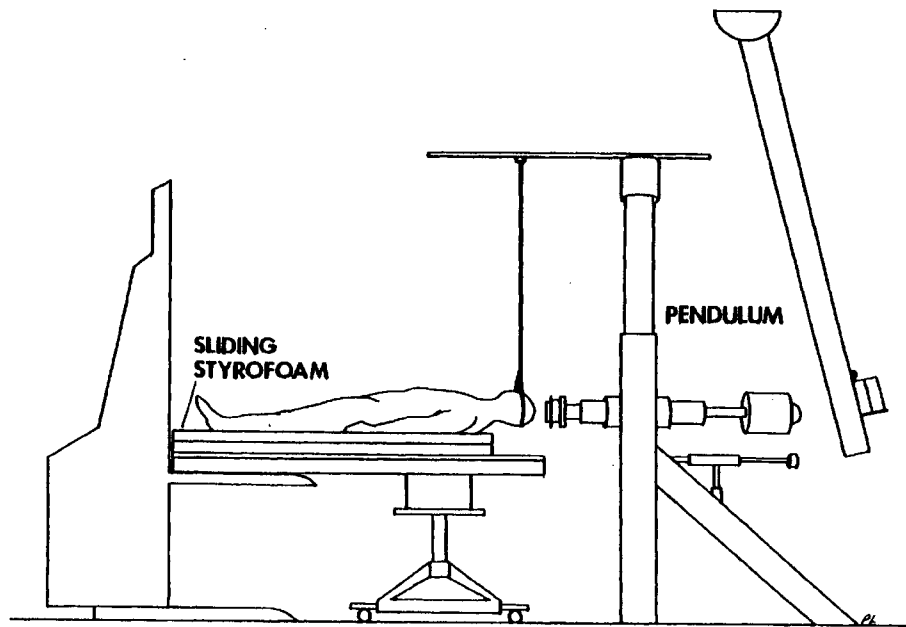
There have been many studies that have examined the response of the whole cervical spine during high speed axial impacts as seen in automotive and sporting accidents. In these events where a person is traveling head-first, the head is arrested while the torso continues to load the cervical spine. The kinematic response of the cervical spinal column and the injuries sustained depend on the load conditions such as direction of impact, velocity, and force. Past studies have used a variety of methods to simulate axial head-first impact. Horizontal impactors have been used to recreate and examine neck injuries experienced during football accidents typically using full cadavers. Vertical impactors are more common with isolated head and/or neck specimens in a servohydraulic or drop mass apparatus, which allows for improved control of the conditions and have been used to induce specific injuries. Drop towers are also used to simulate impact events and are particularly apt for diving and rollover simulations as the impact action mimics the real life scenario where both the head and torso are in motion. The method used in any study should reflect the injury scenario of interest so as to recreate the loading conditions as closely as possible. Several issues are of particular concern in the simulation of axial impact to the head and neck including the management of head position, initial alignment of the spine, and the impact loading conditions. In this work, an axial head to ground type impact was desired to simulate the impact event such as that seen in diving, automotive rollover, cycling, equestrian, and other sporting accidents.

### **2.2 Background**

There are three general approaches used in cervical spine impact studies: horizontal impactor, vertical impactor, and specimen drop.

#### **2.2.1 Horizontal Impactor**

The general approach to the horizontal impactor is to use a full cadaver in a horizontal position and impact the head using a pendulum, Figure 2-1. The cadaver may or may not be restrained. The head is often supported prior to impact so as to maintain posture prior to impact.



Reprinted with permission from SAE paper 811005 © 1981 SAE International

Figure 2-1: Schematic of the horizontal impactor used by Nusholtz and colleagues.<sup>1</sup>

Nusholtz and colleagues used a horizontal impactor to induce hyperflexion and cause flexion type injuries of the cervical spine such as wedge fractures.<sup>1</sup> The impactor used was a 56 kg impactor, which was driven by a pendulum, providing impact speeds of 4.6 to 5.6 m/s. Whole cadavers were positioned prone either inline with or at an angle to the impactor. In either case the head was supported in the desired position prior to impact and the cadaver was not restrained. During impact the head was supported to restrict extension of the spine due to gravity.

The same group performed a similar series of tests to study neck injury resulting from axial impact without limiting the head motion.<sup>2</sup> The impactor in this study was 10kg with a velocity of 7-11 m/s. Whole cadavers were placed either prone or supine in line with the impactor with the head supported on break away paper. Upon impact the head was not constrained and the neck was free to flex or extend. The results do not report the kinematic response of the neck during impact.

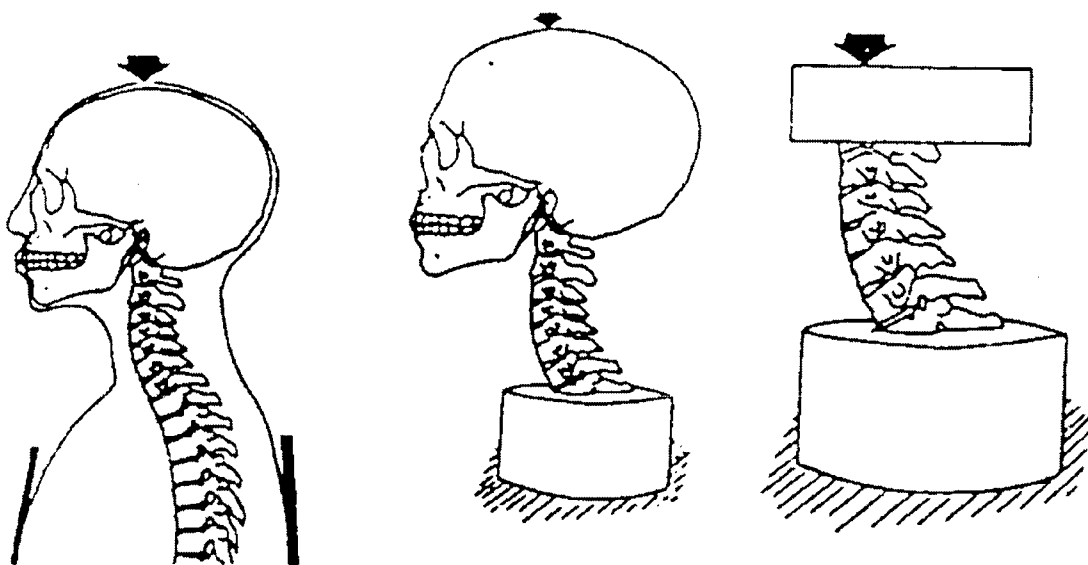
Hodgson and colleagues have also used a horizontal impactor to study injuries resulting from tackling in football.<sup>3</sup> This method is particularly suited to this application as it allows for full reconstruction of the impact conditions of tackling where the direction

of loading is horizontal. Full body cadavers were used in this study. The impactor was a modified dummy leg so as to mimic tackling.

In general the horizontal impactor is not appropriate for use in our study as the gravitational effects are perpendicular to the direction of loading which may influence the response to the cervical spine to impact by inducing a non-physiologic extension due to the head mass and possible sagging of the natural curvature of the spine.

### 2.2.2 Vertical Impactor

During axial impact by a vertical impactor the specimen remains stationary while a mass or hydraulic ram impacts the specimen. This method has been used with full cadaveric specimens as well as the *ex vivo* cervical spine, Figure 2-2. This technique is particularly suited to studies, which aim to examine a particular impact configuration or resulting injury. Burst fractures and canal occlusion of the cervical spine have been studied using this approach.<sup>4</sup>



Reprinted with permission © 1989 ASME

Figure 2-2: Schematic of different specimens prepared for impact in a vertical impactor.<sup>5</sup>

The response of the cervical spine to axial impact using this approach has been extensively studied by Pintar, Yoganandan, and colleagues with a hydraulic piston.<sup>6-12, 5, 13</sup> This group has used whole cadavers, head and neck complexes, and isolated cervical spines. For specimens where the head was still intact it was held in position through contact with the piston or by a mass and spring system,



Figure 2-3. For specimens without full heads, the existing skull section, occiput, or atlas was embedded in polymethyl methacrylate (PMMA) and fixed to the piston. These experiments restrain the head to motion in line with the piston which may influence the response of the head-neck complex. However this allowed for the most control over the direction of impact and the alignment of the specimen. The specimens were tested in a range of loading rates from quasi-static to 5.1 m/s. Axial displacement was controlled by the piston excursion. The specimens were compressed 15-45 mm. This may have led to the specimen being overdriven in the greater displacements. That is, the specimen could suffer injuries beyond those caused by the initial impact.

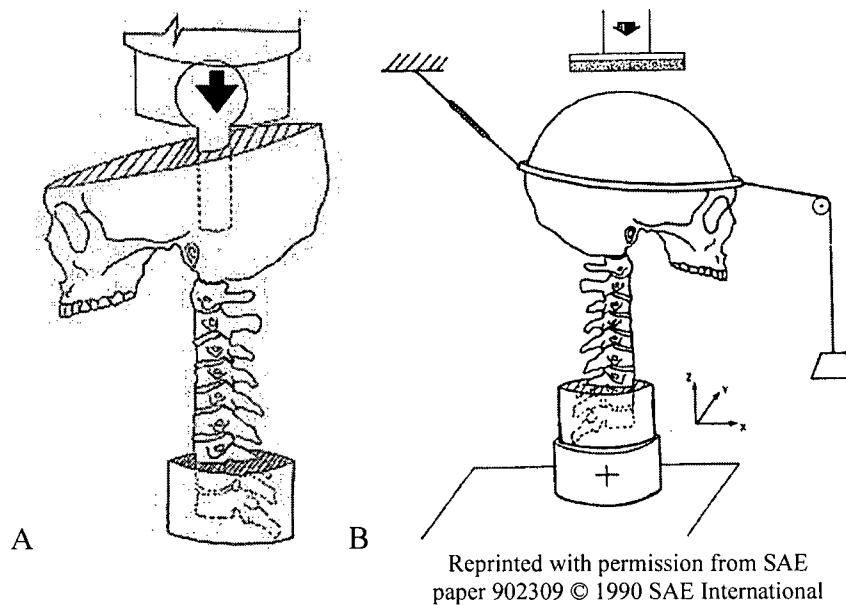


Figure 2-3: Two methods of head restraint used by Yoganandan, Pintar, and colleagues:  
A) direct connection to the piston<sup>13</sup> B) spring and mass system<sup>6</sup>

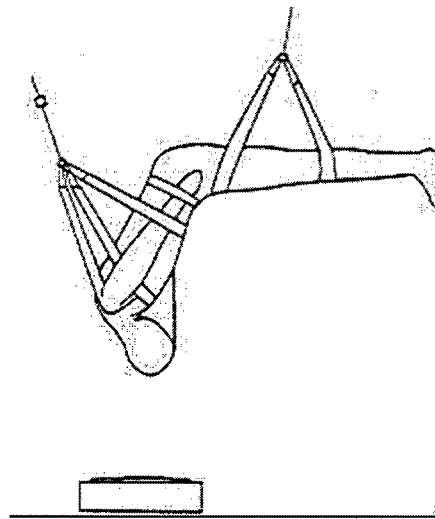
This approach is not appropriate for our purposes. With an upright specimen the weight of the head must be counterbalanced to prevent premature buckling of the spine. In doing so, the response of the head and neck to impact may be affected. Though this is beneficial when certain conditions of head and neck position and loading are needed, it is not conducive to mimicking the impact events seen in head to ground impact.

### 2.2.3 Inverted Drop

The inverted drop replicates the head to ground impact the most realistically as the direction of loading and effects of gravitational acceleration is preserved. Also with this design the mass of the head does not need to be counterbalanced to prevent premature

buckling of the spine. This method has been used with whole cadavers and isolated head-neck complexes.

Nusholtz and colleagues dropped whole cadavers from heights of 0.1 m or ranging between 0.914 to 1.5 m.<sup>1</sup> The cadavers were hoisted using a harness and pulley system and released for a free fall, Figure 2-4. The upper body was positioned in a head down position with the body aligned perpendicular to the impact surface. The head was positioned relative to the torso to adjust the posture of the spine (flexion, extension, or neutral) depending on the desired impact conditions. Similar work was also performed by Yoganandan *et al.*<sup>12</sup>

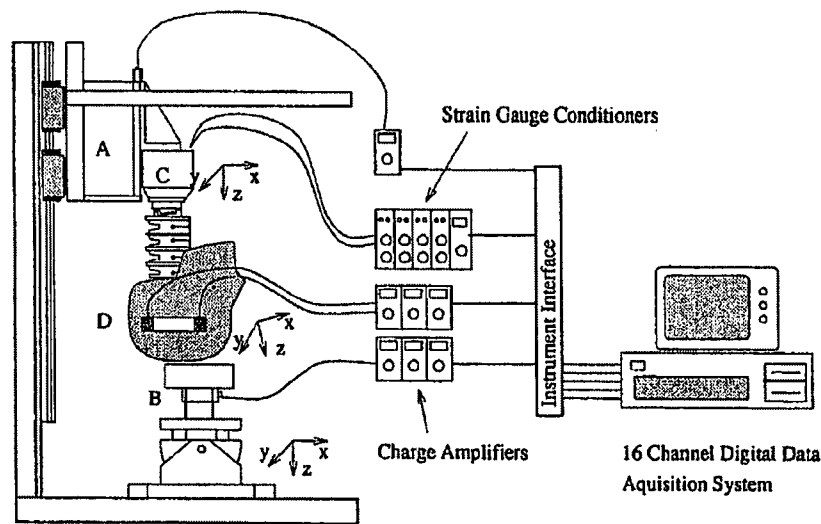


Reprinted with permission from SAE paper 831616 © 1983 SAE International

Figure 2-4: Vertical drop of full body cadavers for head to ground impact simulation.<sup>2</sup>

Axial impact simulation in the inverted position has also been achieved with isolated cadaveric head and neck complexes using a drop tower. Nightingale and colleagues developed a drop track that would simulate head to ground impact using *ex vivo* head and cervical spine (to T1) specimens, Figure 2-5.<sup>14</sup> The carriage of the drop tower was designed to replicate the upper torso mass. The drop height used was based on the predetermined critical velocity for cervical spine injury. The head was positioned with suture material, which effectively compressed the cervical spine and held it in a neutral posture preserving the lordotic curve of the spine until impact. Upon impact the head was no longer restrained. This method of simulating head to ground impact using a drop tower has the most potential for use in this study as it best replicates the mechanical

conditions of impact using a minimum of cadaveric material and allowing precise control of the boundary conditions such as head and spine posture.



Reprinted with permission © 1996 Journal of Bone and Joint Surgery

Figure 2-5: Schematic of the drop tower and instrumentation used by Nightingale and colleagues in their head to ground simulations.<sup>15</sup>

## 2.3 Requirements

Several requirements needed to be addressed in the design of the drop tower. The overall design considerations of the apparatus were to:

- ♦ Induce axial impact injuries using human cadaveric cervical spines (C0-T1 inclusive) with a simulated following torso
- ♦ Provide a head first axial impact
- ♦ Allow for flexibility in instrumentation including load cells to measure impact at the head and at the base of the neck (T1)
- ♦ Allow for flexibility in placement of imaging equipment (both external and radiographic)
- ♦ Have potential for use in future impact studies of other anatomical structures and/or preventative devices
- ♦ Allow a range of impact velocities

### 2.3.1 Drop Height

The minimal acceptable drop height was dictated by the tolerance of the cervical spine to axial impact. It has been previously found that injury to the cervical spine occurs at speeds exceeding 3 m/s.<sup>16, 17, 15</sup> To obtain this velocity in free fall, a drop height of at least

0.46m was required based on frictionless bearings. The actual required height depended on the friction coefficient of the bearings.

It was anticipated that the drop tower would also be used in other studies requiring greater speeds. The maximum drop height was therefore designed to be limited by the height of the ceiling in the laboratory.

### 2.3.2 Specimen Visibility

The line of sight requirements of two imaging systems needed to be addressed. The three dimensional reconstruction of the column kinematics required two high speed digital cameras to be placed such that the lines of sight to the specimen intersected. The high speed x-ray set up required a path clear of metal objects between the x-ray tube, specimen, and image intensifier.

### 2.3.3 Structure

As the drop tower was to be used in several locations it was required to be self-supporting. It could not require attachment to the floor, walls, or ceiling for support. It was required to be stable for all impact heights as a freestanding structure.

As biological specimens were to be used, the structure and all other materials used were required to be corrosion resistant. The structure would be exposed to bleach and saline during testing and clean up.

### 2.3.4 Portability

As the drop tower would be used in a variety of places. It was required to disassemble into pieces that could be transported in a full sized pick up truck.

### 2.3.5 Carriage

There were several design considerations that had to be met by the carriage. It had to weigh less than 15 kg. This corresponds to the mass of the upper torso of a 50<sup>th</sup> percentile male. Included in this mass were a six-axis load cell (0.9 kg) and the specimen mounting cup with dental stone (~2 kg). Other requirements were:

- ♦ To allow for the attachment of a load cell.
- ♦ That since free fall is desired then guides must be low friction
- ♦ To incorporate a release system.

### 2.3.6 Platen

The impact platform was required to not influence the motion of the specimen at impact. Thus it had to be low friction and it could not deform at impact. The platform had to allow for the placement of a uni-axial load cell between it and the bottom frame of the drop tower structure.

### 2.3.7 Release

Due to the presence of x-rays during testing the carriage release system had to allow the user to release the carriage remotely from behind safety shielding.

### 2.3.8 Stoppers

To prevent overdriving of the specimen, stopping mechanism was needed. To allow for specimen variability this needed to be adjustable as well as completely removable.

### 2.3.9 Triggering

A method of triggering the cameras and data collection systems was needed. The camera memory was limited to 0.787 seconds at the 1000 fps collection rate and maximum frame resolution. To ensure that the entire impact of approximately 0.5 seconds was recorded the trigger was designed to occur close to the point of impact.

## 2.4 Materials

### 2.4.1 Structure

The basic frame of the drop tower can be seen in Figure 2-6. The support structure of the drop tower was made of Unistrut (1 5/8 inch series, Wayne, MI, USA), a metal channel framing system. The base frame was a cross shaped frame with four legs in a square configuration. It was 1.75 m tall. The footprint measured 1.17 m on each side. Attached to the frame was a manual hoist for the carriage. A square top frame was used to maintain the alignment of the guides. The top frame also supported a strut, which was fitted with pulleys to raise the carriage to the desired height.

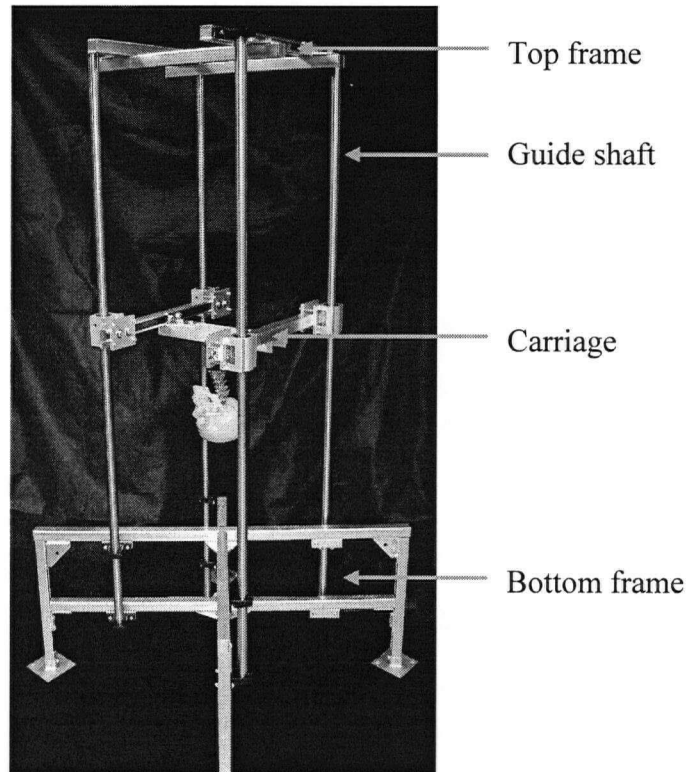


Figure 2-6: Drop tower structure showing only the four guide shafts, top and bottom frames, and basic carriage

#### 2.4.2 Guides

Four solid steel shafts were used as the guides, Figure 2-6. The diameter of each shaft was 38.1 mm. They were arranged in a square measuring 0.60 m per side. Each shaft was 2.30 m long. Shaft supports were bolted to the base frame to support each shaft in two places. Supports on the top frame maintained the alignment of the vertical guides.

#### 2.4.3 Carriage

The carriage was an h-shaped frame, Figure 2-7. Aluminum Unistrut was used for the crosspiece and legs of the h-shape. Ball bearings in pillow blocks (SSUFB-24-CR, Thomson Ball Bushing, USA) were attached to the ends of the legs of the carriage using a grip plate approach (consisting of four bolts and a plate that clamped the pieces together), which allowed for adjustability in their placement. Three of the bearings were self-aligning while the fourth was fixed. This allowed for some misalignment of the guides. The grip plate method was also used to affix a load cell to the carriage cross piece. The total mass of the carriage (including the load cell and specimen mounting cup) was 13.8 kg.

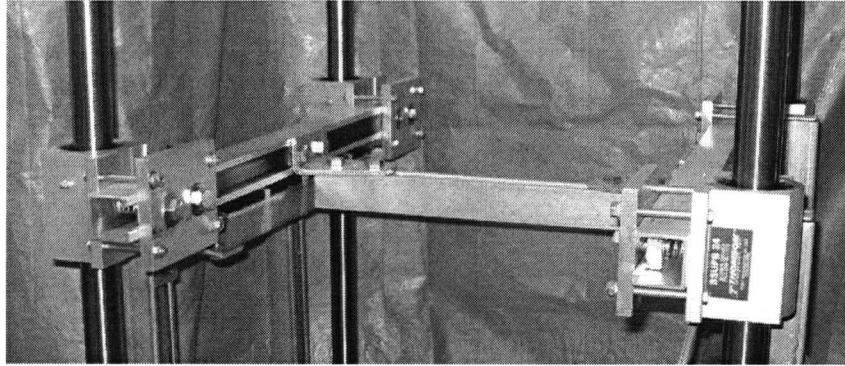


Figure 2-7: Carriage with bearings

#### 2.4.4 Impact platen

The impact platform was a 25.4 mm thick steel plate, Figure 2-8. It measured 0.2 by 0.4 m. Ultra high molecular weight polyethylene tape was used on the top surface to provide a low friction impact surface. The underside of the plate attached to a uni-axial load cell by a 1 ½ inch threaded rod.

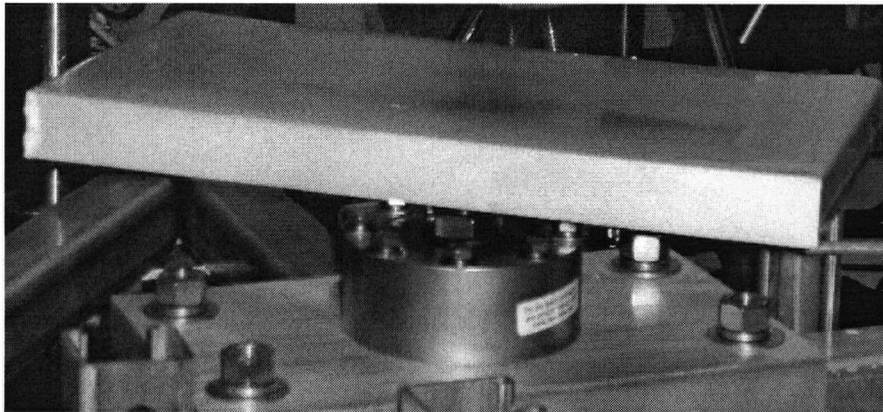


Figure 2-8: Impact platen covered in UHMWPE tape with uni-axial load cell

#### 2.4.5 Release

A snap shackle was selected as the release mechanism. The plunger pin was tethered to a rope so that it could be pulled from outside the shielded area.

#### 2.4.6 Trigger

The cameras were triggered by closing a simple circuit connected to the trigger cable of the cameras. The open circuit consisted of two exposed wires, one at 5 V, the other grounded. As the carriage descended it would brush the exposed wires simultaneously thus closing the circuit and triggering the cameras and data acquisition systems.

#### 2.4.7 Drop Height

It was found through experimentation that there was a small amount of friction in the system. The carriage was loaded to mimic the mass of the specimen and equipment and dropped from a variety of heights. The speed of the carriage at the end of its descent was determined using footage from the high speed digital cameras. A drop height of 0.6 m was found to result in the desired impact speed of 3 m/s when the carriage was fully loaded with load cell, and the prepared specimen (~20kg total mass).

#### 2.5 Conclusion

To induce axial impact injuries to the neck in human cadaveric specimens, a head first, head-to-ground approach was selected. The drop tower constructed for this purpose met all of the design requirements.



## 2.6 References

1. Nusholtz, G.S., et al. Response of the cervical spine to superior-inferior head impact. in 25th Stapp Car Crash Conference, Society of Automotive Engineers. 1981
2. Nusholtz, G.S., et al. Cervical spine injury mechanisms. in 27th Stapp Car Crash Conference, Society of Automotive Engineers. 1983
3. Hodgson, V.R. and L.M. Thomas. Mechanisms of cervical spine injury during impact to the protected head. in 24th Stapp Car Crash Conference, Society of Automotive Engineers. 1980
4. Raynak, G.C., et al. Transducers for dynamic measurement of spine neural-space occlusions. *Journal of Biomechanical Engineering*, 1998: 120(6): p. 787-791.
5. Yoganandan, N., A.J. Sances, and F.A. Pintar. Biomechanical evaluation of the axial compressive responses of the human cadaveric and maniken necks. *Journal of Biomechanical Engineering*, 1989: 111: p. 250-255.
6. Pintar, F., et al. Biodynamics of the total human cadaveric cervical spine. in 34th Stapp Car Crash Conference, Orlando, Florida, USA, Society of Automotive Engineers, Inc., Warrendale, Pennsylvania, USA. 1990
7. Pintar, F.A., et al. Cervical vertebral strain measurements under axial and eccentric loading. *Journal of Biomechanical Engineering*, 1995: 117: p. 474-478.
8. Pintar, F.A., et al. Kinematic and anatomical analysis of the human cervical spinal column under axial loading, Warrendale,PA, 33rd STAPP car crash conference. 1989
9. Pintar, F.A., et al. Dynamic characteristics of the human cervical spine, Warrendale,PA, 39th STAPP car crash conference. 1995
10. Yoganandan, N., et al. Strength and motion analysis of the human head-neck complex. *Journal of Spinal Disorders*, 1991: 4(1): p. 73-85.
11. Yoganandan, N., et al. Strength and kinematic response of dynamic cervical spine injuries. *Spine*, 1991: 16(10 Suppl): p. S511-7.
12. Yoganandan, N., et al. Experimental spinal injuries with vertical impact. *Spine*, 1986: 11(9): p. 855-860.
13. Yoganandan, N., et al. Injury biomechanics of the human cervical column. *Spine*, 1990: 15(10): p. 1031-1039.
14. Nightingale, R.W., *The Dynamics of Head and Cervical Spine Impact*, in Department of Biomedical Engineering, Duke University. 1993.
15. Nightingale, R.W., et al. Dynamic response of the head and cervical spine to axial impact loading. *Journal of Biomechanics*, 1996: 29(3): p. 307-318.
16. McElhaney, J., et al. *Biomechanical Analysis of Swimming Pool Neck Injuries*. Society of Automotive Engineers SP-79, 1979: p. 47-53.
17. Nightingale, R.W., et al. Experimental impact injury to the cervical spine: relating motion of the head and the mechanism of injury. *Journal of Bone and Joint Surgery.American Volume*, 1996: 78-A(3): p. 412-421.

## **Chapter 3: Motion Capture System**

### **3.1 Introduction**

A method of capturing the three-dimensional motion of the spine during impact was required to correlate vertebral motion to the resulting injuries. This motion was characterized by measuring the positions of markers mounted on the vertebrae. The analysis of the three-dimensional marker position data to give three-dimensional rigid body motion is described in Chapter 7. This section addresses the development and performance assessment of the motion capture system. Ideally the system would provide quantitative and qualitative information. For impact the de facto standard rate of capture is 1000 Hz. This rate has also been set as the industry standard by the Society of Automotive Engineers for crash testing.<sup>1</sup> Several methods of motion capture were available, however upon considering the options it was thought that dual, non-planar, high speed digital cameras paired with motion tracking and three-dimensional reconstruction software would best address the motion capture needs of this study.

### **3.2 Background**

There are several methods of motion tracking used in biomechanics. The most common are electromagnetic marker tracking, optical marker tracking, and analog or digital cinematography analysis.

Electromagnetic marker tracking, such as the Flock of Birds (Ascension Technology Corporation, Burlington, VT) and Aurora (Northern Digital Inc., Waterloo, ON) systems, uses active markers containing three perpendicular wire coils to generate a magnetic field. Sensors are used to detect the location of these fields based on strength and can determine orientation of the marker based on the orientation of the three fields. The major advantage of this system is that the user does not need to worry about line of sight to the marker. However, the markers are wired and the magnetic fields can be distorted in the presence of metallic objects and unrelated magnetic fields. Also these systems operate at low speeds (40-144Hz) with a limited number of markers and do not provide qualitative footage of the event.

Optical marker tracking is the most common method used in biomechanics. These systems triangulate the three-dimensional location of a marker from overlapping two dimension projections of its location relative to a camera or optical sensor. This tracking method uses either passive or active markers. Passive optical systems, such as the Vicon MX system (Vicon, Los Angeles, CA), use reflective markers and multiple strobe cameras to determine the location of the marker in a defined volume of space. Software is used to identify, track, and triangulate markers in the volume to recreate the three dimensional locations and motions of markers and associated bodies. The Vicon system operates at a maximum speed of 2000Hz regardless of the number of markers and cameras. Resolution of this system depends on the volume of the space of interest but is given as 0.02 pixels in the Vicon system.

Active optical systems, such as Optotrak (Northern Digital Inc., Waterloo, ON), use LED markers that strobe in succession. Multiple optical sensors detect the two-dimensional location of each marker and triangulate its three-dimensional location. These markers are wired and limit the speed of the system as the maximum speed (4600Hz for the Optotrak) is divided by the number of markers in use. The accuracy and resolution is high (0.1mm and 0.01mm respectively) and the system cannot confuse the markers during testing. The major limitation to optical systems is that neither the active nor passive type provides qualitative footage of the event of interest; they only “record” the markers’ locations.

Digital and/or analog cinematography use several regular or high speed video cameras to record the event of interest. Markers or features on the object of interest can be tracked by hand or by object recognition and tracking software to provide the relevant two-dimensional position data. The two-dimensional marker position data from several cameras is then run through a three-dimensional reconstruction algorithm to yield the three-dimensional position data. This system has the benefit of yielding qualitative footage of the event in addition to the quantitative position data. The speed of the system is dictated by the frame rate of the cameras used. The accuracy and resolution is dependant on several factors such as the cameras’ resolution (frame size), volume of interest, and marker tracking software characteristics and is unique to each set up. By virtue of the high frame rates, potential for high accuracy, and the ability to provide

qualitative information, digital cinematography was determined to be the most appropriate.

### **3.3 Requirements**

A camera based three-dimensional motion capture system can be broken down into three components: the cameras, the marker tracking process, and the three-dimensional reconstruction algorithm.

#### **3.3.1 Cameras**

For the purposes of high speed impact a minimum frame rate of 1000Hz was required as dictated by the Society of Automotive Engineers Standard for Instrumentation for Impact Testing, Part 2.<sup>1</sup> To maximize the spatial resolution of the system, a high camera resolution was needed. Increasing the spatial resolution would also increase the accuracy of the marker tracking as the markers would be represented by a larger area of pixels. Although analog high speed cameras would provide the greatest spatial resolution, the resulting analog footage would not be compatible with the computer based automatic marker tracking program that was required because manual digitization was not practical for this application owing to the large number of markers and images. The current generation of high speed digital cameras typically feature relatively high resolution at the desired frame rate, for example 1632X1200 pixels at 1000 Hz in the Phantom V9.0 cameras (Vision Research Inc., Wayne, NJ), which were considered state of the art at the time of this study.

#### **3.3.2 Marker Tracking**

Several automatic marker tracking software packages have been developed commercially. These software packages are image analysis programs which use object recognition algorithms to identify and track features such as markers in a series of digital images. These algorithms dictate the predictive behaviour of the software and its ability to identify markers despite morphing pixel patterns (i.e. the amount of change of the pixels representing the object of interest allowed by software before it is unrecognizable). Due to the chaotic nature of impact and the resulting chaotic movement of the markers, the path of the object of interest is not predictable. The ability to adjust the constraints of these algorithms could improve the accuracy and efficiency of the tracking software, as

well as its ability to operate with minimal user correction. However, a large majority of these packages have been designed primarily for gait analysis and are rudimentary in terms of the tracking algorithms and have little adjustability of these algorithms by the user.

### 3.3.3 Three-dimensional Reconstruction

Direct linear transformation (DLT) determines the three-dimensional location of an object in space based on multiple two-dimensional camera views of the object. It was adapted for use in biomechanics in 1980 by Miller and colleagues.<sup>2</sup> The method is intended for use with non-metric (i.e. commercially available) cameras placed at any angle relative to each other and the object. This method requires the use of a calibration cage to determine the mathematical relationship between the cameras and the volume of interest.

The accuracy of this three dimensional reconstruction is highly dependent on the precision and construction of the calibration cage and volume of space calibrated.<sup>3-6</sup> The number and placement of calibration markers on the calibration cage has a large influence on the accuracy of the reconstruction. The minimum number of markers needed is six. The algorithm used to solve the DLT dictates this. The mathematical solution involves the construction of a system where a minimum of 11 parameters (known coordinates of 6 control markers) are needed. Additional markers will increase the number of parameters resulting in an over-constrained system whose solution is found by least squares. Increasing the number of control markers to increase the number of known parameters has been shown to increase the accuracy by 150%.<sup>3</sup> It has also been noted that markers on the periphery of the cage have more influence than those within the volume defined by the cage.<sup>3</sup> Outside of the volume defined by the cage it has been found that the error of reconstructed points can be increase to as much as 500% at a distance three times the length of the cage in a particular direction.<sup>5, 6</sup>

## 3.4 Materials and Methods

A set-up consisting of two high speed digital cameras was selected for motion capture purposes. Commercially available marker tracking software was used to digitize the marker positions in each frame from the two cameras. A custom written algorithm was

then employed to reconstruct the three-dimensional coordinates of the markers. Further analysis of the kinematics of the specimen was conducted using this data.

#### 3.4.1 Cameras

The high speed digital cameras used were Phantom V9.0 from Vision Research Inc (Wayne, NJ). A frame rate of 1000 frames per second was used. This allowed for the largest camera resolution of 1632X1200 pixels. Manually adjustable zoom lenses were used to allow for flexibility in camera placement. These lenses have minimal image distortion thus reducing the distortion error. As two cameras were being used, the alignment of the cameras relative to the specimen was allowed to be arbitrary as long as all the markers were visible in both cameras. No literature was found to provide insight into the relationship between non-planar camera placement and the accuracy of a three-dimensional reconstruction.

#### 3.4.2 Marker Tracking Software

The method of motion capture required digital marker tracking. This was done using TEMA software (Image Systems, Linköping, Sweden). The software employed automatic tracking, which was designed to halt and ask for user input if the pixel pattern changed drastically. To maximize accuracy and efficiency of the software the path prediction algorithm was turned off and the pattern recognition algorithm was reduced to 50%. These settings were found by trial to allow for the most efficient tracking of the markers.

Documentation regarding the accuracy of the commercially available marker tracking software was not available. The software relies on algorithms to predict motion of a target and on its ability to compensate for the fluctuating background conditions. In TEMA these parameters can be adjusted for each marker. Additionally manual correction can be used to correct large errors in the tracking path. The static accuracy of the marker tracking software is reported as sub-pixel, meaning that the accuracy is greater than the spatial resolution of one pixel. In our application, a system accuracy study (detailed below) was conducted which incorporated tracking error.

#### 3.4.3 Three dimensional Reconstruction

To reconstruct the three-dimensional motions of the markers the method of direct linear transformation (DLT) as developed by Miller *et al* was used.<sup>2</sup> The reconstruction algorithm was written in Matlab. The code can be found in Appendix A. A custom-built

calibration cage was used to determine the relationship between the camera views and the three-dimensional space of interest, Figure 3-1. To ensure maximal accuracy, the cage was constructed to envelop the volume of space that would contain the specimen during testing and measures 30X20X11.5 cm. Fifteen stainless steel spheres (diameter 4 mm) were mounted into countersunk dimples around the periphery of the cage. The locations of these markers were digitized using a coordinate measurement machine\_(Richards Engineering Co Ltd, Port Coquitlam BC) to an accuracy of 0.0005 mm.

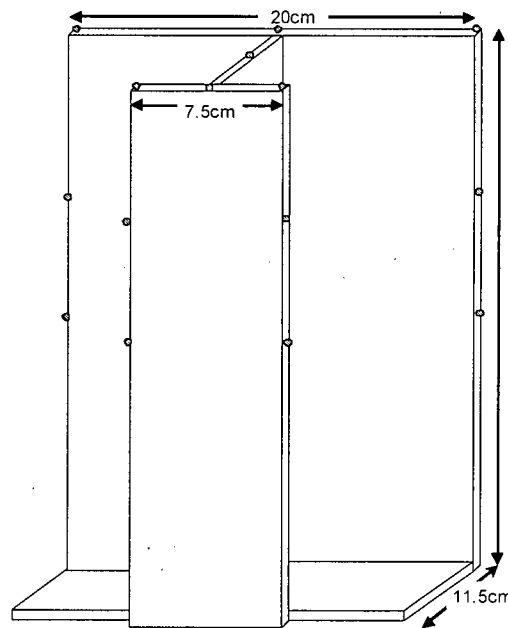


Figure 3-1: Calibration cage constructed for this three dimensional reconstruction system

The DLT algorithm had several steps. The first was to determine the relationship between the two-dimensional camera views and the three-dimensional space. This was calculated using the projection of the known three-dimensional coordinates of the calibration cage on the two-dimensional camera fields of view. This relationship is defined by a vector  $L$  which is an 11 element vector calculated in the following manner:

$$\begin{bmatrix}
 x_1 & y_1 & z_1 & 1 & 0 & 0 & 0 & 0 & -x_1 * u_1 & -y_1 * u_1 & -z_1 * u_1 \\
 x_2 & y_2 & z_2 & 1 & 0 & 0 & 0 & 0 & -x_2 * u_2 & -y_2 * u_2 & -z_2 * u_2 \\
 \vdots & \vdots & \vdots & \vdots & \vdots & \vdots & \vdots & \vdots & \vdots & \vdots & \vdots \\
 x_n & y_n & z_n & 1 & 0 & 0 & 0 & 0 & -x_n * u_n & -y_n * u_n & -z_n * u_n \\
 0 & 0 & 0 & 0 & x_1 & y_1 & z_1 & 1 & -x_1 * v_1 & -y_1 * v_1 & -z_1 * v_1 \\
 0 & 0 & 0 & 0 & x_2 & y_2 & z_2 & 1 & -x_2 * v_2 & -y_2 * v_2 & -z_2 * v_2 \\
 \vdots & \vdots & \vdots & \vdots & \vdots & \vdots & \vdots & \vdots & \vdots & \vdots & \vdots \\
 0 & 0 & 0 & 0 & x_n & y_n & z_n & 1 & -x_n * v_n & -y_n * v_n & -z_n * v_n
 \end{bmatrix}
 \begin{bmatrix}
 L_1 \\
 \vdots \\
 L_{11}
 \end{bmatrix}
 =
 \begin{bmatrix}
 u_1 \\
 u_2 \\
 \vdots \\
 u_n \\
 v_1 \\
 v_2 \\
 \vdots \\
 v_n
 \end{bmatrix}$$

Where  $x$ ,  $y$ , and  $z$  are the known three-dimensional coordinates of  $n$  markers in space and  $u$  and  $v$  are the two-dimensional camera based coordinates for the same markers. One  $L$  vector is calculated for each camera. To solve for  $L$  in the above equation a minimum of 11 coordinates (6 markers) is needed. To improve the congruity, more markers can be included and a least squares method can be used to solve for the 11  $L$  vector elements. These  $L$  vectors are then used to transform two sets of two-dimensional marker data from the two cameras into the three-dimensional marker positions using the following:

$$\begin{bmatrix}
 L_9^1 * u_n^1 - L_1^1 & L_{10}^1 * u_n^1 - L_2^1 & L_{11}^1 * u_n^1 - L_3^1 \\
 L_9^1 * v_n^1 - L_5^1 & L_{10}^1 * v_n^1 - L_6^1 & L_{11}^1 * v_n^1 - L_7^1 \\
 L_9^2 * u_n^2 - L_1^2 & L_{10}^2 * u_n^2 - L_2^2 & L_{11}^2 * u_n^2 - L_3^2 \\
 L_9^2 * v_n^2 - L_5^2 & L_{10}^2 * v_n^2 - L_6^2 & L_{11}^2 * v_n^2 - L_7^2
 \end{bmatrix}
 \begin{bmatrix}
 x_n \\
 y_n \\
 z_n
 \end{bmatrix}
 =
 \begin{bmatrix}
 L_4^1 \\
 L_8^1 \\
 L_4^2 \\
 L_8^2
 \end{bmatrix}$$

Where  $L_n^m$  is the  $n^{\text{th}}$  element in the  $L$  vector of the  $m^{\text{th}}$  camera,  $u_n^m$  and  $v_n^m$  are the two-dimensional coordinates of the  $n^{\text{th}}$  marker in the  $m^{\text{th}}$  camera, and  $x_n$ ,  $y_n$ , and  $z_n$  are the three-dimensional coordinates of the  $n^{\text{th}}$  marker in space.

The accuracy of the DLT algorithm and marker tracking program developed for this project was assessed statically using the calibration cage. A minimum of six markers is needed to calibrate the system. To improve the accuracy of the DLT algorithm a least squares method was employed to solve for the calibration constants as the accuracy of the method has been shown to increase with an increasing number of calibration points. The accuracy of the DLT algorithm was assessed for six, eight, and ten calibration points. The three dimensional coordinates of five other markers were calculated using the algorithm and compared to their measure coordinate using the root mean squared (RMS) of the differences.



#### 3.4.4 Repeatability Assessment

The repeatability of the system was assessed using high speed footage of one of the cervical impact events. The video footage was processed 3 times and the difference between the sets of results was calculated to assess repeatability.

### 3.5 Results

#### 3.5.1 Spatial Resolution

The spatial resolution of the cameras dictated the accuracy of that component on the system. The Phantom V9.0 cameras have a resolution of 1632X1200 pixels at the desired frame rate. Due to the three dimensional nature, the spatial resolution was determined by averaging the resolution based on the nearest and furthest marker relative to the camera. As each camera was placed slightly differently for each specimen an average spatial resolution was calculated. The two dimensional spatial resolution was approximately 0.182 mm/pixel.

#### 3.5.2 Accuracy

Accuracy of the tracking software appeared to be influenced by several factors: disruptions in the line of sight to the target; chaotic movement of the target; and changing light/shadows in the region surrounding the target. The isolated accuracy of this step of the procedure was not quantified. However several observations were made regarding the software's performance. Adjusting the settings of the program's algorithms was found to improve its performance. The most influential was the tracker tolerance control. Reducing this control was found to increase the chance that the program would not report the marker as lost when it was. Increasing this value caused the program to halt at an increased frequency to ask for user feedback on the marker location. Setting this value to 50% provided the best performance.

The precision with which one could target the centre of the marker influenced the accuracy of the marker tracking. This value was based on spatial resolution and the diameter of the marker. The markers used during tracking were 5 mm at 0.182mm/pixel. Thus, the precision with which one could select the centre of the marker was determined to be 3.6% of the marker's diameter. However, since the marker tracking program was capable of sub-pixel accuracy, this value was, in reality, smaller. The documentation did

not provide a quantitative value for the sub-pixel quantity and therefore a finer measure of this precision was not calculable.

The calibration of the three dimensional space was influenced by the number of markers used. The effect of the number of calibration points on the accuracy of the reconstruction is summarized in Table 3-1. The influence of the least squares approach was assessed. It was found that employing the least squares approach increased the accuracy of the reconstruction.

Table 3-1: Assessment of accuracy of the DLT algorithm

Number of Markers	Used Least Squares?	Accuracy (mm)
6	No	0.4247
8	Yes	0.3302
10	Yes	0.3164

### 3.5.3 Repeatability of Marker Tracking

The 3 paths from the repeatability trials are plotted in Figure 3-2. Trials 1 and 3 follow each other very well. However trial 2 is offset from these values by 1.5 pixels (0.273 mm) in the x-direction and 0.5 pixels (0.091 mm) in the y-direction. This could be due to misplacement of the initial tracking location (i.e. not on the centre of the marker) since this is manually set. In all cases the marker was lost at 4ms and had to be manually replaced within the image.

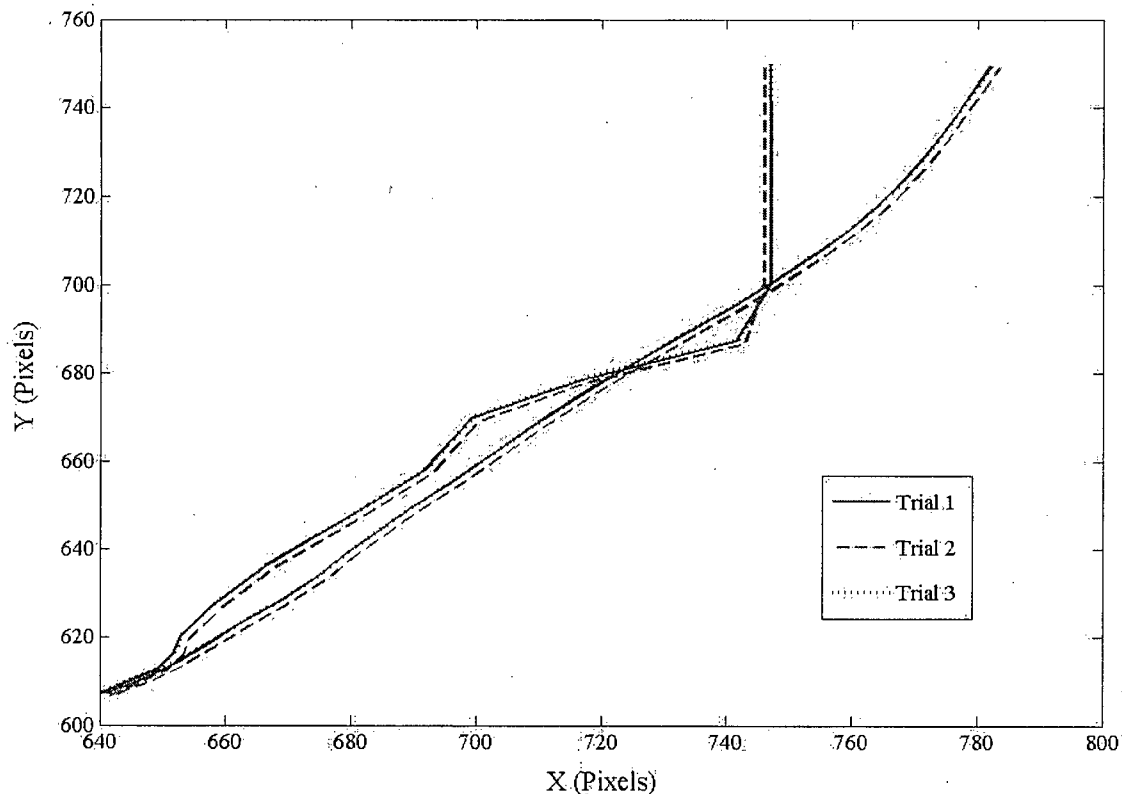


Figure 3-2: Repeatability assessment of marker tracking software: three repetitions of tracking one marker.

### 3.6 Discussion

The overall goal of the kinematic capture system was to return quantitative measures of the motion of the spine during impact. Though several systems are available, a camera and marker based system was selected as it would also return qualitative results. The accompanying digitization methods allowed the system to be relatively automatic. However, due to the multi-step approach for the video analysis, error was a concern but the system was ultimately found to have an acceptable overall accuracy of less than 0.4247 which is the error associated with using 6 markers to calibrate the DLT algorithm.

The cameras selected were the best available at the time of this work. Due to their high resolution the error associated with pixelization of the event was minimal. The placement of the cameras during testing may not have been optimal. As was stated, no literature was found that addressed non-metric camera placement in stereo-photogrammetry. The majority of the literature in this field addresses photogrammetry using parallel metric cameras and therefore was not relevant to our use. Placement of the

cameras relative to each other and to the specimen was based on line of sight. It was felt that the most important issue was being able to see every marker in both cameras while keeping one camera plane as close to lateral as possible.

The automated marker tracking program used in this procedure was commercially available software designed for use in a range of industries. This is in contrast to the majority of software, which is designed for use in biomechanical studies of human motion. It was found that these traditionally utilized programs did not have the high level of user interaction that was necessary. That is, the user was able to adjust the selected software settings to enhance tracking while in the other packages these controls were not available. However, although the software was very good it required supervision with the occasional correction. Assessment of the repeatability of this software revealed the sensitivity to initial marker identification. However the paths followed are parallel for multiple runs of the same marker regardless of initial identification.

The use of direct linear transformation in this system allows for relatively easy three-dimensional reconstruction of motion. Based on the accuracy of the algorithm as assessed using the calibration cage, the optimal calibration procedure would be to use the maximum number of calibration points available and employ a least squares algorithm in the solution.

### **3.7 Conclusions**

The use of two high speed digital cameras in conjunction with marker tracking and DLT software satisfied the needs of the motion capture system. Based on the results of the assessment of the system, the following recommendations were made for use in three-dimensional motion capture:

- Ensure accurate placement of marker tracker in the initial frame during marker tracking in TEMA
- Use 50% tracker tolerance in the tracking software
- To use the maximum number of calibration points on the calibration cage that can be seen in both cameras in the DLT algorithm
- Limit the camera field of view to the specimen to reduce the “dead” space in the field of view thereby maximizing the spatial resolution of the camera.

### 3.8 References

1. Society of Automotive Engineers, Instrumentation for Impact Test—Part 2: Photographic Instrumentation, SAE. 2003.
2. Miller, N.R., R. Shapiro, and T.M. McLaughlin. A technique for obtaining spatial kinematic parameters of segments of biomechanical systems from cinematographic data. *J Biomech*, 1980: 13(7): p. 535-47.
3. Challis, J.H. and D.G. Kerwin. Accuracy assessment and control point configuration when using the DLT for photogrammetry. *J Biomech*, 1992: 25(9): p. 1053-8.
4. Chen, L., C.W. Armstrong, and D.D. Raftopoulos. An investigation on the accuracy of three-dimensional space reconstruction using the direct linear transformation technique. *J Biomech*, 1994: 27(4): p. 493-500.
5. Hinrichs, R.N. and S.P. McLean. NLT and extrapolated DLT: 3-D cinematography alternatives for enlarging the volume of calibration. *J Biomech*, 1995: 28(10): p. 1219-23.
6. Wood, G.A. and R.N. Marshall. The accuracy of DLT extrapolation in three-dimensional film analysis. *J Biomech*, 1986: 19(9): p. 781-5.

## Chapter 4: Kinetic Data Acquisition

### 4.1 Introduction

During axial head to ground impact, the reaction forces and moments at the base of the neck are needed to determine the kinetics throughout the spine. The axial reaction at the head during impact provides information on the characteristics of the impact. This chapter describes the instrumentation used to quantify the forces and moments experienced by the specimen during axial head to ground impact. Two load cells were used: a multi-axis load cell at the base of the spine and a uni-axial load cell at the impact platform. The manufacturer supplied calibration constants were validated prior to use to check performance.

### 4.2 Background

The tolerance of the full cervical spine is highly dependent on the loading conditions. As the ligamentous cervical spine is unstable in quasistatic and low speed axial loading,<sup>1</sup> high speed cervical spine loading conditions provide the most relevant information for our purposes. In high speed loading, the tolerance of the osteo-ligamentous cervical spine ranges from 1289 N to 6840 N.<sup>2-6</sup> This wide range of values reflects differences in loading conditions such as speed, orientation, impact surface, or age of the specimen. Nightingale and colleagues<sup>7</sup> report forces and moments at the base of the neck (T1) during head-first drop tests with conditions similar to those of this study (level, unpadded impact surface). They also reflect tilted and/or padded impact surfaces. The average peak values of axial ( $F_z$ ) and anterior/posterior shear ( $F_x$ ) loads and the moment in the sagittal plane ( $M_y$ ) for the three flat, rigid impacts are summarized in Table 4-1.

Table 4-1: Average peak forces and moments from Nightingale and colleagues (given in our coordinate system as seen in Figure 4-1)<sup>7</sup>

<b>Force or moment</b>	<b>Average (Std Dev)</b>
$F_z$	1574 N (256 N)
$F_y$	2999 N (654 N)
$M_x$	102.3 Nm (38.7 Nm)

In high speed axial impact tests, the axial force measured at the platen in response to the impact is related to the speed, mass of the impactor/specimen, and surface conditions. Although not an indicator of injury, the axial force at the impact platen is important to understand the dependant behaviour between the head and neck at impact. This dependency is a measure of the connection between two ends of a column, especially an articulated one such as the spine: the more coupled the column the more influence a disturbance at one end will have on the other. Nightingale and colleagues reported an average axial impact force at the impact surface of  $8306\text{N} \pm 1796\text{N}$  for hard surface conditions.<sup>7</sup>

Two load cells were needed to quantify the kinetics during our tests. To quantify the forces and moment seen in the neck during impact a multi-axial load cell was needed at the caudal end of the cervical spine specimen at the carriage. Head impact would be quantified at the impact platen, Figure 4-1. As the head-platen interface was not constrained, a single axis load cell to measure the impact force at this location was thought to be sufficient. The tolerance of the cervical spine to impact and reported impact loads were used to determine the load range requirements of these load cells.

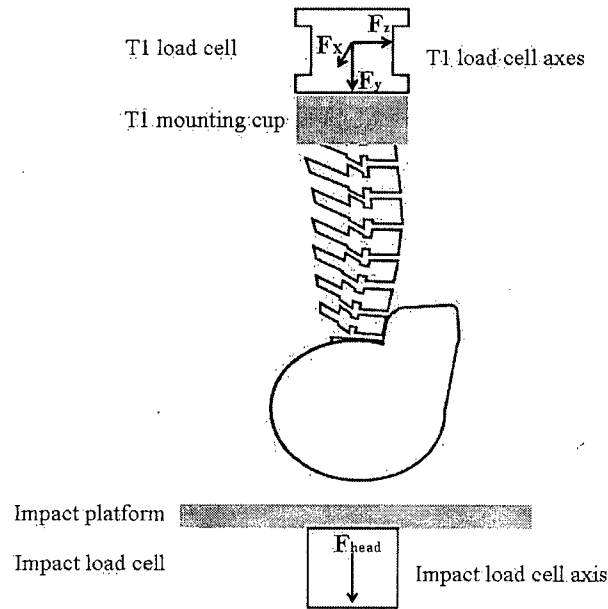


Figure 4-1: Location and orientation of the load cells and their axes in the set up

### 4.3 Methods and Materials

#### 4.3.1 Transducers

Based on results of a similar study<sup>7</sup> two transducers were selected. For the multi-axial transducer to be placed at the caudal end of the specimen, a 6-axis load cell with a 4450N axial force range was chosen (MC3A, AMTI, Watertown, MA). The ranges of the 6 channels are listed in Table 4-2. This is a strain gauge bridge based transducer. A low profile 20kN uni-axial load cell (Omega Engineering, Inc., Laval, QC, Canada) was selected to measure the head impact forces at the platen.

Table 4-2: Load specifications for the multi-axis load cell

Force or moment	Range
$F_x, F_z$	2224.1 N
$F_y$	4448.2 N
$M_x$	113 Nm
$M_y, M_z$	56.5 Nm



#### 4.3.2 Data Collection

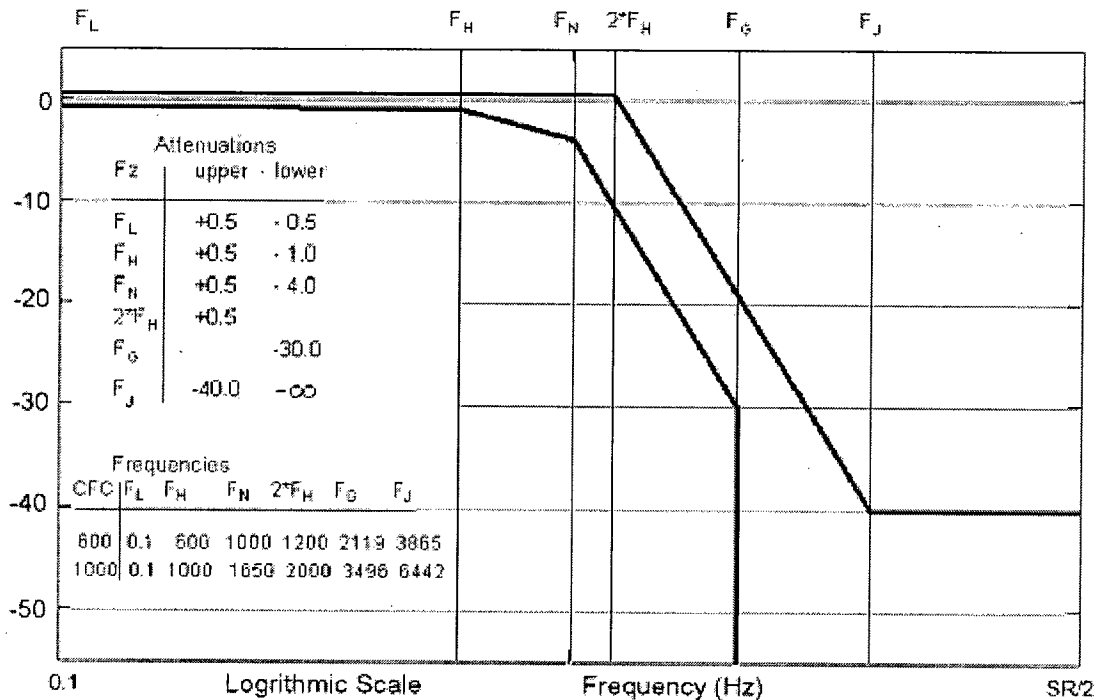
The analogue signals were amplified such that the full range of the transducers was available before being collected by the data acquisition (DAQ) system. The DAQ system used was personal computer based. The PCI board (DT-3010, Data Translation, Marlboro, MA) has a 12 bit resolution and can sample at 1.25MHz which is sufficient for impact data collection as dictated by the Society of Automotive Engineers standard for data collection during impact testing.<sup>8</sup> The software for data acquisition was embedded in the high speed digital camera control software so as to synchronize the two data streams (video and load cells). Due to the nature of the program there was only one collection rate available, which was dependent on the number of data channels of interest and the camera frame rate. As our settings were 1000fps for the camera and 7 channels of data, this acquisition rate was 146 kHz. Data processing was done in Matlab.

#### 4.3.3 Data Synchronization

Due to the complex nature of this set up and the multiple data collection systems in place, a method of synchronizing the data acquisition was needed. The high speed digital camera control software was designed to incorporate analogue data collection. The software time stamps the data based on the master camera's clock and also writes the associated frame into the data file.

#### 4.3.4 Filtering

The Society of Automotive Engineers' standard for data collection of head and neck impacts<sup>8</sup> provided the requirements for the data filter, Figure 4-2. The cutoff frequencies dictated by the standard are dependant of the data type. For neck forces the "channel frequency class" (CFC) 1000 is required while CFC 600 is used for neck moments. The cutoff frequencies are 1650Hz and 1000Hz respectively. A 4<sup>th</sup> order Butterworth filter was deemed sufficient as it provided the required decay of approximately -80dB/decade after the cut off. It was applied digitally during data processing.

Figure 4-2: SAE data filter requirements for neck impacts<sup>8</sup>

#### 4.3.5 Calibration

Both load cells were factory calibrated. The manufacturer supplied calibration values were validated for both load cells in the primary loading directions: axial in the y direction for both load cells and the moments in the sagittal and lateral plane (about the x-axis and z-axis respectively) for the multi-axial. The multi-axial load cell calibration values are given in matrix form to account for crosstalk. For the single axis load cell at the impact platform, a series of weights were used to verify the manufacturers' values. The multi-axial load cell was validated in the axial direction (y) using weights and for the x and z moments using weights hung from lever arms. In the latter cases, validating the moments required combined loading of both the moment and the y-axis.

### 4.4 Results

#### 4.4.1 Calibration/Validation

Validation of the load cells was done using assorted masses and comparing the actual mass to the mass measured by the load cells according to the manufactures' calibration constants. For the six axis load cell the supplied calibration values were in matrix form. Three masses were used to confirm the calibration of the y direction component of force

(including the two from the validation of the angular components) and two masses on a lever arm were used to confirm the y and z rotational components of the calibration matrix, Figure 4-3. For the uni-axial, load cell two masses were used to validate the calibration constant, Figure 4-4. In both figures the straight line represents the ideal validation line (where actual and measured mass are equal).

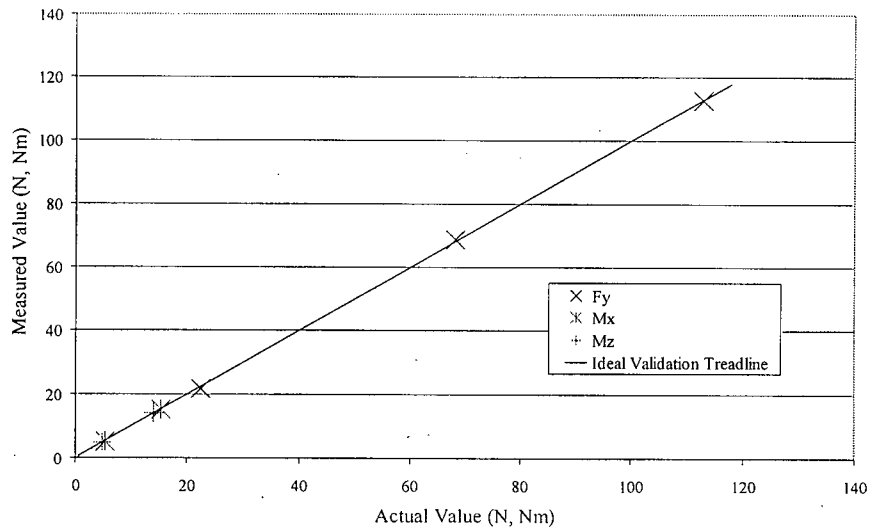


Figure 4-3: Validation of the y direction and x and z rotational components of the calibration matrix of the 6 axis load cell.

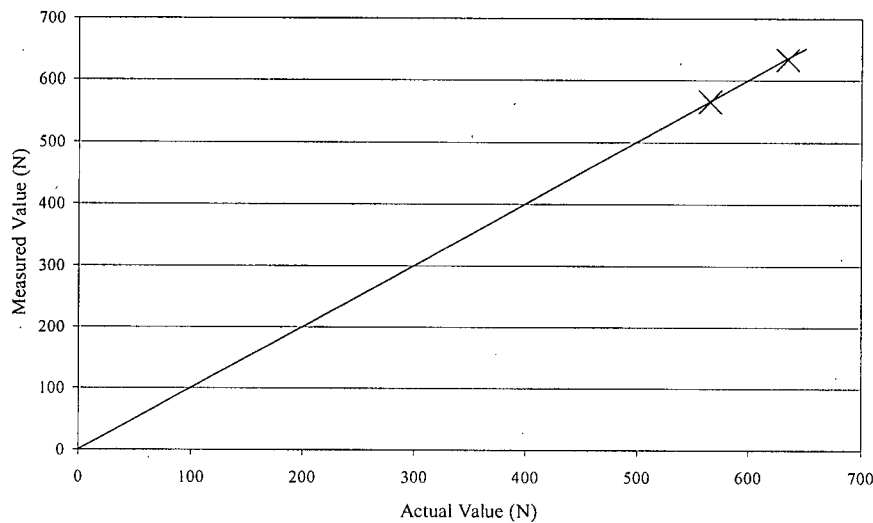


Figure 4-4: Validation of the calibration value of the uni-axial load cell

#### **4.5 Discussion**

A validation of the load cells was opted for as the load cells had been calibrated by the manufacturer. The validation procedure was only done for the principal loading axes on the six axis load cell and for the lower end of the uni-axial load cell. The results of these validations indicate that there is little or no deviation of the sensors from the manufacturer supplied calibration constants.

#### **4.6 Conclusion**

Two load cells were selected to measure the forces and moments and the head and neck during our axial head to ground impact tests. The data acquisition system employed to collect the analogue data synchronized the collection to the high speed digital camera footage. Filtering was preformed after collection using a finite impulse response filter as per the SAE standards for impact testing.

#### 4.7 References

1. Panjabi, M.M., et al. Critical load of the human cervical spine: an *in vitro* experimental study. *Clinical Biomechanics*, 1998: 13(1): p. 11-17.
2. Maiman, D.J., et al. Compression injuries of the cervical spine: a biomechanical analysis. *Neurosurgery*, 1983: 13(3): p. 254-260.
3. McElhaney, J.H., et al. Cervical spine compression responses, Warrendale,PA, 27th Stapp car crash conference. 1983
4. Nightingale, R.W., The Dynamics of Head and Cervical Spine Impact, in Department of Biomedical Engineering, Duke University. 1993.
5. Pintar, F.A., et al. Dynamic characteristics of the human cervical spine, Warrendale,PA, 39th STAPP car crash conference. 1995
6. Yoganandan, N., et al. Strength and kinematic response of dynamic cervical spine injuries. *Spine*, 1991: 16(10 Suppl): p. S511-7.
7. Nightingale, R.W., et al. Dynamic response of the head and cervical spine to axial impact loading. *Journal of Biomechanics*, 1996: 29(3): p. 307-318.
8. Society of Automotive Engineers, Instrumentation for Impact Test—Part 1—Electronic Instrumentation - J211b, SAE. 2003.

## Chapter 5: Follower Preload

### 5.1 Introduction

The unstable nature of an *ex vivo* spine specimen provides many challenges for biomechanical testing. Although functional spinal units are stable under most loading conditions, longer sections of spine have been shown to be unable to bear significant vertical load without buckling and damage to the hard and soft tissues.<sup>1, 2</sup> There is considerable discrepancy between the reported *in vivo* loads seen during normal daily activity and the load carrying capacity of the *ex vivo* spine.<sup>1, 3-5, 2, 6</sup> To improve the biofidelity of biomechanical tests using longer spine specimens, a modified loading method that would allow for physiologic loads was needed.

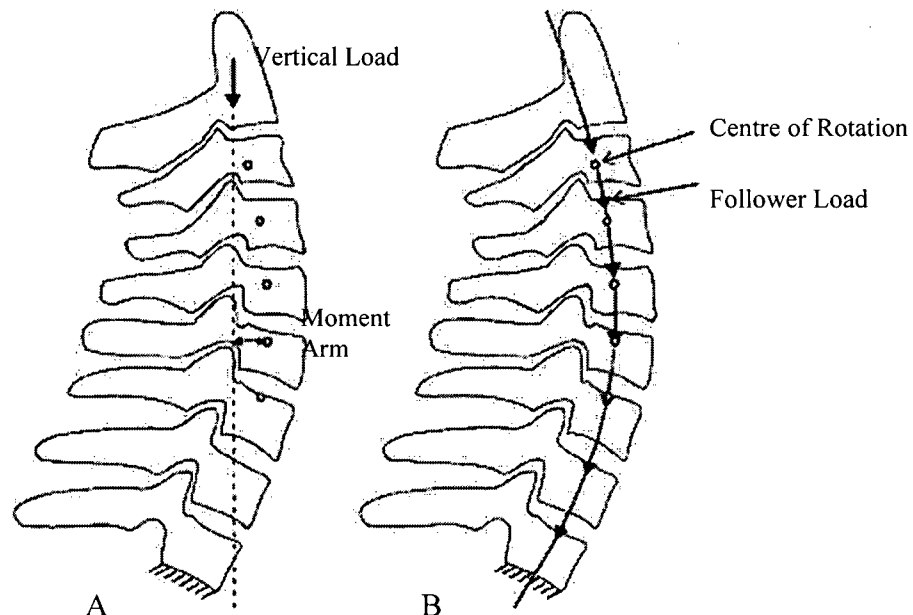
It has been found that by applying a load such that it follows the natural curvature of the spine, physiologic loads can be applied to the spine without compromising the structure. These follower loads have been adapted to preload *in vitro* spines to simulate physiologic compression for use in a variety of biomechanical tests.<sup>7-9</sup> However no systems have been applied to an axial impact model.

The use of a follower preload in our impact study called for an application method that was required to work with unique constraints. The nature of our study required the entire follower load application be mounted and applied to the specimen without adding significant weight to the set up. The set up was constrained to the specimen, surrogate head, and drop tower carriage; the system would have to be independent of apparatus beyond these spatial limits. The specimen integrity in terms of bony and soft tissues had to be maintained during application as did the biomechanical response of the specimen during impact.

### 5.2 Background

Cervical spine instability in the sagittal plane and the resulting damage to the tissues is a result of large bending moments and shear forces that occur simultaneously with pure vertical compression, Figure 5-1A.<sup>1</sup> These moments and forces result in the hyperflexion/extension or buckling of the spine. To reduce these moments and forces the path of the compressive force must be tangent to the natural curvature of the spine

passing through the centres of rotation of each vertebral body, Figure 5-1B. Patwardhan and colleagues.<sup>10, 11</sup> dubbed this loading pattern a “follower load” and hypothesized that since each vertebra would be loaded in almost pure compression, a longer spinal segment would be able to bear physiologic loads under these conditions.

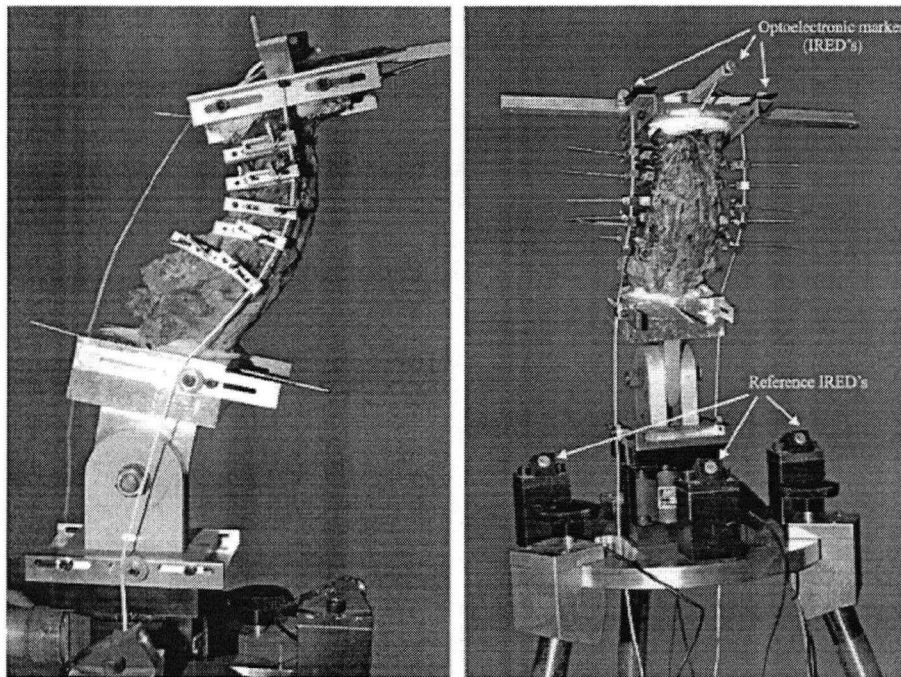


Reprinted with permission © 2000 Lippincott, Williams & Wilkins

Figure 5-1: Illustration of the loading path of a vertical load (A) and a follower load<sup>10</sup>

This approach was first developed for the lumbar spine (L1-S1). Patwardhan *et al* used bilateral cables which passed through guides mounted on each vertebra.<sup>11</sup> These guides consisted of tubes mounted on swivel rod ends. The rods were mounted on U-shaped braces that were pinned to the vertebral bodies. The rods allowed for 10mm of anterior-posterior placement adjustment to assess the effect of error in the path of the cables. The cable was anchored at the L1 level and loaded by a mechanical lever system below the sacral level. The sagittal tilt at L1 was used to quantify the effect of the loading method. Both vertical and follower compressive loads were applied to the specimen in neutral and flexed positions. It was found that the load carrying capacity of the lumbar spine increased drastically with the use of a follower load in all conditions. It was also noted that as long as the follower load passed through a small region around the centre of rotation, the loading capacity and the tilt of the cranial vertebra (L1) were not greatly affected.

Another commonly used section of spine, which suffers from similar issues, is the cervical spine. The instability of the cervical spine under vertical compressive loading was noted by Panjabi and colleagues<sup>2</sup> who reported buckling at 10N. Patwardhan applied the same follower load concept to the cervical spine (C2-T1) as he did to the lumbar spine.<sup>10</sup> The method of preload application was similar to the method used in the lumbar spine study. The guide design differed slightly. For this method the guide scaffolding was mounted to the sides of the vertebral body and was bolted and wired in place, Figure 5-2. The guides themselves were holes drilled in the end of the arms of the scaffolding. The arms were adjustable to allow for path correction. The sagittal tilt at C2 was used to quantify the effect of the loading method. Both vertical and follower compressive loads were applied to the specimen in neutral and flexed positions. It was found that the load carrying capacity of the cervical spine increased drastically with the use of a follower load in all conditions.



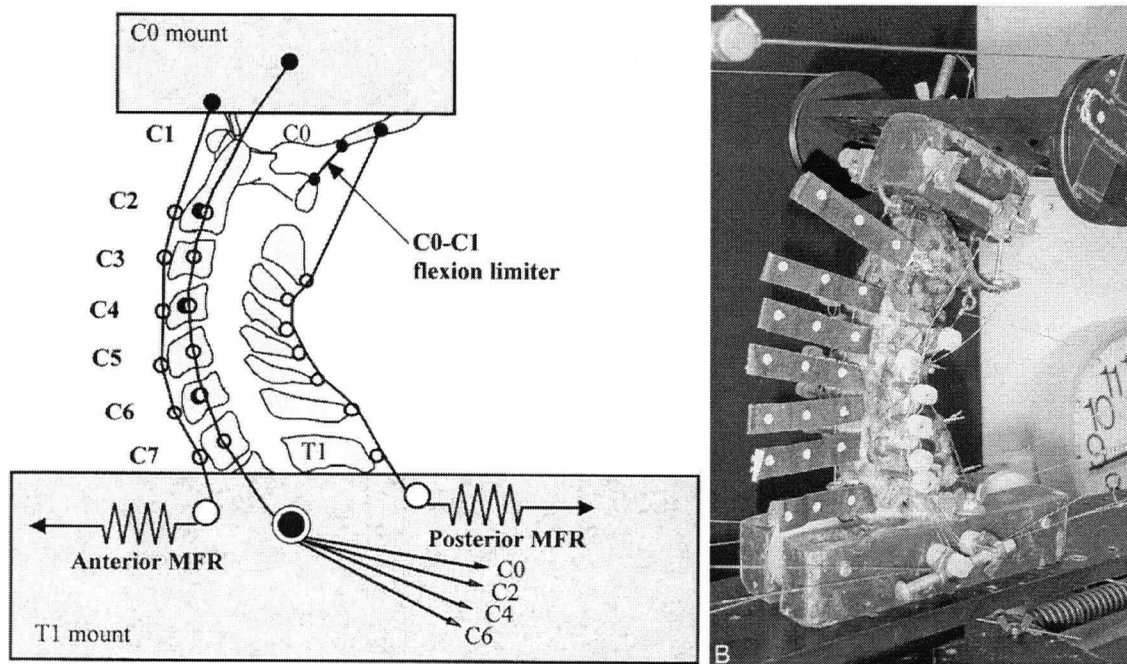
Reprinted with permission © 2000 Lippincott, Williams & Wilkins

Figure 5-2: Patwardhan and colleagues' apparatus for follower load application in the cervical spine<sup>10</sup>.

Several methods of preload application have since been developed for use in the cervical spine. Panjabi and colleagues<sup>9</sup> developed a cervical spine model for



biomechanical testing that included muscle force replication. The goal of this model was to improve the biofidelity of *in vitro* cervical spine biomechanical behaviour in terms of the load-displacement curve. The resulting model was more complex than the basic bilateral cables approach taken by Patwardhan. Panjabi's model used multiple lateral cables to simulate the segmental nature of cervical musculature Figure 5-3. The lateral cable guides were rods inserted into the vertebral body. The nylon cable was then woven around the posts and loaded caudally. Four cables were used on each side and were anchored at C0, C2, C4, and C6. They were each loaded to 30N. Anterior and posterior cables were also installed. These guides were screw eyes for the anterior and wire loops for the posterior. These cables were attached to tension springs (1N/mm) such that the cables were not loaded while in a neutral position and there was no lag between motion and loading. A slight variation of this method was used to create a novel cervical spine model to study whiplash.<sup>7</sup> For the purposes of axial impact, this model is inappropriate as the lateral guides compromise the vertebral bodies' integrity by creating stress concentrations.



Reprinted with permission © 2001 Lippincott, Williams & Wilkins

Figure 5-3: The complex follower load application developed by Panjabi and colleagues to simulate cervical musculature<sup>9</sup>

In developing a new protocol for biomechanical tests of whole cervical spines, Miura and colleagues<sup>8</sup> developed a much simpler method of preload application. They

used two bilateral cables that passed through simple guides mounted on the lateral masses. To achieve the correct placement of the guides the anterior arch of the transverse process was removed. This allowed a more posterior placement of the guides, which better aligned the load path with the centres of rotation. For the purposes of their work the cable was anchored at C2 and was loaded to 100N.

### **5.3 Materials and Methods**

#### **5.3.1 Guides**

The follower load system used in this experiment was a modified version of that developed by Miura.<sup>8</sup> Like Miura's method the follower load was applied using bilateral cables. The cable material was 50 lbs test braided fishing line (Berkley Gorilla Tough, Spirit Lake, Iowa). This material was chosen because it is flexible, has low friction, and has a relatively high modulus of elasticity.

The cable passed through guides mounted on the lateral masses of each vertebra between C3 and C7 (five in all). The guides were 1 mm screw eyes. To mount the guides the arch of the transverse process was removed from the vertebra. The guide was then screwed into the lateral mass from the anterior, Figure 5-4. This placed the eye of the guide in the approximate location of the transverse axis of the centre of rotation of each vertebral pair, Figure 5-5.<sup>12</sup> No guides were mounted to C1 and C2 due to the lack of appropriate mounting locations.

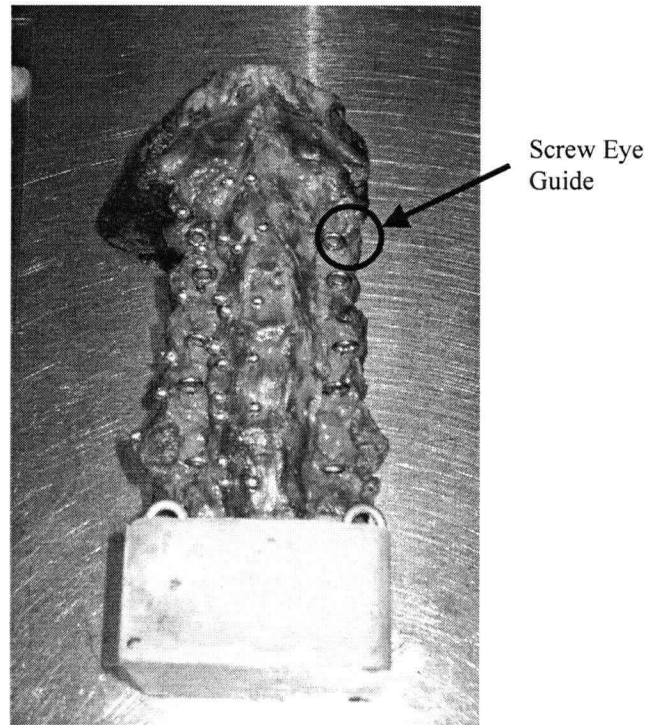
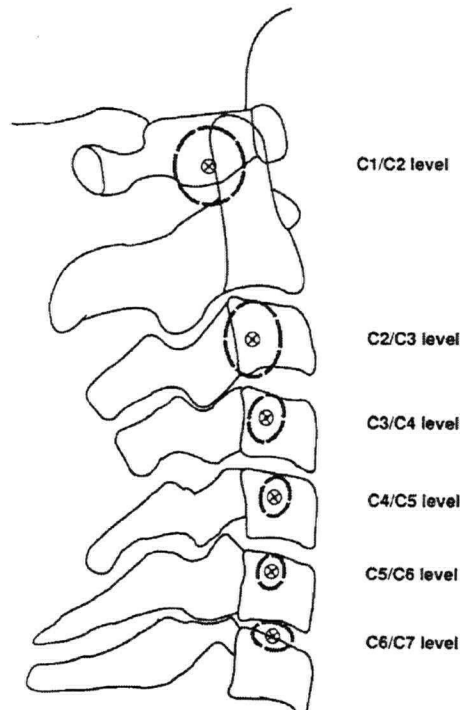


Figure 5-4: Placement of screw eyes in lateral masses of the C3 through C7 vertebrae



Reprinted with permission from Elsevier © 1991

Figure 5-5: Positions of the centres of rotations for each cervical vertebral pair from in vivo flexion/extension measurements<sup>12</sup>

### 5.3.2 Load Application

Springs provided the required load to the cables. Initially the cable was anchored to the occiput. Tension springs were attached between the cable and the carriage to provide the load. However this required the cables to change direction. A system of pulleys was considered to solve this issue. However this was abandoned for a simpler solution. The final design required the cable to be anchored inferiorly to an eye bolt embedded in the dental stone with the T1 and T2 vertebra of the specimen. This fixture was further stabilized with a washer and nut on the bolt before being embedded. Load was applied to the cable using compression springs mounted in the surrogate head mounted to the occiput (see Chapter 7). The springs used were steel and rated 10.7lbs/in (1.874N/mm). These springs were compressed in line with the cable as it passed anteriorly to the occiput and C1 Figure 5-6.

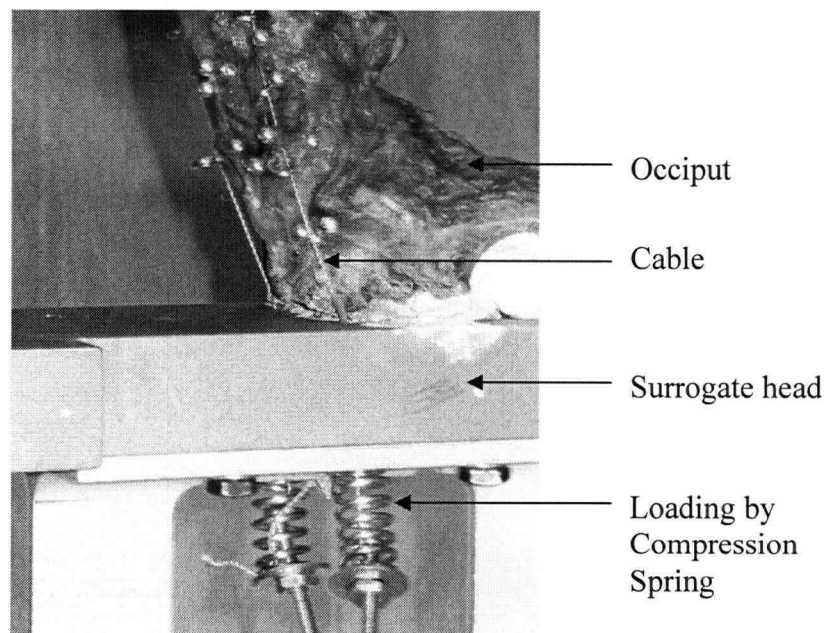


Figure 5-6: Load application by compression spring at the surrogate head in the developed follower preload system (specimen is inverted)

A simple tension adjusting device was used to compress the springs to provide the load in the cable. The cable was secured to the head of a small bolt and clamped by a nut. The bolt was then passed through the centre of the spring such that the threaded portion of the bolt could be accessed from the free end of the spring. A washer and nut were threaded to the bolt to provide a loading surface between the bolt and the spring. As the

nut was tightened the spring would compress and the tension in the cable would increase. The load applied was 125N, which accounted for the counter balancing of the weight of the surrogate head (4.36 kg) and the reported *in vivo* load of the cervical spine. *In vivo* measurement of intervertebral disc pressures have been used to determine the force acting on the spine. This value ranges between 75 N and 155 N in upright postures.<sup>3, 13, 14</sup> In this model, the compression of the neck is approximately 80 N when the specimen is not in free fall. During the drop, this compression increases to 125 N.

## 5.4 Results

There was no quantitative validation done for the follower preload application method. The following qualitative observations were made during testing.

### 5.4.1 Lower Cervical Spine

The response of lower cervical spine (C2-C7) to the application of the follower preload was as expected in all cases. By removing the transverse processes and mounting the guides to the anterior face of the lateral masses, the load path was able to pass approximately through the published locations of the centres of rotation for flexion/extension. When the preload was applied the lower cervical spine assumed a lordotic curvature. A decrease in the laxity of the spine was noted. Also, the specimen was able to support the mass of the head without buckling while upright. When the specimen was inverted the natural lordotic curve was not lost and the spine did not straighten as it has in similar studies.<sup>15, 16</sup>

### 5.4.2 Upper Cervical Spine

There were many difficulties with applying the preload to the occipital/atlas/axial complex. Due to limitations of the guide system and anatomy, the cable was unable to precisely follow the inherent internal loading path through C1. The resulting load was slightly anterior to the desired location, Figure 5-6. This resulted in slight flexion of the atlanto-occipital joint.

## 5.5 Discussion

A follower preload has been previously shown to improve the biofidelity of the *in vitro* cervical spine in biomechanical tests. However it has not been used in an axial impact test as was required in our study. Previously developed methods provided a foundation for the

development of a system appropriate for our use. There were several unique conditions that required consideration: the weight of the set up; the spatial limitations; and the specimen integrity in terms of both the tissue quality and the biomechanical response. Our method accounts for these in its design.

Through the lower cervical spine (C2-C7) the response of the specimens to the follower preload was as desired. By removing the transverse processes, the path of the follower preload was able to follow the centres of rotation. Removal of these processes did not compromise the integrity of the specimen nor influence the biomechanics of the response. Since most of the injuries were expected to occur in the vertebral bodies, and spinous processes of these vertebrae, mounting the guides on the lateral masses would not predispose these areas to injury.

At the upper cervical spine (Co-C2 or the occipito-atlanto-axial complex), application of the preload was not so straightforward. The anatomy of the vertebral bodies at these points did not allow for mounting of guides that would force the preload into an appropriate path. Since the atlas (C1) has no vertebral body, the load is transmitted though the lateral masses. Mounting a guide to these would compromise the integrity of the bone. Also the atlas is wider than the lower cervical vertebrae: the cable would have to take several 90° bends to pass around the lateral masses of the atlas. Though pulleys could have allowed this without adding friction to the system there would have been some unusual lateral loads that may have influenced the biomechanical response of the upper cervical spine. As well, the problem of mounting the pulley guides would have still been an issue.

There has been one method developed that accounts for this issue. Panjabi's multiple muscle system is the only other system that has included the upper cervical spine<sup>9</sup>. However since they were not concerned with maintaining the structural integrity of the vertebral body they used rods for guides. This allowed them to place the preload at a distance from the bodies, which caused the loading cable to pass around the axis and atlas as desired. This method was inappropriate for our application, as we needed to maintain the vertebral body's structure to study its injury tolerance.

The anchoring point in the head was selected to be as posterior as possible without compromising the atlanto-occipital joint. Ideally this point would have been more

posterior in every specimen. This resulted in some flexion. This was corrected in the experiments by using thin nylon line to lift the posterior of the surrogate head, putting the joint into a neutral position and correctly positioning the head for impact. This is not an uncommon practice in axial impact. In studies without a follower preload, such as the work by Nightingale and colleagues,<sup>17, 15, 16</sup> the head and cervical spine were pre-positioned to ensure the proper posture, such as a lordotic curve and correct head posture. Nightingale and colleagues used suture material for this purpose in their model.

## **5.6 Conclusion**

Although several methods of preload application have been developed for use in biomechanical studies of the spine, none have been developed for use in an axial impact. A method that would apply a simple follower preload to the entire cervical spine was developed. This method addressed the issue of maintenance of specimen integrity, spatial limitations, and weight restrictions. The overall resultant curvature of the cervical spine specimen in the presence of this follower preload was a neutral lordotic curve with some flexion at the atlanto-occipital joint.

## 5.7 References

1. Crisco, J.J., et al. Euler stability of the human ligamentous lumbar spine. PartII:experiment. *Clinical Biomechanics*, 1992: 7: p. 27-32.
2. Panjabi, M.M., et al. Critical load of the human cervical spine: an *in vitro* experimental study. *Clinical Biomechanics*, 1998: 13(1): p. 11-17.
3. Hattori, S., et al. Cervical intradiscal pressure in movements and traction of the cervical spine. *Zeitschrift fur Orthopadie*, 1981: 119: p. 568-569.
4. Moroney, S.P., A.B. Schultz, and J.A.A. Miller. Analysis and measurement of neck loads. *Journal of Orthopaedic Research*, 1988: 6: p. 713-720.
5. Nachemson, A.L. Disc pressure measurements. *Spine*, 1981: 6(1): p. 93-97.
6. Wilke, H.J., et al. New in vivo measurements of pressures in the intervertebral disc in daily life. *Spine*, 1999: 24(8): p. 755-762.
7. Ivancic, P., et al. Biofidelic whole cervical spine model with muscle force replication for whiplash simulation. *European Spine Journal*, 2005: 14(4): p. 346-355.
8. Miura, T., M.M. Panjabi, and P.A. Crompton. A method to simulate in vivo cervical spine kinematics using in vitro compressive preload. *Spine*, 2002: 27(1): p. 43-8.
9. Panjabi, M.M., et al. Development of a system for in vitro neck muscle force replication in whole cervical spine experiments. *Spine*, 2001: 26(20): p. 2214-9.
10. Patwardhan, A.G., et al. Load-carrying capacity of the human cervical spine in compression is increased under a follower load. *Spine*, 2000: 25(12): p. 1548-54.
11. Patwardhan, A.G., et al. A follower load increases the load-carrying capacity of the lumbar spine in compression. *Spine*, 1999: 24(10): p. 1003-1009.
12. Dvorak, J., et al. In vivo flexion/extension of the normal cervical spine. *J.Orthop.Res.*, 1991: 9(6): p. 828-834.
13. Pooni, J.S., et al. Comparison of the structure of human intervertebral discs in the cervical, thoracic and lumbar regions of the spine. *Surgical and Radiologic Anatomy*, 1986: 8: p. 175-182.
14. White, A.A. and M.M. Panjabi. *Clinical biomechanics of the spine*. 2nd ed, J.B. Lippincott Company, New York. 1990.
15. Nightingale, R.W., et al. Experimental impact injury to the cervical spine: relating motion of the head and the mechanism of injury. *Journal of Bone and Joint Surgery.American Volume*, 1996: 78-A(3): p. 412-421.
16. Nightingale, R.W., et al. Dynamic response of the head and cervical spine to axial impact loading. *Journal of Biomechanics*, 1996: 29(3): p. 307-318.
17. Nightingale, R.W., *The Dynamics of Head and Cervical Spine Impact*, in Department of Biomedical Engineering, Duke University. 1993.



## **Chapter 6: High Speed Cineradiography**

### **6.1 Introduction**

One of the goals of this study was to quantify the deformation of the spinal cord in the spinal canal during axial head to ground impact due to bony trauma encroaching on the canal space. To reduce the influence of the setup on the cord response a non-invasive, remote method of observing the spinal cord was desired. Since the cord is situated in the bony spinal canal, a radiographic-based approach was proposed. An industrial generator and x-ray tube were selected to generate the x-rays while an image intensifier with an internally mounted high speed digital camera recorded the resulting radiographic images.

### **6.2 Background**

#### **6.2.1 X-ray Generation**

X-ray generation is a two step process. X-ray or Roentgen radiation is emitted as high speed electrons interact with a target atom. High energy electrons are produced by a high power generator. The target is made of a material with a high atomic number such as tungsten. The electrons slow during the interaction and release energy in the form of x-ray photons. In an x-ray machine, this happens in the x-ray tube.

The energy of the emitted x-ray photons is dependent on the energy of the electrons. The higher the energy, the higher the quality of the x-ray beam. Beam quality is a measure of its penetrating power. Thus an increase in electron energy will allow more x-rays to pass through an object. Too little energy in the beam and the object will be under exposed and be a dark mass in the image, too much energy and the object will be over exposed and not visible. The number of electrons striking the target is a function of the current of the generator output. The rate of electrons striking the target causing the release of x-ray photons dictates the quantity or intensity of the beam. The higher the intensity, the faster the image will develop.

The emergent x-ray beam is conically shaped. The angle of the beam is influenced by the size of the target. This is referred to as the focal spot. A smaller focal spot produces a smaller, more focused x-ray beam. The more focused the beam the less scatter and shadowing on the resulting image.

The generator also influences the x-ray beam. Any variation in the electron stream's power will be seen in the x-ray beam as a change in the exposure. Generators run off of alternating current thus the stream of electrons is sinusoidal. The resulting x-ray beam alternates between high and low quality and the resulting cineradiograph will have a periodic lightening and darkening pattern which causes some frames to be underexposed and unusable. To minimize this phenomenon some generators rectify and smooth the output. This produces a more constant source of electrons and results in less variation in the image.

### 6.2.2 Radiographic image capture

X-ray image intensifiers are commonly used in fluoroscopy as they provide an instantaneous view of the radiograph output. They consist of a phosphor screen, image intensifier unit, and an image capture device, Figure 6-1. The phosphor screen (A) is a thin coating of a phosphorescent compound that is sensitive to radiation. The resulting image is further intensified from a barely visible image to one that can be detected by a camera by the image intensifier components in the following manner: the image on the phosphorescent screen (A) is detected by a photocathode (C) which emits electrons in the presence of light; the electrons are accelerated through a vacuum (C) to the microchannel plate (D) which emits more electrons; these electrons are further accelerated (E) to a phosphor screen (F) which emits photons in response to the bombardment of electrons. Since the number of electrons is increased at the microchannel plate, the final phosphor screen produces more photons than the initial screen did resulting in an intensified image. This image is then captured by a camera which outputs the image to an external monitor for observation.<sup>1</sup>

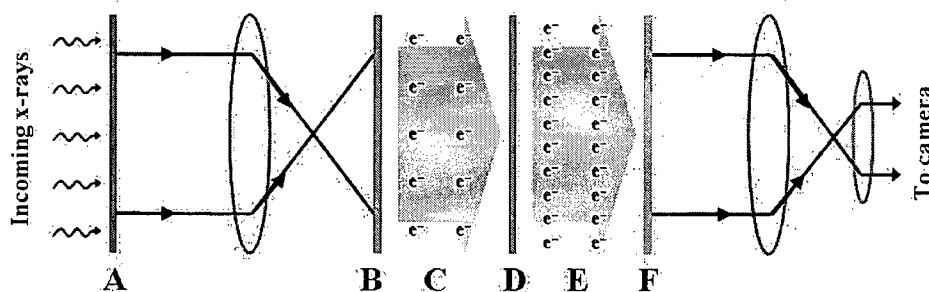


Figure 6-1: Schematic of an x-ray image intensifier showing the major components referred to above. A) phosphorescent screen B) photocathode C) first vacuum D) microchannel plate E) amplified electron stream F) phosphor screen

The maximum speed of the set up was limited by the refresh rate of the screen and the frame rate of the camera. Also the camera sensitivity and shutter speed would further limit the frame rate as the output image may be dim and a slower shutter speed would improve the image intensity. However a fast shutter speed was needed to reduce blur. The camera settings were a matter of trial and error to find a balance between these two components of image quality. Digital cameras have an advantage over analog film cameras in that the sensors used in digital cameras can be more sensitive to light than film.

### 6.2.3 Cineradiography in Biomechanics

Cineradiography is a useful tool in biomechanics. It has been used to study high speed motions in animals, joint motion, and whiplash. High speed cineradiography has been used with frame rates between 90 and 500 fps.<sup>2-7</sup> The lower frame rates have been used to measure vertebral motion in low-speed rear-end impacts in human volunteers using common fluoroscopic equipment enhanced with an improved image capture system to allow for a faster frame rate.<sup>3, 5</sup> *In vivo* studies in animals have used the higher frame rates to study movements such as Snelderwaard and colleagues investigation in tongue motion in lizards.<sup>6</sup> This particular study used a Philips Optimus M 200 medical fluoroscope modified with a high speed digital camera to obtain a frame rate of 500 fps. Bi-planar x-rays systems have been used to determine knee kinematics in dogs at 250 fps.<sup>7</sup> This study employed to high power x-ray generators and sources (150kV, no model given) and an image intensifier and high speed digital camera. No details regarding the components of this system were given.

The use of high speed x-ray *in vitro* has been used to study low-speed rear-end impacts using whole human cadavers.<sup>4</sup> This study used a bi-planar x-ray set up. This consisted of two x-ray generators and two photo-multiplier tubes. In each tube there was a high speed video camera which ran at 250 fps. The details of the components were not given.

## 6.3 Requirements

The aim of the high speed cineradiography system in our application was to provide visualization of the cervical spine at 1000fps. Previous work has been conducted to

identify the required exposure rate to obtain adequate images for analysis. It was found that an exposure of 0.06mR was needed at the image intensifier screen for each exposure.<sup>8</sup>

The high speed x-ray system for this study had to meet the following requirements:

- The generator had to rectify and smooth the incoming AC power to minimize the pulsating image intensity.
- The x-ray machine was required to provide 0.06 mR/ms (or 3.6 R/min) at 1m from the x-ray tube.
- The image intensifier had to have a refresh rate of greater than 1000 Hz. The refresh rate would ideally be faster than the fastest shutter speed on the digital camera
- The internally-mounted camera had to have a frame rate of at least 1000 fps. It also must have been able to fit inside the body of the image intensifier unit.

## **6.4 Methods & Materials**

### **6.4.1 Generator**

To achieve the required voltage output and to avoid the pulsing phenomenon a high power generator was needed. A 160 kV industrial generator (MG160, Phillips, Germany) was selected. This generator output a relatively smooth, non-pulsing voltage of up to 160 kV from a 220 V source. It used full wave rectification and two capacitors for smoothing, producing minimum ripple in the output potential.

### **6.4.2 X-ray Tube**

The x-ray tube selected for this system was a Comet MXR 160 (Comet AG, Switzerland). This tube had the option of either a small (0.4X0.4 mm) or large focal spot (1.5X1.5 mm). The small focal spot was found to output sufficient x-ray radiation and was used as it resulted in a better image, as there were fewer scattered x-rays.

### **6.4.3 Image Intensifier**

The image intensifier had a cesium iodide (CsI) x-ray screen paired with a high definition image intensifier (PT93XP43, Precise Optics, Bay Shore, NY). Mounted within the casing to record the output image was a high speed digital camera (Kodak Motion Corder

Analyzer SR, Redlake). The frame rate used was 1000 fps with the shutter speed set at 1/1000 to maximize the amount exposure. At this frame rate the camera had a resolution of 256X240 pixels and captured an area on the CsI screen of approximately 90X85 mm. Cesium iodide has a decay time of 5  $\mu$ s. This was fast enough for blur to not be an issue in the video images. The digital output was monitored and reviewed through a black and white monitor and the complete cineradiographic video was downloaded to a personal computer for further processing and analysis.

#### 6.4.4 X-ray Machine Settings

Determination of the x-ray machine settings (i.e. voltage and current) for each specimen was done by placing the specimen in the path of the x-rays where it would fall during testing. The output image from the image intensifier was viewed in real time using a black and white television monitor. The settings on the machine were adjusted until a satisfactory image was obtained.

#### 6.4.5 Synchronization

To ease data analysis the cineradiographic video needed to be synchronized with the external high speed digital video and load cells. As the camera used in the x-ray system was an older, different model camera than the external cameras used for kinematic analysis of the spinal column, frame-by-frame synchronization was not possible. Synchronization of the first frame was all that was possible. The accuracy of this approach to synchronization is dependant on the accuracy of the internal clock of the cameras and the frame rate accuracy (i.e. the frame rates of all cameras were equal).

### 6.5 Results

#### 6.5.1 X-ray Machine Settings

The x-ray machine settings used varied with each specimen. The variation can be attributed to the size of the specimen and the distances between the image intensifier, specimen, and x-ray tube. The x-ray tube was placed 0.4 m from the specimen and the image intensifier was placed on the other side of the specimen 0.6 m from the tube, 0.2 m from the specimen, Figure 6-2. Assessment with a Geiger counter of this tube, specimen, and generator set up with these distances indicated that the desired exposure rate of 0.06 mR/ms was obtainable with a tube voltage of 75 kV and 5 mA. During testing the tube

voltage was adjusted between 75-80 kV to obtain the best x-ray image possible. This was due to variation between specimens in terms of size and bone quality.

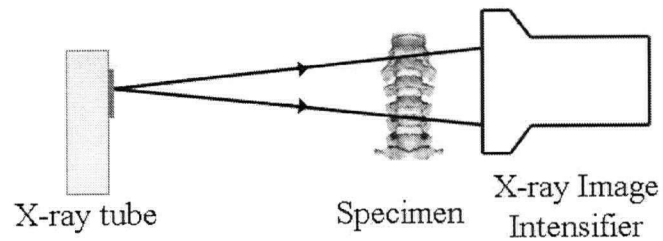


Figure 6-2: Placement of x-ray tube and image intensifier relative to the specimen

### 6.5.2 Resulting Image

A typical output image can be seen in Figure 6-3.

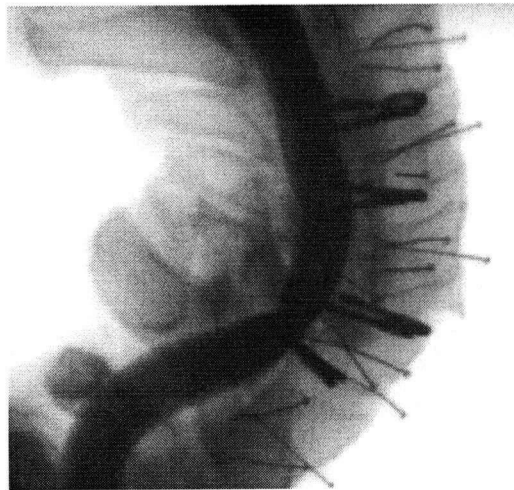


Figure 6-3: Typical x-ray image from the high speed image system. Specimen is an inverted cervical spine that has been prepared for testing

## 6.6 Discussion

This system is novel in that it is the fastest high speed x-ray currently reported in use for biomechanics. It is able to obtain such high speeds as it uses cadaveric specimens and therefore subject exposure to x-rays is not a concern as it is with human or animal subjects. This system provides a method of observing internal structure behaviour without having to remove obstructing structures such as the lamina or spinous process. This is particularly useful in the spine where the removal of structures (i.e. laminectomy) can alter the biomechanical response of the specimen.

The accuracy of the system was not assessed experimentally. The physics of x-rays indicate that there would be no error in the image on the intensifier screen. The x-rays travel in straight lines radiating from a point and project a slightly magnified image on the screen much like a shadow from an object in a beam of light, Figure 6-2. The image intensifier and internally mounted high speed camera would be the source of any distortion to the image. The degree of distortion was not assessed during manufacture and assembly of the image intensifier. The distortion introduced by the camera and lens is minimal as per the cameras used in the kinematics set up. Other studies using similar set ups have not reported measures of distortion of their images due to these two components. Based on the physics of the system we can assume that the accuracy of the system is greater than the resolution which is 0.33 mm/pixel because our analysis is capable of subpixel accuracy.

As the system is not being operated at full power, it may be possible to run the system faster with a few adjustments. A newer, faster digital camera would allow for a faster frame rate. With the advances in high speed digital cameras an upgrade would also provide a larger resolution further improving the system by improving image quality and size. The limiting factors are the sensitivity of the camera to light, the power of the x-ray machine, and the size of the anatomy of interest. Use of a faster camera requires a faster shutter speed. Increasing the camera shutter speed would reduce the amount of light allowed through the aperture. The intensity of the image output by the image intensifier can not be increased and therefore the camera's light sensitivity becomes the limitation. The power of the x-ray machine will dictate the quality and quantity of the produced x-rays. A faster frame rate and shutter speed mean that there is less time for an image to develop and therefore the beam quality would have to be increased which requires more power. Also larger anatomical specimens (i.e. the lumbar spine) would require a higher power beam to produce an image, which would reduce the speed of the system as a slower frame rate would be required.

Another future development option for the high speed x-ray system is the introduction of a second x-ray machine and image intensifier to create a high speed Radio Stereometric Analysis (RSA) set up: This would allow research requiring high speed x-ray to be expanded into three dimensions.

### **6.7 Conclusion**

A non-invasive method of observing the spinal cord during head to ground impact was needed. This high speed x-ray set up can be used to observe the sagittal profile of the cord and bony anatomy during the injury event. This is done by pairing a high power x-ray machine with an image intensifier and high speed digital camera. The system outputs cineradiographic footage of the x-ray images at 1000 fps. There is potential with some modification to the system to operate at a faster speed.



## 6.8 References

1. Graham, D.T. and P.J. Cloke. Principles of radiological physics. 4th ed, Churchill Livingstone, Edinburgh ; New York. 2003: 448 p.
2. Anderst, W.J. and S. Tashman. A method to estimate in vivo dynamic articular surface interaction. J Biomech, 2003: 36(9): p. 1291-9.
3. Kaneoka, K., et al. Motion analysis of cervical vertebrae during whiplash loading. Spine, 1999: 24(8): p. 763-9; discussion 770.
4. Luan, F., et al. Qualitative analysis of neck kinematics during low-speed rear-end impact. Clin Biomech (Bristol, Avon), 2000: 15(9): p. 649-57.
5. Matsushita, T., et al. X-ray study of the human neck motion due to head inertia loading, Warrendale,PA, 38th STAPP car crash conference. 1994
6. Snelderwaard, P., J.H. De Groot, and S.M. Deban. Digital video combined with conventional radiography creates an excellent high-speed X-ray video system. J Biomech, 2002: 35(7): p. 1007-9.
7. You, B.M., et al. In vivo measurement of 3-D skeletal kinematics from sequences of biplane radiographs: application to knee kinematics. IEEE Trans Med Imaging, 2001: 20(6): p. 514-25.
8. Sjøvold, S. and A. Choo, High Speed X-ray Source - Specification Testing, University of British Columbia: Vancouver, Canada. 2003.

## Chapter 7: Response of the Cervical Spine to Head-First High Speed Axial Impact in the Presence of Follower Preload

### 7.1 Introduction

Axial impact injuries to the cervical spine mimicking head first impact such as those that occur when diving into shallow water have been widely studied in terms of the mechanical response of the spinal column to impact. This field of research is primarily limited to *in vitro* and mathematical models with some *in vivo* tests in animals. An *in vitro* model has the greatest potential to be the most biofidelic model available.

Ligamentous spine specimens have the same material properties (bone and soft tissue) and the same range of motion as *in vivo* spines.<sup>1</sup> However, they need to be externally stabilized and pre-positioned as *in vitro* specimens are less stable. This instability could be attributed to the lack of the physiologic muscle forces in *in vitro* models, that are present *in vivo*. It may also contribute to the buckling response of the cervical spine to impact seen during many high speed impact studies using *in vitro* specimens.<sup>2,3</sup>

First order buckling has been seen in quasistatic loading conditions. It has been found that the *in vitro* cervical spine will buckle under 10N of load.<sup>4</sup> However, the cervical spine can support the load of the head (approximately 50N) *in vivo* without buckling. The buckling response of the *in vitro* spine at lower loads is not in line with the stable *in vivo* load-bearing behaviour.

It has been found that the spine can support physiologic loads *in vivo* when the load is applied such that it follows the curvature of the spine.<sup>5</sup> This may explain how the neck is stabilized *in vivo*. Methods of applying compression to simulate muscle force in *in vitro* models have been developed from this finding.<sup>6</sup> This has not been applied to an *in vitro* axial impact model. The inclusion of a follower preload on such a model may eliminate the snap through and complex buckling patterns previously seen and provide a more biofidelic response to axial impact.

## 7.2 Background

### 7.2.1 Buckling

Two modes of buckling have been identified during high speed axial impact. The first is a simple buckling pattern where the cervical spine is hyper-extended/flexed due to loading (referred to as a first order mode), Figure 7-1 A. This mode results in a cluster of injuries typically associated with hyperextension or flexion motion such as spinous process and tear drop fractures in hyperextension and wedge fractures in hyperflexion.<sup>1</sup> A more complicated second order buckling pattern which occurs prior to the first order mode is characterized by flexion in the upper cervical spine paired with extension in the lower spine creating a serpentine shape,<sup>7</sup> Figure 7-1 B. This mode of buckling has been associated with complicated injury pattern involving both hyperflexion and hyperextension injuries in the same specimen in *in vitro* studies.<sup>8, 3, 9-13</sup> This mode of injury was reported by Nightingale and colleagues where it was seen in the high speed digital video footage in some of the rigid impacts during their *in vitro* testing.<sup>3</sup> It was found to be a transient response of the cervical column with the specimen moving into a first-order buckling pattern as the impact progressed.

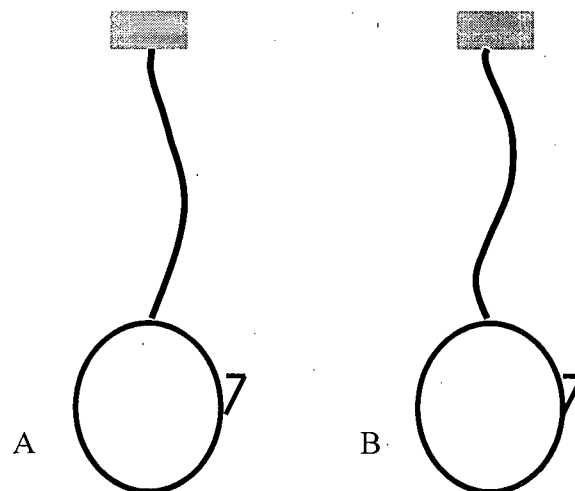


Figure 7-1: Two buckling modes seen during axial impact of the cervical spine. A is the first order mode, B is the second order or serpentine mode

In some of Nightingale and colleagues' impacts a "snap through buckling" response was seen.<sup>3</sup> Snap through buckling is identified as a sudden change in axial

deformation (a bowing of the spinal column) accompanied by a sharp decrease in measured axial load and an increase in the anterior posterior moment. This term is used to identify a local event (1 to 3 vertebrae) and differentiate it from the relatively slower buckling of the entire spine specimen. The snap through buckling typically occurred immediately after impact as the specimen changed posture in less than 1 ms.<sup>3</sup>

Slower first order buckling has been reported in *in vitro* quasistatic loading conditions with loads of 10 N.<sup>4</sup> However, studies have measured the *in vivo* intradiscal pressures and loads in the cervical spine and have found them to be between 310 and 910 kPa depending on activity.<sup>14</sup> Based on a disc area of 255 mm<sup>2</sup> this corresponds to a force of 53 to 155 N.<sup>15, 1</sup> Mathematical modeling based on muscle activity estimates neck loads between 578 and 1175 N.<sup>16</sup> The *in vivo* loads are inconsistent with the *in vitro* buckling. It has been found that the spine can support physiologic loads *in vivo* when the load is applied using mechanical guides such that it follows the curvature of the spine.<sup>5</sup> Patwardan and colleagues were able to apply 250N of load to the *in vitro* cervical spine in this manner without buckling.

### 7.2.2 Influence of preload

Panjabi *et al* adapted the follower load method to the cervical spine to develop a system that simulated physiologic *in vivo* muscle forces for *in vitro* studies.<sup>17</sup> This muscle system has been used in whiplash simulation.<sup>6</sup> The preload used in this experiment ranged from 120 N in the upper cervical spine to 300 N in the lower cervical spine. It was found that with the simulated muscle system acting on the cervical spine, the spine could support the load of the 3.3kg surrogate head in an upright, neutral posture without buckling and without requiring a counterbalance whereas in earlier studies a counter balance had been used.<sup>3, 9</sup> This consistent with the hypothesis that the stabilization of the head neck complex *in vivo* is due to muscle forces acting on the cervical spine.

Cervical spine biomechanics are influenced by the presence of a follower preload.<sup>18</sup> Miura and colleagues found that the spine was stiffer in some directions with an applied follower load. The range of motion of the spine remained similar to the ranges found in non-preloaded specimens, but the forces and moments needed to induce motion in the preloaded specimens increased. These increased forces and moments corresponded better with the forces and moments estimated in *in vivo* motion studies.<sup>16</sup>

In a mathematical model of a segmented column representing the cervical spine, Nightingale and colleagues found that stiffening the segmented structure increased the tolerance of the cervical spine model to loading and eliminated the second order buckling response.<sup>19</sup> By increasing the apparent stiffness of the *in vitro* cervical spine model it is expected that the snap through and complex buckling response of the spine will be eliminated.

### 7.2.3 Goals

In this author's opinion, the snap-through buckling seen in impact tests is related to the instability of the *in vitro* cervical spine, the application of a follower preload to simulate musculature would increase the stiffness of the specimen during the initial impact thereby mitigating the snap through buckling response and eliminating the second order buckling pattern reported in previous studies. A method of simulating dynamic head first axial impact to the cervical spine that allows the incorporation of simulated musculature is needed. The individual methodologies of impact and musculature simulation have been previously described in Chapters 2 and 5 of this manuscript. Both of these were incorporated into the procedure used to fulfill this goal.

This study will assess the influence of simulated musculature, in the form of a follower load, on the biomechanical response of the cervical spine during head first impact. It is hypothesized that the snap through and complex buckling behaviours seen in previous studies<sup>2,3</sup> will be mitigated by the presence of the follower load.

## 7.3 Methods

### 7.3.1 Specimen Preparation

Six human cadaveric cervical spines (occiput to T2) were prepared for impact testing. Each specimen was dissected free of soft tissues while preserving the osteo-ligamentous structures. The spinal cord and dura mater were removed from the canal. A surrogate cord with biofidelic material properties was inserted into the canal for a parallel study (see Chapter 8). The transverse processes of C3-C7 were removed to allow anterior access to the lateral masses, Figure 7-2. This was done in preparation for the application of the follower preload. Four photoreflective marker pins were inserted into the vertebral bodies and lateral masses at each level between C2-C7 for kinematic analysis. The T1

and T2 vertebrae were mounted in dental stone such that the C4-C5 disc was horizontal while the neutral posture lordosis of the spine was maintained.

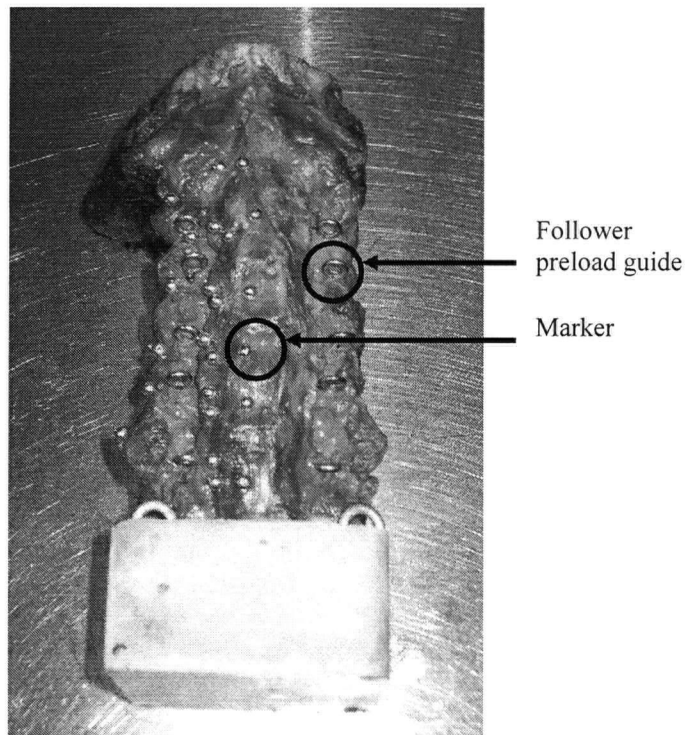


Figure 7-2: Specimen during preparation showing the location of the preload guides, after the removal of the transverse processes, and markers for motion tracking.

A surrogate head with inertia, mass (4.36 kg) and head shape properties that match those of the human head was mounted to the occiput, Figure 7-3. This head was designed as an University of British Columbia Department of Mechanical Engineering undergraduate final design project (Appendix D).<sup>20</sup> A slab of 1 inch stainless steel was used to create the main mass of the head. A triangular three bolt pattern was used to mount this steel mass to the occiput of the specimen. The void left in between the steel and the bone was filled with epoxy putty (Magic Bond Epoxy Putty, ITW Devon, Davners, MA). The impact surface of the surrogate head was aluminium cast in the form of the crown of the human skull. A piece of leather was upholstered to the surface to mimic the scalp. An I-beam acted as a spacer between the impact surface and the main mass of the surrogate head. Alignment of the surrogate head on the specimen was ensured using a through hole in the head that corresponded to the location of the foramen magnum.

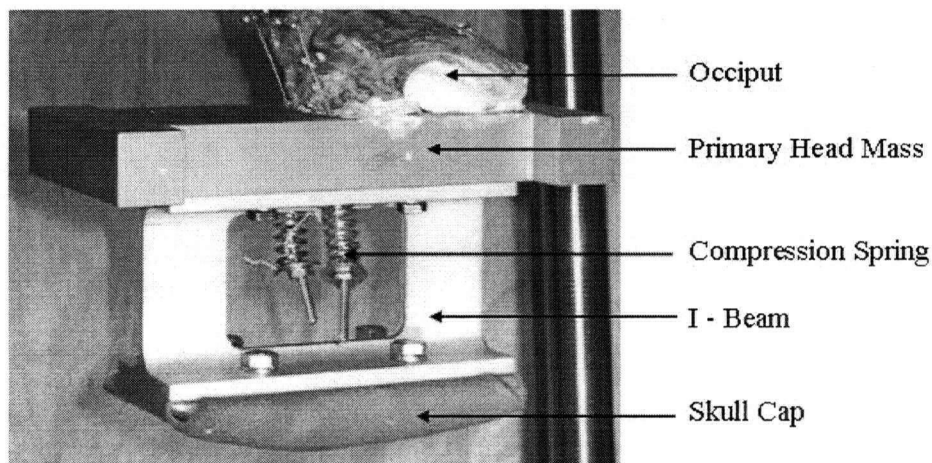


Figure 7-3: Surrogate head (mass = 4.36 kg) showing its components and the compression springs for follower preload application

### 7.3.2 Preload Application

The follower load system used in this experiment was a modified version of that developed by Miura and colleagues.<sup>18</sup> Like Miura's method, the follower load was applied using bilateral cables. The cable passed through guides mounted on the lateral masses of each vertebra between C3 and C7. To mount the guides, the transverse processes were removed from the vertebra. The guide was then screwed into the lateral mass from the anterior, Figure 7-2. This placed the eye of the guide in the approximate location of the transverse axis of the centre of rotation of each vertebral pair.<sup>21</sup> No guides were mounted to C1 and C2 due to the lack of appropriate mounting locations. The cables were anchored caudally to an eye bolt embedded in the dental stone aligned laterally to the T1 and T2 vertebra. A load of 125 N was applied using compressive springs (1.874 N/mm) mounted in the surrogate head. As two springs were used, each was compressed 33 mm. These springs were compressed in line with the cable as it passed anteriorly to the occiput and C1. During the drop the compression in the neck was 125 N and approximately 80N when not in free fall. Further details on this system can be found in Chapter 5. The range of motion and resulting curvature of the specimen were assessed by hand during application. After application, the specimens remained in compression for approximately 15 minutes prior to testing.

### 7.3.3 Impact Simulation

Axial impact was applied using a four shaft, self-supporting drop tower with a lightweight carriage as described in detail in Chapter 2. The carriage weight approximated the upper torso weight of a cadaver specimen (~15 kg). The cervical spine specimens were attached to the carriage in an inverted orientation such that when the carriage was released, head-first impact occurred against the impact platen. A drop height of 0.6 m was used to obtain an impact velocity of 3 m/s. To prevent the specimen from being overdriven, stoppers were used to limit axial compression of the spine to 30mm.

### 7.3.4 Load and Motion Analysis

Two load cells were mounted on the drop tower to measure the neck reaction forces and moments, and the axial impact force at the head. The load cell at the neck, T1, was a 6-axis load cell (MC3A, AMTI, Watertown, MA) with a maximum axial force of 4450 N. The T1 load cell was mounted between the T1 mounting cup and the carriage. Under the impact platen a 20kN uni-axial load cell (LC, Omega Engineering Inc., Stamford, CT, USA) measured the axial impact of the head. Orientation of the reference axis is given in Figure 7-4. Data acquisition was done at 146 kHz using a personal computer-based data acquisition system. The signals were digitally filtered in Matlab using a 4<sup>th</sup> order Butterworth filter.

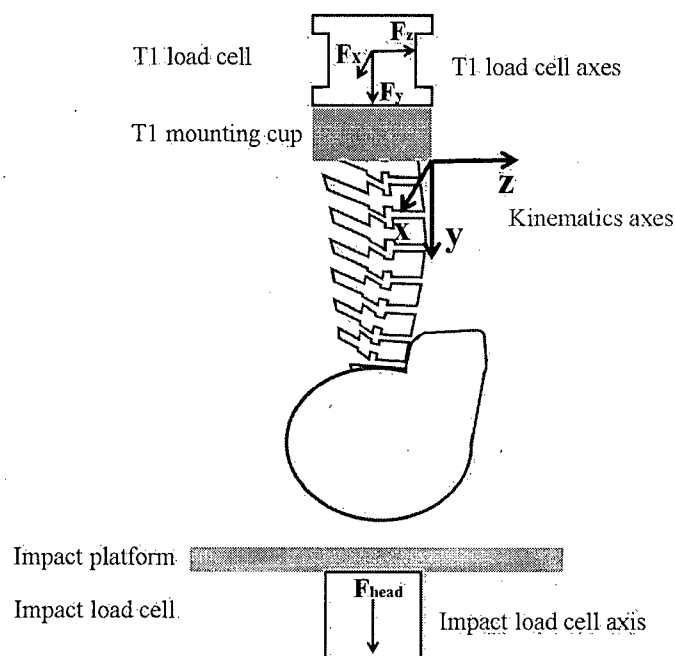


Figure 7-4: Location and orientation of axes of the load cells and 3D marker coordinates.



Two high speed digital cameras (Phantom V9.0, Vision Research Inc) were used to capture the impact event at 1000 fps. The two camera views allowed for 3D reconstruction of the marker motion. Each marker was tracked using a motion tracking software (TEMA, Image Systems AB, Sweden). Direct linear transformation (DLT) was used to reconstruct the 3D paths of each marker. The load cell output and digital camera collection were synchronized using a built in feature of the camera control software. This feature time stamped each sample taken by the data acquisition system according to the current frame. Thus for each video frame there were 146 samples taken on each data channel (7 in total: 6 for the multi-axial load cell at T1 and one for the uni-axial load cell at the head).

#### 7.3.5 Injury Analysis

Diagnosis of injuries in the specimens was done by inspection of the specimens and diagnostic radiographs by a spine surgeon (Dr. Eyal Itshayek). The surgeon also examined the high speed external and x-ray video footage to identify the injury events.

### 7.4 Results

#### 7.4.1 Qualitative Description of Individual Impacts

**H1091** The donor was a 72 year old male. The specimen responded in hyperextension about C4/5 during impact. Maximum hyperextension was reached approximately 12ms after initial impact. Injury occurred as the hyperextension reached its maximum. As the carriage rebounded, the head moved into flexion while the spine remained in extension. The preload cable on the right side failed at the guide hole in the surrogate head at approximately 90ms after initial impact.

Post injury examination revealed a fracture of the C4 spinous process, disruption of the anterior longitudinal ligament (ALL), opening of the C4/5 intervertebral disc, and an avulsion fracture on the superior surface of C5. All of these injuries are consistent with a hyperextension injury mechanism.<sup>1</sup> Some increased joint space was noted at C2/3 and the dens was fractured at its base. The occiput was cut slightly smaller than was desired in this specimen. This resulted with the surrogate head being mounted too anteriorly, which caused the preload to be anchored slightly more forward than the intended path.

**H1096** The donor was a 68 year old female. There was some stiffness at the lower cervical spine in this specimen. The injury mechanism was a dislocation of the atlanto-axial (AA) complex with the axis moving anteriorly with respect to the atlas. This dislocation started 4ms after impact with C2 reaching a maximum anterior displacement at 12ms. Prior to the dislocation the lower cervical spine was put into slight extension. It was also noted that the head began rebounding at 13ms after impact, 1ms before the carriage.

Post injury examination showed extensive injury to the AA structures. Included in these injuries were fractures of the arches of C1, bilateral disruption of the facet joints between C1 and C2, and a fracture of the dens at its base.

**H1116** The specimen was an 84 year old female. The injury mechanism was a fracture dislocation at C3/4. The specimen's extension response to loading was smooth. Noticeable opening of the C3/4 intervertebral space and dislocation started at 8ms. The dislocation continued until 13ms when the carriage began rebounding and the spine was unloaded.

Examination of the specimen showed injuries around the C3/4 spinal unit. The intervertebral disc space was opened and the ALL disrupted. There was also a fracture of the spinous process of C3. Avulsion fractures on the anterior inferior lips of C2 and C3 were found. Air was seen in the C3/4 facets.

**H1177** The specimen was a 65 year old female. The mechanism of injury was hyperextension about C4/5/6. The maximum extension was reached at 12ms. Injuries observed in post impact examination were more indicative of hyperextension about C4/5. There was an avulsion fracture on the anterior inferior lip of C4 and also a fracture of the spinous process of C4. The C4/5 disc was opened and the ALL disrupted. A dens fracture and a tear drop on the anterior inferior lip of C2 were also found.

**H1183** The donor was a 71 year old female. There was noticeable laxity of the atlanto-occipital (AO) complex but the specimen was found to be stiff on manual manipulation through the lower cervical spine. Head impact occurred with slight flexion of the

surrogate head. Dislocation at the AA complex could be seen 3ms after impact. C2 slid anteriorly on C1 until it reached a maximum displacement and was constrained by the ligaments around the structure at 7ms. At this time C1 moved anteriorly relative to the occiput putting the head into relative flexion. Maximum displacement of C2 relative to the occiput was reached at 14ms. At this time the carriage began rebounding. As the head lifted off the platform there was a large space between C1 and C2. It appeared as though the specimen would have been decapitated if the preload had not been present.

Post-traumatic examination of the specimen revealed significant injuries at the AA and AO complexes to the bones and ligaments. The bilateral fracture of the anterior arch of C1 and a dens fracture through the base were consistent with AA dislocations. The ligaments of the AO complex were disrupted, as were both facet capsules of C1/2.

**H1184** The donor was a male of unspecified age. The injury mechanism was hyperextension about C4/5. Disruption of the ALL at C4/5 was seen at 10ms. The specimen continued to be loaded until 14ms. Post impact inspection of the specimen confirmed the disruption of the ALL at C4/5. Also identified were an avulsion fracture on the anterior inferior lip of C4, a spinous process fracture of C4, and anterior disruption of the left facet capsule of C4/5.

#### 7.4.2 Kinematic Response to Impact

Marker motion was plotted in each axis (x, y, and z). The y-axis graphs were all similar. Each was a parabolic curve tracing the descent and rebound of the mounting cup onto and off of the spine. The x-axis plots show the transverse motion of the markers (i.e. motion out of the sagittal plane). There was some small motion in this plane: less than 10 mm at any level in any specimen. This motion could be due to anatomical asymmetry or small loading differences between the bilateral follower preloads. Of most interest were the z-axis graphs which trace the sagittal motion of the specimen. A typical set of traces is shown in Figure 7-5 through Figure 7-7. The traces for the other specimens can be found in Appendix B.

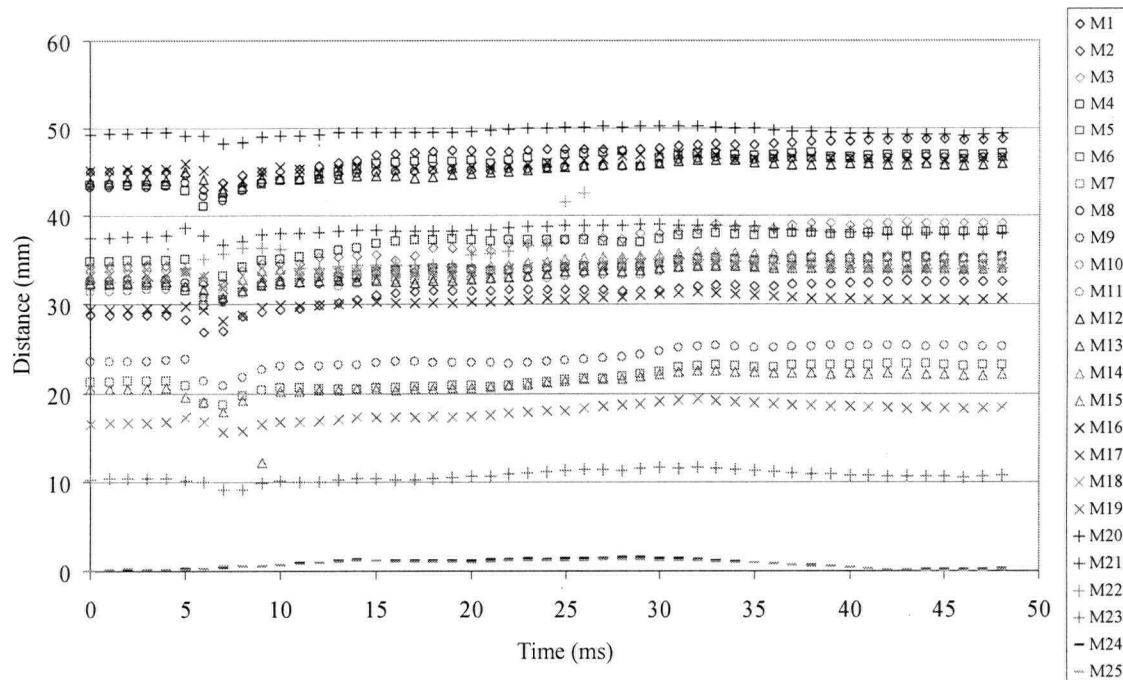


Figure 7-5: Marker motion along the x-axis for the 25 markers of specimen H1091. Markers 1 through 3 were on C2, 4 to 8 on C3, 9 to 11 on C4, 12 to 15 on C5, 16 to 19 on C6 and 20 to 23 on C7. Markers 24 and 25 were on the mounting cup.

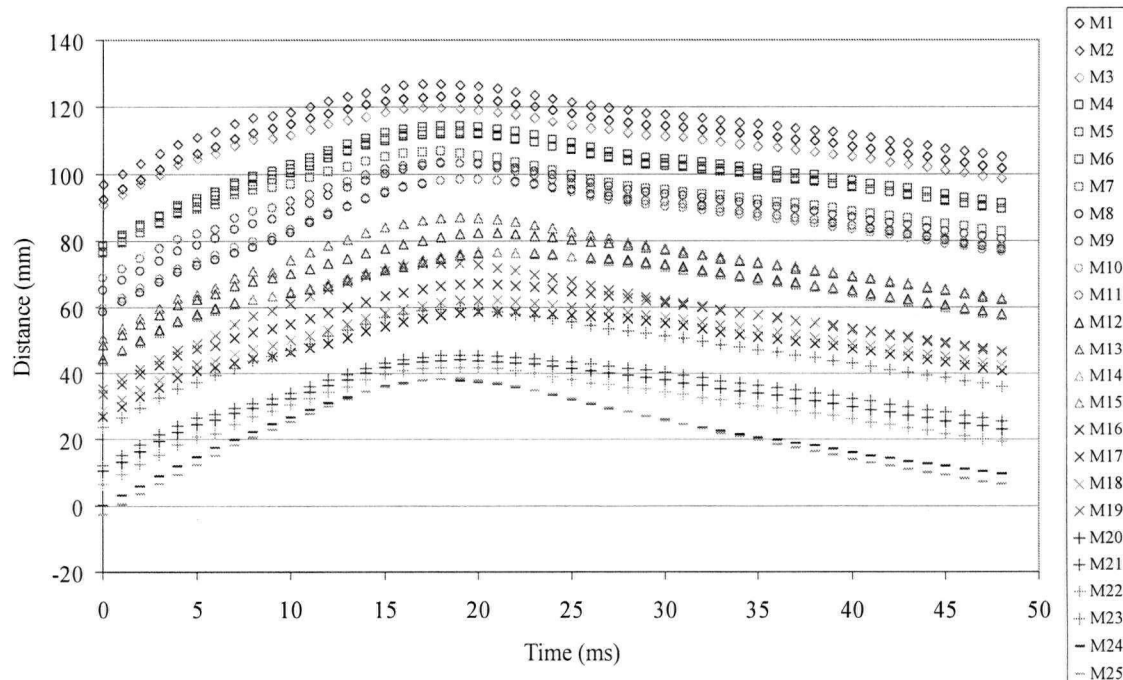


Figure 7-6: Marker motion along the y-axis for the 25 markers of specimen H1091.

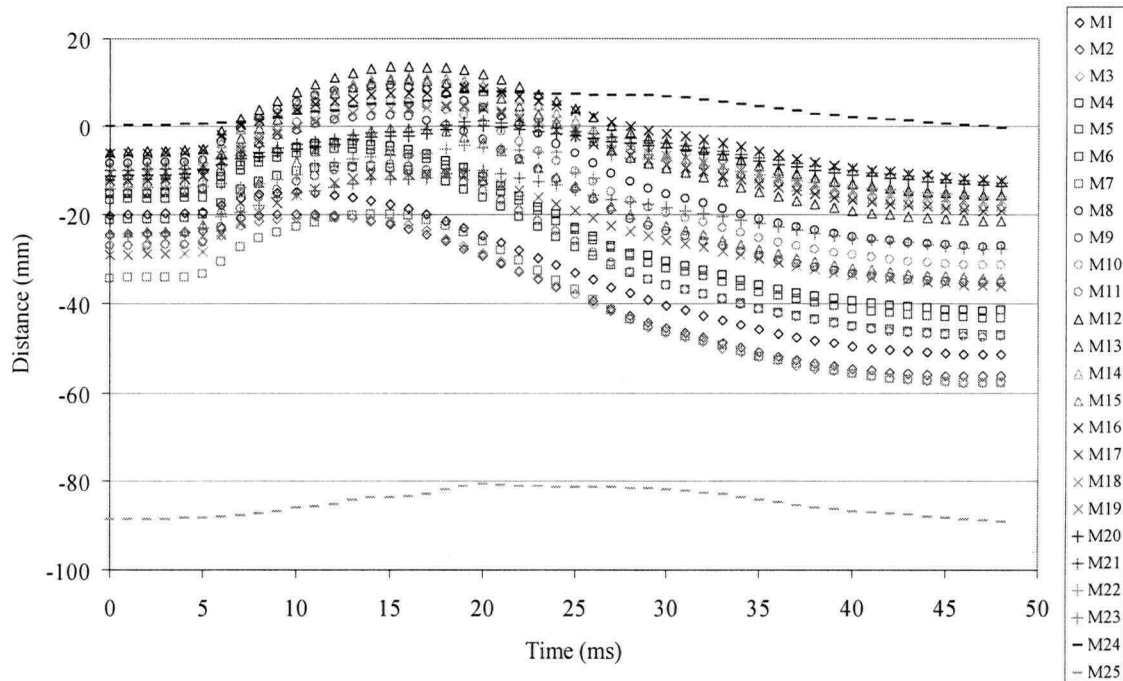


Figure 7-7: Marker motion along the z-axis for the 25 markers of specimen H1091.

By only plotting one marker from each vertebra (the most anteriorly placed marker) in the z-axis plot, the motion of each vertebra can be more easily compared between specimens. Figure 7-8 through Figure 7-13 show these pared down plots.

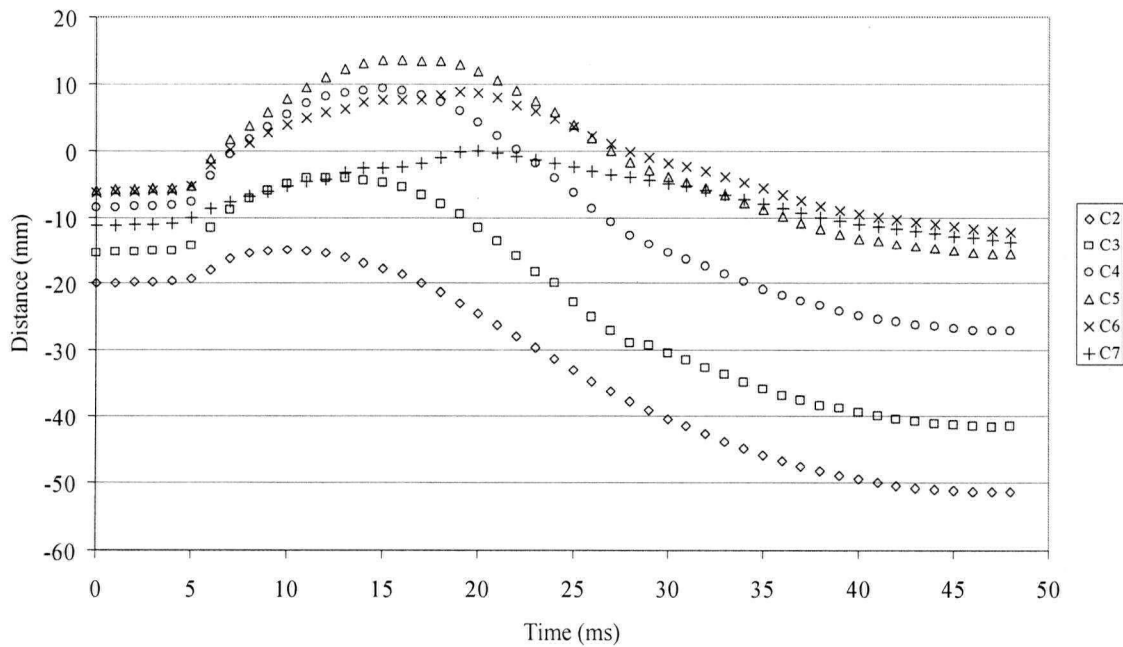


Figure 7-8: Z-axis trace of specimen H1091 (Hyperextension injury)

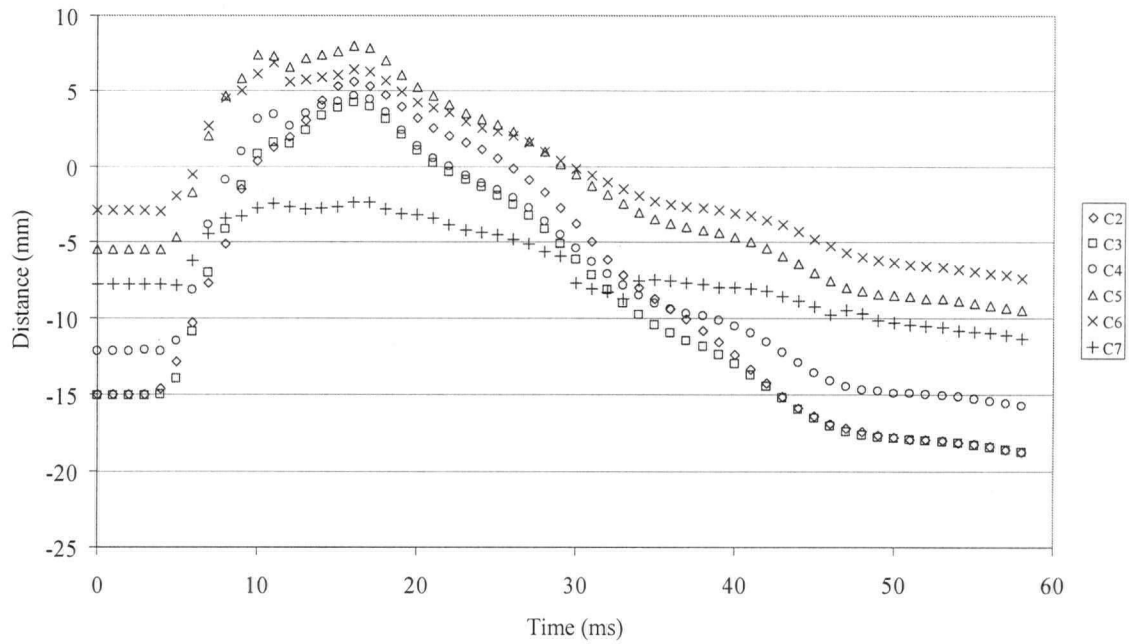


Figure 7-9: Z-axis trace of specimen H1096 (AA Dislocation)

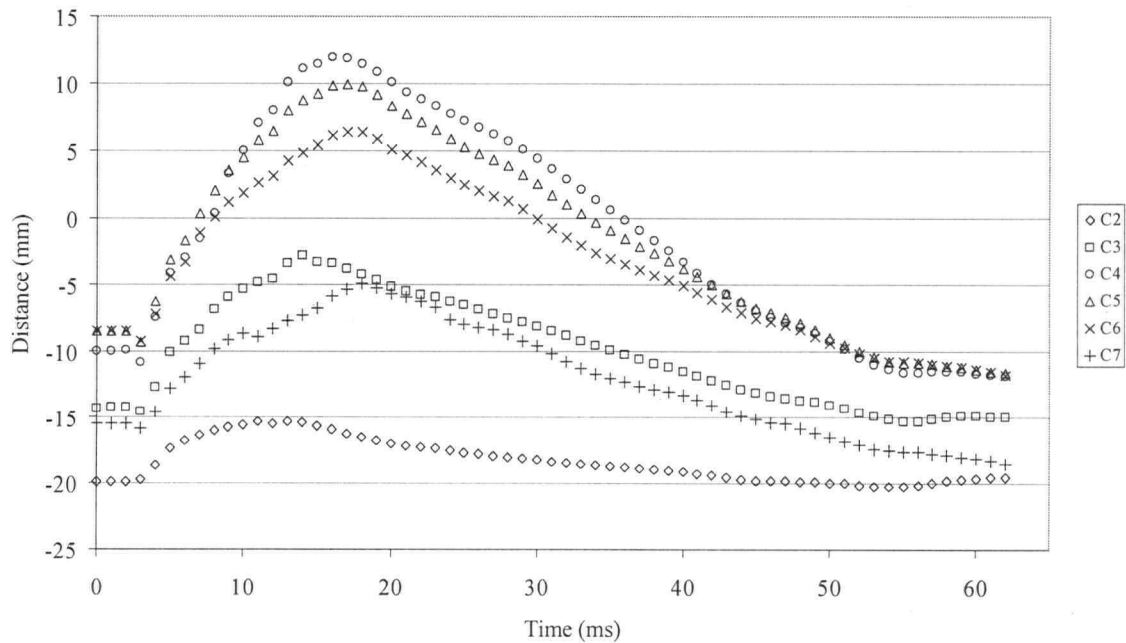


Figure 7-10: Z-axis trace of specimen H1116 (Fx Dislocation about C3/4)

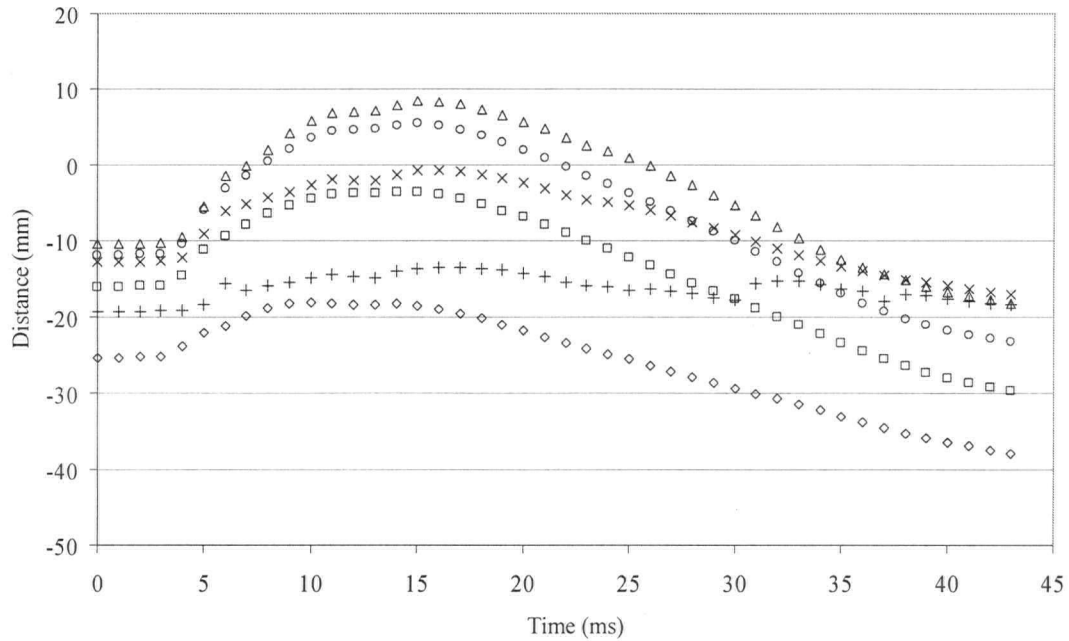


Figure 7-11: Z-axis trace of specimen H1177 (Hyperextension injury)

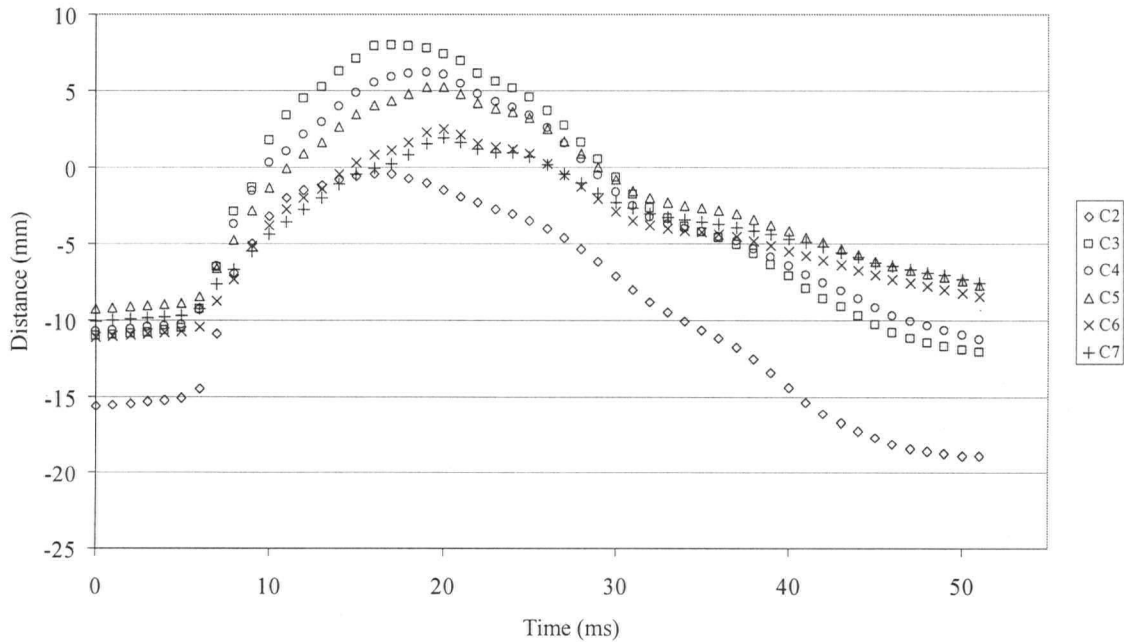


Figure 7-12: Z-axis trace of specimen H1183 (AA Dislocation)

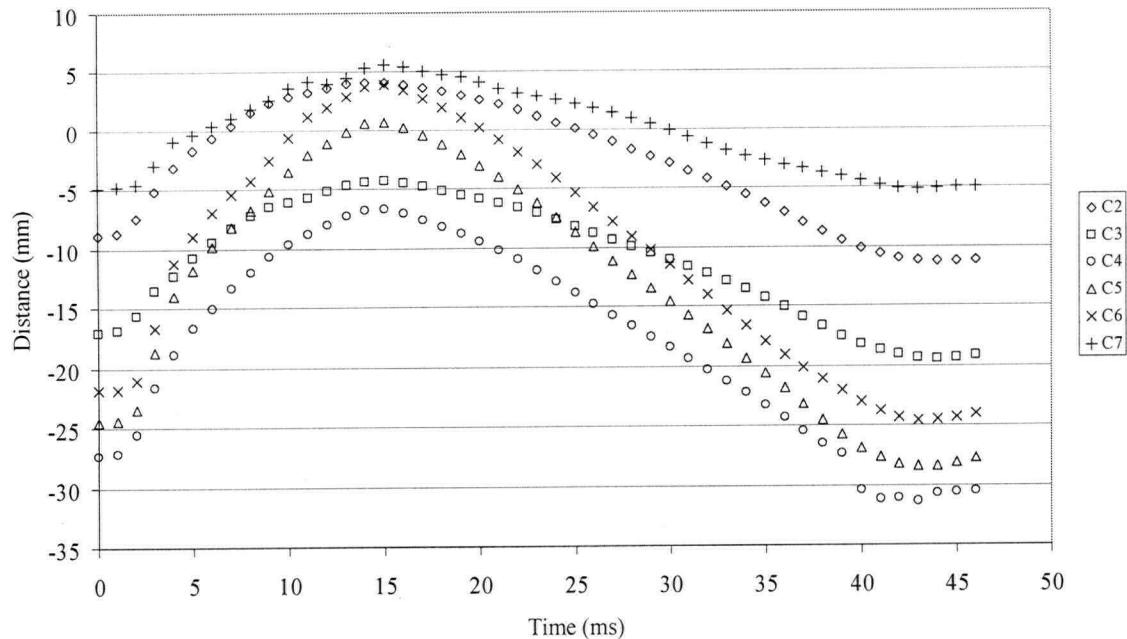


Figure 7-13: Z-axis trace of specimen H1184 (Hyperextension injury)

The three specimens that suffered hyperextension injuries, H1091, H1177, and H1184, all show similar z-axis plots. These plots are characterized by a smooth parabolic-like curve once deformation begins. The plots belonging to the atlanto-axial dislocation specimens, H1096 and H1183, show a steeper curve during spine loading in comparison with the hyperextension graphs. Specimen H1116 suffered a fracture dislocation injury. The curve for this injury is a combination of the other two types. Most notable in this curve is the large difference in translated distance between the vertebrae closest to the dislocation at C3/4 and furthest (i.e. C2 and C7).

#### 7.4.3 Kinetic Data

The following set of plots in Figure 7-14 show the force and moment traces of the load cell at T1 during the first 60 ms of the impact of an example specimen (H1096). Subfigures a through c are the reaction forces (x, y, and z) at T1, and d through f are the reaction moments about x, y, and z. The trace of the axial reaction force at T1 for each specimen can be seen in Figure 7-15. The complete results of all six specimens can be found in Appendix C. For specimens H1116, H1183, and H1184 technical problems with the uni-axial load cell amplifier resulted in the loss of the axial impact response at the impact platen.



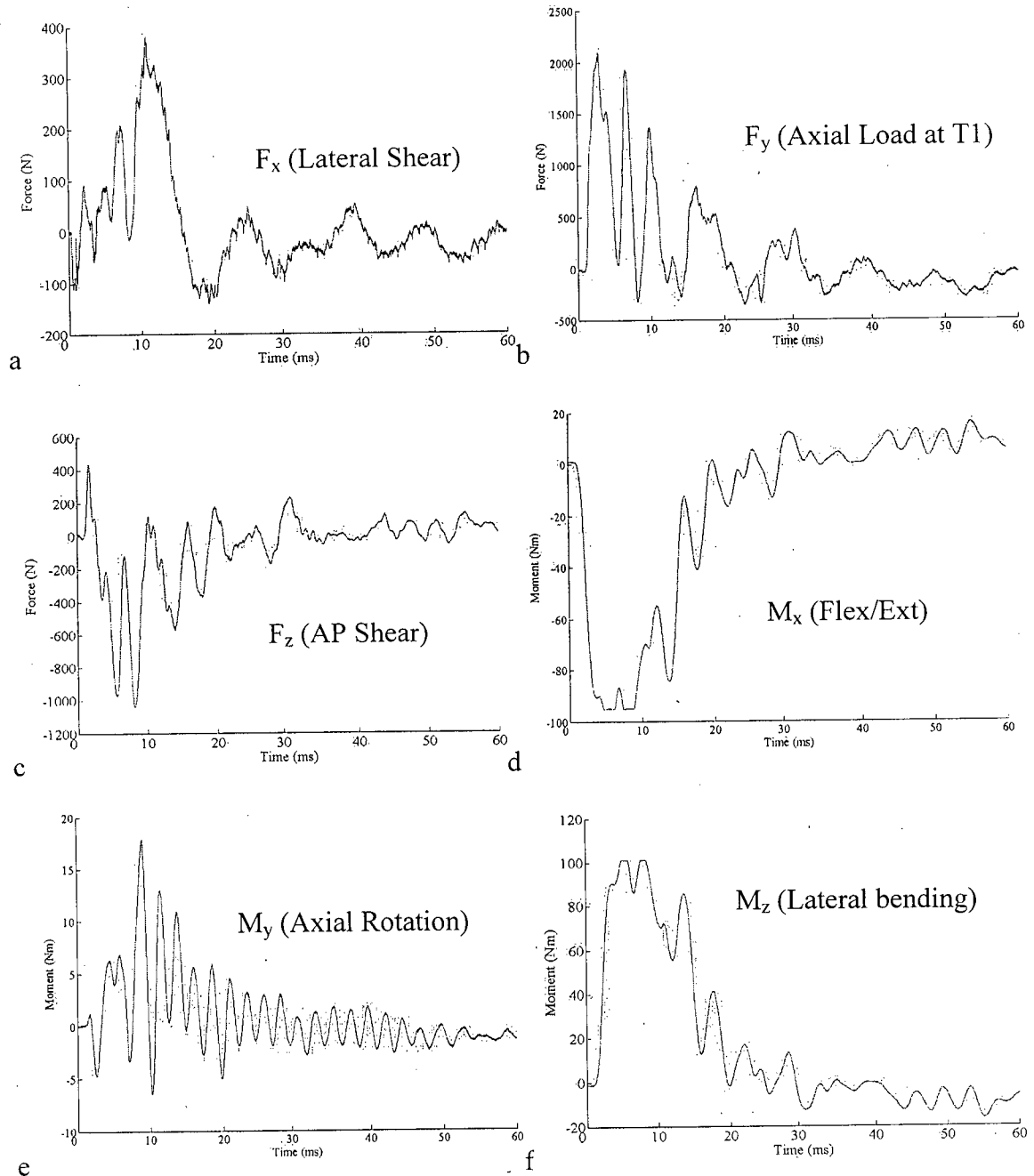


Figure 7-14: Force /Moment traces from the load cell at T1 of specimen H1096.

Some ringing was noted in the load cell traces, in particular in the axial rotation. Inspection of results from other axial impact tests by another group, this ringing phenomenon has been seen previously but not at this amplitude. This seems to indicate that the ringing is coming from the apparatus. Sources could be the connections at the bearings or between pieces of the structure.

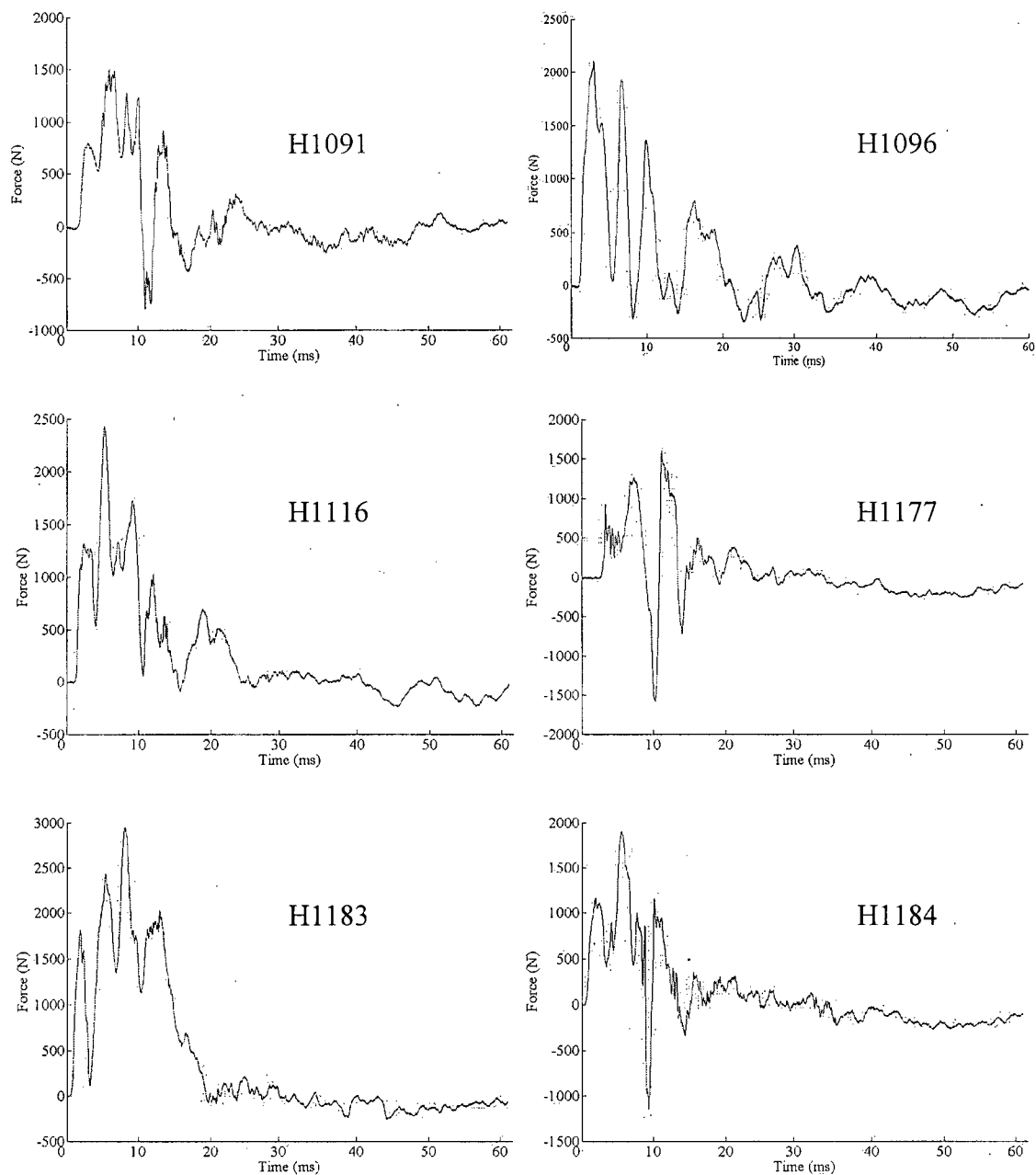


Figure 7-15: The axial reaction forces at T1 for each of the specimens

The head impact and neck axial reaction force trace were used to define two events, Figure 7-16. The first event (Impact) is marked by the significant spike in the head impact trace and was the head impact. During the first half of this event the forces and moments at T1 were zero. The second event (Neck Loading) is the loading of the cervical spine by the carriage seen in the neck reaction force. The lag between impact and

the onset of T1 axial loading shows the degree of decoupling between the head and torso due to the compliance of the cervical spine. The head reaction force, presented as the maximum impact force during spine loading, was the local maximum after the initial impact spike in the impact trace. These values are summarized in Table 7-1 and the graphs for each specimen can be found in Appendix C. Cervical spine injury by fracture and/or dislocation was marked by a drop in the axial load at T1.

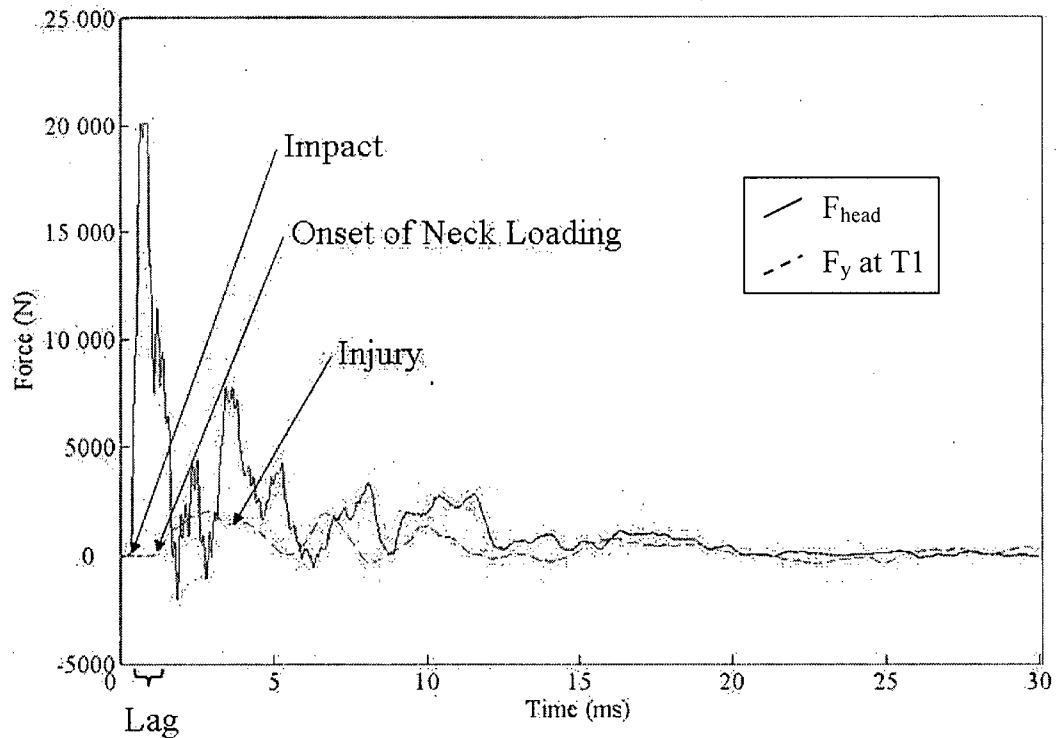


Figure 7-16: Head impact and neck axial load traces showing the key analysis points: Impact, Onset of Neck Loading, Injury (determined from x-ray footage), and Lag using specimen H1096

Table 7-1: Summary of maximum principal forces, time of each, lag time, and time to primary injury event

Specimen	Max during Impact $F_{\text{head}}$ [time to max]	Max During Spine Loading $F_{\text{head}}$ [time to max]	Max Axial Response $F_y$ at T1/2 [time to max]	Lag	Time to Onset of Deformation of the Spine
H1091	15 040 N [0.55 ms]	3109.1 N [11.12 ms]	1502.0 N [4.00 ms]	0.92 ms	5 ms
H1096	20 094 N [0.42 ms]	7827.5 N [3.18 ms]	2105.4 N [2.74 ms]	0.81 ms	6 ms
H1116	N/A	N/A	2426.2 N [5.21 ms]*	~1 ms*	4 ms
H1177	20 094 N [0.49 ms]	2288.6 N [9.14 ms]	1220.2 N** [4.95 ms] 1599.0 N [9.28 ms]	0.82 ms	5 ms
H1183	N/A	N/A	2950.7 N [8.14 ms]*	~0.5 ms*	7 ms
H1184	N/A	N/A	1905.9 N [5.53 ms]*	~0.5 ms*	3 ms
Averages (STD)	N/A	N/A	2018.4 N [5.10 ms]	<1 ms	5 ms

\*In reference to the first frame of impact as the exact time of impact is unavailable due to failure of the head impact load cell

\*\* Local maxima, followed by a negative force and then the maximum value as given.

*Italics indicate saturation of the sensor*

#### 7.4.4 Buckling

All of the specimens responded to impact in a first order extension mode. The serpentine deformation seen by Nightingale was not seen in any of the specimens tested in our study. The kinematic and kinetic data was analyzed for the sudden change in axial deformation (a bowing of the spinal column occurring in under 1 ms) and the accompanying sharp decrease in the axial load and increase in the flexion/extension moment that defines snap through buckling. This response was not seen in any of the specimens tested. In specimen H1116 a slight jog in the path can be seen at 4 ms. This is not snap through buckling as the motion is towards the posterior and is uniform across

the lower vertebrae. In snap through buckling an increase in anterior curvature across the lower vertebrae would be seen as well as posterior curvature in the upper vertebrae.

## 7.5 Discussion

A drop tower was used to provide a head first head to ground impact. The apparatus measured the force and moment response at the impact platform and T1. High speed digital cameras were used to capture the impact event and reconstruct the three-dimensional motions of the vertebra during impact. To simulate musculature a follower preload was applied to the cervical spine specimen using a modified version of Muira and colleagues method of follower load application.<sup>18</sup> The load applied was based on *in vivo* disc pressures and sizes.<sup>14, 16</sup>

Previous work on cervical spine biomechanics during head to ground simulation has largely focused on injury mechanisms and the affect of pre-injury conditions such as posture and impact surface parameters. In several of these studies a higher order serpentine buckling response has been seen and a snap through buckling response noted. It is unknown whether these phenomena occur in real life accidents. Their occurrence in *in vitro* studies is often associates with complex injury patterns. One of the common factors in all of these studies is that none accounted for the presences of musculature and the forces they exert on the cervical spine *in vivo*. Neck muscles are thought to act as stablizers of the otherwise instable cervical spinal column.

The addition of a follower preload to a cervical spine has been associated with an increase in stiffness of the specimen.<sup>18</sup> In this study this increase in stiffness was seen in the increased degree of coupling between the head and T1. Lag between impact and the onset of loading at T1 is a measure of this coupling behaviour. In all specimen tested in this study, the lag was less than 1ms. Nightingale and colleagues saw lags of 1.5 ms to 2.1 ms in rigid, level impacts.<sup>7</sup> In this model the surrogate head may have also contributed to the increase in stiffness of the specimen. However, the potential for axial compression of an *in vitro* skull is negligible in comparison to that of the uncompressed cervical spine. Thus the influence of replacing the head on the change in lag was minimal.

The second order buckling mode seen in previous studies was not seen in this study. The average axial T1 load seen in this study was lower than previously reported

loads. It has been shown in a mathematical model that an increase in stiffness of the cervical spine leads to smaller second order mode deformation at higher loads.<sup>19</sup> However, the application of the follower load induced a lordotic curve in the specimens. This may predispose the specimens to extension and the first order response.

Snap through buckling has been defined as a sudden change in posture of the specimen (apparently less than 1 ms), which is accompanied by a sudden decrease in axial neck load and an increase in anterior posture moment. In this study there was no evidence of the sudden change in posture as all the specimens responded with a first mode deformation (extension) over several frames.

#### 7.5.1 Limitations

The limitations of the methodologies and analysis performed in this aspect of the project are outlined here:

- The mounting of the surrogate head may not be accurate. This could cause the loading vector through the spine to be directed anteriorly or posteriorly to the point desired.
- In simulating musculature, one can only recreate the forces. The voluntary control of human muscles in response to an impact event can not be simulated. Thus the static nature of the follower preload may not accurately reflect the real life scenario.
- The head impact axial load cell was saturated this load cell was selected based on the results of the work by Nightingale and colleagues.<sup>9</sup> This could be an affect of the surrogate head. While efforts were made to make the head model as biofidelic as possible the stiffness of the head maybe greater than that of a real head.
- The sagittal moments in the neck load cell were saturated. This could be attributed to the spring like behaviour of the spine in the presence of the follower preload.
- The unloading of the springs at impact would change the preload upon impact. However the rate of this is not known. Also it is not known if the follower preload reloaded upon rebound.

## 7.6 Conclusion

The presence of a follower preload during axial impact of the cervical spine acts to stiffen the specimen. The shortened lag between impact and T1 axial loading and the mitigation of the occurrence of the higher order serpentine buckling and snap through buckling patterns seen in previous tests are a result of the stiffening of the specimen. Stiffening of the cervical spine upon application of a follower load has been previously noted and is comparable to the stiffness of the *in vivo* spine in flexion and extension. Simulating the forces of musculature using a follower preload influenced the response of cervical spine during the impact event. However, as the response of the cervical spine and muscles to head to ground axial impact during real life events is unknown, the biofidelity of an *in vitro* model can not be completely affirmed.

## 7.7 References

1. White, A.A. and M.M. Panjabi. Clinical biomechanics of the spine. 2nd ed, J.B. Lippincott Company, New York. 1990.
2. Alem, N.M., G.S. Nusholtz, and J.W. Melvin. Head and Neck Response to Axial Impacts. in 28th Stapp Car Crash Conference, Chicago, Illinois, USA, Society of Automotive Engineers, Inc., Warrendale, Pennsylvania, USA. 1984
3. Nightingale, R.W., et al. Experimental impact injury to the cervical spine: relating motion of the head and the mechanism of injury. *Journal of Bone and Joint Surgery.American Volume*, 1996: 78-A(3): p. 412-421.
4. Panjabi, M.M., et al. Critical load of the human cervical spine: an *in vitro* experimental study. *Clinical Biomechanics*, 1998: 13(1): p. 11-17.
5. Patwardhan, A.G., et al. Load-carrying capacity of the human cervical spine in compression is increased under a follower load. *Spine*, 2000: 25(12): p. 1548-54.
6. Ivancic, P., et al. Biofidelic whole cervical spine model with muscle force replication for whiplash simulation. *European Spine Journal*, 2005: 14(4): p. 346-355.
7. Nightingale, R.W., The Dynamics of Head and Cervical Spine Impact, in Department of Biomedical Engineering, Duke University. 1993.
8. Hodgson, V.R. and L.M. Thomas. Mechanisms of cervical spine injury during impact to the protected head. in 24th Stapp Car Crash Conference, Society of Automotive Engineers. 1980
9. Nightingale, R.W., et al. Dynamic response of the head and cervical spine to axial impact loading. *Journal of Biomechanics*, 1996: 29(3): p. 307-318.
10. Nusholtz, G.S., et al. Cervical spine injury mechanisms. in 27th Stapp Car Crash Conference, Society of Automotive Engineers. 1983
11. Nusholtz, G.S., et al. Response of the cervical spine to superior-inferior head impact. in 25th Stapp Car Crash Conference, Society of Automotive Engineers. 1981
12. Pintar, F., et al. Biodynamics of the total human cadaveric cervical spine. in 34th Stapp Car Crash Conference, Orlando, Florida, USA, Society of Automotive Engineers, Inc., Warrendale, Pennsylvania, USA. 1990
13. Pintar, F.A., et al. Kinematic and anatomical analysis of the human cervical spinal column under axial loading, Warrendale,PA, 33rd STAPP car crash conference. 1989
14. Hattori, S., et al. Cervical intradiscal pressure in movements and traction of the cervical spine. *Zeitschrift fur Orthopadie*, 1981: 119: p. 568-569.
15. Pooni, J.S., et al. Comparison of the structure of human intervertebral discs in the cervical, thoracic and lumbar regions of the spine. *Surgical and Radiologic Anatomy*, 1986: 8: p. 175-182.
16. Moroney, S.P., A.B. Schultz, and J.A.A. Miller. Analysis and measurement of neck loads. *Journal of Orthopaedic Research*, 1988: 6: p. 713-720.
17. Panjabi, M.M., et al. Development of a system for in vitro neck muscle force replication in whole cervical spine experiments. *Spine*, 2001: 26(20): p. 2214-9.
18. Miura, T., M.M. Panjabi, and P.A. Cripton. A method to simulate in vivo cervical spine kinematics using in vitro compressive preload. *Spine*, 2002: 27(1): p. 43-8.



19. Nightingale, R.W., et al. Inertial properties and loading rates affect buckling modes and injury mechanisms in the cervical spine. *J.Biomech.*, 2000: 33(2): p. 191-197.
20. Chang, L., C. Clarke, and P.L. Morley, *Physical Model of the Human Head*, in *Mechanical Engineering*, University of British Columbia: Vancouver. 2005.
21. Dvorak, J., et al. In vivo flexion/extension of the normal cervical spine. *J.Orthop.Res.*, 1991: 9(6): p. 828-834.

## Chapter 8: Spinal Cord Deformation during Axial Impact Induced Injuries in the Cervical Spine

### 8.1 Introduction

Spinal cord injury sustained during head to ground impact is the result of bony insult to the soft cord tissue. This insult results in a cascade of biochemical effects leading to cellular injury and necrosis, which can cause paralysis and even death of the injured individual. Cord injury has been widely studied at a cellular level in animals by simulating the cord injury using an impactor or other mechanical disruption of the cord and column.<sup>1</sup> The degree of compression, velocity of the impact, and the viscous response of the cord have all been correlated with the probability of recover from neurological trauma in ferrets *in vivo*.<sup>2</sup>

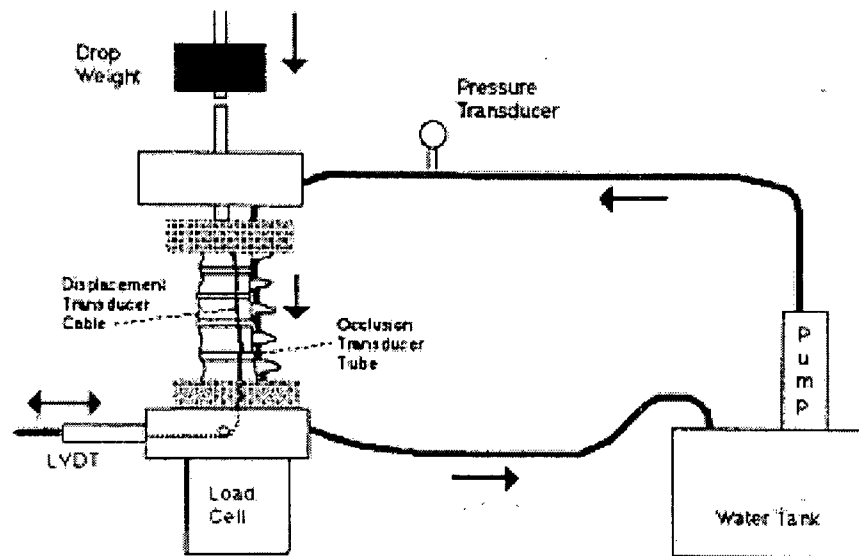
The relationship between bony events and spinal cord deformation during an injury event is not well established. It has been shown that the post-traumatic measure of cord deformation is not indicative of the maximum transient cord deformation resulting from bone encroaching into the canal during the injury event. Several studies confirmed this hypothesis by recording the recoiling action of bony fragments during burst fracture events,<sup>3-7</sup> or measuring pressure at the bone-cord interface.<sup>8</sup> While these studies have provided some information on the degree of canal encroachment that occurs during injury, none have been able to provide a complete sagittal profile of the bony intrusion. Three studies have provided a discontinuous profile with a few discrete points which did not allow for continuous evaluation of the cord deformation.<sup>4, 8, 5</sup> However due to the unpredictable nature of spinal cord injury, these methods may miss vital information. Direct visualization of the sagittal profile of the cord during deformation would provide a more accurate picture of the injury event. Furthermore, the majority of the previous tests did not address the issue of maintaining the biofidelity of the bone-cord interface. Only one study has done so.<sup>8</sup> They used a gelatin based model with pressure sensors mounted on the anterior surface. The gelatin was matched for its material properties to that of *in vivo* feline spinal cord. However, the use of pressure sensors at discrete points did not produce a continuous sagittal profile of cord deformation.

## 8.2 Background

A large amount of the previous work done on spinal cord deformation used canal occlusion during injury as a measure of cord compression. Canal occlusion can be defined as the reduction in cross sectional area of the spinal canal due to intrusion of bony anatomy or the intervertebral disc into the canal. Cord compression is an aspect of the spinal cord deformation as a result of assault from the intruding bony anatomy. These measures differ as the spinal cord does not fill the canal and thus the canal occlusion measure may over estimate the degree of cord compression. Furthermore, some of the studies used physical transducers to measure occlusion. These transducers had different transverse material properties than the *in vivo* spinal cord which changes the bone-cord interfaces resulting in non-physiologic responses.

The common focus of previous work in this area was the relationship between transient and post-injury occlusion or cord compression. Transient occlusion is the degree of occlusion during the injury event. The general hypothesis is that the post-injury or residual occlusion seen in the clinical setting does not reflect the true maximum amount of canal occlusion. This is especially evident in clinical cases where no residual occlusion can be seen in imaging studies (MRI, x-ray, CT) but evidence of spinal cord contusion can be seen.

Chang and colleagues were one of the first groups to examine canal occlusion during injury simulation.<sup>3</sup> In addition to the hypothesis that post-traumatic measures of canal occlusion underestimate transient canal occlusion, they were interested in the changes in length of the spinal segment and so developed methods to measure post-traumatic column deformation. They used a fluid filled flexible plastic tube to measure canal occlusion via the pressure of the fluid, Figure 8-1. During injury events, the intruding bony anatomy compressed the tubing, changing the volume and increasing the measured pressure. They also took pre- and post-traumatic images of the specimens. An impactor was used to cause burst fractures in the cervical spine column.



Reprinted with permission © 1994 Lippincott, Williams & Wilkins

Figure 8-1: Experimental set up of the water pressure based occlusion transducer<sup>3</sup>

The transducer was limited in its range and was not sensitive to multiple level burst fractures. The transducer was only able to measure to a maximum 55% occlusion and therefore an “official” maximum occlusion was never determined. The group reassessed the model and made improvements. They conducted a similar study using their improved transducer which had an increased range to 70% occlusion.<sup>9</sup> From the results it appears that the extent of occlusion exceeded the transducer limit as all the specimens reached 70% occlusion. They reported in both studies that the post traumatic level of injury was less than that seen during injury.

Concurrently the group developed a new approach.<sup>5</sup> The design of the transducer was similar to their previous transducer in that it was a fluid filled plastic tube. However it used a voltage profile approach to measuring canal occlusion. A saline solution was used as the core fluid and a current was passed through it. Eight electrodes were placed along the tubes length to measure the voltage drop along the length, Figure 8-2. The principle of operation was that a change in cross sectional area would change the resistance in that section which would be picked up by the transducer. This allowed the transducer to be sensitive to level. The tubing used for this transducer had a slightly large diameter than the previous design which increased the sensor’s range. However we were unable to find results of an occlusion study utilizing this device.

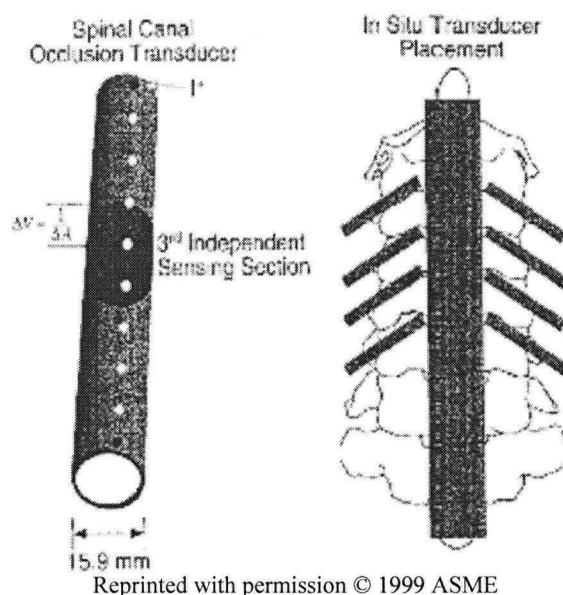
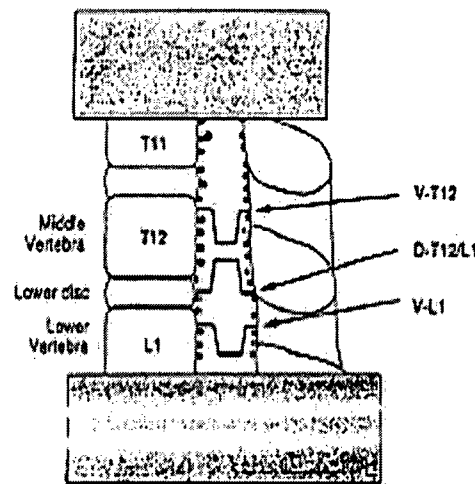


Figure 8-2: Transducer developed by Raynak and colleagues to measure occlusion via changes in the core fluid's electrical resistance<sup>5</sup>

There were several limitations with both of these transducers. In neither case were the properties of the plastic tubing in terms of its biofidelity reported (i.e. its concordance in material properties between the artificial and *in vivo* cords). Using a material that has similar material properties to the *in vivo* spinal cord would provide a more realistic interface between the bone and transducer. The influence of the tubing in these transducers could include a reaction force to the incoming bony fragments, a stiff response to impact and a lack of a defining profile of occlusion. Also, both systems were associated with a large number of external components (i.e. pumps and connective tubing), which made them impractical for non-stationary tests such as in a drop tower injury simulation.

Panjabi and colleagues used a series of strain gauged transducers to measure canal occlusion at certain points on the vertebral body and disc during simulated burst fracture in functional spinal units.<sup>4</sup> These transducers were thin metal “bridges” instrumented with strain gauges to measure the change in diameter of the canal, Figure 8-3. Three transducers were placed in the canal, one at the intervertebral disc and two at vertebral end plates. Small metallic spheres were used to trace the outline of the posterior and anterior borders of the canal to aid in analysis of the pre and post injury static

radiographs. These were fixed to the respective longitudinal ligaments. The results of this study indicated that during impact the canal was occluded to 33.3% (average value) compared to a final canal occlusion level of 18% (average value) as seen in the radiographs. The obvious limitation of this set up is the limited sensitivity as a burst fracture could occur anywhere in the vertebral body and the maximum occlusion could be easily missed due to the placement of these transducers. However the goal of this study was to measure occlusion at these specific locations. Also, as with the previous device, this device did not address the issue of the biofidelity of the bone-transducer interface. Of additional concern is the effect of the glue used to mount the spheres on the longitudinal ligaments of the specimen.

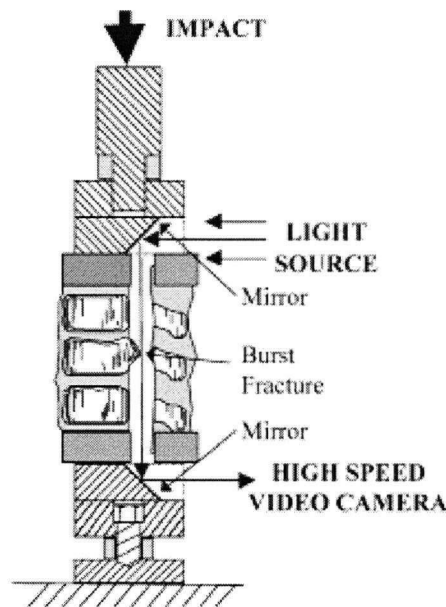


Reprinted with permission © 1995 Lippincott, Williams & Wilkins

Figure 8-3: Transducer placement used by Panjabi and colleagues<sup>4</sup>

More recently Wilcox and colleagues proposed a method that measured canal occlusion by viewing the canal in a superior-inferior manner yielding a cross-sectional view of the canal.<sup>6, 7</sup> To track occlusion during a simulated injury, a light source was directed by mirrors into the canal and to a high speed camera, Figure 8-4. The resulting image encompassed all occlusion within the segment but did not indicate the location of occlusion in the longitudinal direction. The direct measurement of the event was unique to this approach. Wilcox et al reported a typical set of results for a specimen as a maximum occlusion of approximately 65% during impact and a final occlusion of 25% (impact energy of 110 J). A newer study in 2003 by the same group reported a similar

experiment and yielded results indicating a maximum occlusion of approximately 80% in high energy injured specimens (140 J) and 20% in lower energy (60 J) specimens<sup>6</sup>. The final canal occlusions for these specimens were approximately 50% and 5% respectively. The error of their method was determined using CT scans to compare final occlusion levels between video and CT results and was found to be about  $\pm 10\%$ . The video footage was also able to confirm the recoiling action of the bony fragments during impact. This method would not be appropriate for dynamic head to ground impact or for longer spinal segments where lordosis interferes with the line of sight through the canal.



Reprinted with permission © 2004 Lippincott, Williams & Wilkins

Figure 8-4: Setup used by Wilcox and colleagues to capture the transverse profile of canal occlusion during simulated burst fracture injury.<sup>6</sup>

Two groups have studied spinal cord deformation using physical surrogate spinal cords: Pintar and colleagues<sup>8</sup> measured pressure on the cord and Bilston and colleagues<sup>10</sup> measured cord deformation during hyperflexion and extension. Pintar and colleagues work was to measure the pressure at the bone-cord interface. They developed a surrogate spinal cord that was outfitted with pressure transducers. This cord was placed in the canal during head to ground impact simulation. The surrogate cord was created out of gelatin and sausage casing. The gelatin concentration was mixed such that its transverse compression response matched that of *in vivo* feline spinal cord. Seven piezo-electric

pressure transducers were attached anteriorly along the length of the cord. This gave a pressure profile at discrete points along the anterior of the cord, Figure 8-5. The major limitation with this transducer is that only contusions at discrete points on the anterior side were captured. Also with some of the ten specimens, the pressure transducers were saturated.

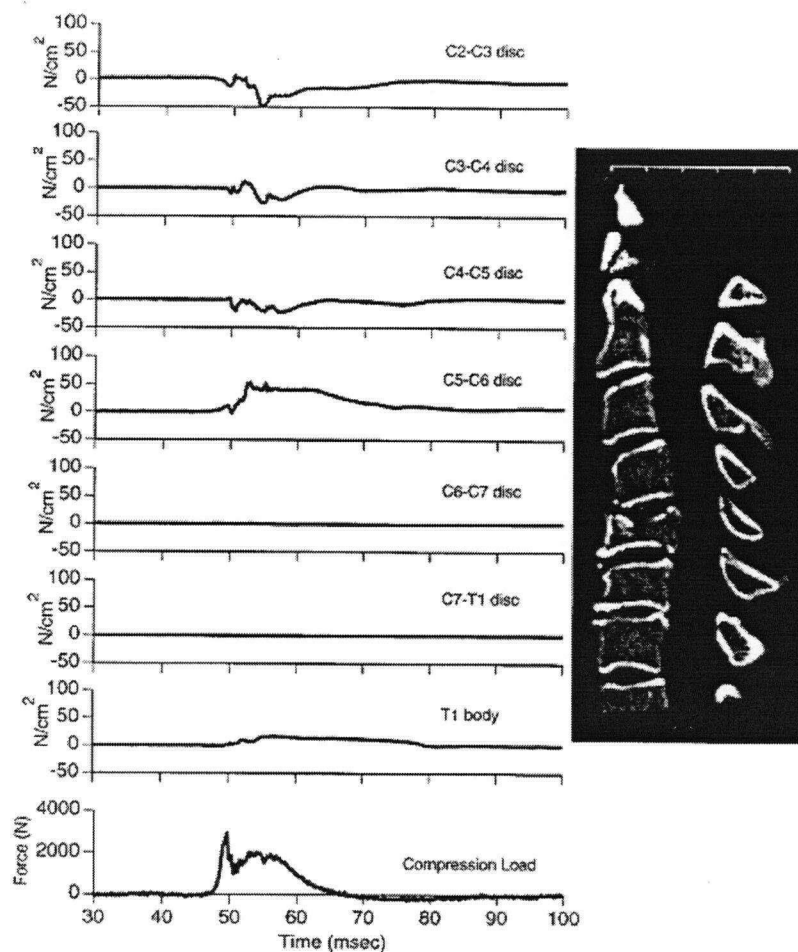
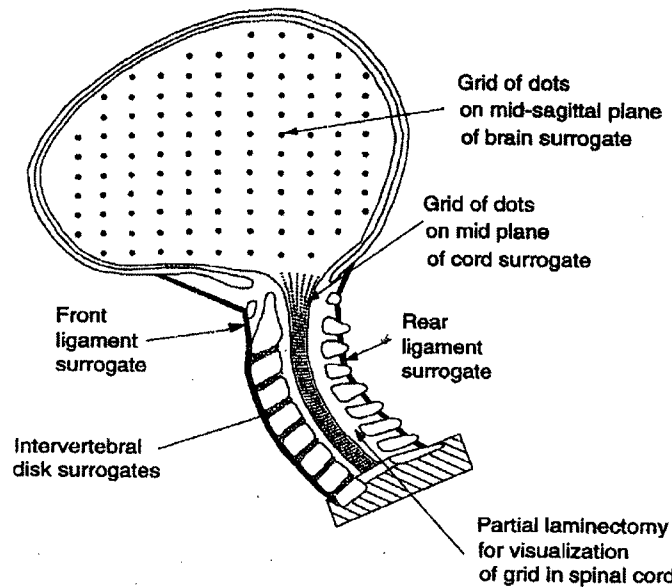


Figure 8-5: Typical pressure trace recordings from the instrumented surrogate spinal cord developed by Pintar and colleagues<sup>8</sup>

Bilston and colleagues' surrogate cord was silicone gel with a grid of black markers. This was placed in the spinal canal and cranial cavity of a plastic spine and skull model, Figure 8-6. The surrogate cord was visible through a partial laminectomy. The marker motion was recorded using a high speed digital camera (1000fps). Only hyperflexion and extension motions were simulated in this study. This set up is inappropriate for axial impact as the bony structure is compromised by the laminectomy.





Reprinted with permission from ISSN#1358-8265 © 1997 Woodhead Publishing Limited

Figure 8-6: Bilston and colleagues' spine and skull model with the surrogate spinal cord<sup>10</sup>

### 8.2.1 Goals

The results of these previous studies have not yielded a complete longitudinal profile of spinal cord compression and deformation during injury. Visualization of the cord's longitudinal profile during these injury events would provide information regarding the patterns of spinal cord deformation. The goals of this section of this study were to develop a methodology to visualize and measure spinal cord deformation resulting from common cervical spine bony injuries experienced during axial head to ground impact, and to simulate the bone-cord interface of the model by using a surrogate cord with *in vivo* like properties. This insight into cord deformation could be used to improve biofidelity of animal studies examining injury at a cellular level by providing real life impact characteristics; assess the performance of injury prevention devices; and provide information for clinicians on the transient deformation of the cord associated with various injury modes.

## 8.3 Materials and Methods

### 8.3.1 Specimens Preparation

Six human cadaveric cervical spines (occiput to T2) were prepared for impact testing, Figure 8-7. Each specimen was dissected free of muscle tissue while preserving the

osteo-ligamentous structures. The spinal cord and dura mater were removed from the canal. The transverse processes of C3-C7 were removed to allow anterior access to the lateral masses for preload guides, Chapter 5. Care was taken to ensure that the guide screws did not disrupt the facet joints. Four photoreflective marker pins were inserted into the vertebral bodies and lateral masses at each level between C2-C7 for kinematic analysis. The T1 and T2 vertebrae were mounted in dental stone such that the C4-C5 disc was horizontal while the neutral posture lordosis of the spine was maintained. The addition of a follower preload simulated musculature to improve the biofidelity of the kinematic response to the axial impact. A surrogate head with inertia, mass and head shape properties that match those of the human head was mounted to the occiput, see Appendix D for more details.

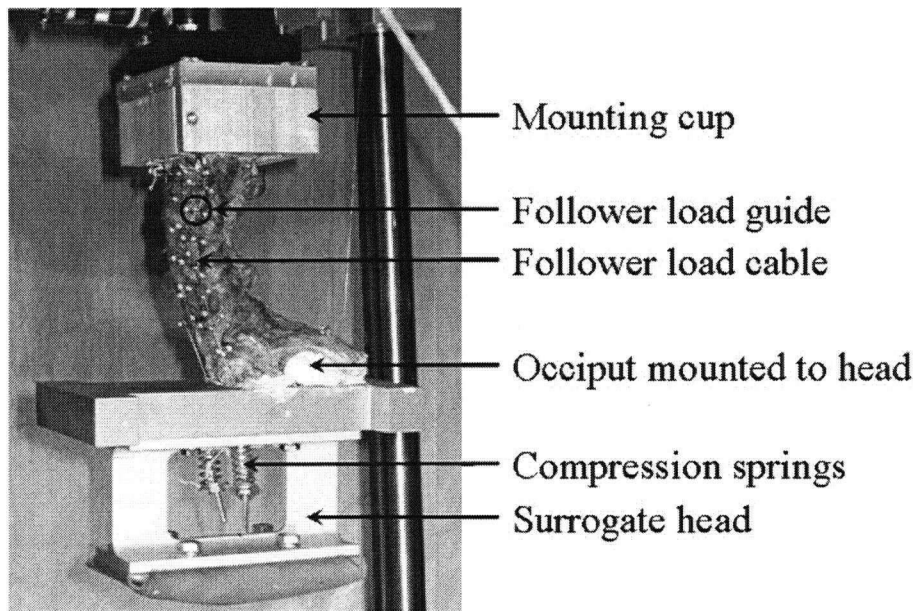


Figure 8-7: Specimen prepared for testing with follower load, surrogate head, and markers in place

### 8.3.2 Surrogate Spinal Cord

To visualize the spinal cord in the canal a high speed x-ray setup was used, Chapter 6. As the natural spinal cord is not radiodense and does not maintain its material properties after death,<sup>11</sup> the x-ray was paired with a radiodense surrogate spinal cord. The biofidelic surrogate spinal was developed by Reed.<sup>12</sup> The surrogate cord was made from an elastomeric gel (QM Skin 30, Quantum Silicones). This is a two part gel that sets within

24 hours. This material was found to have similar material properties to the *in vivo* canine and feline spinal cord in quasistatic tension and transverse compression. However the material has not been matched for viscoelastic effects in transverse impact. Although silicone is radiodense, its atomic number is very close to that of bone, which makes it difficult to differentiate the materials in a radiographic image. Barium sulphate ( $\text{BaSO}_4$ ) was added to the QM Skin to increase the radiodensity of the surrogate cord. Several concentrations of barium sulphate were tested to find the minimum concentration needed to provide sufficient contrast in the high speed x-ray. A concentration of  $275 \text{ mgBaSO}_4/\text{mL}_{\text{QM Skin}}$  was used. One of the major uses of QM Skin is in the film industry as a material for facial prostheses because it can hold a powdered pigment without losing its ability to set. The surrogate cord material properties in quasi-static tension and transverse compression were reassessed to ensure that the addition of the  $\text{BaSO}_4$  did not change them.<sup>13</sup>

The methods used to construct the cord were adapted from Reed.<sup>12</sup> The final cord was trimmed to have an oval profile with diameters of 12 mm transversely and 6 mm sagittally to match the physiology of the cord *in vivo*.<sup>14</sup> Its length was 17 cm, which was sufficient to fill the spinal canal of the embedded specimen. The dura mater and cerebral spinal fluid were left out of this model, as the methods of simulating these structures had not been fully developed at the time of this experimental work. The nerve roots and tethering ligaments were also not modeled.

### 8.3.3 High Speed X-ray

High speed cineradiography was used to observe the surrogate cord during injury in the sagittal plane. This setup was composed of a high powered industrial x-ray source (Philips MG-160 generator with Comet MXR-160 tube) and image intensifier (PT93XP43, Precise Optics) with an internally mounted high speed digital camera (Kodak Ektapro). The tube was set 0.4 m from the specimen and the image intensifier was 0.2 m from the specimen. The machine was run at 75 kV and 5 mA. The images were captured at 1000 fps. See Chapter 6 for more details about this system.

### 8.3.4 Drop Tower and Procedure

Axial impact was applied using a four shaft, self supporting drop tower with a light-weight carriage as described in Chapter 2. The carriage weight approximated the upper

torso weight of a cadaver specimen (~15 kg). The cervical spine specimens were mounted to the carriage in an inverted orientation such that when the carriage was released head-first impact occurred against the impact platen. Prior to head impact, the specimens had a neutral posture with physiologic lordosis due to the application of a follower load to the spine that was applied to simulate pre-impact muscle forces. A drop height of 0.6 m was used to obtain an impact velocity of 3 m/s.

The x-ray machine exposure settings were determined prior to the carriage being raised to ensure adequate exposure levels. The machine was switched on once the carriage was raised to the desired drop height. The high speed digital cameras, including the one associated with the high speed x-ray system were triggered by a simple electromechanical switch that was activated approximately 10 cm before impact as the carriage dropped. This allowed the first frames of the high speed digital cameras and high speed x-ray to be synchronized.

### 8.3.5 Analysis

The deformation of the surrogate spinal cord was measured at intervals of approximately 1.5mm along the length of the cord by digitizing each of the high-speed cineradiograph images with a precision digitizing tablet and image analysis software (ImageJ, National Institute of Health, USA), Figure 8-8. Landmarks on the bony anatomy were used to establish measurement regions where the number of measurements was kept constant throughout the analysis. Where the cord and spine were elongated, the distance between measurement intervals was increased to keep the number of measurements consistent throughout the event. Where longitudinal compression was seen, the spacing was decreased. The distance between the measurements was also measured and recorded. Transverse (anterior-posterior) compression was reported as a percentage based on the initial sagittal diameter of the cord as measured in the first radiograph of the sequence prior to any deformation. The first frame of the measured sequence was defined as the frame occurring right at impact. Measurement of the cord diameter was repeated in each frame until the cord diameter reached a steady state. Velocity of cord deformation was determined using the initial mathematical tangent modulus of the cord deformation curve along the straightest portion of the curve at the location of maximum injury. The viscous response was the product of velocity and compression as defined by Kearney and

colleagues.<sup>2</sup> Injury mode was determined by the external high speed video footage and from diagnosis by a spine surgeon (E.I.) upon examination of the specimens.

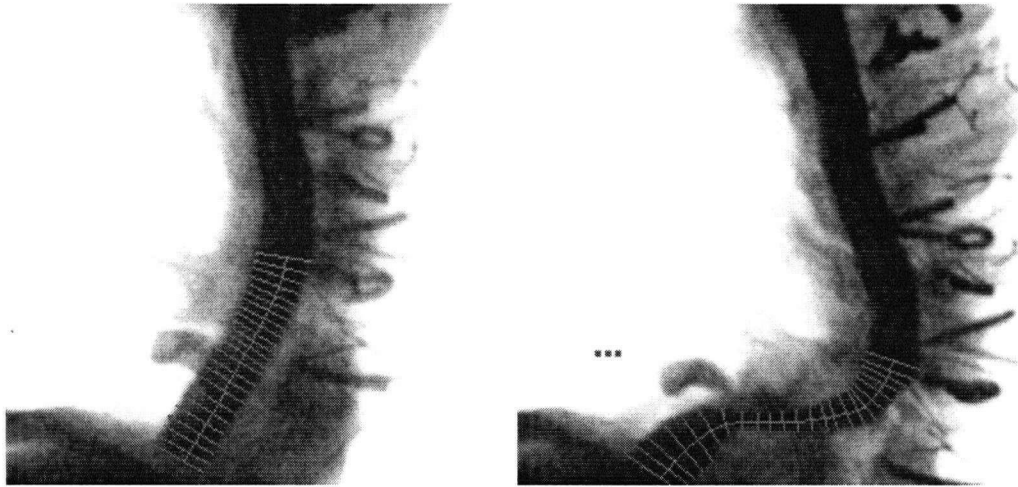


Figure 8-8: Example of two frames from the same specimen (the first frame on the left and one from maximum deformation on the right) during analysis of cord deformation showing transverse measurements of the deformation and the longitudinal measurements

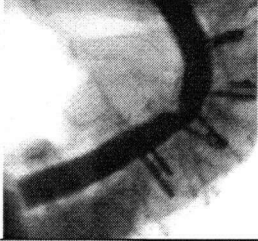
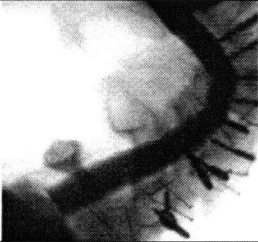




## 8.4 Results

### 8.4.1 Spinal Cord Deformation

A variety of injuries were seen in the 6 drop tests. Table 8-1 lists the specimens with their primary injury and characteristics of the maximum deformation. Further details of the injuries can be found in the results of Chapter 7. The images shown in Table 8-1 correspond to the time of maximum compression of the cord.

The cord deformation at the maximum compression during the atlantoaxial (AA) dislocation type injuries (N=2) resulted in a much larger deformation in comparison to the hyperextension (N=3) and fracture-dislocation type (N=1). The average maximum transverse compression was 49% ( $\pm 18.3\%$ ). The average length (cranial-caudal) of the compression of all 6 specimens was 12.2 mm ( $\pm 9.6$  mm). However when the AA dislocations were disregarded the average fell to 6.5 mm ( $\pm 1$  mm). In all six specimens the final deformation of the cord in terms of transverse compression was zero. Inspection of the specimens by dissection showed that while there was evidence of trauma to the bony structures there was no residual canal encroachment.

Table 8-1: Summary of the bony injuries modes and the associated spinal cord deformation as seen at the maximum compression

Specimen	Primary Injury	Deformation Pattern	Percent Compression (Max)	Length of Compressed Area
H1091	Hyperextension about C4/5		50%	6.5 mm
H1177	Hyperextension about C5/6		36%	5.1 mm
H1184	Hyperextension about C4/5		19%	6.7 mm
H1096	Atlantoaxial dislocation		53%	17.7 mm
H1183	Atlantoaxial dislocation		78%	29.5 mm
H1116	Fracture dislocation at C3/4		58%	7.7 mm

Hyperextension injuries were the most common injury mode. The deformation during these hyperextension injuries was typically a small concave indent on the posterior surface of the cord which compressed the cord at its apex to no more than 50%. This was in keeping with the pinch mechanism of injury associated with hyperextension injuries clinically. The length of this defect was at most 6.7 mm. Injury modes associated with hyperextension about an intervertebral disc resulted in a more acute insult to the spinal cord. In all three specimens that suffered this mode, the trauma was inflicted by the posterior elements of the inferior vertebra at the level of the body of the superior one. For example, hyperextension about C4/5 would result in trauma to the cord at the level of the body of the C4 vertebra by the posterior elements of C5.

The next most common mode seen in this study was the atlanto-axial dislocation. One of the specimens classified by this mode has the largest defect in terms of percent of compression and length of the deformed region. The other saw less transverse compression and had a length of almost half the first which was still longer than seen in the specimens associated with other injury modes. The cord deformation associated with the AA dislocation mode seems to be sensitive to severity of this dislocation. Further examination of the specimen's injuries and the video footage is needed to determine the severity of the dislocations in these two specimens. Initial observations indicated that the specimen first discussed here did in fact suffer a more severe dislocation injury.

The bony insult in this mode was the result a distraction type motion of the C2 vertebra. The C2 vertebral body moved anteriorly which caused the posterior elements to pull the cord anteriorly as well. Since C1 and, to an extent, the subaxial spine have not moved, the cord is pulled into a U-shape towards the anterior. This is more evident in the less severe dislocation of H1096. Further deformation of the cord in H1183 is the result of the cord being pulled over the anterior arch of C1. It was thought that the cord in these cases also was deformed in axial tension due to the elongation of the path of the canal as a result of the distraction. With this surrogate model we were unable to confirm this as fiducial markers were not incorporated to allow longitudinal deformation measurements.

The last injury mode seen was the fracture dislocation. This mode is a combination of the previously discussed modes. There was only one specimen in this classification. As with the hyperextension modes the deformation was an indentation to

the posterior surface of the spinal cord by the posterior elements of the inferior vertebra. The difference appears to be that the extent of compression and length of the indentation is greater than with hyperextension. This appears to be due to the anterior motion of the vertebra as it dislocates.

#### 8.4.2 Spinal Cord Compression Time Course

Table 8-2 summarizes the characteristics of each deformation including the maximum compression and time specific compression values. More specimens are needed to be able to make conclusions about the relationships between injury mode and the pattern of deformation of the spinal cord. The transverse compression profiles along the length of the surrogate cord for the time course of the injury for each specimen are shown in Figure 8-9 through Figure 8-14 as three-dimensional surface plots. Note that the distance axis is the distance along the cord about the point of maximum compression with the positive distances in the cranial direction and the negative in the caudal direction. The negative compression values are indicative of twisting or longitudinal compression of the cord within the canal during injury. Both of these can cause the cord to appear wider than it actually is.

Table 8-2: Deformation characteristics

<b>Specimen</b>	<b>Injury Mode</b>	<b>Percent Compression (Max)</b>	<b>Time to Max.</b>	<b>Time spent at &gt;10% of Max</b>	<b>Time spent at &gt;75% of Max</b>
H1091	Hyperextension	50%	11 ms	23 ms	5 ms
H1177	Hyperextension	36%	8 ms	23 ms	1 ms
H1184	Hyperextension	19%	11 ms	21 ms	2 ms
H1096	AA Dislocation	53%	15 ms	24 ms	6 ms
H1183	AA Dislocation	78%	14 ms	29 ms	21 ms
H1116	Fx Dislocation	58%	15 ms	31 ms	9 ms
<b>Average (STD)</b>		<b>49% (18.3%)</b>	<b>12.3 ms (2.8 ms)</b>	<b>23.5 ms (6.1 ms)</b>	<b>7.3 ms (7.3 ms)</b>

The three specimens classified as hyperextension injury had the smallest deformation lengths and the least amount of compression. The time courses of the three specimens were very similar, Figure 8-9 through Figure 8-11. All three specimens spent less than 5 ms at more than 75% of the maximum compression and 23 ms at more than 10%. The time to maximum was also very similar in all three specimens. In some of the



specimens an enlargement of the cord caudal to the point of injury could be seen. This could be attributed to the shortening of the canal which could compress the surrogate cord lengthwise or cause it to twist.

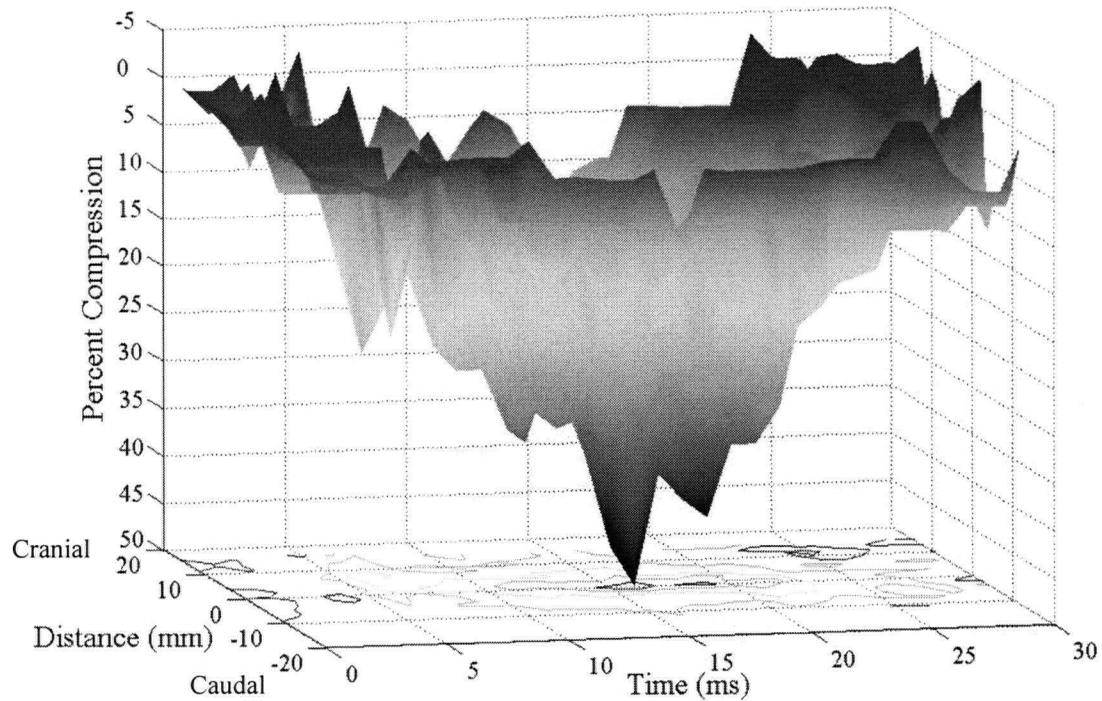


Figure 8-9: Time course plot of spinal cord deformation of specimen H1091

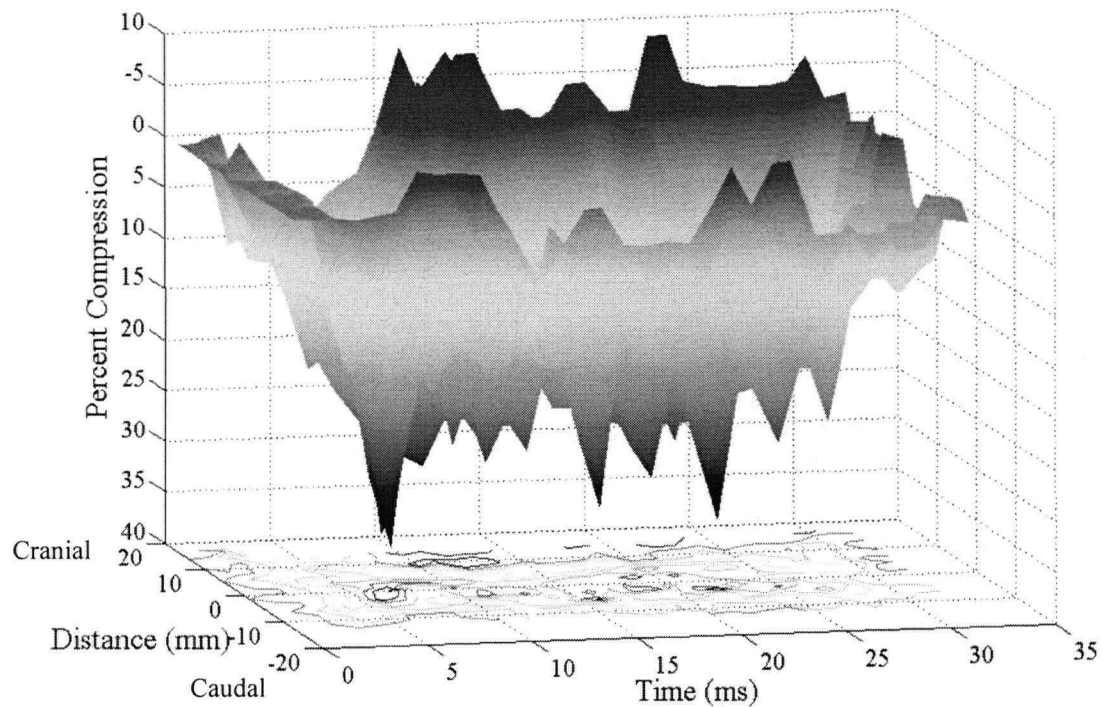


Figure 8-10: Time course plot of spinal cord deformation of specimen H1177

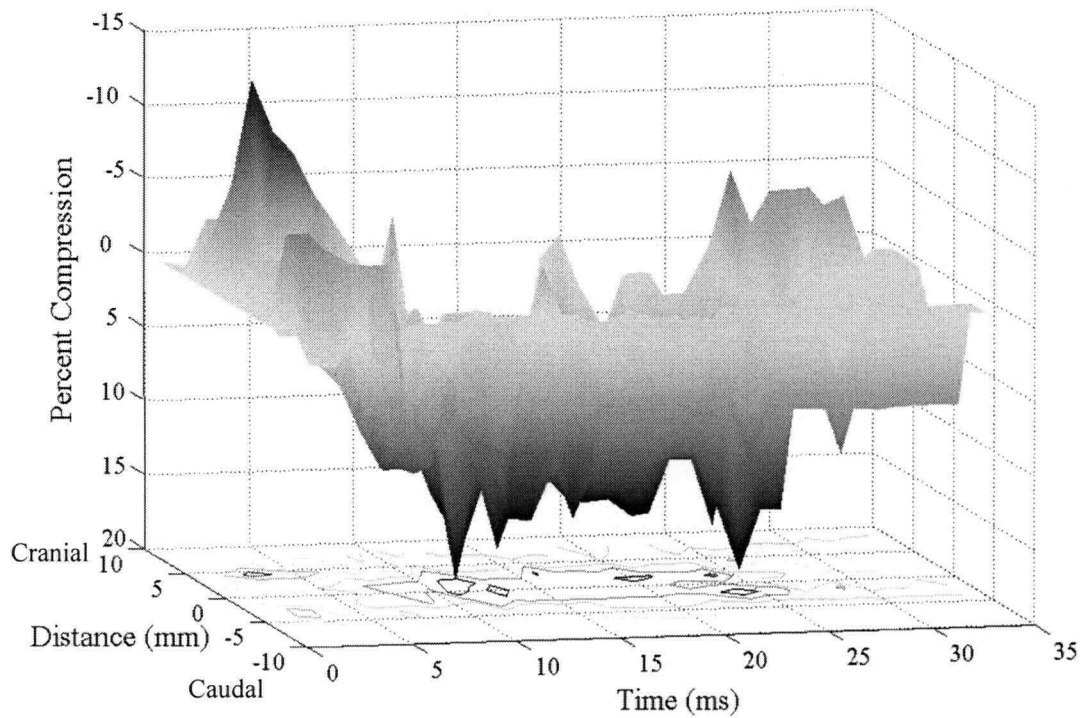


Figure 8-11: Time course plot of spinal cord deformation of specimen H1184

The atlantoaxial dislocations had smoother three-dimensional time course surface than the hyperextensions, Figure 8-12 and Figure 8-13. These specimens spent more time at greater than 75% compression than the hyperextension and slightly more time with more than 10% compression. These specimens took the longest to reach maximum compression. Specimen H1183, Figure 8-13, had a longer time of compression with 29 ms spent with more than 10% compression in comparison with 21 ms for specimen H1096.

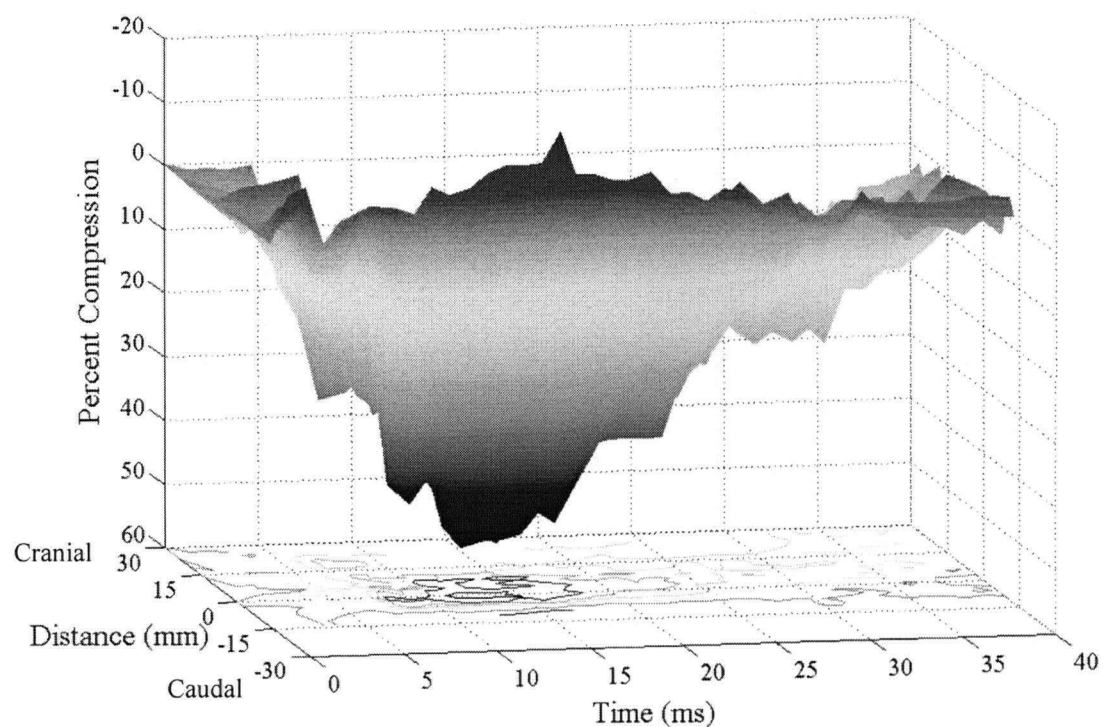


Figure 8-12: Time course plot of spinal cord deformation of specimen H1096

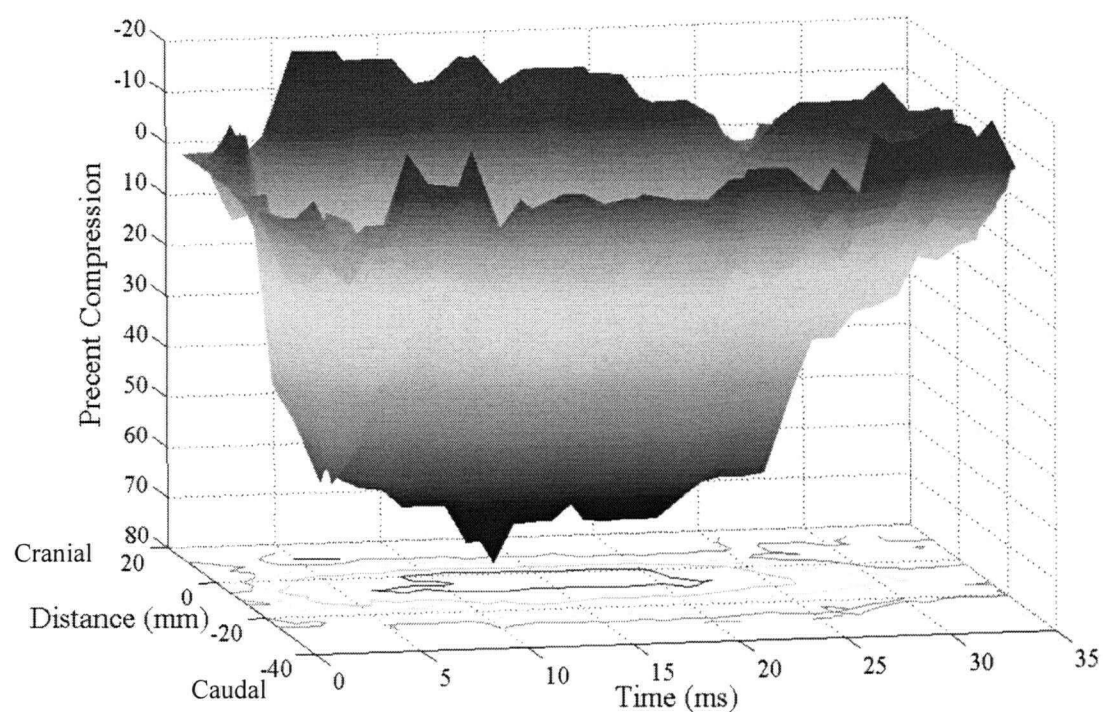


Figure 8-13: Time course plot of spinal cord deformation of specimen H1183

There was only one specimen with a fracture dislocation injury, Figure 8-14. This specimen spent the most time in a compressed state, 31 ms. However when it's profile is compared to that of specimen H1183 it is clear that the degree of compression was more severe in the AA dislocation as this specimen spent 21 ms at greater than 75% compression and only 8 ms between 10% and 75%. Specimen H1116's long compression time appears to be evidence of a slower recoiling action of the bony anatomy.

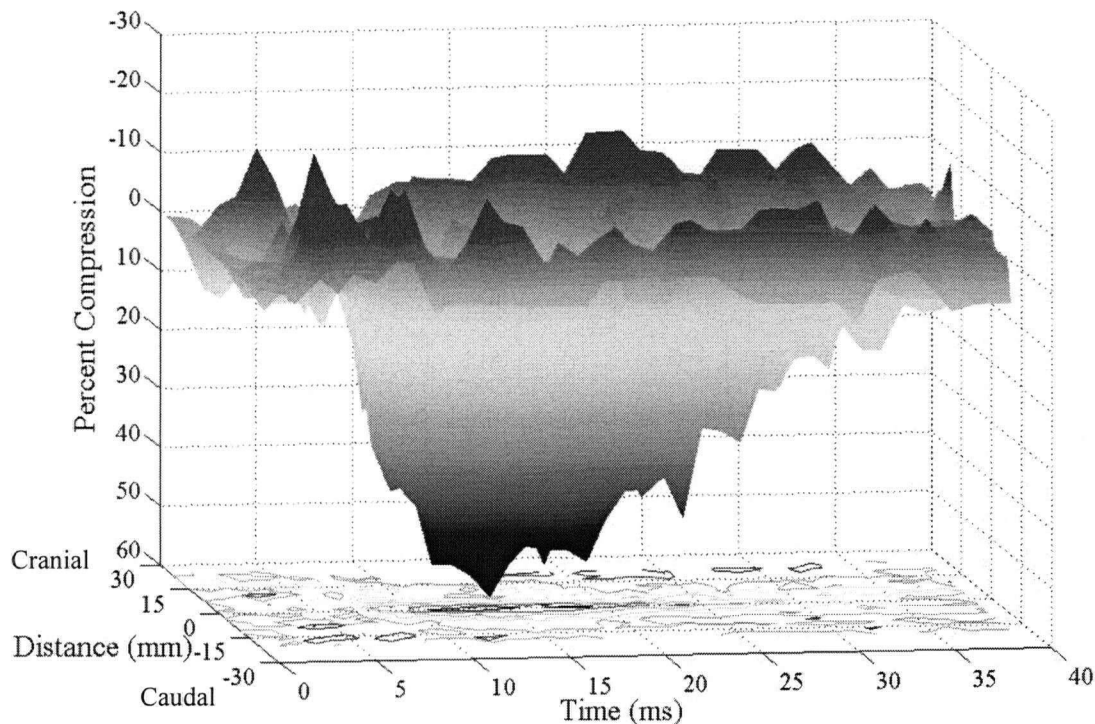


Figure 8-14: Time course plot of spinal cord deformation of specimen H1116

The velocity of spinal cord injury was determined from the descending portion of the above surfaces. The curve at the point of maximum compression in the distance axis was used. The tangent of the straightest part of the descending portion was determined to be the velocity of impact. These velocities are summarized in Table 8-3. The viscous response of the cord to impact was calculated by multiplying these velocities by the maximum compression of the cord. Probability of recovery from neurological trauma has found to have the best correlation with the viscous response.<sup>2</sup> The probability of any recovery, as determined by Kearney and colleagues, associated with the calculated viscous response is also given in Table 8-3.

Table 8-3: Velocity of the cord compression and viscous response of the cord to impact

Specimen	Compression	Velocity (m/s)	Viscous response (m/s)	Probability of any recovery <sup>2</sup>
H1091	50%	1.2 m/s	0.6 m/s	85%
H1177	36%	1.1 m/s	0.4 m/s	92%
H1184	19%	0.3 m/s	0.06 m/s	95%
H1096	53%	5 m/s	2.7m/s	8%
H1183	78%	2.4 m/s	1.9/s	25%
H1116	58%	1.8 m/s	1 m/s	75%

#### 8.4.3 Spinal Kinetics and Cord Injury

As only 6 specimens were tested in this project, definite conclusions cannot be made. However we can examine the data for patterns. Table 8-4 gives the peak axial response at the neck, some select cord deformation values and the time to the occurrence of these values. There appears to be no relationship between the time of peak axial force at the neck and the time of maximum transverse cord compression. When the maximum compression of the cord was plotted against the maximum axial response at the neck, Figure 8-15, relationships between the values via the injury mode can be identified. That is, the injuries that were associated with high peak loads (dislocations at AA and lower on the cervical spine) had the greatest transverse compression of the cord. The hyperextension injuries had a lower peak axial force and less cord deformation.

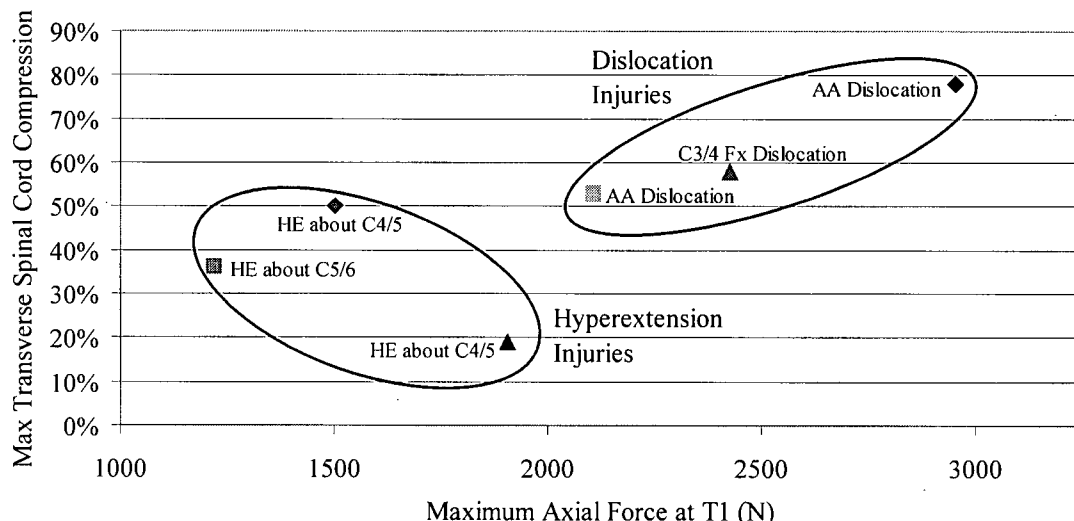


Figure 8-15: Maximum cord compression versus maximum axial response at the neck during impact to illustrate their relationship via injury mode

Table 8-4: Summary of axial impact characteristics and cord deformation characteristics

Specimen	Associated Injury Mode	Maximum $F_y$ at T1/2	Time to Maximum $F_y$	Time to "Maximum" Column Deformation	Percent Compression (Maximum)	Length of Compressed Area	Time to Max Compression
H1091	Hyperextension about C4/5	1502.0 N	4.00 ms	12 ms	50%	6.5 mm	11 ms
H1177	Hyperextension about C5/6	1220.2 N 1599.0 N	4.95 ms 9.28 ms	12 ms	36%	5.1 mm	8 ms
H1184	Hyperextension about C4/5	1905.9 N	5.53 ms	14 ms	19%	6.7 mm	11 ms
H1183	Atlantoaxial Dislocation	2950.7 N	8.14 ms	14 ms	78%	29.5 mm	14 ms
H1096	Atlantoaxial Dislocation	2105.4 N	2.74 ms	12 ms	53%	17.7 mm	15 ms
H1116	Fracture Dislocation at C3/4	2426.2 N	5.21 ms	13 ms	58%	7.7 mm	15 ms
<b>Averages</b>		2018.4 N	5.10 ms	12.8 ms	49% (18.3%)	12.2 mm (9.6 mm)	12.3 ms (2.8 ms)

## 8.5 Discussion

This section of the project focused on developing a method of visualizing the spinal cord deformation in the canal while preserving the biofidelity of the bone-cord interface. To do so, a high speed x-ray set up was paired with a radiodense biofidelic surrogate spinal cord. The cord showed clearly against the bone allowing for measurement of the deformations. The surrogate cord used was the most recent model that had been developed in our laboratory. Although not an identical material match, it was felt that this model provided the most biofidelic interface at this time. Using the biofidelic cord allowed the bone-cord interaction to be as close to *in vivo* conditions as possible in an *in vitro* model. The high speed x-ray allowed for visualization of the cord within the canal at 1000fps. The output of this system was cineradiographic footage of the cord deformation from which the cord deformation can be measured and characterized.

The use of a biofidelic surrogate cord model addressed a limitation of many of the previous studies on canal occlusion. Namely the issues surrounding the bone-transducer interface. The majority of the previously developed transducers did not attempt to match the material properties of the *in vivo* spinal cord.<sup>9, 3-5</sup> As the bone encroaches into the canal space the transducer would resist its motion. If this resistive response is not similar to the interface between the bony and spinal cord, the resulting motion of the bone such as its recoil action would be unrealistic. Wilcox and colleagues' approach does not use a transducer, which eliminates this issue. However since the motion of the bony anatomy is not resisted their method may overestimate the canal occlusion and possible cord compression.

The use of a surrogate cord based transducer that is designed to mimic the material response of the *in vivo* spinal cord addresses these issues. Bilston and colleagues' surrogate cord model<sup>10</sup> was not appropriate for use in an impact study as it was not radiopaque and tended to be brittle. Pintar and colleagues' model did not provide a continuous sagittal profile of spinal cord deformation as was desired in this work.

The biofidelic surrogate cord used in this study was felt to be the most biofidelic available at the time of testing. It had been matched for *in vivo* spinal cord material properties in tension and quasistatic transverse compression. However it had not been matched for viscoelastic transverse compression. Missing in the model used in this study

were the dura mater and cerebral spinal fluid. It has been shown that these structures affect the impact response of the cord.<sup>12</sup> However the methods to include these structures in our model had not been fully developed at the time of testing. Also missing were the nerve roots and tethering ligaments, which limit the migration of the spinal cord in the canal. Migration of the cord can be seen in the cineradiography footage before and after injury. However the compression of the cord by the bony anatomy “pins” the cord in place eliminating this motion during injury.

Comparison with other studies on cord deformation and canal occlusion is difficult. This work did not focus on one particular injury whereas the others did, namely burst fracture injuries.<sup>9, 4, 15</sup> Since none of our specimens suffered burst fractures during the impact event comparison of the results of this and previous studies is difficult.

The work by Pintar and colleagues is most comparable to our results.<sup>8</sup> Their transducer measured the pressures applied at discrete positions along the cord’s anterior surface. However as evidenced by our results, the posterior elements may cause the most drastic deformations while the anterior surface of the cord is pushed against the anterior wall of the canal. During hyperextension the deformation is small and localized. Using Pintar and colleagues’ approach this type of cord deformation would have been missed or underestimated. The larger atlanto-axial dislocation spinal cord deformations would have been detected by several of their sensors. However the axial elongation would not have been identified as it was in the x-ray footage. Pintar was able to obtain several flexion type injuries and reported the protrusion of the anterior elements of the vertebra into the canal, which is opposite to our extension type injuries. In these cases their sensor placement was more suitable.

Overall, our results agree with previous studies’ hypotheses that transient canal occlusion is more significant than the residual occlusion. However unlike the past studies where there was some degree of post-traumatic occlusion, none of our specimens had any despite the range of injuries. The sample size in this study was too small to make any definitive conclusions about the relationship between bony injury mode and spinal cord deformation.

The probability of any recovery associated with the measured spinal cord deformation and viscous response allows for translation of these experimental results into



clinical measures of effects of neurological trauma. Kearney and colleagues study impacted *in vivo* spinal cord tissue between the C6 and C7 vertebrae by a controlled impact mechanism and assessed the recovery of the animal after injury.<sup>2</sup> The velocities and compressions measured in our specimen correlate to those used in their study further confirming the clinical relevance of these injuries.

#### 8.5.1 Limitations

This study used a novel set up of a surrogate spinal cord and high speed x-ray to measure spinal cord deformation during dynamic head to ground impact. This approach yielded the desired information however there were several limitations and issues raised that need to be addressed in any future work with this system. These limitations are listed here along with suggested solutions.

- ◆ Only one dimension was recorded. To fully illustrate cord deformation multiple views are needed. The introduction of another high speed x-ray setup would create a biplanar x-ray set up which could provide a three dimensional representation of the event.
- ◆ While the cord was the most state of the art currently available it had not been fully matched for viscoelastic transverse compression although this material property had been assessed during its development. Further development of the cord to improve its response to dynamic transverse compression and to include the dura mater and cerebral spinal fluid in its construction would improve the biofidelity of the interaction. The current cord model may tend to overestimate the cord compression and velocity of compression as it lacks these outer layers.
- ◆ The surrogate cord is not anchored in the canal. The real spinal cord is anchored by the nerve roots and various tethers. This leaves the potential for error in sagittal diameter due to twisting and motion of the surrogate cord within the canal.
- ◆ The cord appears as a solid mass in the canal which makes longitudinal deformation impossible to quantify. The possibility of using fiducial markers needs to be considered and tested.

## 8.6 Conclusion

To fully assess the relationship between bony and cord injuries in the cervical spine and to make conclusions about the patterns of inflicted deformation, more specimens need to be studied. These limited results indicate the following patterns:

- ♦ Dislocations at the upper levels of the spine were associated with the largest region of deformations and have the potential to inflict the greatest transverse compression.
- ♦ Hyperextension injuries resulted in the smallest regions of deformation but could suffer a wide range of amounts of transverse compression.

These results were in agreement with the conclusions of previous works that residual compression of the cord is not indicative of the maximum compression seen during the injury event. However, no burst fractures were captured so side-by-side comparison to previous results could not be made.

Additionally, when the axial reaction force at the neck is considered, a trend between axial force and cord compression via the injury type. The dislocation type injury tended towards the greater axial forces and greater deformations whereas the hyperextension injuries tended toward the lesser loads and less severe deformations. In considering the probability of recovery associated with the viscous response of the cord it could be seen that the dislocation type injuries resulted in a smaller probability than the hyperextension type.

## 8.7 References

1. Kwon, B.K., T.R. Oxland, and W. Tetzlaff. Animal models used in spinal cord regeneration research. *Spine*, 2002: 27(14): p. 1504-10.
2. Kearney, P.A., et al. Interaction of Contact Velocity and Cord Compression in Determining the SEverity of Spinal Cord Injury. *Journal of Neurotrauma*, 1988: 5(3): p. 187-208.
3. Chang, D.G., et al. Geometric changes in the cervical spinal canal during impact. *Spine*, 1994: 19(8): p. 973-980.
4. Panjabi, M.M., et al. Dynamic canal encroachment during thoracolumbar burst fractures. *J Spinal Disord*, 1995: 8(1): p. 39-48.
5. Raynak, G.C., et al. Transducers for dynamic measurement of spine neural-space occlusions. *Journal of Biomechanical Engineering*, 1998: 120(6): p. 787-791.
6. Wilcox, R.K., et al. A dynamic study of thoracolumbar burst fractures. *J Bone Joint Surg Am*, 2003: 85-A(11): p. 2184-9.
7. Wilcox, R.K., et al. Measurement of canal occlusion during the thoracolumbar burst fracture process. *J Biomech*, 2002: 35(3): p. 381-4.
8. Pintar, F., et al. Cervical Spine Bony Injury and the Potential for Cord Injury. in *Proceedings of the 5th CDC Symposium for Injury Prevention*. 1995
9. Carter, J.W., et al. Canal geometry changes associated with axial compressive cervical spine fracture. *Spine*, 2000: 25(1): p. 46-54.
10. Bilston, L.E. and L.E. Thibault. Biomechanics of cervical spinal cord injury in flexion and extension: a physical model to estimate spinal cord deformations. *International Journal of Crashworthiness*, 1997: 2(2): p. 207-218.
11. Oakland, R.J., et al. The biomechanical response of spinal cord tissue to uniaxial loading. *Proc Inst Mech Eng [H]*, 2006: 220(4): p. 489-92.
12. Reed, S.G., *The Human Spinal Cord: An Improved Surrogate Model*, in Department of Mechanical Engineering, Univeristy of British Columbia: Vancouver, Canada. 2005.
13. Jones, C.F. and A. Saari, QM Skin30 Surrogate Cords with BaSO4 - quasistatic tensile and compressive properties: unpublished data. 2006.
14. Kameyama, T., Y. Hashizume, and G. Sobue. Morphologic features of the normal human cadaveric spinal cord. *Spine*, 1996: 21(11): p. 1285-90.
15. Wilcox, R.K., et al. A dynamic investigation of the burst fracture process using a combined experimental and finite element approach. *Eur Spine J*, 2004: 13: p. 481-488.

## **Chapter 9: Conclusion**

### **9.1 Summary**

The overall goal of this project was to quantify the deformation of the spinal cord and the response of the cervical spine to axial head first impact in the presence of simulated musculature. This project was divided into two main studies: the effect of simulated musculature on the response of the cervical spine to axial impact and the deformation of the spinal cord during cervical spine injury during axial impact. Six human cadaveric cervical spines (occiput to T2 inclusive) were axially impacted in a head first drop test. A drop tower was used to simulate head to ground impact. Musculature was simulated using a physiologic follower preload. Two high speed digital cameras were used to capture the response of the cervical spine during the impact. Markers on the spine were used to reconstruct three dimensional motion of the spine. The force and moments at T1 of the specimen were recorded as was the axial reaction force at the impact platen. The spinal cord deformation was quantified using a high speed x-ray set up and a biofidelic radiodense surrogate spinal cord.

### **9.2 Spinal Column Response and Cord Injury**

The two focuses of this work were on the spinal column kinematics in the presence of a follower preload and cord deformation during axial injury. The major conclusions found in each focus studies are summarized here with respect to the goals and hypothesis set for each.

#### **9.2.1 Spinal Column Response in the Presence of Physiologic Preload**

Follower preload methodologies have been developed to simulate the effects of musculature in biomechanical testing. However, the use of follower preload in an axial head first impact had not been done before. It was hypothesized that the addition of a follower preload would eliminate the snap through and complex buckling patterns seen in previous axial impact tests. Analysis of the high speed digital camera footage and reaction load traces confirmed our hypothesis.

### 9.2.2 Spinal Cord Deformation during Injury

The second major study (Chapter 8) presented the results from a novel method of visualizing and quantifying spinal cord deformation during axially induced spinal injury. The goals of this study were to obtain a continuous sagittal profile of the cord during injury and to find relationships between cord deformation, injury, and other injury parameters such as reaction forces. This was the first study of its kind to provide direct visualization of the spinal cord during an impact event. The resulting cord deformations and compression velocities were compared to existing *in vivo* experimental data to assess the clinical relevance of the induced injuries and the expected neurological outcomes of such injuries in real life.

The six specimens that were tested in this initial study provided too small a sample size to draw definite conclusions but the following patterns emerge:

- Hyperflexion injuries resulted in smaller deformation areas and transverse compressions in the spinal cord. The expected neurological outcome had a high probability of recovery
- Dislocation (both in the upper and lower cervical spine) injuries were found to have greater transverse compressions. The expected neurological outcomes were dependant of location and severity of the dislocation
- Atlantoaxial dislocations had larger areas of deformation and the lowest probability of recovery in the neurological outcome assessment.

## 9.3 Apparatus Performance Evaluation

The apparatus and procedures developed to complete these studies were discussed in Chapters 2 through 6 of this manuscript. Their performance in the two focus studies will be discussed here.

### 9.3.1 Drop Tower

The drop tower provided adequate velocity to induce injury in all 6 specimens tested. The drop height used during testing was established during development and had been determined to provide the required 3 m/s. As higher order kinematics (i.e. velocity and acceleration) from motion capture systems such as cameras are unreliable, the exact velocity of the carriage at impact was not calculated from the high speed footage.

During the initial stages of protocol development it was found that the drop tower would move with large impacts. Additional weights had to be added to the base to prevent motion as permanent fixation to the floor was not possible. Upon impact the carriage was allowed to descend an additional 2.5 cm before being arrested by stoppers. This was to prevent overdriving of the specimen. The carriage did rebound slightly upon impacting the stoppers. The second impact was non injurious in all specimens and was not analyzed.

The following recommendation for improvement will enhance the performance and usability of the drop tower.

- Instrumentation should be added to the carriage to measure acceleration and to determine velocity at impact.
- New stoppers which are more robust and easier to adjust are needed.
- A new method of arresting the carriage upon rebound and preventing this second impact is needed.

### 9.3.2 Cervical Spine Motion

Kinematic analysis of the marker motion data (i.e. Euler angles) from this study has not been completed. The relative motions of the pins were used to assess the response of specimen to impact and to determine whether buckling occurred. This was sufficient for this purpose. The kinematics was needed to provide grounds for comparison to assess the performance of preventative devices and to compare the effect of the presence of physiologic follower preload on specimen response to the response of non preloaded specimens.

The following suggestions should be considered to improve the accuracy of the three dimensional reconstruction and subsequent kinematic analysis.

- Assess the effect of relative camera placement on accuracy
- Assess the accuracy of the marker tracking software using a known three dimensional complex motion.

### 9.3.3 Kinetic Data Acquisition

For several of the specimens the axial load cell at the impact platen was saturated. Though a similar study was used to specify the load cell, the higher data collection rate of our study allowed for more data points to be taken at the time of the initial impact

impulse. Thus our system was able to capture a greater peak force. The actual maximum is secondary to the time profile the load cell provided. The duration of the impact was still calculable. An accelerometer array is needed in the surrogate head to calculate the impulse of the impact and to confirm the impact velocity.

At T1, the multiaxis load cell was saturated in the moment in the sagittal plan. This is the primary moment of interest in these injury events. However the most important data channel (the axial reaction force) was not saturated.

The following adjustments are recommended to improve this system:

- Reduce the data acquisition rate to reduce the volume of data making the data more manageable
- Increase the range of the axial load cell at the impact platen
- Increase the range of the sagittal moment of the load cell at T1

#### 9.3.4 Follower Preload

A follower preload was used to simulate musculature. Further work is needed on this system to improve its biofidelity. This includes:

- Confirmation that the elimination of buckling was not an artifact of the drop tower methodology and the use of a surrogate head. A comparison study which uses the same apparatus but does not employ the follower preload is needed.
- Improving the path of the follower load in the upper cervical spine.
- Assessing the behaviour of the springs at impact to determine their unloading rate.

#### 9.3.5 High Speed Cineradiography and Surrogate Cord

An older model high speed digital camera was used in the image intensifier. The images resulting from this camera were pixilated and had a small field of view. However it was still possible to work with these images and we were able to capture the region of interest for all 6 impact events. Also, the camera's frame rate could not be dictated and controlled by one of the other high speed digital cameras used to record the motion of the spinal column. Thus the x-ray images may not have been exactly synchronized with the column footage.

With the combined use of the high speed x-ray set up and the radiodense surrogate we were able to provide a continuous profile of cord deformation during injury. The surrogate cord used was the most biofidelic model available at the time of testing. Its

properties in quasistatic tension and transverse compression were similar to those measured in *in vivo* animals. However the viscoelastic properties were not matched. Also a surrogate dura and CSF were not incorporated into the model as methods to do so have not been developed. Only the transverse compression of the cord during injury was measured as the cord showed as a dark mass in the digital images.

The following improvements can be made to the high speed cineradiography system and surrogate cord to improve their function.

- A newer model camera that would allow for an increased frame rate (the conditions for this have been discussed in Chapter 6), better resolution, and a bigger field of view is needed.
- The newer camera must be compatible with the external high speed cameras in terms of synchronization.
- The surrogate cord needs to be improved by incorporating the matters, cerebral spinal fluid, and nerve roots, and by addressing the viscoelastic effects of the material.
- Discrete markers need to be incorporated into the cord to allow for longitudinal deformation measurements.

#### 9.3.6 Surrogate Head

A surrogate head was used as the only the response of the cervical spine was of interest. Using a generic head eliminated variation in skull shape at the point of impact. The head was developed to match the mass and inertial properties of a human head. To maintain the biofidelity of the impact interface the skull shaped section was upholstered with leather. This leather interacted with the Teflon coated impact platen which provided a virtually frictionless surface. Head alignment on spine was difficult and may not have been ideal in all cases. Improvements to this device are needed especially with the following aspects:

- Attachment to occiput: the current attachment by three screws is difficult to align and the anterior screw must often be replaced by a wire.
- Alignment with spine and angles of attachment
- Interaction with follower load, especially with loading mechanism: the head redesign should incorporate the current spring approach



- Stiffness of the surrogate head should be assessed as it may influence the measure of lag response of the specimens during impact

#### **9.4 Future Directions**

Only a small sample of specimens was tested in this study. This limited the ability to draw firm conclusions about the relationship between spinal column (bony) and spinal cord injury. More specimens are needed to form a catalogue of injuries and to link injury patterns and parameters to these injuries. This catalogue would provide a useful base on which to compare the influence of different impact conditions and the effectiveness of preventative devices.

The procedures and equipment developed for this project have much potential for adaptation for use in other studies into spinal cord injury. The drop tower was designed to be adaptable to allow for the study of different impact conditions such as inclined and padded impact surfaces. As all of the motion capture and cord deformation procedures do not influence the response of the specimen and are can be run in parallel to any other motion capture system, they can be easily employed in all cervical spine testing and would provide further insight into the relationship between bony and cord injury.

## Appendix A: Matlab Code

This appendix contains the Matlab code used for the direct linear transformation and the three-dimensional reconstruction.

### A.1 Calibration of Space

This algorithm determines the relationship between the camera and the volume of interest. A calibration cage is used to provide the known three-dimensional coordinates. The function is run once for each camera to produce two “L” vectors.

```
function [L] = Calib_DLT2D(u2D, X3D);

%Created by Amy Saari December 2004

%Calculates the L vector for direct linear transformation camera
%calibration. Function arguments are the 2D camera coordinates and the 3D
%object coordinates (u2D and u3D respectively). Object must have at least 6
%coordinates available for use. Function returns the L vector (L).

%Check for size of u2D and X3D
[m,n] = size (u2D);

if (m < 6) %error returned if u is too small
    error('Must have at least 6 2D coordinates')
end

[r,s] = size (X3D);

if (r < 6) %error returned if u is too small
    error('Must have at least 6 3D coordinates')
end

%Determine L

%Create M matrix from X3D and u2D
M=[X3D(1:m,:) ones(m,1) zeros(m,4) -X3D(1:m,1).*u2D(1:m,1) -X3D(1:m,2).*u2D(1:m,1) -
X3D(1:m,3).*u2D(1:m,1);
zeros(m,4) X3D(1:m,:) ones(m,1) -X3D(1:m,1).*u2D(1:m,2) -X3D(1:m,2).*u2D(1:m,2) -X3D(1:m,3).*u2D(1:m,2)];

UV = [u2D(1:m,1); u2D(1:m,2)];

L = M\UV; %calculates L

Return
```

## A.2 Three-Dimensional Reconstruction

This algorithm reconstructs the three-dimensional coordinates of any number of markers as seen in two cameras. The algorithm uses the L vectors calculated in the above algorithm for each camera and the two sets of two dimensional marker coordinates from each camera. The marker coordinate data must be in the following format: each row corresponds to a frame, the marker coordinates are given in the columns (x1, y1, x2, y2... xn, yn). The three dimensional coordinates are returned in a similar manner but with extra columns for the z coordinates.

```
function [x] = DLT( URaw1, URaw2, L1, L2);

%Created by Amy Saari December 2004

%Computes the global coordinates in 3D for m points from 2 2D images.
%Arguments are the two arrays of 2D camera coordinates (u1 and u2) (tX2m+1) where m is
%the number of markers and t is the number of frames) and the two L vectors
%for the cameras. The function returns an array of 3D marker coordinates in [x] (tX3m)

temp = 0;

[m1,n1] = size(URaw1);
[m2,n2] = size(URaw2);

if (m1 ~= m2 || n1 ~= n2) %error message if u1 and u2 are not the same length
    error('u1 and u2 not the same length')
end

U1 = URaw1(:,2:n1);
U2 = URaw2(:,2:n2);

n = (n1-1)/2; %number of markers present

i = 1; %counter for while loop
while (i <= m1) %while loop for each frame

    u1 = U1(i,:);
    u2 = U2(i,:);

    k = 1;
    while (k <= n) %while loop used to calculate each marker in the frame

        x1 = u1(2*k-1);
        y1 = u1(2*k);
        x2 = u2(2*k-1);
        y2 = u2(2*k);

        L = [L1(9)*x1-L1(1) L1(10)*x1-L1(2) L1(11)*x1-L1(3);
            L1(9)*y1-L1(5) L1(10)*y1-L1(6) L1(11)*y1-L1(7);
            L2(9)*x2-L2(1) L2(10)*x2-L2(2) L2(11)*x2-L2(3);
            L2(9)*y2-L2(5) L2(10)*y2-L2(6) L2(11)*y2-L2(7)];

        u = [L1(4)-x1;
```

```
L1(8)-y1;  
L2(4)-x2;  
L2(8)-y2];  
  
g = L\u;  
  
temp(3*k-2:3*k) = g';    %hold in temp vector until frame (row) is finished  
  
k = k + 1;  
  
end  
  
x(i,:) = temp;           %put contents of temp in appropriate row in x  
  
i = i + 1;  
  
end  
  
return
```

## Appendix B: Relative Marker Motion

This appendix contains the plots of the relative marker motion of each specimen as described in Chapter 7. For each specimen there are three plots one for each direction. The location of the markers is also given in a reference frame from the digital high speed footage for each specimen. The coordinate system used is illustrated in Figure B-1.

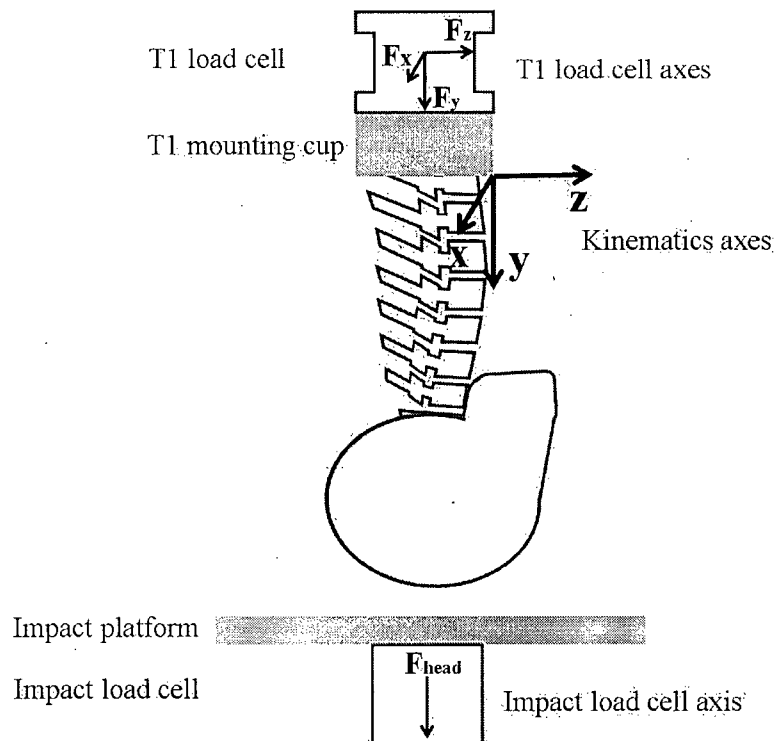


Figure B-1: Location and orientation of coordinate system used in the three-dimensional reconstruction relative to the specimen and load cell axes

### B.1 H1091 Marker Motion

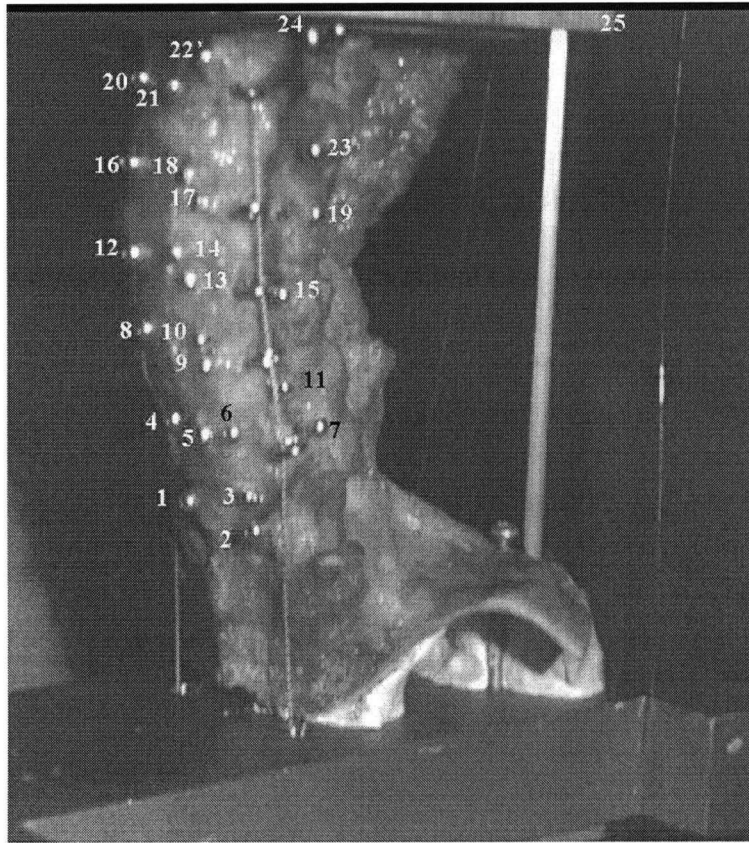


Figure B-2: Location of markers on specimen H1091

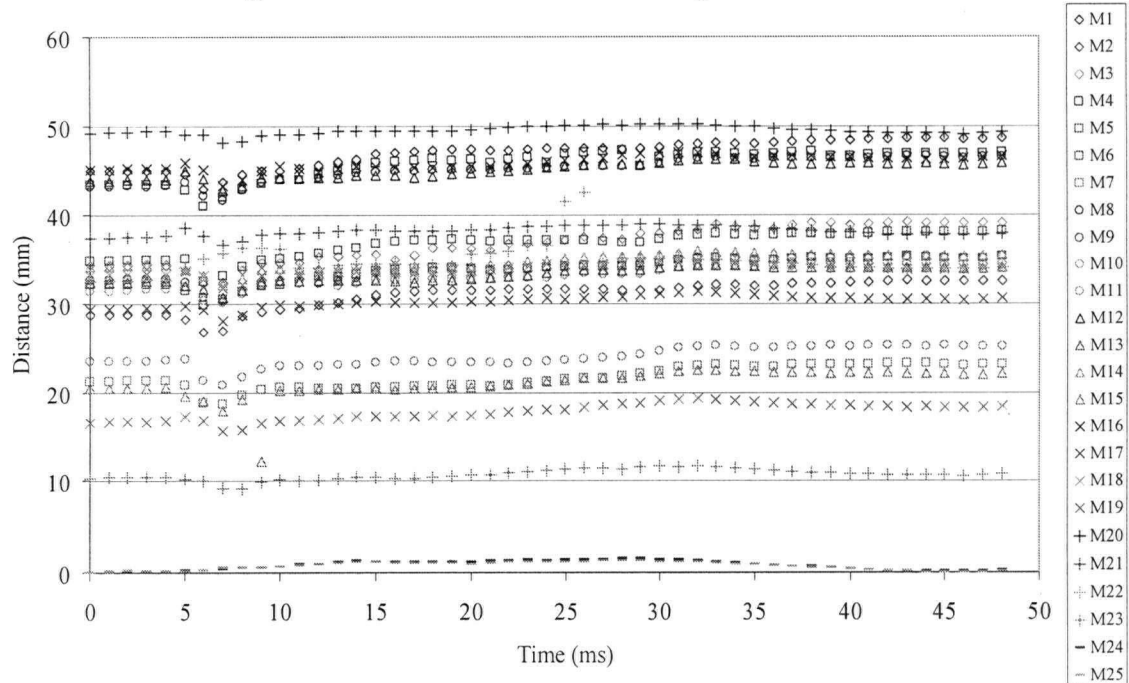


Figure B-3: Marker motion along the x-axis of H1091

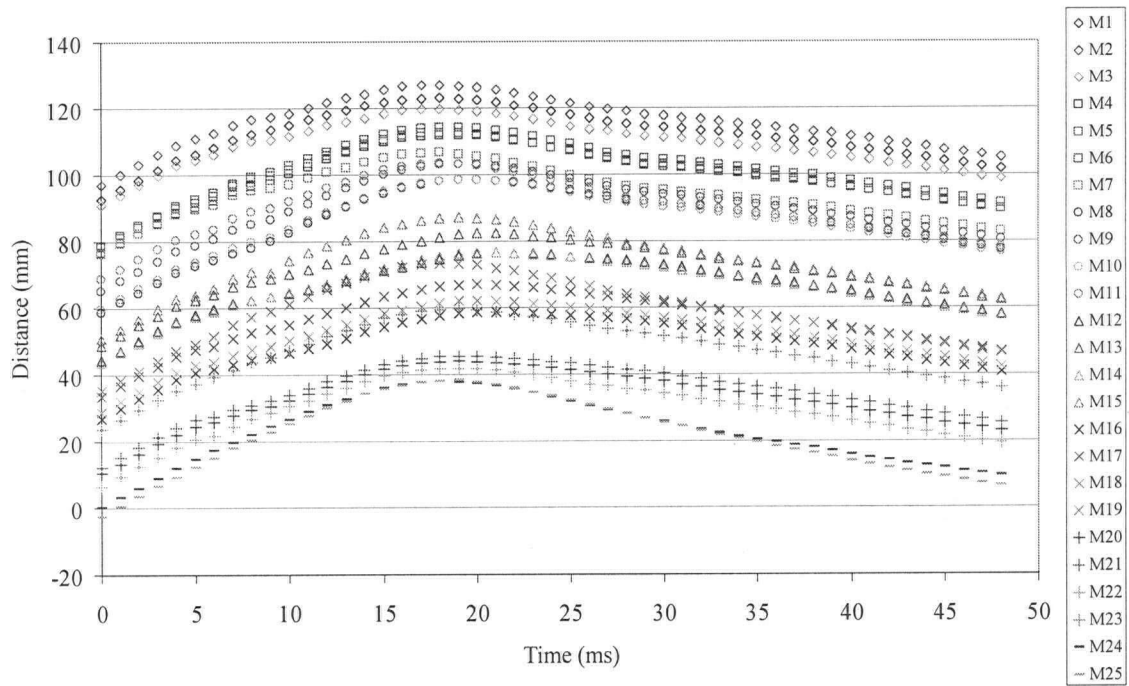


Figure B-4: Marker motion along the y-axis of H1091

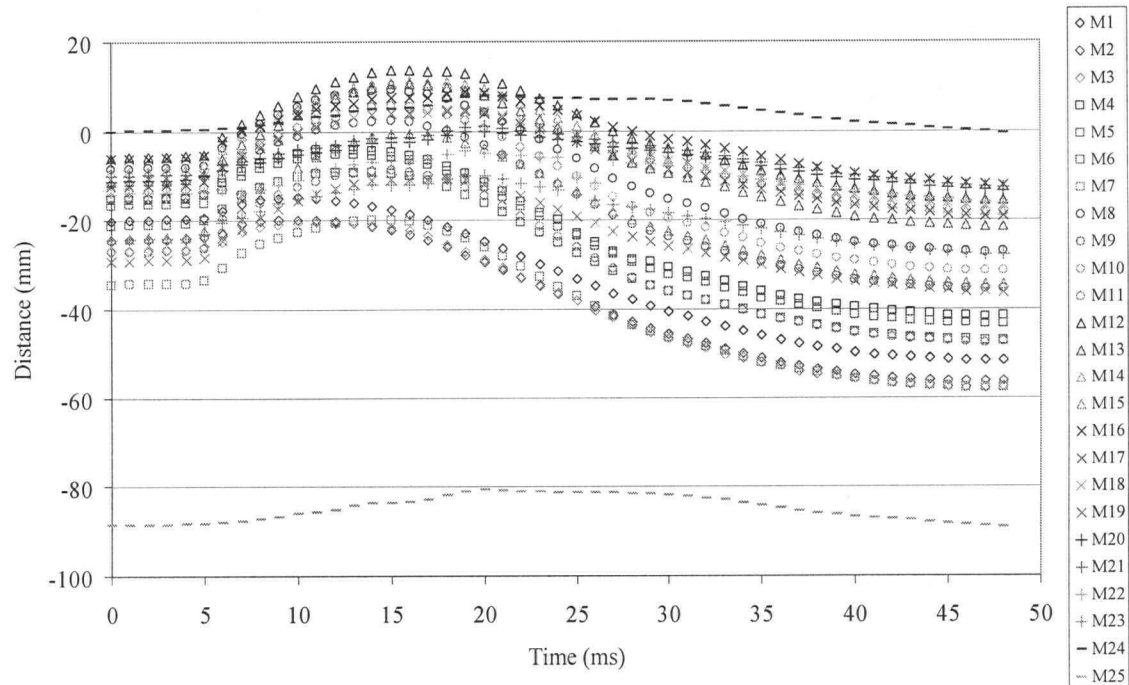


Figure B-5: Marker motion along the z-axis of H1091

## B.2 H1096 Marker Motion

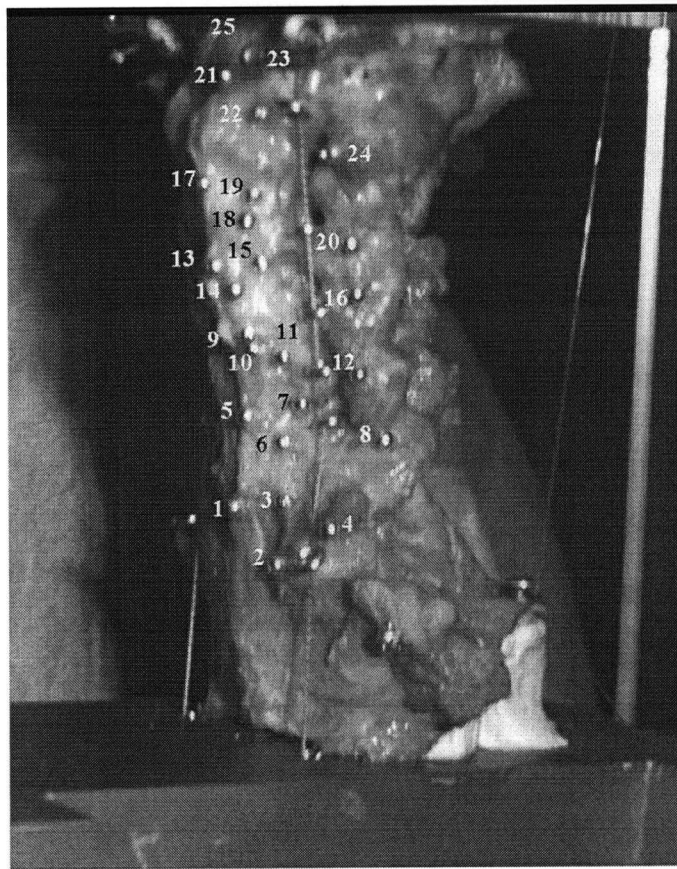


Figure B-6: Location of markers on specimen H1096

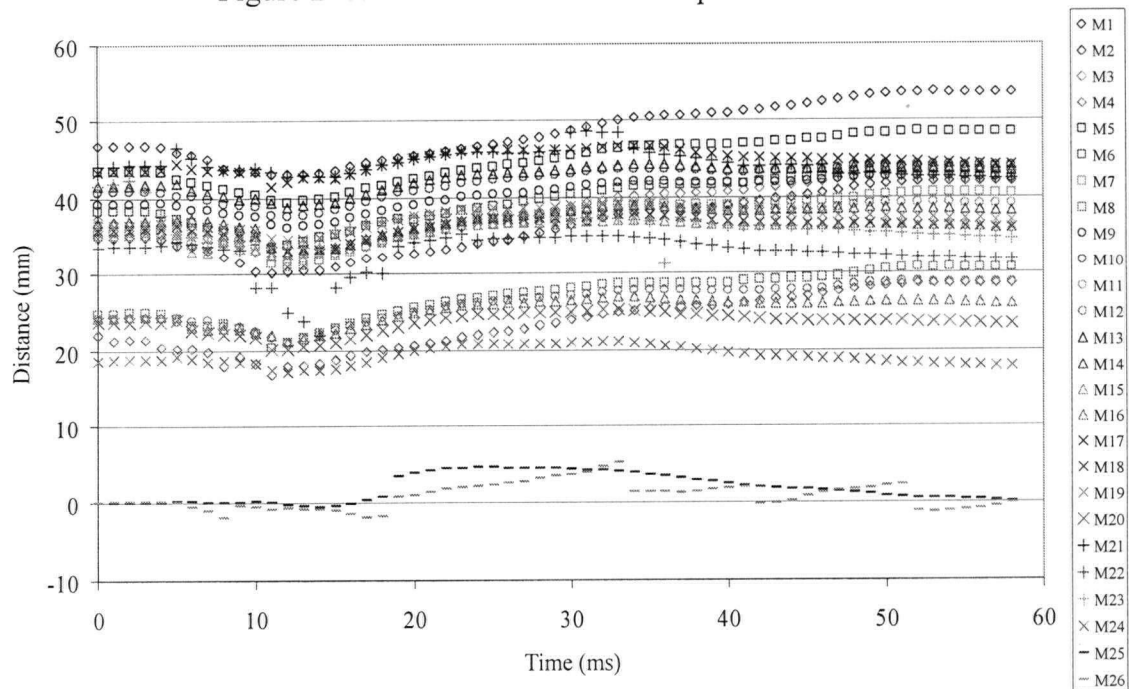


Figure B-7: Marker motion along the x-axis of H1096



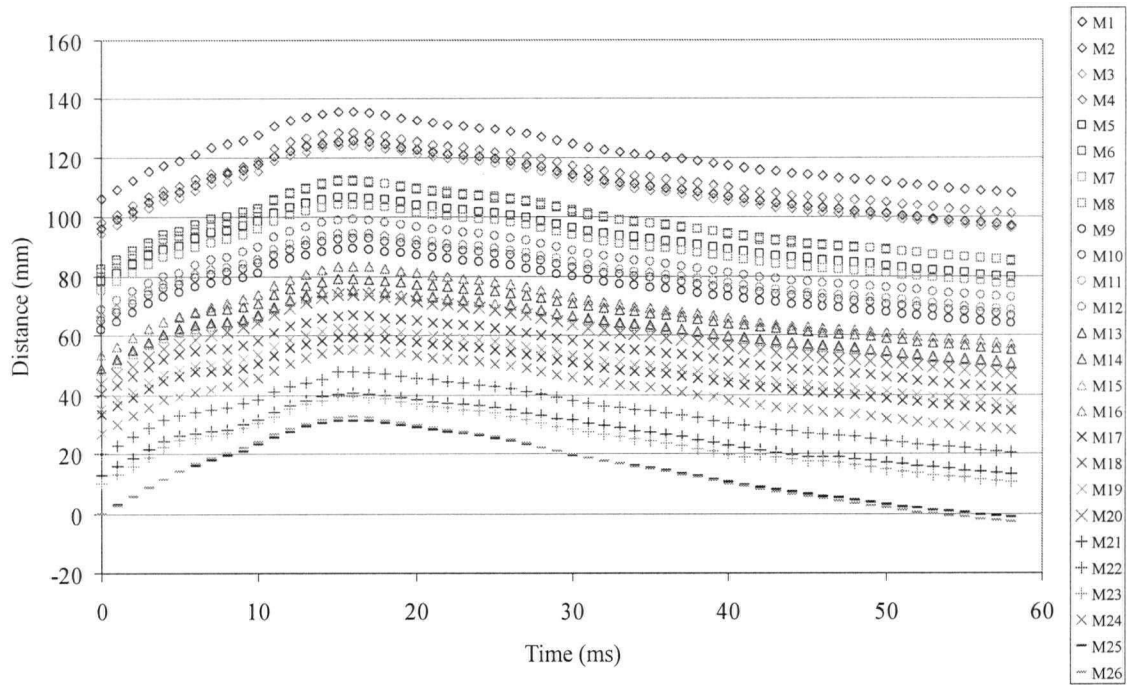


Figure B-8: Marker motion along the y-axis of H1096

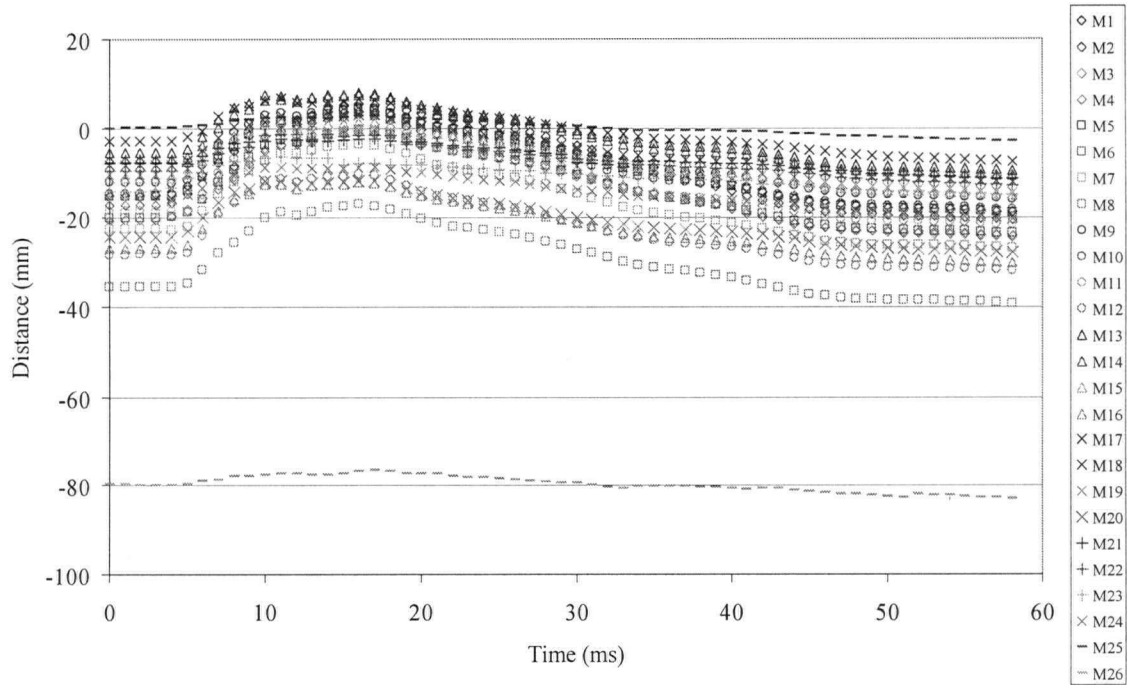


Figure B-9: Marker motion along the z-axis of H1096

## B.3 H1116 Marker Motion

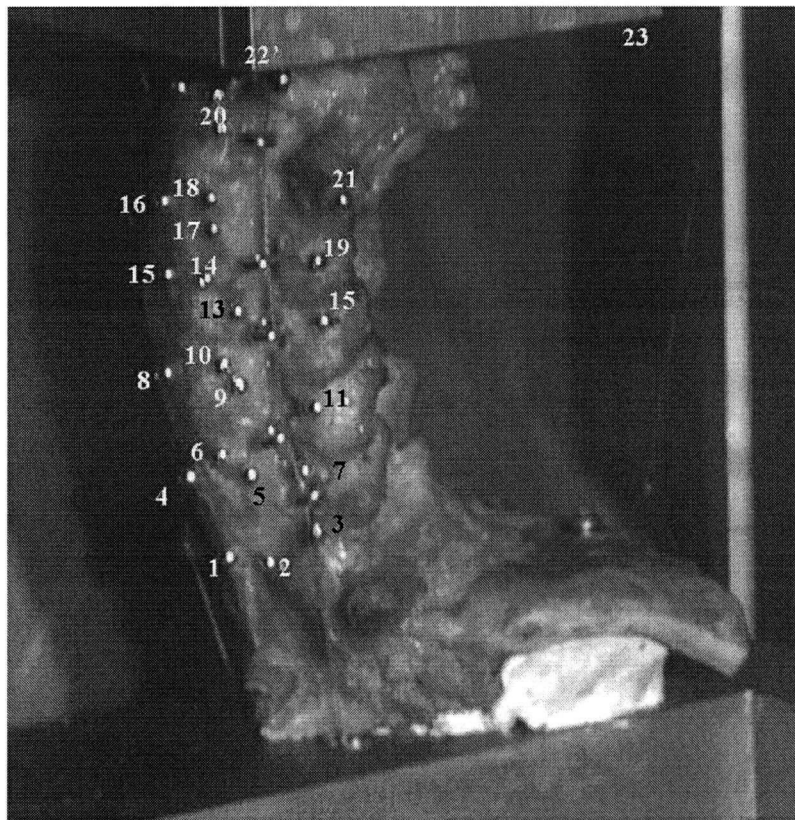


Figure B-10: Location of markers on specimen H1116

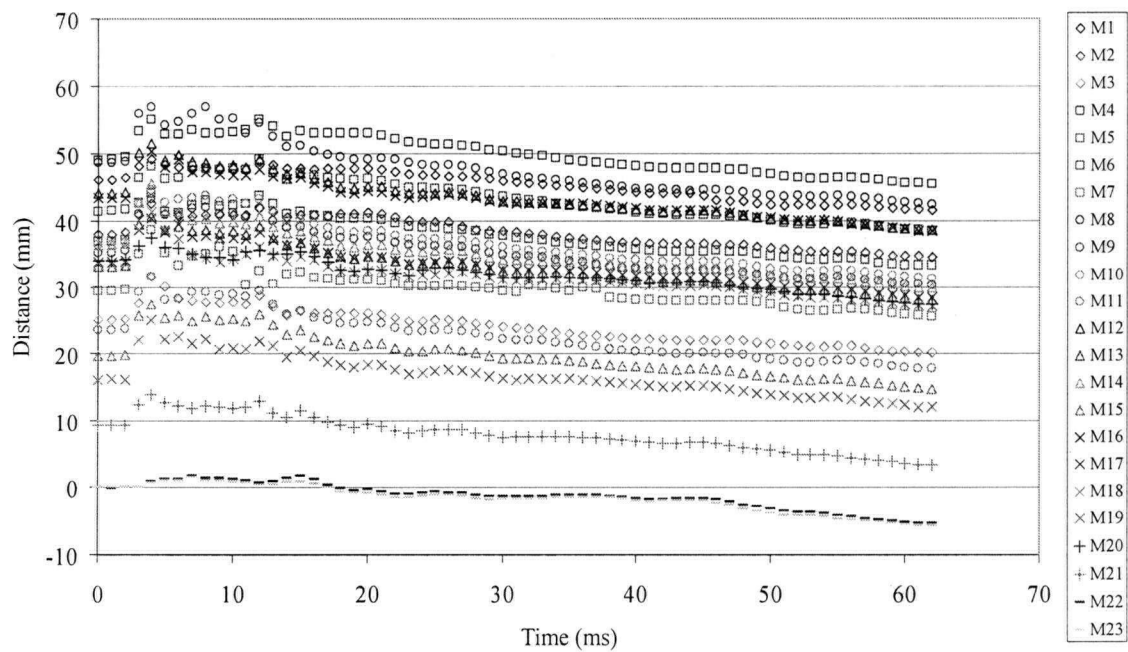


Figure B-11: Marker motion along the x-axis of H1116

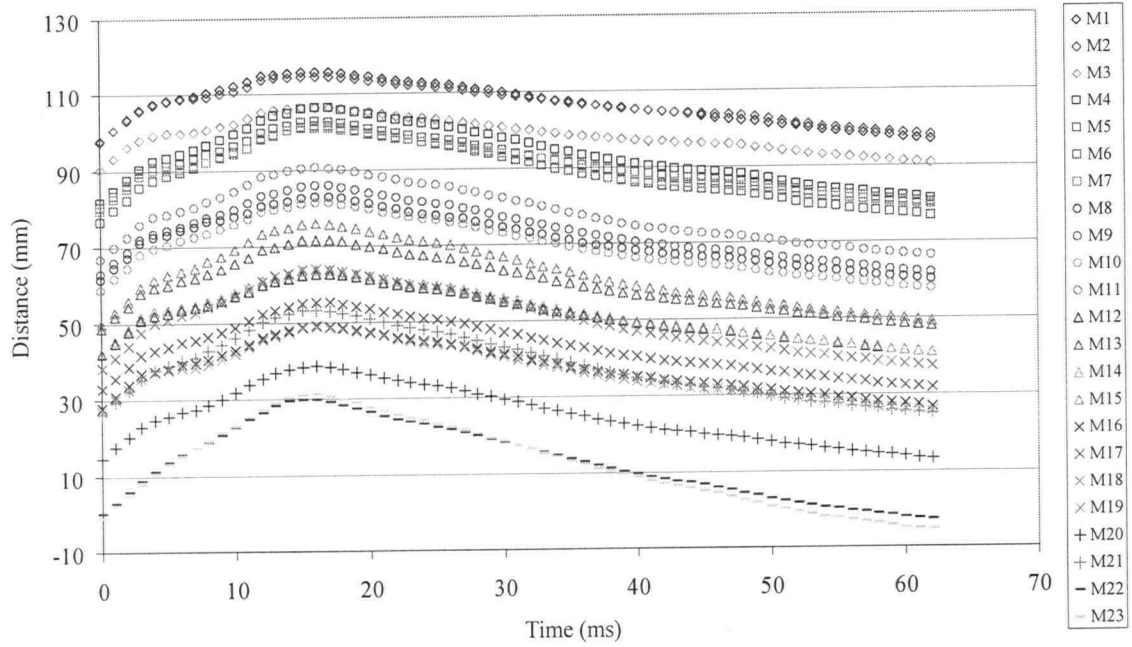


Figure B-12: Marker motion along the y-axis of H1116

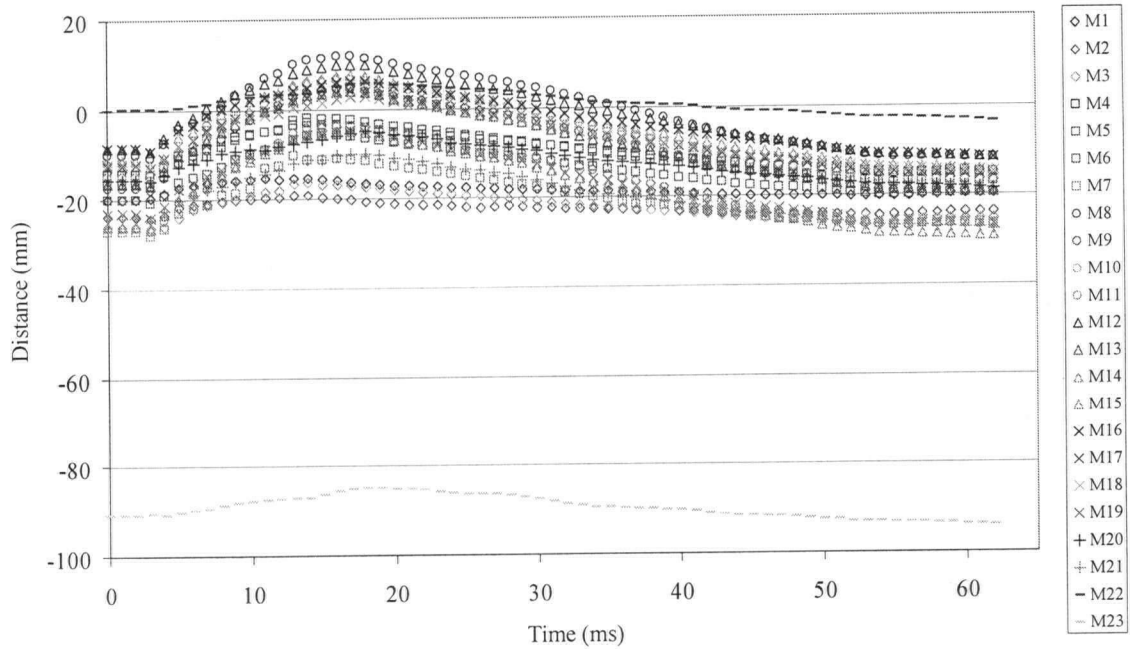


Figure B-13: Marker motion along the z-axis of H1116

## B.4 H1177 Marker Motion

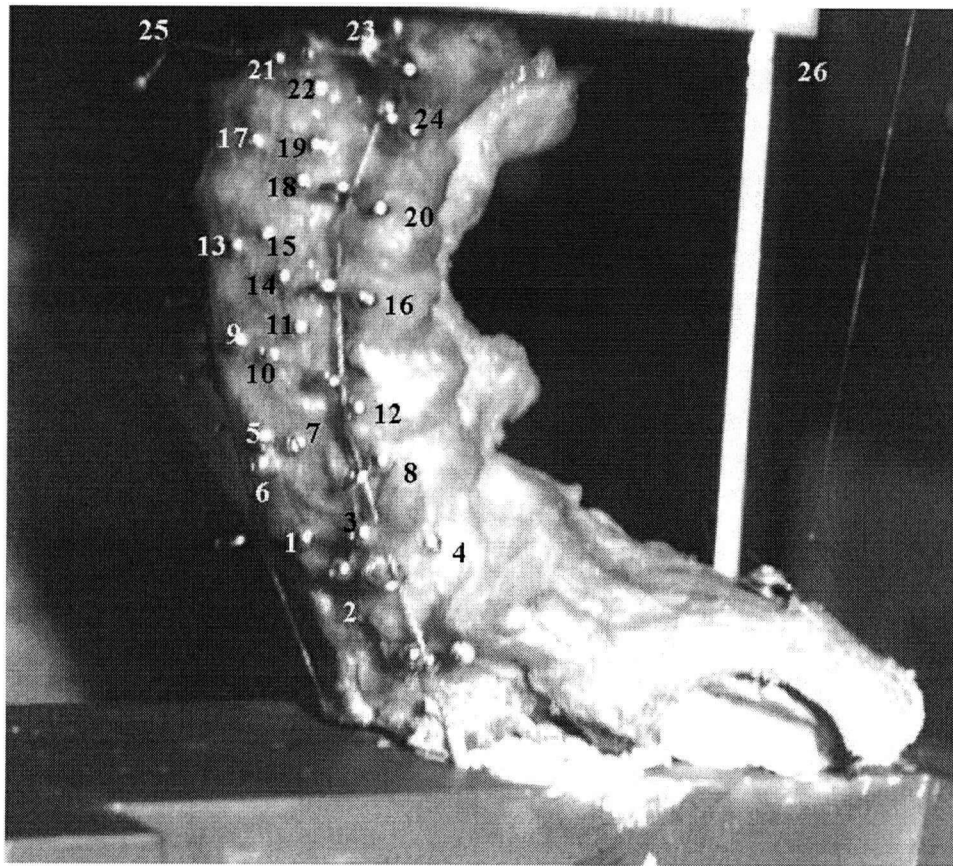


Figure B-14: Location of markers on specimen H1177

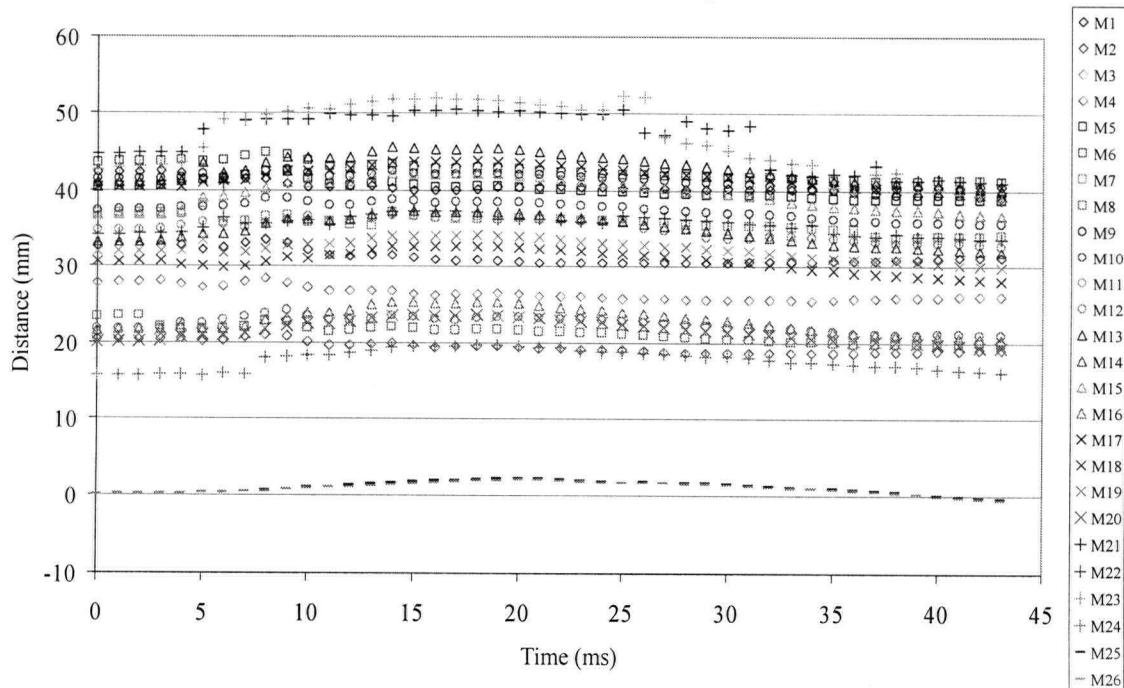


Figure B-15: Marker motion along the x-axis of H1177

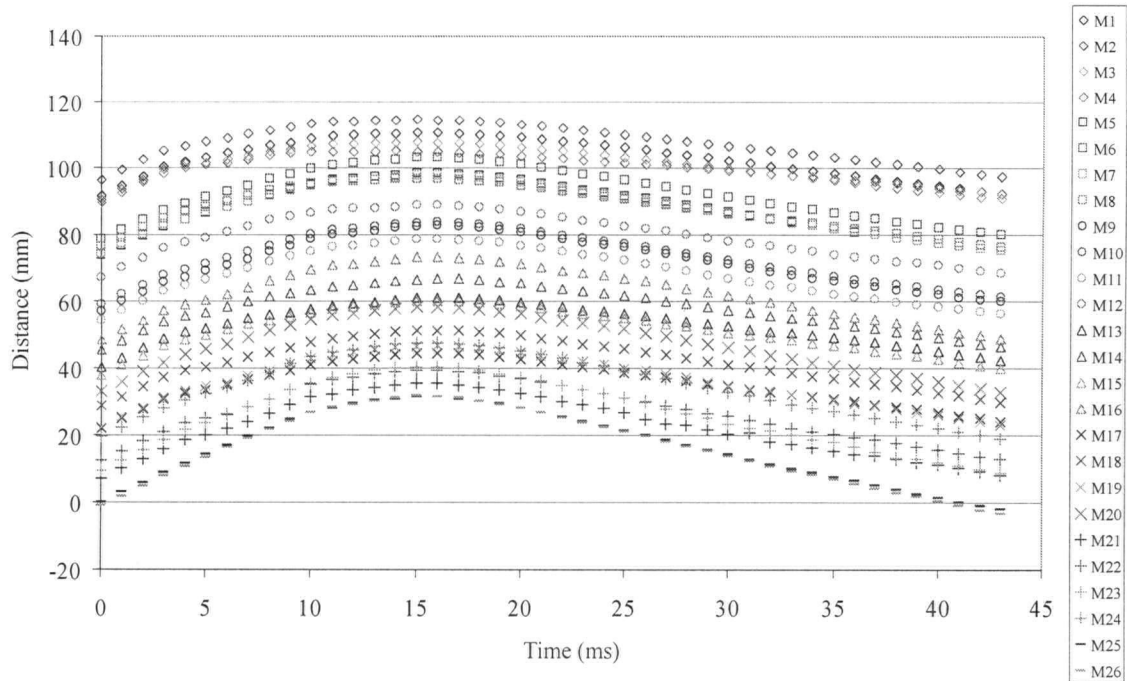


Figure B-16: Marker motion along the y-axis of H1177

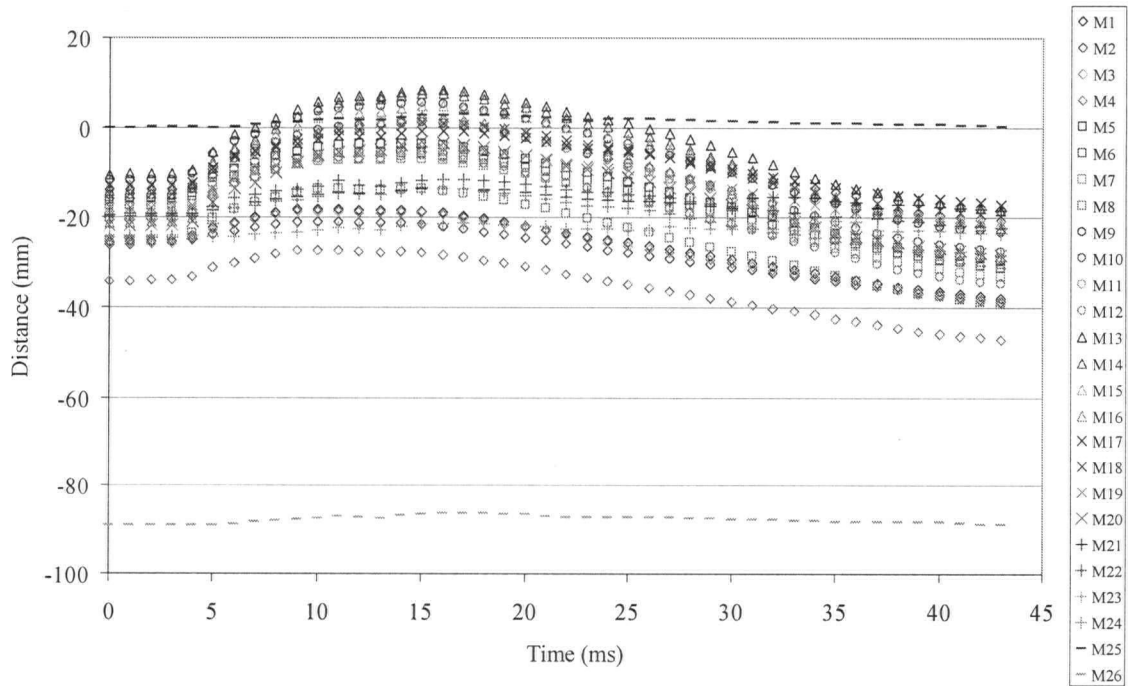


Figure B-17: Marker motion along the z-axis of H1177

## B.5 H1183 Marker Motion

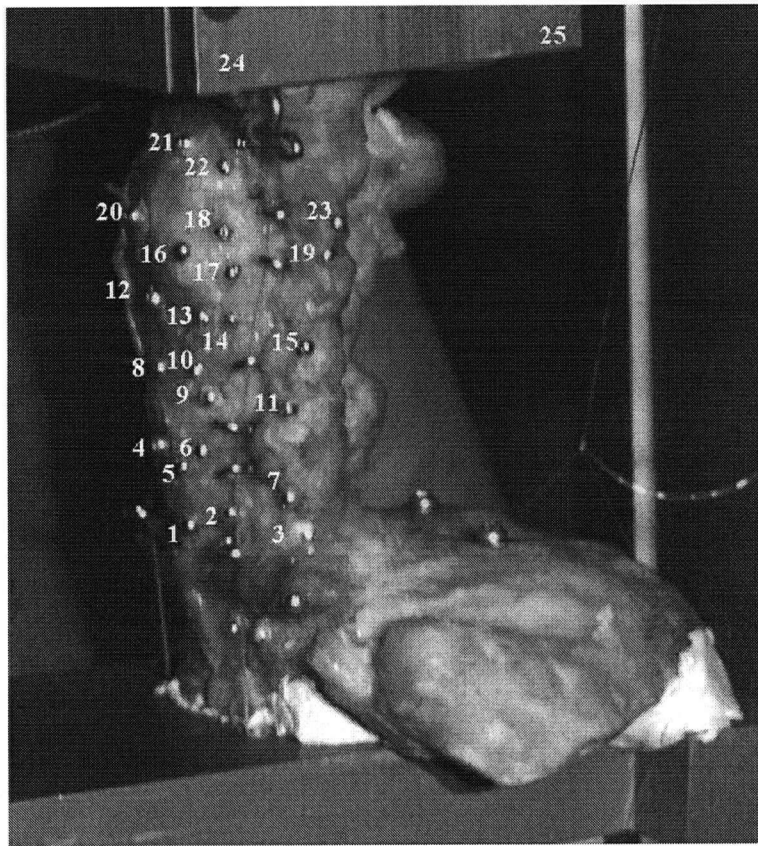


Figure B-18: Location of markers on specimen H1183

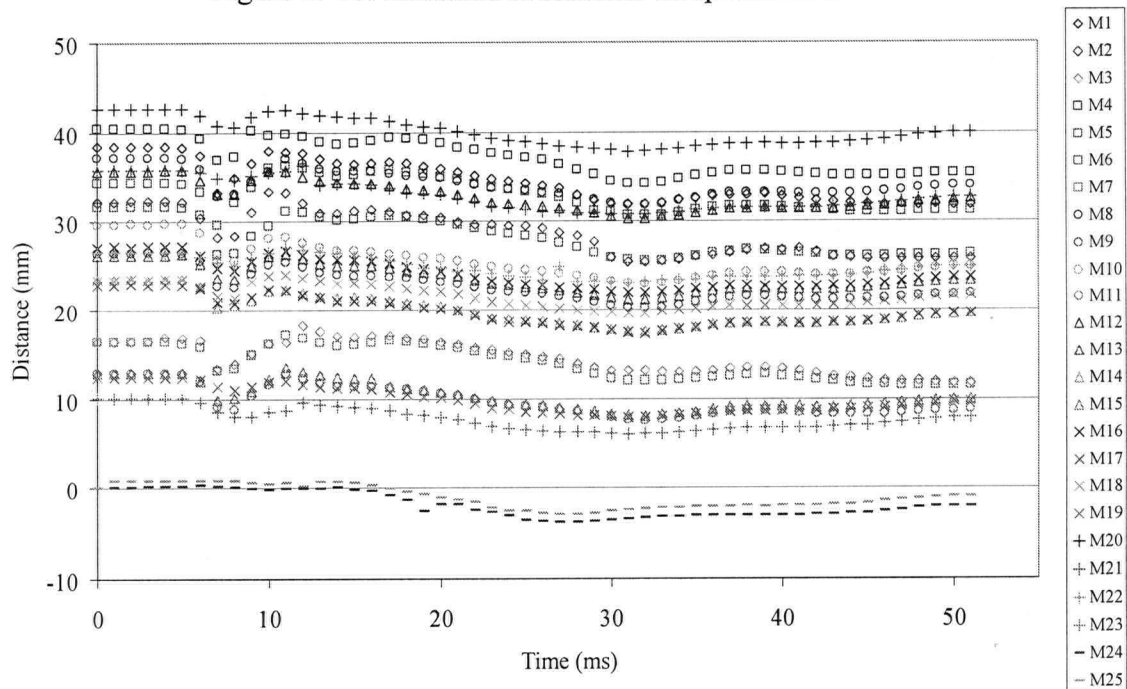


Figure B-19: Marker motion along the x-axis of H1183



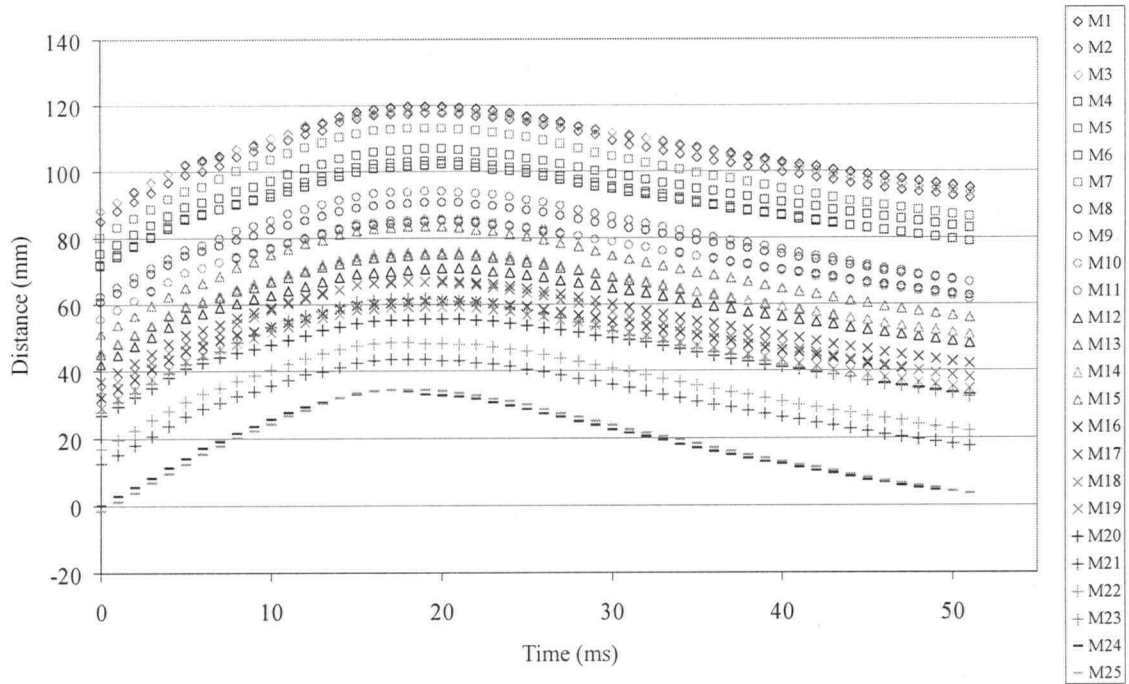


Figure B-20: Marker motion along the y-axis of H1183

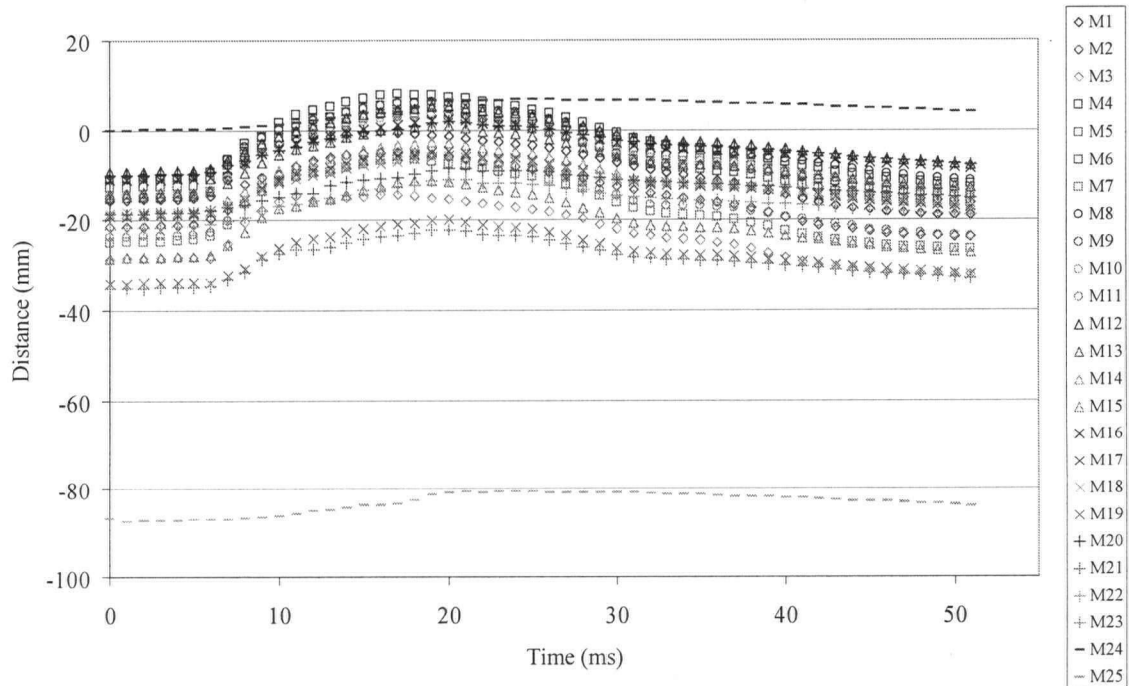


Figure B-21: Marker motion along the z-axis of H1183

## B.6 H1184 Marker Motion

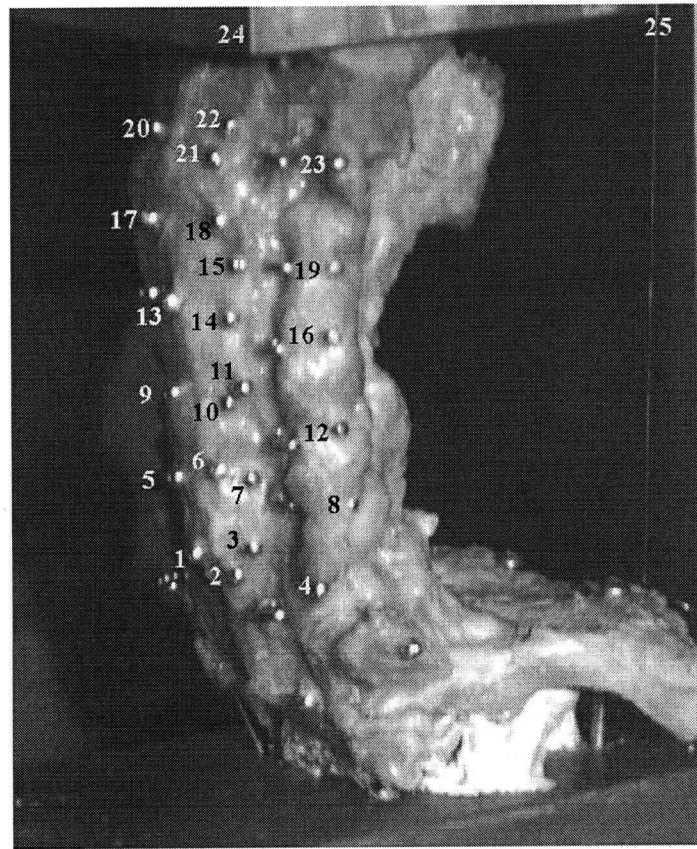


Figure B-22: Location of markers on specimen H1184

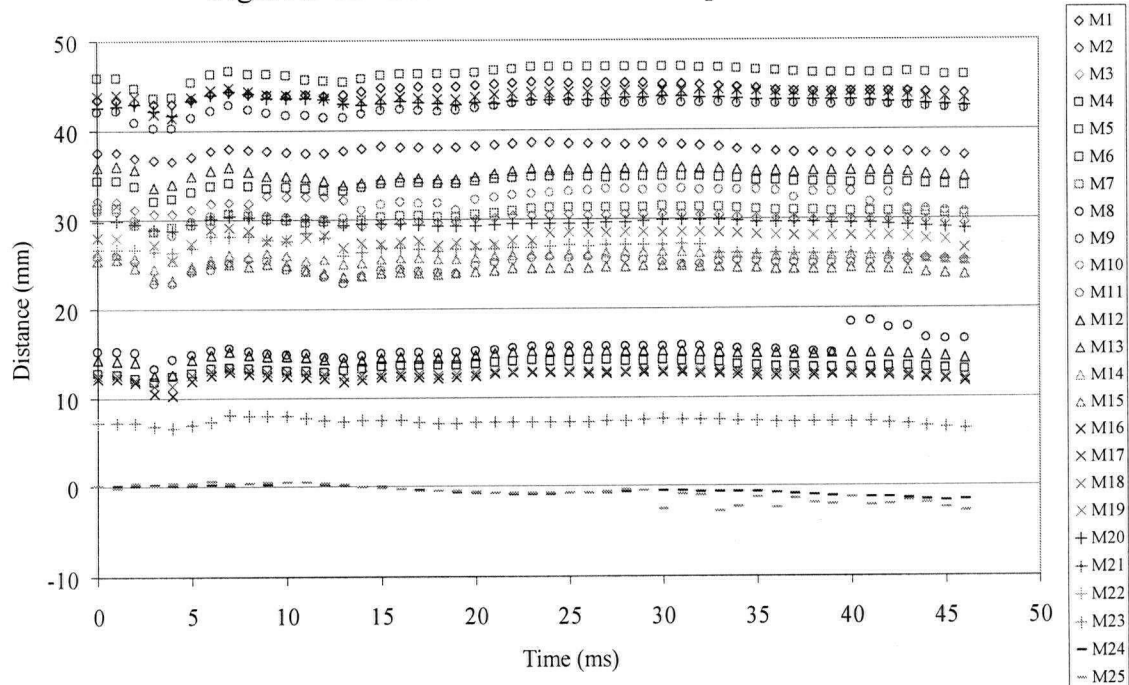


Figure B-23: Marker motion along the x-axis of H1184



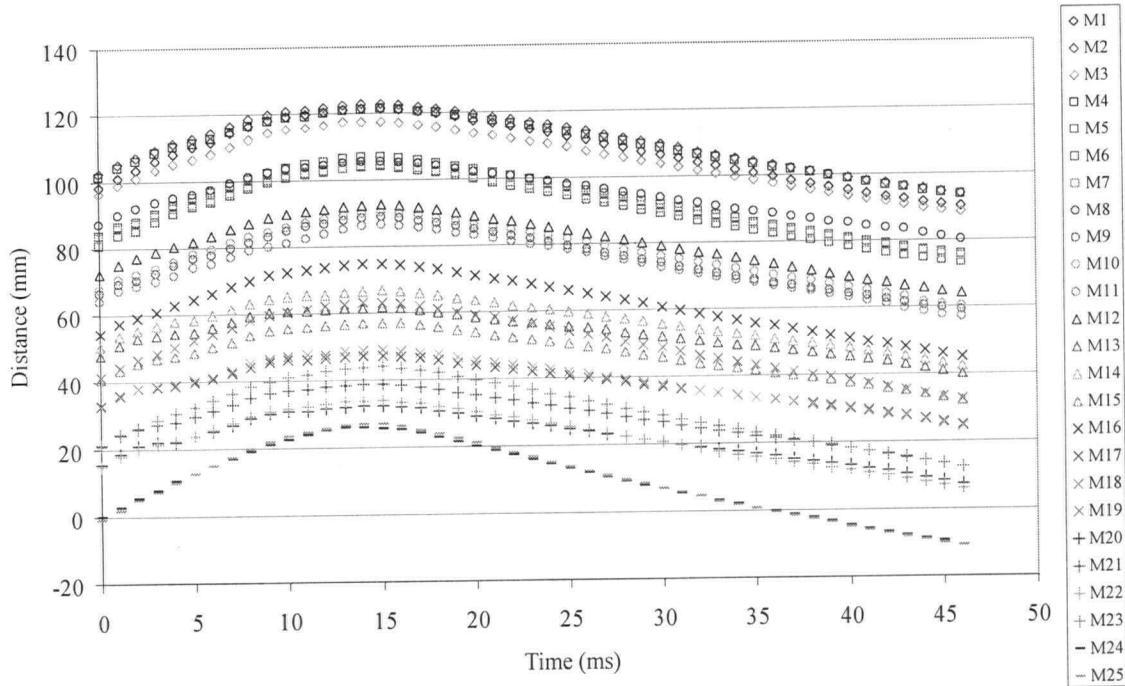


Figure B-24: Marker motion along the y-axis of H1184

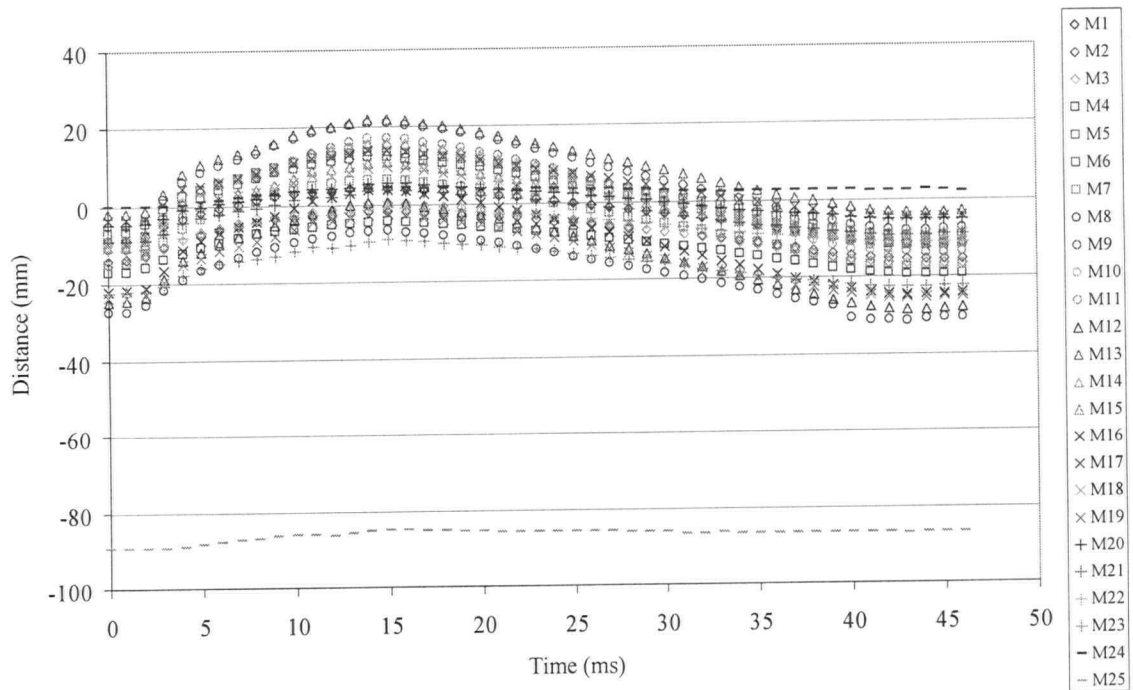


Figure B-25: Marker motion along the z-axis of H1184

## Appendix C: Load Cell Traces

This appendix contains the load cell traces for all six specimens as was described in Chapter 7. For each specimen there were 7 channels: 6 for the multi-axis load cell and one for the uni-axis load cell. Also given here is a comparison between the load trace at the impact load cell and the z-axis of the multi-axis load cell. The orientation of the axes of the load cells is illustrated in Figure C-1.

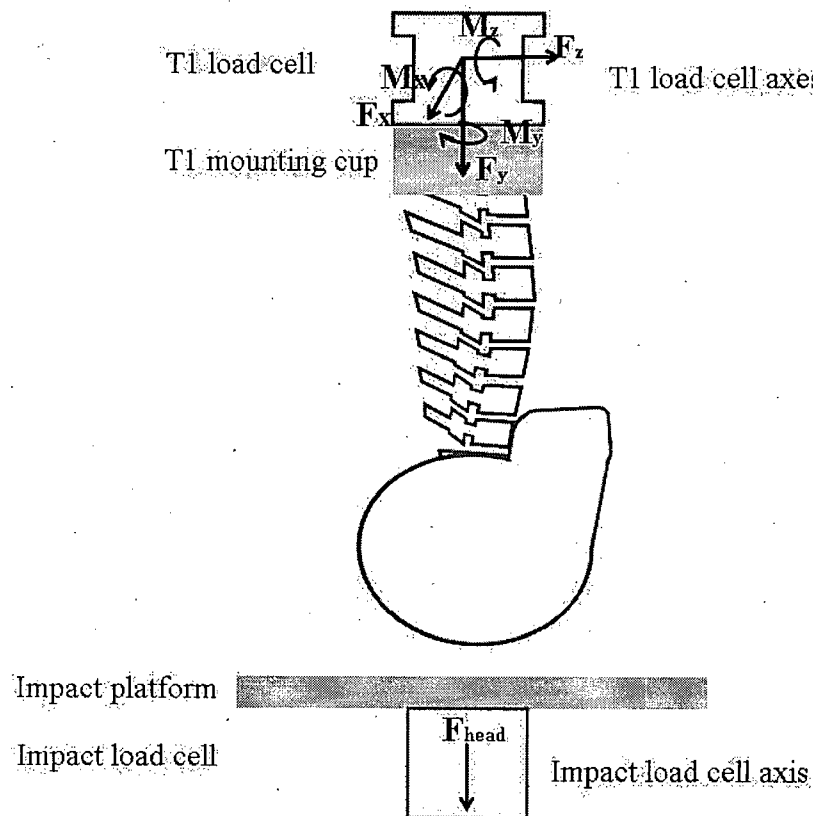
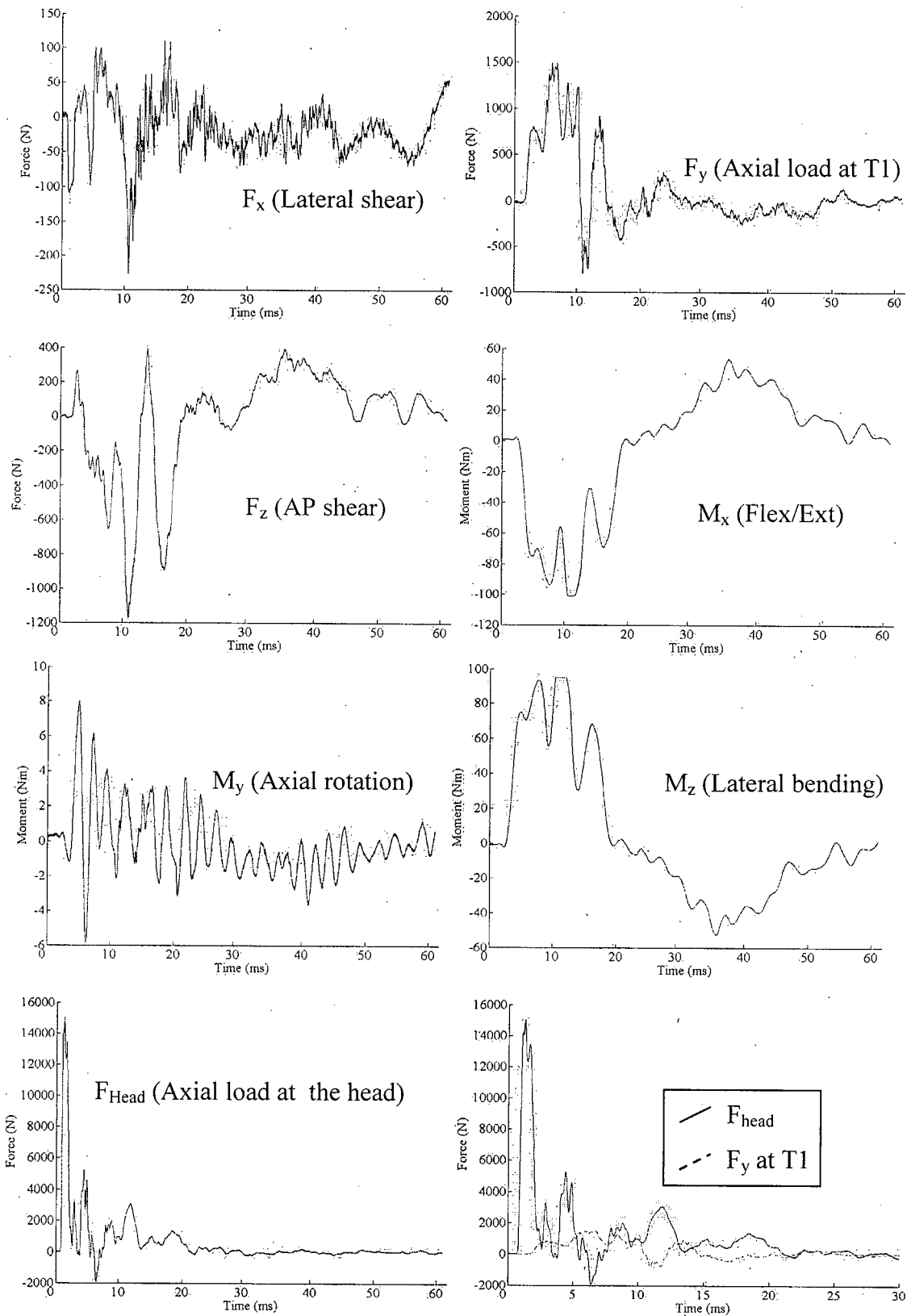
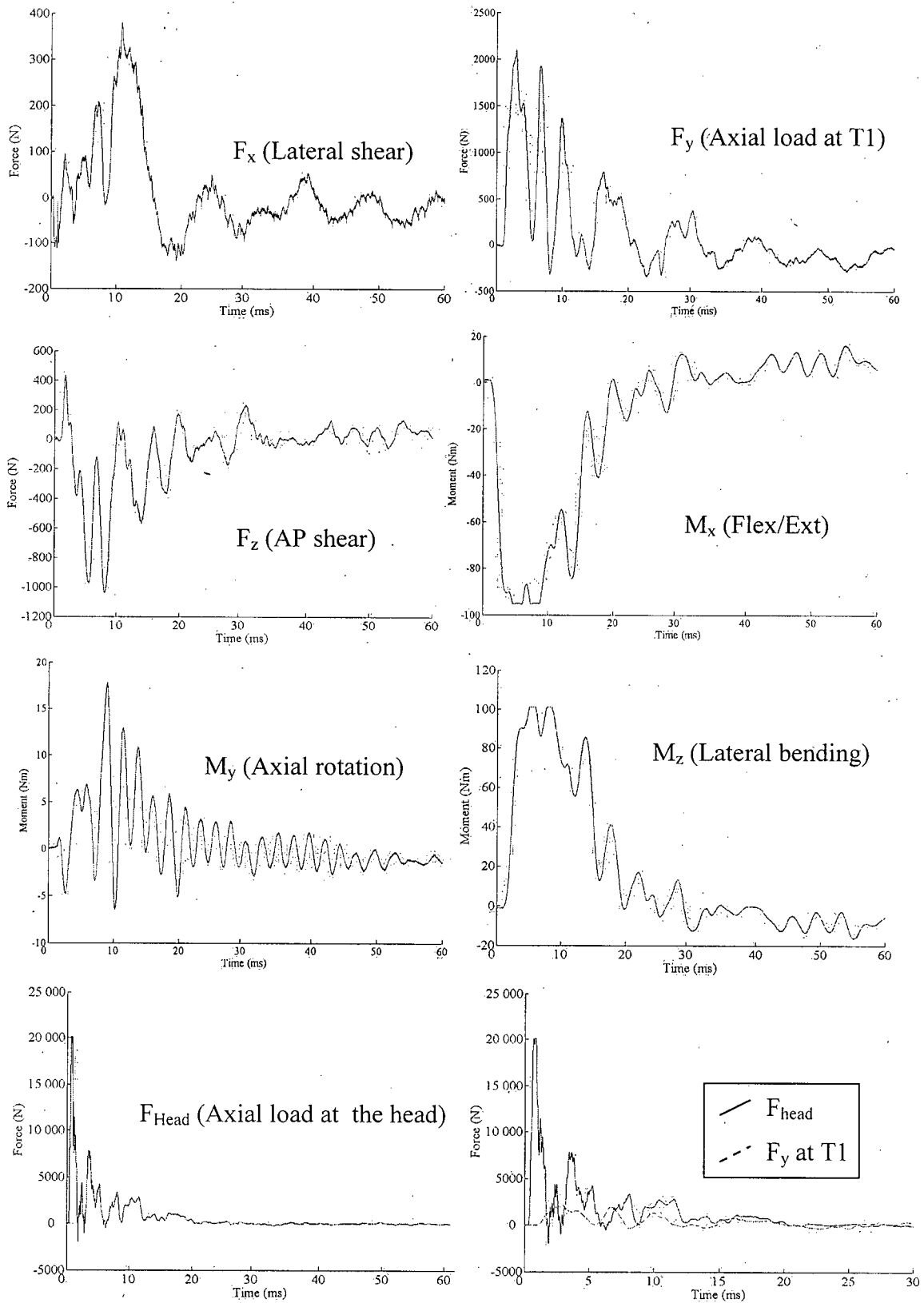


Figure C-1: Location and orientation of axes of load cells relative to the specimen

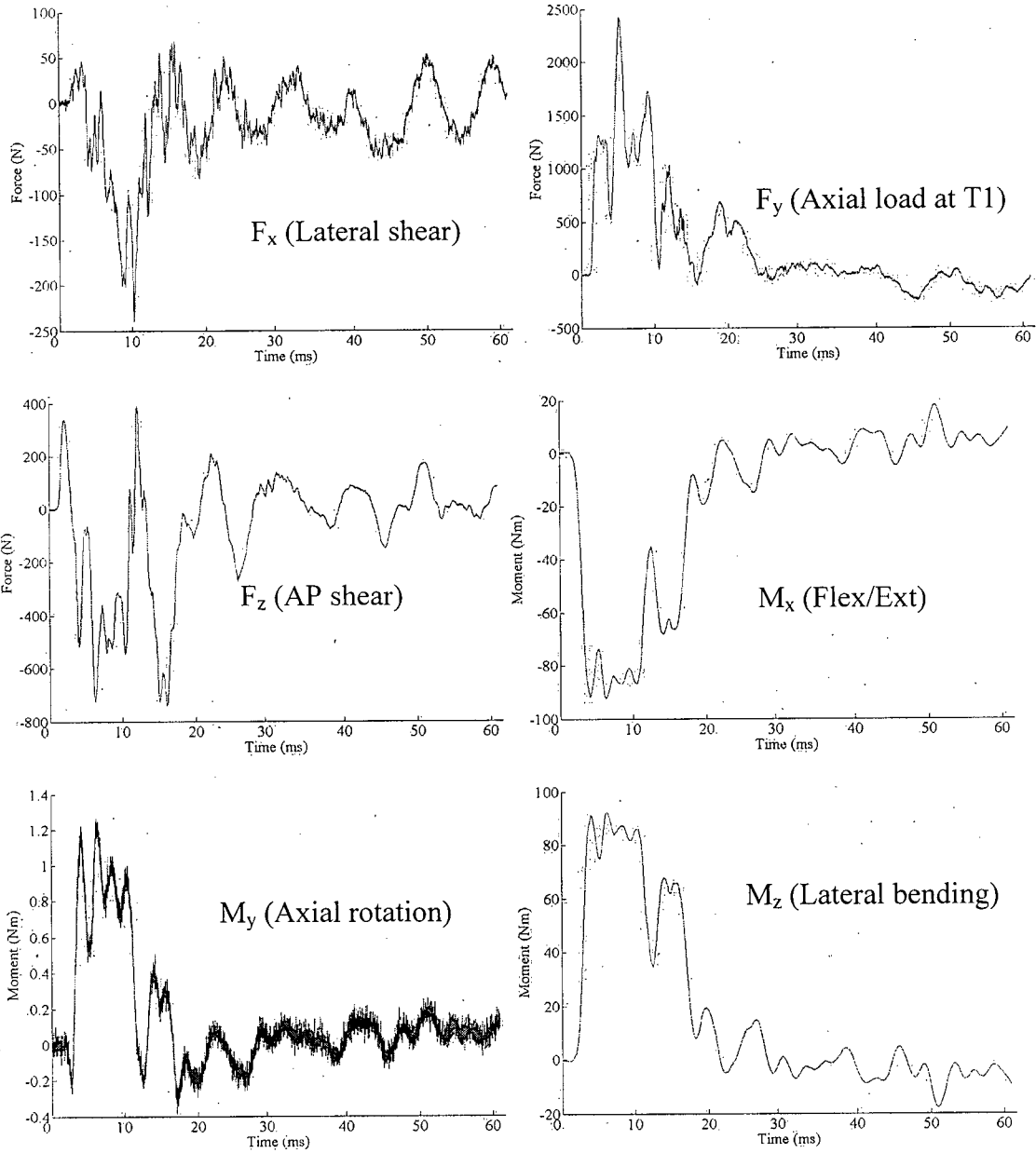
## C.1 H1091 Load Cell Traces



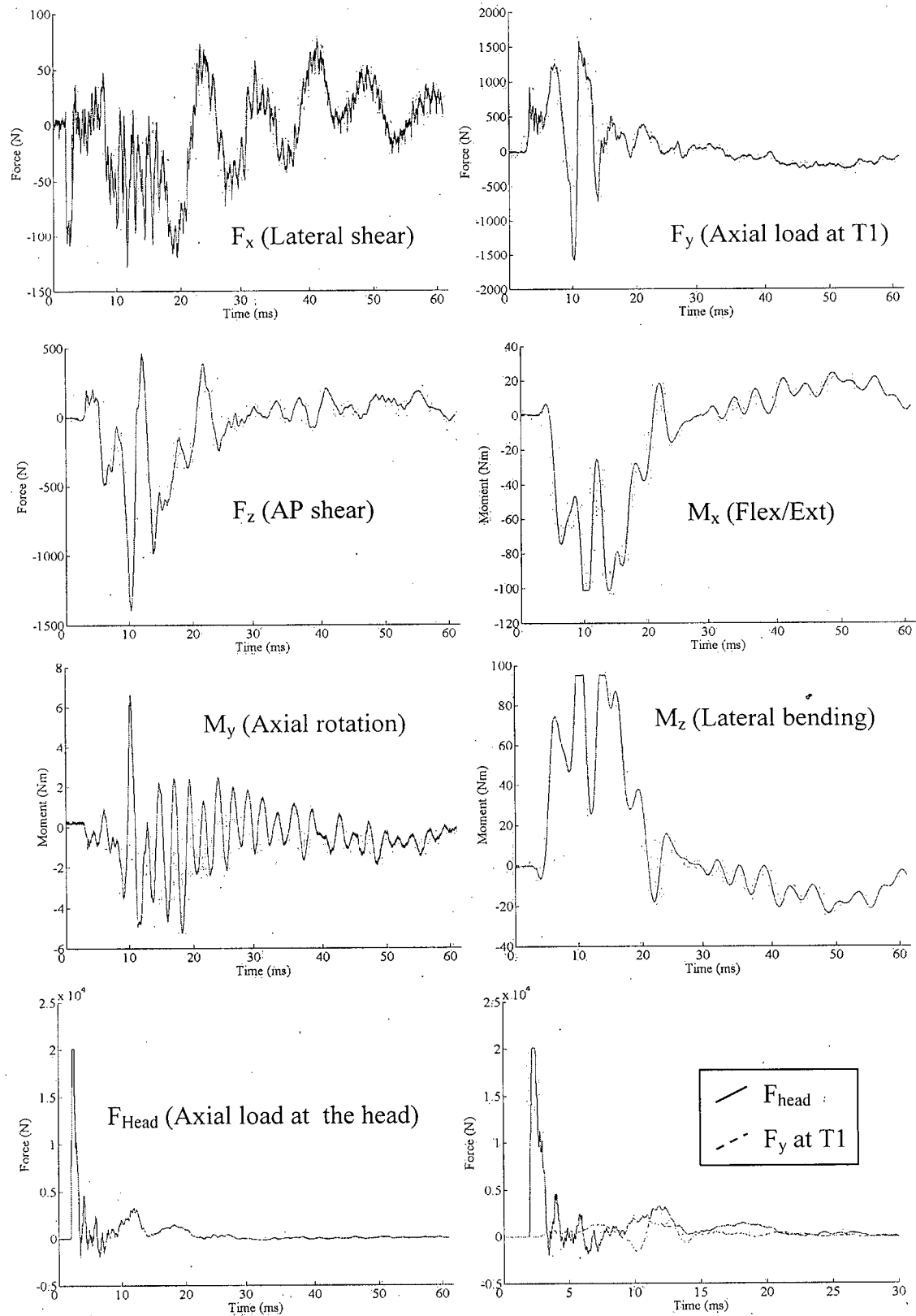
## C.2 H1096 Load Cell Traces

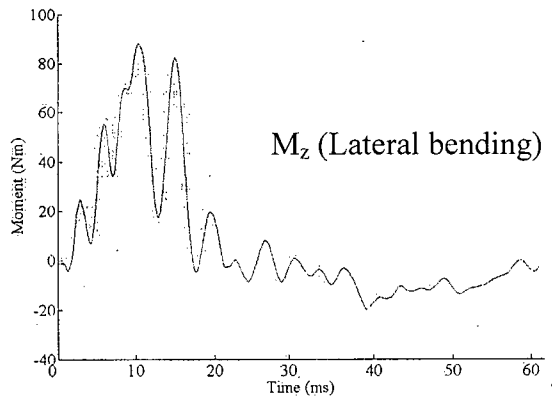
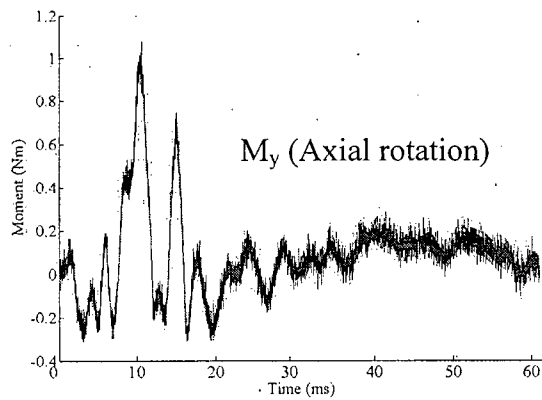
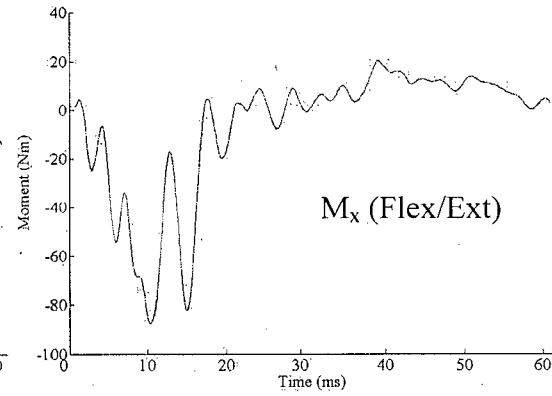
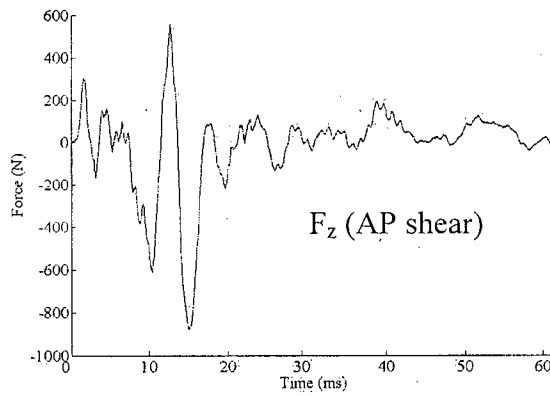
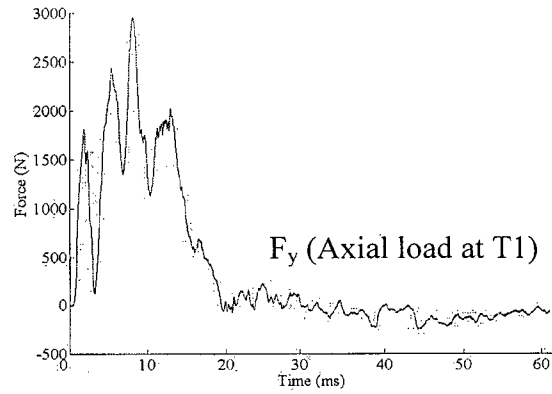
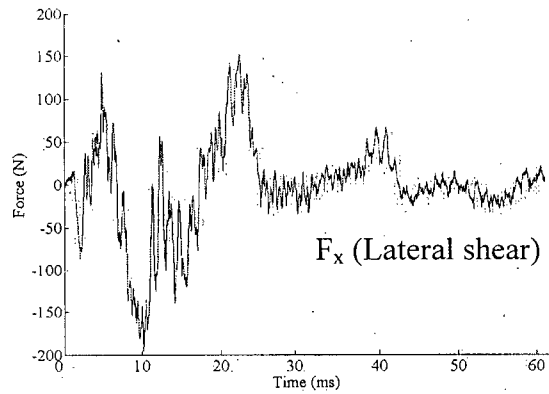


## C.3 H1116 Load Cell Traces

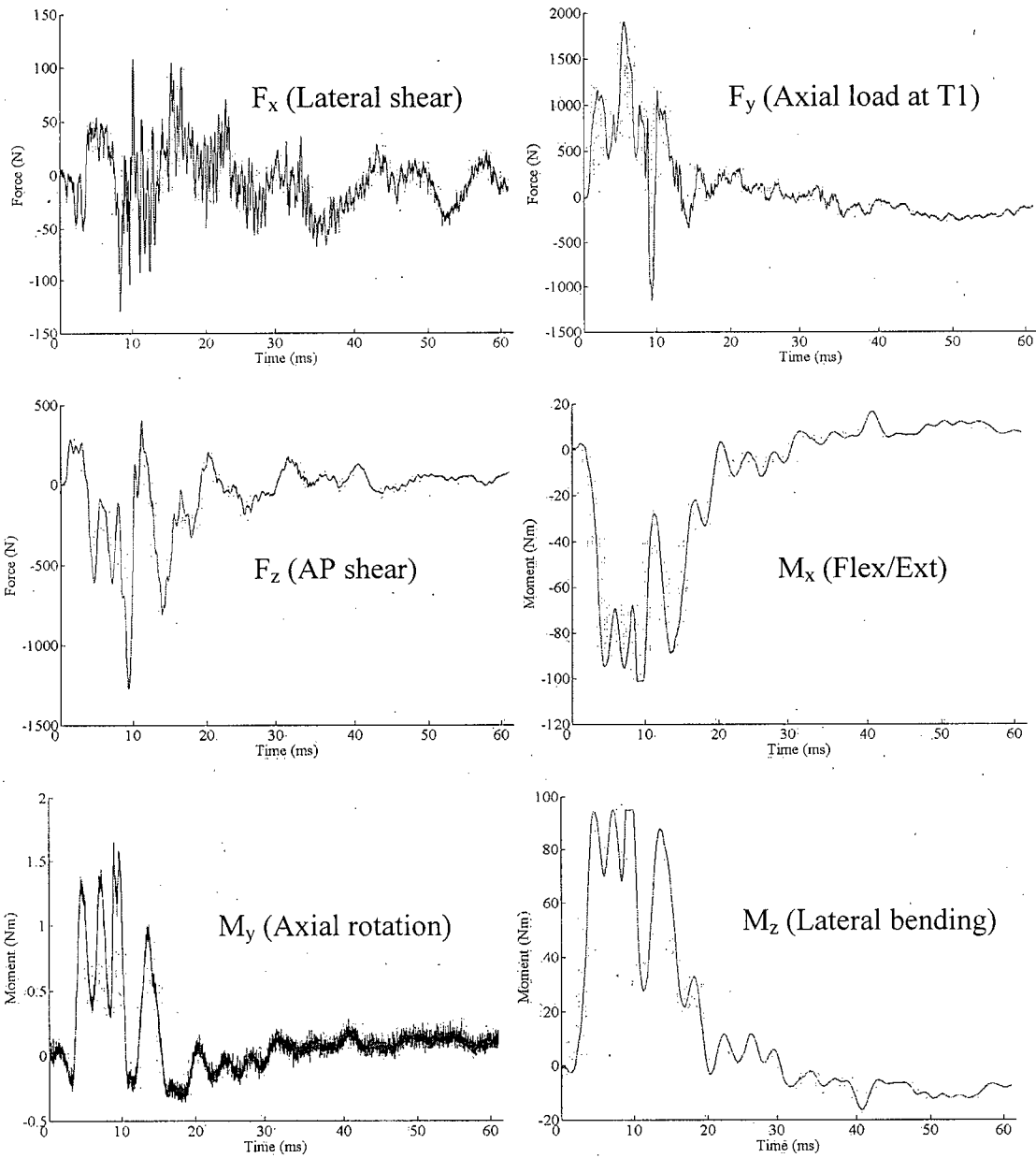


## C.4 H1177 Load Cell Traces



**C.5 H1183 Load Cell Traces**

## C.6 H1184 Load Cell Traces





## **Appendix D: Surrogate Head Design**

Attached is a copy of the final design report for the surrogate human head written by Chang, Clark, and Morley for their final year mechanical engineering design project in the Department of Mechanical Engineering at the University of British Columbia from April 2005.

**MECH 456**  
**Physical Model of the Human Head**  
**Final Report**

**Submitted to: Dr. Hodgson**

**Lynn Chang 39339007**

**Chris Clarke 49055023**

**Philip Morley 57089005**

**Date Submitted: April 8, 2005**

**Word Count: ~2900 Words**

## **Abstract**

The purpose of this project is to create a surrogate head model that can be used in axial impact tests. Our client, the Injury Biomechanics Lab at the University of British Columbia, will use this head to perform vertical drop tests on human cadaver cervical spines with surrogate spinal cords. The major requirements for the head model are to: replicate the mass, inertia properties, and impact behaviour of the human head, withstand repeated impact testing, be instrumented for acceleration, and mount easily to cadaver cervical spines. Three conceptual models were developed to meet these requirements. Of these, a fundamental design was chosen and has been fully specified. The main components of this design include a base plate, I-beam frame, and skull cap. The base plate is mounted to the occipital bone of cervical spine specimens with a layer of epoxy putty used for alignment and force transfer. The frame consists of an aluminum I-beam and contains a mounting location for the accelerometer. The skull cap will be a sand cast replicate of a typical head model. Prototypes have been produced of the base plate and frame and a final assembly is expected by the end of April. Further development of the head model may include impact force response matching and the application of a skin layer.

# Table of Contents

ABSTRACT.....	II
TABLE OF CONTENTS.....	III
LIST OF FIGURES .....	IV
LIST OF TABLES .....	IV
1.0 - INTRODUCTION .....	1
2.0 - DISCUSSION.....	3
2.1 - SUMMARY OF CONCEPT ANALYSIS .....	3
2.2 - TECHNICAL ANALYSIS .....	4
2.2.1 - <i>System Level Design</i> .....	4
2.2.2 - <i>Configuration Design</i> .....	6
2.2.3 - <i>Parametric Design</i> .....	8
2.3 - MANUFACTURING ANALYSIS .....	9
2.3.1 - <i>Base Plate</i> .....	9
2.3.2 - <i>Frame</i> .....	10
2.3.3 - <i>Skull Cap</i> .....	10
2.4 - PROTOTYPING .....	10
2.4.1 - <i>Occipital Bone Mounting Methods</i> .....	11
2.4.2 - <i>Surrogate Model Shape</i> .....	12
3.0 - CONCLUSIONS.....	13
3.1 - RECOMMENDATIONS .....	13
APPENDICES .....	14
APPENDIX A - PROJECT PROPOSAL.....	15
APPENDIX B - CONCEPTUAL ANALYSIS REPORT .....	32
APPENDIX C - TECHNICAL DRAWINGS .....	24
APPENDIX D - BILL OF MATERIALS .....	25
APPENDIX E - CALCULATIONS .....	26

## List of Figures

FIGURE 1: TYPICAL DROP TEST APPARATUS .....	1
FIGURE 2: SCHEMATIC DIAGRAM OF THE FUNDAMENTAL HEAD DESIGN .....	5
FIGURE 3: REVISED SCHEMATIC DIAGRAM OF THE HEAD DESIGN .....	6
FIGURE 4: HEAD COORDINATE SYSTEM FROM WALKER <sup>1</sup> .....	7
FIGURE 5: OCCIPITAL MOUNT PROTOTYPE .....	11
FIGURE 6: FRAME PROTOTYPE OF MOUNTING HOLES.....	12

## List of Tables

TABLE 1: VALUES FOR MASS, CENTER OF MASS AND MASS MOMENT OF INERTIA OF HEAD <sup>1</sup> .....	7
TABLE 2: MASS, MASS MOMENT OF INERTIA AND CENTER OF MASS RESULTS FROM EXCEL.....	8
TABLE 3: MASS, MASS MOMENT OF INERTIA AND CENTER OF MASS RESULTS FROM CAD MODEL .....	9

## 1.0 - Introduction

Over the past 3 months, a physical model of the human head has been in development by three Mechanical Engineering undergraduate students as their 4<sup>th</sup> year capstone project. The head model will be used in the Injury Biomechanics Laboratory as part of an upcoming study on cervical spine injuries resulting from axial impact drop tests. The experiments will be performed in a custom-built drop tower with the head model attached to cervical spine specimens mounted in an inverted position to the underside of the carriage. The objective of this study will be to examine the mechanisms of cervical spine fracture and spinal cord deformations during axial impact. Loads at the head surface and base of neck will be recorded along with head accelerations and positions of the vertebrae. Figure 1 illustrates a typical axial impact drop test apparatus. As opposed to using cadaver heads with the cervical spine specimens, a surrogate head will be used to ensure consistent instrumentation and system parameters between all tests.

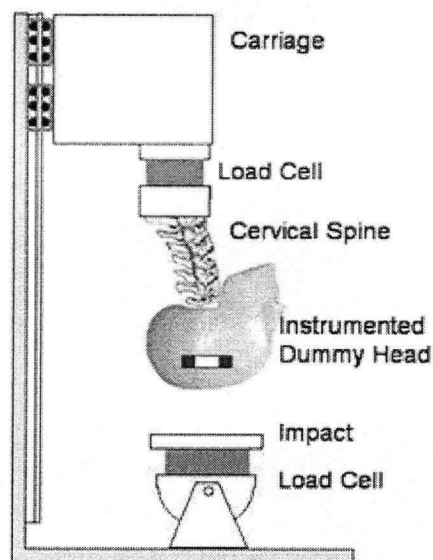


Figure 1: Typical Drop Test Apparatus

The goal of this project was to have a physical model of the human head designed and built by the end of April. At this time, most of the design details have been finalized and fabrication of the head model components has begun. Biofidelity of this model was obtained by matching physical parameters of the human head. The ideal mass and inertia values were obtained from published literature while the curvature of the top surface was matched to that of a typical head foam model.

The structural integrity of this model is important as it will be subjected to multiple impacts and must not deform or fail during the experiments. The dimensions and strengths of each component are such that the applied loads will not produce stresses beyond the strength limit of the materials. Mounting between the head model and cervical spine specimens is fairly simple and allows for both translational and rotational alignment adjustments. Sufficient space has been allocated for an accelerometer to be mounted in the model, but no mounting holes have been provided as the accelerometer has not been specified.

More details on the requirements and intended use of the head model can be found in the project proposal included in Appendix A.

## **2.0 - Discussion**

### **2.1 - Summary of Concept Analysis**

The three primary conceptual alternatives were the Sawbones model, the modified Hybrid III, and the fundamental design. Both Sawbones and Hybrid III concepts utilized an existing head model and modified them to match our specifications. The Sawbones head is a solid plastic piece that had geometric shape of human head. The Hybrid III head is the head from Hybrid III crush test dummy developed by General Motor Inc. Finally, the fundamental design concept was originally intended to model the head as a mass-spring system. Both the Sawbones and Hybrid III models were limited in the fact that both models have existing shape and design. The modification of these designs to match the required specifications is difficult whereas the fundamental model consists of fabricating the head from scratch and has no such limitations.

The Hybrid III concept involves purchasing of a Hybrid III model and modifying the mounting locations of the accelerometers and the occipital bone. This would have been done by removing the neck mounting plate and replacing it with a custom design. The Hybrid III already has matching mass and inertia properties, so no modifications were needed in this area.

The Sawbones concept consists of purchasing one of their head models and modifying it. A hole would need to be drilled in the back to mount the accelerometer, and modifications made in order to mount the occipital bone. Mass is to be added at specific locations to meet the mass and inertia properties.

For the fundamental design, a complete head model has to be designed and manufactured although the head does not need to resemble a head as long the properties of the head are matched. This involves the design and manufacture of a skull cap, frame, and mounting for the occipital bone and accelerometer.



The fundamental design concept has been selected for further development as the head model to be used for axial impact testing in the Injury Biomechanics Laboratory. A weighted score of 4.6 out of 5 suggests that this design was superior to the others with respect to the functional requirements and their solutions. Most of the advantages to this concept result from the fact that there was complete control over the properties and dimensions of the unit. As the design was "from scratch", there were no existing constraints that would require extra work or risk a compromise of requirements. Also, the flexibility in the components used for this design would easily allow for any modifications that would be needed in the future. Most of the other designs did not easily allow for customization to meet the needs of this application.

Please refer to Appendix B for more detail analysis of the conceptual alternatives.

## **2.2 - Technical Analysis**

The next step after completing the conceptual alternative analysis was to start the in-depth technical analysis for the proposed design. First, the basic components of the design were defined. Next step was to specify the general dimensions and shape of the components. Finally, detail calculations were done to ensure that the overall head design had the correct mass, mass moment of inertia and center of mass properties.

### **2.2.1 - System Level Design**

The basic building blocks of the initial proposed fundamental design were the skull cap, the frame, the accelerometer, the weight block, the occipital bone mounting base, and the epoxy putty. The main requirements for the skull cap were the material strength and top geometry. The skull cap needed be strong enough to withstand forty repetitive impact testing. It also needed to represent the top curvature of the human head. The next element was the frame. The purpose of the frame was to encase the

accelerometer and to connect the mounting base with the skull cap. The accelerometer would be provided by the client and the size of the accelerometer could be modified to fit the design. The weight block was to be placed strategically along the beam to obtain the correct mass and inertia of the head. The weight block would be constructed of aluminum casing with lead encapsulated and bolted to the frame. The last two elements of the design were the occipital bone mounting base and the epoxy putty. The mounting base was to attach the occipital bone to the frame whereas the epoxy putty would be inserted between the mounting and the occipital bone to avoid stress concentration on the bone. Figure 2 is the schematic diagram of the initial proposed fundamental head design.

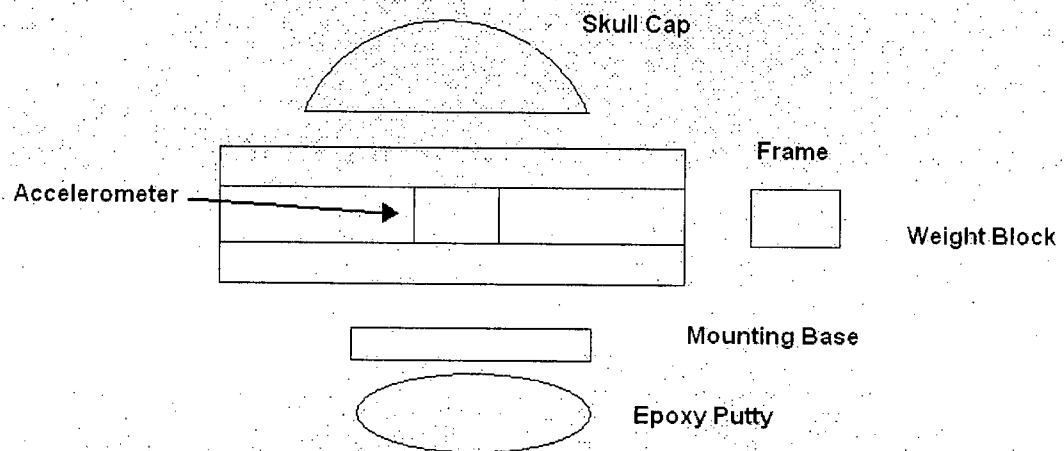


**Figure 2: Schematic Diagram of the Fundamental Head Design**

A prototype of the mounting base and the frame were made to validate the concept. However, the prototypes had shown that the mounting base is not needed for mounting the occipital bone to the frame-skull cap assembly. Hence, the basic components of the head design were reconsidered and re-defined. Although the mounting plate was proven to be unnecessary, the center of gravity calculation done in

the parametric design stage had shown that a large portion of the mass was needed in the area close to the occipital bone. A base plate was, therefore, brought back to the design, but for the purpose of increasing mass weight, not for the mounting function. In addition, the weight block, which initially used to balance the mass, mass moment of inertia and center of gravity, becomes inadequate in its function when calculation was performed, and therefore, is taken out the design. A revised schematic diagram is shown in Figure 3.

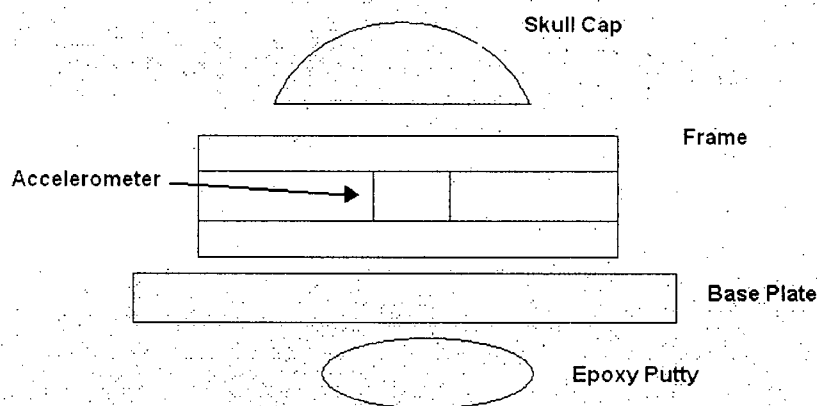


**Figure 3: Revised Schematic Diagram of the Head Design**

### 2.2.2 - Configuration Design

Once the basic functions of the elements had been defined, the general dimensions were then determined from anthropometric data taken from Walker<sup>1</sup> and

<sup>1</sup> Walker L, Harris E, Pontius U. (1973). Mass, Volume, Center of Mass and Mass Moment of Inertia of Head and Head and Neck of Human Body. In Proceedings of the 17<sup>th</sup> Stapp Car Crash Conference, P525-537.

Jurgens<sup>2</sup>. The coordinate system used to reference the dimensions in the head design is taken from Walker. The coordinate system is shown in Figure 4.

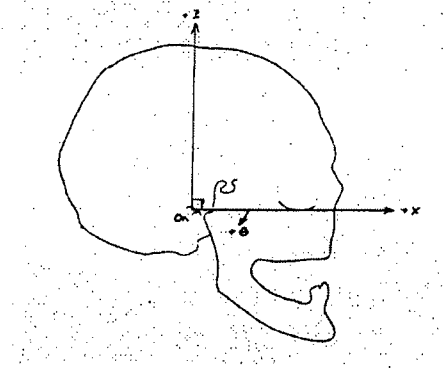


**Figure 4: Head Coordinate System from Walker<sup>1</sup>**

The mean value for the height of the head is 12.9 cm with standard deviation of 0.6 cm. The height of the head was measured from the external auditory meatus to the top of the head. The external auditory meatus is the origin of the reference axis used in dimensioning the head model. The head length, which is the distance between center most prominent point between the eyebrows and the most backward projection of the head, is 19.8 cm +/- 1.5 cm. The center of mass is given by the distance from the origin of the x-axis and the angle rotated clockwise, which is converted to x and y values shown in Table 1. Table 1 also lists the mean and standard deviation for the mass and inertia values. The average age of the group in which the data was taken was 62 years with a range from 41 to 79 years. The age group corresponds very closely with the age of cadaver specimen that will be use in the axial impact test.

**Table 1: Values for Mass, Center of Mass and Mass Moment of Inertia of Head<sup>1</sup>**

	Mass	x	y	Inertia
	(g)	(cm)	(cm)	(kg-cm <sup>2</sup> )
<b>MEAN</b>	4376.00	1.38	2.41	233.24
<b>SD</b>	591.00	0.82	1.07	36.61

<sup>2</sup> Jurgens H, Aune I, Pieper U. (1990). International Data on Anthropometry. Federal Institute for Occupational Safety and Health.

Given these dimensions and values, the basic dimensions of the components were identified. The head frame should not be longer than 19.8 cm +/- 1.5 cm. The overall head assembly height should not be greater than 12.9 cm +/- 0.6 cm. The skull cap dimension is based on the head length and breadth as well. All the dimensions are converted to imperial units in the parametric design stage for manufacturing convenience.

### 2.2.3 - Parametric Design

The parameters that needed to be taken into consideration when designing the head model were mass, mass moment of inertia, and center of mass of the head. After the basic components and dimensions of the design have been specified, such as the height and the length of the head, other dimensions and properties were calculated and adjusted so that these parameters of the head were within an acceptable range. Additionally, materials were specified based on the mass calculation.

An Excel spreadsheet was created to optimize the overall head properties. First, the approximate volume of each component was calculated based on the dimensions found in the configuration process. The overall mass was then calculated for various combinations of materials to obtain the desired mass. The specific dimensions of each component were also calculated to have the most optimal combination of mass, center of mass, and mass moment of inertia. Table 2 summarizes the dimensions and the properties calculated with Excel spreadsheet. Please see Appendix E for the detail of the calculation.

Table 2: Mass, Mass Moment of Inertia and Center of Mass Results from Excel

EXCEL RESULTS								
Layer	Width (in)	Height (in)	Depth (in)	Density (lb/in <sup>3</sup> )	Mass (lb)	Inertia (lb-in <sup>2</sup> )	Cg to Cg Dist (in)	Iyy about Cg (lb-in <sup>2</sup> )
Skull Cap	8.00	1.00	3.00	0.29	6.94	37.57	-0.50	39.30
Frame	7.00	3.00	2.50	0.10	1.12	5.41	-2.50	12.41
Base Plate	7.00	1.00	2.50	0.10	1.50	6.25	-4.50	36.63
Total		5.00			9.56			88.34
Cg Height	1.36							

Once the rough dimensions had been determined using Excel spreadsheet, a CAD model was built. The mass, center of mass and mass moment of inertia were again calculated using Pro/Engineer software. Based on the CAD model calculation, the shape of base plate was modified to optimize the overall inertia property and the values of these properties were re-calculated (shown in Table 3). There was some variation between the Pro/Engineer values and the Excel spreadsheet value because the volume calculated in Excel spreadsheet is based on rectangular skull cap while the CAD model had skull cap shape like the Sawbones model.

**Table 3: Mass, Mass Moment of Inertia and Center of Mass Results from CAD Model**

PRO/E RESULTS		
Mass	9.61	lb
Iyy about Cg	69.03	lb in <sup>2</sup>
Cgz (from Ref)	1.160	in

## 2.3 - Manufacturing Analysis

The head model consists of three components: The base plate, frame, and skull cap. Stock materials will be used to fabricate the base plate and frame and the skull cap will originate as an aluminum sand casting. Assembly and dimensioned production drawings can be found in Appendix C.

### 2.3.1 - Base Plate

The primary function of the base plate is to provide mounting locations for the occipital bone and head frame. In addition, the base plate is responsible for most of the head mass and inertia properties. To meet both these criteria, careful attention must be given to the overall dimensions of the plate and the location of the mounting holes. The plate will be machined from 1" thick stainless steel flat bar stock. Dimensions can be taken directly from the production drawings and used to set up cuts taken on a milling machine. The locations for most of the holes to be drilled are referenced from the

anterior plate edge while some are dimensioned with respect to the large hole near the plate centre. This hole will locate the surrogate spinal cord, which must be a certain distance away from the occipital bone and, as such, the occipital mounting hole locations are referenced from it. The estimated time needed to manufacture the base plate is 5 hours.

### **2.3.2 - Frame**

The frame consists of a 3" high, 2.5" wide aluminum I-beam mounted between the base plate and skull cap. A window in the centre of the web will be milled-out and is where the accelerometer array will be mounted. As the accelerometer has not been specified, no mounting holes have been provided. 8 holes must be drilled in the flanges to provide mounting points for the base plate and skull cap. Both ends of the I-beam will be machined flat, although only one of them is used to reference the mounting hole locations. Fabrication of the frame should take approximately 4 hours.

### **2.3.3 - Skull Cap**

Using a Sawbones head model to create a mould, an aluminum sand casting of the top surface of a typical human head will be made. The inferior and both lateral surfaces will be milled to the dimensions given in the production drawings. Mounting holes will then be drilled using either the anterior or posterior ends as a reference point. In addition to producing the sand casting, machine of the skull cap will take 3 hours.

## **2.4 - Prototyping**

Several prototypes are made to ensure that the various components are practical and reasonable. Prototypes have provided essential information that would not

otherwise be obvious. For instance, through prototyping, the mounting plate component that is first specified in the system level design process becomes dispensable.

#### **2.4.1 – Occipital Bone Mounting Methods**

The head model will be mounted to the occipital bone that will still be attached to cadaver cervical spines. The mounting of the head model consisted of fasteners passed through holes drilled in the occipital bones and attached to the mounting base, to which the head model would then be mounted. To avoid stress concentrations around the bolts that would lead to premature occipital bone fracture, epoxy putty would be placed between the mounting base and the occipital bone so that there was no direct contact between the base plate and the occipital bone.

A prototype of the occipital mount (shown in Figure 5) was made as a proof-of-concept for this particular mounting design. We found that this design allowed for easy assembly as well as provided good alignment capabilities.

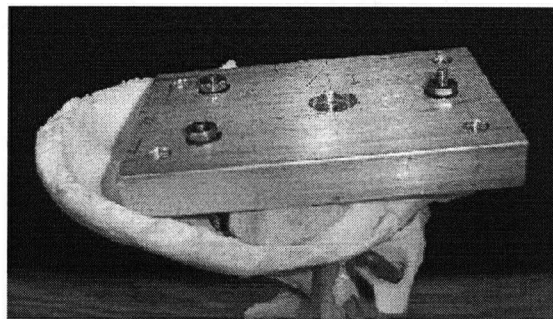


**Figure 5: Occipital Mount Prototype**

Although the occipital mount prototype has demonstrated the feasibility of the design, it was recognized that the mounting base was not required. The simplicity of the occipital mount allowed for it to be easily incorporated into the head frame. A prototype of the frame (shown in Figure 5) was fabricated and the occipital mounting holes were produced in it. This prototype showed that there was no need for an additional mounting plate.



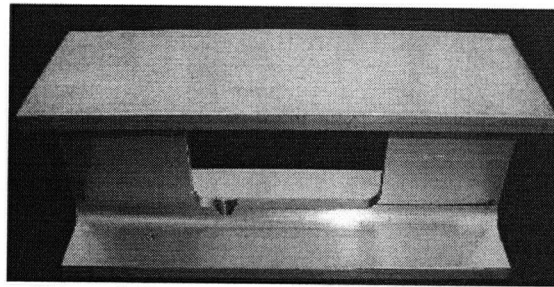


**Figure 6: Frame Prototype of Mounting Holes**

#### **2.4.2 – Surrogate Model Shape**

The curvature for the top of the head is a crucial factor for the impact testing as it is the first contact point during the impact. Nevertheless, it would be difficult to machine an aluminum piece to shape like a head. The Sawbones head model was therefore used as a prototype. The geometry and the dimensions of the Sawbones head were examined and measured to ensure that they were within the acceptable range. The skull piece was then fabricated by casting. The mould would be made from Sawbones model.

### **3.0 - Conclusions**

Of the three conceptual alternatives derived from the head model requirements, the fundamental design was selected as it allows for the best match of physical parameters. The final design consists of a base plate attached to the occipital bone through a layer of epoxy putty, an I-beam frame which houses the accelerometer, and a skull cap with typical human head curvature. The components of the head model can be manufactured in-house, with the exception of the skull cap, which will originate as a sand casting. Prototypes of the occipital mount and frame have been produced, resulting in a better visualization of the head model, and have contributed to further refinement of the design.

#### **3.1 - Recommendations**

Future development of the head model may include impact force response matching and the application of a skin-like material. Impact testing of the head model can be performed in the IBL drop tower and the force response compared to that found in the literature that describes the impact response of a human head. The response of the head model will be somewhat affected by a skin layer on the skull cap surface. As such, it may be necessary to use a skin layer in order to match the impact properties. One possible method of implementing skin would be to have a sheet of silicone placed over the skull cap and anchored below the top flange of the I-beam frame.